Pioneering Investigations into Organometallic Electrochemistry

Thomas Dann

A thesis submitted in accordance with the requirements for the degree of Doctor of Philosophy by research at the University of East Anglia

School of Chemistry

University of East Anglia

March 2014

Abstract

Recently there has been a large effort to take advantage of electrochemistry to develop and understand novel chemical processes and reactivity. This thesis contains investigations into the synthesis and electrochemical properties of three diverse organometallic systems.

In chapter 2, the first experimental determination of a an unsupported Au^{II}-Au^{II} bond is reported. The electrochemical characterisation of gold(III) hydride, hydroxide and chloride pincer complexes based on a backbone of a doubly cyclometalated 2,6-bis(4'-*tert*-butylphenyl) pyridine ligand was performed, in which it was determined that upon reduction of the Au^{III} complexes, an unsupported Au^{II} dimer is formed, confirmed by characterisation of an authentic sample of the dimer. Using digital simulation, the reduction potentials of the hydride and hydroxide along with the oxidation potential of the dimer were determined, allowing the construction of a Hess cycle, from which the bond energy of the gold-gold bond in the dimer and the difference of the Au-OH and Au-H bond energies could be estimated.

In chapter 3, the redox non-innocent behaviour of the ligands in zinc(II) bis(formazanate) complexes is investigated. These complexes have been electrochemically characterised by cyclic voltammetry, showing remarkably facile reduction to a radical anion, and further reduction to a dianion. Simulation of the cyclic voltammetry recorded for these compounds yielded optimised values of formal potentials, E^0, and electron transfer rate constants, k^0.

In chapter 4, the synthesis and electrochemical characterisation of the first known examples of triazole-substituted cymantrene and cyrhetrene complexes are reported. The compounds η^5-(-phenyltriazol-1-yl)cyclopentadienyl tricarbonyl manganese(I), with a phenyl, 3-aminophenyl or 4-aminophenyl substituent on the 4-position of the triazole ring were prepared via the copper(I)-catalyzed azide-alkyne cycloaddition (1,3-CuAAC) reaction. Cyclic voltammetric characterization of the redox behavior of each of the three cymantrene–triazole complexes is presented together with digital simulations, in-situ

infrared spectroelectrochemistry, and DFT calculations to extract the associated kinetic and thermodynamic parameters. The synthesis and characterisation of the rhenium(I) analogues of the phenyl and 4-amino triazole substituted complexes are also reported.

In chapter 5, the use of diazirines as carbene precursors for carbon surface modification is investigated, via the synthesis and characterisation of diazirine derivatised cymantrene and cyrhetrene. The surface modification of glassy carbon electrodes was attempted via irradiation of the half-sandwhich diazirine bearing complexes, resulting in oxidation waves visible on the electrode by cyclic voltammetric analysis.

Acknowledgements

Firstly I would like to express my gratitude to my supervisor, Dr. Gregory G. Wildgoose for the opportunity to be in his reseach group and embark on this exciting and groundbreaking research, and I am thankful for his enthusiastic guidance throughout.

I am also grateful to a number of individuals who made this work possible. In particular Professor Manfred Bochmann and Dr Simon Lancaster for access and use of their resources and guidance on this research project; Dr. Edwin Otten and Mu-Chieh Chang for their collaboration, Dr. David Day for his collaboration and guidance; Dr. Robin Blagg for his advice and crystallography expertise and Elliot Lawrence and James Butress for their support and friendship. Thanks also goes out to the students and post-docs within 1.34b whose help has been outstanding.

I would also like to acknowledge Dr. David Huges for his expert elucidation of crystal structures and Dr. Joseph Wright and Dr. Vasily Oganesyan for their input and DFT calculations.

Finally I would like my family for their tremendous support throughout all my studies, with special thoughts to my parents Chris and Mary who are always there for me.

This research was funded by a Dean's Studentship from the University of East Anglia.

Contents

Abstract i

Acknowledgements iii

List of Abbreviations ix

1. Introduction to Organometallic Electrochemistry 1

1.1. Early Organometallic Electrochemistry 1

1.1.1. Electrochemical Studies of Sandwich Compounds 2

1.2. Mechanistic Electrochemistry 3

1.2.1. 17 and 19 Electron Complexes 7

1.2.2. Dimerisation 8

1.2.3. Electrochemistry with Chemical Redox Agents 9

1.2.4. Ligand exchange 10

1.2.5. Electrochemical effects of ligand derivatisation 11

1.2.6. Catalysis of organic molecule transformations 12

1.2.7. Mixed-valence compounds 14

1.3. Electrochemical Techniques and Analysis 16

1.3.1. Diffusion 16

1.3.2. Migration 16

1.3.3. Convection 17

1.3.4. Electrode Kinetics 18

1.3.5. Cyclic voltammetry 20

1.3.6. Digital Simulation in Electrochemistry 23

1.4. Surface Bound Electrochemistry . . . 24
1.4.1. Graphite . . . 24
1.4.2. Glassy carbon electrodes . . . 26
1.4.3. Carbon nanotubes . . . 27
1.4.4. Modification methods . . . 28
1.4.5. Diazonium salt reduction . . . 29
1.4.6. Lithium alkyne salt oxidation . . . 31
1.4.7. Exploitation of CNT edge plane defects . . . 32
1.5. Modification with Non-heterocyclic Carbenes . . . 33
1.5.1. Diazirines as carbene precursors for surface modification . . . 35
1.6. Surface Characterisation Techniques . . . 36
1.6.1. X-ray Photoelectron Spectroscopy . . . 36

2. The electrochemistry of gold(III) pincer complexes 43
2.1. Introduction to the organometallic chemistry of gold . . . 43
2.2. Electrochemistry of organogold compounds . . . 47
2.3. Gold pincer complexes . . . 48
2.4. Gold(II) chemistry . . . 49
2.5. Electrochemical characterisation of Gold(III) hydroxide, hydride and chloride complexes . . . 50
2.6. Electrochemical Simulations . . . 59
2.7. Thermodynamic Cycle of Reductive Condensation . . . 63
2.8. DFT Calculations . . . 65
2.9. Conclusions . . . 67

3. Bis(formazanate) zinc compounds 71
3.1. Introduction to redox non-innocent ligands . . . 71
3.2. Synthesis of bis(formazanate) zinc compounds . . . 73
3.3. Cylic Voltammetric Analysis . . . 75
3.3.1. Chemical reduction of zinc formazante compounds . . . 80
3.3.2. DFT calculations . . . 83
3.4. Conclusion . . . 84

4. Piano stool–triazole "Click" Products **88**

4.1. Introduction to cymantrene . . . 88
4.2. Redox Chemistry . . . 89
4.3. Ligand Exchange - Replacing the Carbonyls . . . 90
4.4. Cyrhetrene . . . 90
4.5. Redox Chemistry . . . 91
4.6. Surface bound organometallic chemistry . . . 92
4.7. Introduction to triazole chemistry . . . 93
4.8. Organometallic triazole chemistry . . . 96
4.9. Synthesis and characterisation of cymantrene triazole derivatives . . . 97
4.10. Cyclic voltammetric characterisation . . . 104
4.11. Synthesis and characterisation of cyrhetrene triazole complexes . . . 118
4.12. Crystallographic analysis of triazole derivatised cyrhetrene . . . 119
4.13. Electrochemical characterisation of cyrhetrene triazole derivatives . . . 121
4.14. Surface bound electrochemistry . . . 124
4.14.1. Triazole derivatised phenyldiazonium reduction method . . . 124
4.14.2. Surface coverage estimation . . . 125
4.14.3. Electrode surface 1,3-CuAAC of cymantrene azide . . . 126
4.15. Conclusions . . . 129

5. Diazirine derivatised cymantrene and cyrhetrene **134**

5.1. Using carbene forming diazirines for organometallic electrode modification . . . 134
5.2. Preparation and characterisation of cymantrene derivatives . . . 136
5.2.1. Preparation and characterisation of methylcarboxylate cymantrene . . . 137
5.2.2. Preparation and characterisation of carboxyl cymantrene . . . 139
5.2.3. Preparation and characterisation of diazirine derivatised cymantrene . . . 140
5.3. Cyrhetrene derivatives . . . 146
5.3.1. Cyrhetrene carboxylic acid . . . 146
5.3.2. Cyrhetrene diazirine . . . 146
5.3.3. Cyclic voltammetric characterisation . . . 148

5.4. Surface Bound Electrochemistry . . . 149
5.4.1. Modification with cymantrene derivatives - diazirine method . . . 149
5.4.2. Characterisation with X-ray Photoelectron Spectroscopy . . . 151
5.4.3. Surface coverage estimation: carbene insertion method . . . 154
5.4.4. Modification with cyrhetrene diazirine derivative . . . 155
5.5. Characterisation with X-ray Photoelectron Spectroscopy . . . 156
5.6. Conclusion . . . 158

6. Conclusion **161**

7. Methods and Materials **163**
7.1. General Considerations . . . 163
7.2. X-ray Crystallography . . . 163
7.3. Electrochemistry . . . 164
7.3.1. 2,2,2-Trifluoro-1-(3-methoxyphenyl)ethanone . . . 165
7.3.2. 2,2,2-Trifluoro-1-(3-methoxyphenyl)ethanone oxime . . . 165
7.3.3. O-Tosyl-2,2,2-trifluoro-1-(3-methoxyphenyl)ethanone oxime . . . 166
7.3.4. 3-(Trifluoromethyl)-3-(3-methoxyphenyl)diaziridine . . . 166
7.3.5. 3-(Trifluoromethyl)-3-(3-methoxyphenyl)diazirine . . . 167
7.3.6. 3-(Trifluoromethyl)-3-(3-hydroxyphenyl)diazirine . . . 167
7.3.7. Cymantrene azide $CymN_3$ **12** . . . 167
7.3.8. Cyrhetrene azide, $CyrN_3$ **19** . . . 168
7.4. Synthesis of cymantrene derivatives . . . 168
7.4.1. η^5-methylcarboxylate cyclopentadienyl tricarbonyl manganese(I) **23** . . . 168
7.4.2. η^5-[carboxyl]cyclopentadienyl tricarbonyl manganese(I) **24** - method I . . . 169
7.4.3. η^5-[carboxyl]cyclopentadienyl tricarbonyl manganese(I) **24** method II . . . 169
7.4.4. η^5-[4-phenyltriazol-1-yl]cyclopentadienyl tricarbonyl manganese(I) **13** . . . 169
7.4.5. η^5-[4-(amino)-4-phenyltriazol-1-yl]cyclopentadienyl tricarbonyl manganese(I) **14** . . . 170
7.4.6. η^5-[3-(amino)-4-phenyltriazol-1-yl]cyclopentadienyl tricarbonyl manganese(I) **15** . . . 171

7.4.7. 3-[3-(Trifluoromethyl)diazirin-3-yl]phenyl cymantrene monocarboxylate **28** 171
7.5. Synthesis of cyrhetrene derivatives 172
7.5.1. η^5-[carboxyl]cyclopentadienyl tricarbonyl rhenium(I) 172
7.5.2. 3-[3-(Trifluoromethyl)diazirin-3-yl]phenyl cyrhetrene monocarboxylate **30** 172
7.5.3. η^5-[4-phenyltriazol-1-yl]cyclopentadienyl tricarbonyl rhenium(I) **20** . . . 173
7.5.4. η^5-[4-(amino)-4-phenyltriazol-1-yl]cyclopentadienyl tricarbonyl rhenium(I) **21** 173

A. Crystallography Data **175**

List of Figures

1.1. Chemically and Electrochemically reversible voltammogram 4

1.2. Simulated voltammogram of an EC mechanism at varying scan rates 5

1.3. Example of an *EC* mechanism 5

1.4. Simulated voltammogram of an ECE mechanism at varying scan rates 6

1.5. Example of an *ECE* mechanism 7

1.6. The 1-electron oxidation and reactivity of an Ru indenyl complex, Nu = MeCN, thf 7

1.7. Dimerisation of the half-sandwich chromium carbonyl complex η^5-$C_5H_5Cr(CO)_3$] 9

1.8. The discovery that nitrosium cation is a 1-electron oxidant for half-sandwich complexes 9

1.9. The unusual reactivity of oxidised monocarbonyl cobalt half sandwhich complexes 11

1.10. Catalytic biphenyl synthesis driven by a contantly applied reductive potential, where dppe = bis(diphenylphosphino)ethane 13

1.11. The biferrocenes investigated by Henrickson 15

1.12. The superphane complexes investigated by Geiger, where n = 1, 3, 5 15

1.13. The potential applied to the electrode in a cyclic voltammetry experiment . . . 20

1.14. The inert atmophere cell with three electrodes employed for the electrochemical measurements recorded 22

1.15. The inert atmophere cell employed for bulk electrolysis 23

1.16. Discrete model of the solution adjacent to the electrode 24

1.17. Representation of the crystal structure of graphite 25

1.18. Schematic of pyrolytic graphite, with functional groups found on edge planes . 25

1.19. Schematic of the structure of a glassy carbon electrode 26

1.20. Schematic of a single wall (left) and a multiwalled CNT (right) 27
1.21. The forms of nanotubes, defined by their roll up vector 28
1.22. Nanotube morphologies 28
1.23. Methods for modifying a surface via a covalent bond, **a)** a gold-thiol SAM, **b)** Surface modification by oxidation of an amine, **c)** Surface modification by reduction of a diazonium salt 30

2.1. Examples of cyclometallated gold(III) compounds 44
2.2. Examples of unsupported gold(II) complexes 47
2.3. The gold(III) cyclometallated complexes that have been previously electrochemically characterised 47
2.4. Chemical formation of gold(II) dimer 50
2.5. The gold pincer complexes under investigation. 51
2.6. Full range cyclic voltammogram of **2** in CH_2Cl_2 (1.5 mmol dm^{-3}, 50 mmol dm^{-3} [^{n}Bu$_4$N][B(C$_6$F$_5$)$_4$]) at a scan rate of 100 mV s^{-1}. 52
2.7. Full range cyclic voltammogram of **3** in CH_2Cl_2 (1.5 mM, 0.05 M [^{n}Bu$_4$N][B(C$_6$F$_5$)$_4$]) at a scan rate of 100 mV s^{-1} 53
2.8. Full range cyclic voltammogram of **1** in CH_2Cl_2 (1.5 mmol dm^{-3}, 0.05 M [^{n}Bu$_4$N][B(C$_6$F$_5$)$_4$]) at a scan rate of 100 mV s^{-1} 54
2.9. Full range cyclic voltammogram of **4** in CH_2Cl_2 (1.5 mmol dm^{-3}, 0.05 M [^{n}Bu$_4$N][B(C$_6$F$_5$)$_4$]) at a scan rate of 100 mV s^{-1} 55
2.10. Cyclic voltammogram of **2** in CH_2Cl_2 (1.5 mmol dm^{-3}, 0.05 M [^{n}Bu$_4$N][B(C$_6$F$_5$)$_4$]) at scan rates of 100, 300 and 750 mV s^{-1} 56
2.11. Cyclic voltammogram of **3** in CH_2Cl_2 (1.5 mmol dm^{-3}, 0.05 M [^{n}Bu$_4$N][B(C$_6$F$_5$)$_4$]) at a scan rates of 100, 300 and 750 mV s^{-1} 57
2.12. Cyclic voltammogram of **1** in CH_2Cl_2 (1.5 mmol dm^{-3}, 0.05 M [^{n}Bu$_4$N][B(C$_6$F$_5$)$_4$]) at a scan rates of 100, 300 and 750 mV s^{-1} 58
2.13. Cyclic voltammogram of **4** in CH_2Cl_2 (1.5 mmol dm^{-3}, 0.05 M [^{n}Bu$_4$N][B(C$_6$F$_5$)$_4$]) at a scan rates of 100, 300 and 750 mV s^{-1} 59
2.14. Experimental vs. simulated voltammetry for compound **2** 61
2.15. Experimental vs. simulated voltammetry for compound **4** 62

2.16. DFT energies of gold(III) pincer reduction products 66

3.1. The electron transfer series of a nickel dithiolate, showing redox non-innonce of the ligand 72
3.2. Redox-non innocence of a ruthenium iminoquinone with acac ligands 72
3.3. a) β-diketiminate b) formazanate c) vedazyl radical d) 'metalloverdazyl' 73
3.4. Molecular structure of compound **7** 74
3.5. Thirty repeat cyclic voltammograms of a 2.5 mM solution of **5** in THF with $[^{n}Bu_4N][B(C_6F_5)_4]$ electrolyte recorded at 100 $mV\,s^{-1}$ 75
3.6. Thirty repeat cyclic voltammograms of a 2.5 mM solution of **6** in THF with $[^{n}Bu_4N][B(C_6F_5)_4]$ electrolyte recorded at 100 $mV\,s^{-1}$ 76
3.7. Thirty repeat cyclic voltammograms of a 2.5 mM solution of **7** in THF with $[^{n}Bu_4N][B(C_6F_5)_4]$ electrolyte recorded at 100 $mV\,s^{-1}$ 77
3.8. Experimental vs. simulated voltammetry for compounds **5** and **6** 78
3.9. Experimental vs. simulated voltammetry for compound **7** 79
3.10. Synthesis of mono and dianionic zinc formazanates 80
3.11. Molecular structures of **8** and **9** 82
3.12. SOMO and spin density of the singly and doubly reduced *p*-tolyl complex . . . 84

4.1. Examples of recently published work on cymantrene, top: water splitting, bottom: alkane coordination 89
4.2. The electrochemical oxidation of cymantrene to form the radical cation 90
4.3. The electrochemical oxidation and dimerisation of cyrhetrene 91
4.4. Cycloaddition of oxidised cyclic alkenes 92
4.5. Cylcoaddition products from cyclopentene and cis-cyclooctene 92
4.6. Attachment of cobaltocenium to GCE via diazonium reduction 93
4.7. Postulated copper catalysed mechanism of the regioselective 1,3 cycloaddition . 94
4.8. Examples of coordination complexes of 2-pyridyl-1,2,3-triazole ligands 95
4.9. The tripodal triazole ligand used by Schweinfurth 96
4.10. Examples of ferrocenyl triazoles prepared by Molina *et al.* 96
4.11. Ruthenium triazolyl hydrogenation catalyst 97
4.12. Crystal structure of compound **13** 100

4.13. Crystal packing of compound **13** 101
4.14. Crystal structure of compound **15** 101
4.15. Crystal packing of molecules of **15**, viewing along the αaxis 103
4.16. Atom labels for the triazole moiety 104
4.17. Cyclic voltammetry of **13**, repeat scans 105
4.18. Cyclic voltammetry of **13** at varying scan rates 106
4.19. Spectroelectrochemistry of compound **13** 108
4.20. Predicted IR spectrum of **13** (solid line) and its oxidised form (dotted line) . . 109
4.21. SOMO of **13** 110
4.22. Experimental vs. simulated voltammetry for compound **13** 112
4.23. Cyclic voltammetry of **14** at varied scan rates 115
4.24. Experimental vs. simulated voltammetry for compound **14** 116
4.25. Cyclic voltammetry of **15** 118
4.26. Molecular structure of compound **20** 120
4.27. Cyclic voltammetry of compound **20** 122
4.28. Cyclic voltammetry of compound **21** 123
4.29. Attachment of 3-amino triazole derivatised cymantrene to a GCE 124
4.30. Surface bound voltammetry of compound **15** 125
4.31. 'In situ' formation of triazole derivatised cymantrene at the GCE 127

5.1. Diazirine inter and intramolecular reactions 135
5.2. Reactivity of Brunner's diazirine 135
5.3. Surface modification with diazirine derivatised ferrocene 136
5.4. Cyclic voltammetry of cymantrene methyl ester 138
5.5. Scan rate variation of cymantrene methyl ester 139
5.6. COSY ^{1}H NMR of **28** 142
5.7. HSQC ^{13}C and ^{1H} NMR of **28** 143
5.8. Azine formed upon photochemical dimerisation of diazirine 143
5.9. Cystal structure of diazirine derivatised cymantrene 144
5.10. Cyclic voltammetry of diazirine derivatised cymantrene 145
5.11. Scan rate variation of diazirine derivatised cymantrene 146

5.12. Cyrhetrene diazirine derivative preparation 147
5.13. COSY NMR of compound **30** 148
5.14. Cyclic voltammetry of diazirine derivatised cyrhetrene 149
5.15. Modification of the GCE via diazirine photolysis 150
5.16. Voltammogram of electrode treated with **28** 150
5.17. XPS survey spectra with signals from F 1s, O 1s and C 1s resulting from graphite (top) and hollow-tube MWCNT (bottom) modified with **28** 152
5.18. Peak fitted regions for F1s and Mn2p signal regions of cymantrene modified graphite and MWCNTs 153
5.19. Voltammogram of electrode treated with **30** 155
5.20. Responce of cyrhetrene diazirine treated electrode upon the presence of cyclopentene. Black: 0 mM, Red 0.5 mM, Green, 1.0 mM, Blue 2.0 mM C_5H_8 156
5.21. XPS survey spectra with signals from F 1s, O 1s and C 1s resulting from graphite (top) and hollow-tube MWCNT (bottom) modified with **30** 157
5.22. Peak fitted regions for F1s and Mn2p signal regions of cyrhetrene modified graphite and MWCNTs 158

List of Tables

2.1. Simulated parameters of the reduction of **2** and **3** and the oxidation of **4** . . . 60

2.2. Relative energies of electrochemical steps in kJ mol^{-1} 65

3.1. Selected bond lengths in **7** 74

3.2. Simulated parameters of the reduction of compounds **5** **6** and **7** 79

3.3. Selected Bond Lengths in **8** and **9** 81

3.4. Selected Bond Lengths in **11** 83

4.1. IR stretches for **12**, **13**, **14** and **15** 99

4.2. Selected bond lengths (Å) for compounds **13** and **15** 102

4.3. Mean bonds lengths of **13** and **15** 104

4.4. Redox parameters, associated chemical equilibria and rate constants determined from digital simulation of CVs for compounds **13** and **14** 117

4.5. vcm^{-1} bands for cyrhetrene and **19**, **20** and **21** 119

4.6. Selected bond lengths of the two molecules of **20** in the asymmetic unit 120

5.1. Bond lengths of **28**, cymantrene and 3-aryl-3trifluoromethyl diazirine 144

A.1. Crystal structure analysis of compound **13** 175

A.2. Crystal structure analysis of compound **15** 176

A.3. Crystal structure analysis of compound **20** 176

A.4. Crystal structure analysis of compound **28** 177

List of Schemes

1.1. Schematic for a typical electron-chain-transfer catalytic system 12

1.2. The catalysis of ligand exchange on an 18-electron manganese(I) complex by its oxidised form[1] 13

1.3. Reaction between electrogenerated Pt hydride and half sandwhich rhenium carbonyl 14

1.4. The reaction of organometallic alkynyl lithium salts with a GCE upon oxidation 31

1.5. An overview of the methods of edge-plane defect chemistry 33

1.6. Summary of the methods used to covalently modify the basal-plane of CNTS . 35

2.1. Examples of homobridged gold(II) complexes 46

2.2. Preparation of gold(III) cyclometallated chloride complex 49

2.3. Preparation of gold(III) pincer complexes 49

2.4. Electron transfer steps for I and D, where X = H, Cl. 55

2.5. Relationship between **3**, **2**, **4** and water 63

2.6. Overall reaction in DFT analysis 65

2.7. The 6 electrochemical and chemical reaction steps upon gold(III) pincer reduction 65

3.1. Zinc formazanate preparation 74

4.1. The Huisgen 1,3 dipolar cycloaddition 93

4.2. Regiogselective triazole formation 94

4.3. Preparation of cymantrene triazoles 98

4.4. The proposed mechanism and parameters used in the digital simulation of the voltammetry of **13** 111

4.5. The proposed mechanism and parameters used in the digital simulation of the voltammetry of **14** 114
4.6. Preparation of cymantrene triazoles 118

5.1. Preparation of cymantrene methyl ester 137
5.2. Preparation of cymantrene carboxylic acid 140
5.3. Preparation of 3-aryl-3-trifluormethyl-diazirine 140
5.4. Cymantrene diazirine derivative preparation 141

List of Abbreviations

AFM	Atomic force microscopy
CNT	Carbon nanotube
COSY	Correlation spectroscopy
Cp	Cyclopentadienyl
CVD	Chemical vapour deposition
DC	Direct current
DCC	N,N'-Dicyclohexylcarbodiimide
DFT	Density functional theory
DMAP	4-Dimethylaminopyridine
EPR	Electron paramagnetic resonance
ETC	Electron transfer chain
FTIR	Fourier transform infra-red spectroscopy
GCE	Glassy carbon electrode
HOMO	Highest occupied molecular orbital
HOPG	Highly oriented pyrolytic graphite
HSQC	Heteronuclear single quantum coherence spectroscopy
LMCT	Ligand to metal charge transfer
LUMO	Lowest unoccupied molecular orbital
MeCN	Acetonitrile
MLCT	Metal to ligand charge transfer
MWCNT	Multi-walled carbon nanotube
NHC	N-Heterocyclic carbene
NMR	Nuclear magnetic resonance spectroscopy
Nu	Nucleophile
SAM	Self assembling monolayer
SCE	Saturated calomel electrode
SOMO	Singly occupied molecular orbital
SWCNT	Single wall carbon nanotube
THF	Tetrahydrofuran
WCA	Weakly coordinating anion

1. Introduction to Organometallic Electrochemistry

Electrochemistry is considered by many to be an analytical technique primarily used to measure the redox potentials of compounds versus a standard. However over the last few decades, more and more organometallic chemists are embracing electrochemistry for its power to influence the electronic structure and chemical reactivity of a complex. This is where the term *molecular* electrochemistry arises, distinguishing the simple measuremeant of reduction potentials from the ability to access novel reactivity or obtain mechanistically valuable information.

A huge advantage of molecular electrochemistry is its application in electrosynthesis. In electrosynthesis, electrons are involved as the reagent or the catalyst and extremly energy efficient and selective processes can be set up, in constrast to thermally driven reactions. At the turn of the 21st century there are growing concerns over the use of raw materials and energy and the effect on the environment this has. With this in mind in can be seen that electrodes provide a convenient way to selectively achieve a highly reactive intermediate under milder conditions than by heating alone.

1.1. Early Organometallic Electrochemistry

The electrochemical properties of organometallic compounds have been studied since early in the 20th century. The main analytical method employed in this early era of electrochemistry was DC polarography. In this method, a fixed potential is applied across the electrode-solution interface, where the electrode usually consists of mercury. The resulting current is then measured across a series of different potentials, to gather the required data points to plot a full polarogram. An alternative procedure is to measure the current at a potential that is

sweeping across the desired range so slowly as to be considered constant. The advantage of this procedure is that it allows automatic plotting of data. The potential range of this method is rather limited in the anodic region from the thermodynamically facile oxidation of mercury to mercury(I). The cathodic region is limited by the potential at which either the solvent or the electroyte is reduced. The results that are extracted from a conventional polarogram are the wave height where the current is limited by diffusion (i_d), the halfwave potential ($E_{1/2}$) and the slope of the polarographic step.[1] The main focus of main-group organometallic electrochemistry in this era were compounds of magnesium, partly due to the interest in Grignard reagents, and mercury compounds of the type RHgX and R_2Hg. Many main-group organometallics of group IV and group V were studied by polarography and EPR in this time period as well.[1]

1.1.1. Electrochemical Studies of Sandwich Compounds

Very shortly after the publication of the structure of ferrocene, its electrochemical behaviour was studied by Page and Wilkinson.[2] Using DC polarography with a dropping mercury electrode, it was determined that ferrocene undergoes a one-electron oxidation in ethanol to form the ferrocenium cation. Additionally, with the use of controlled potential coulometry, it was determined that the ferrocene/ferrocenium reaction was reversible.[2] This reversibility was confirmed by Kuwana and co-workers, who performed the first analysis of ferrocene using the technique of chronopotentiometry with a platinum working electrode.[3] Subsequently, the polarography of 1,1'-diethylferrocene was reported by Walker and co-workers, showing the same electrochemical reversibilty with a substituent on the cyclopentadienyl ring.[4] A detailed study of the effect of substituents on ferrocene was carried out by Kuwana, in collaboration with the synthetic research group of George Hoh. The work determined that the oxidation potential of ferrocene was sensitive to substituent effects, such as the addition of alkyl, hydroxyl, ketones and acids to the cyclopentadienyl ring. The results were significant, in that the oxidation potentials followed Taft σ^* values, so that the lower the oxidation potential of the compound the more susceptible it was to electrophilic attack. Iron was not the only transition metal organometallic under study at this time.The electrochemical properties of sandwhich complexes of ruthenium, osmium, cobalt and nickel were also reported. Following this, a large amount of work was carried out on a huge range of ferrocene derivatives, with such

side groups as hydroxyls, methoxys, nitrophenyls and pyrazolyls among others. The potentials of these derivatives range from -0.385 to 0.624 V vs SCE as extremes for the pyridyl-pyrazole substituted and formyl substitued ferrocene respectfully.[5,6] A very extensive survey of transition metal complexes was undertaken by Dessy and co-workers in the late 1960s, that included σ and π-complexed organometallics from groups IV to VIII in the periodic table. The metals included were titanium and zirconium, vanadium, chromium, molybdenum and tungsten, manganese and rhenium and iridium, nickel and platinum. For each complex, the halfwave potentials, cathodic and anodic cyclic voltammetry, number of electrons and the fraction returned after electrolysis for each redox process were reported.[7–10] The usual experimental procedure for this analytical electrochemical characterisation included polarography, cyclic voltammetry then bulk electrolysis and cyclic voltammetry of the electrolysis products. Finally a back electrolysis would be attempted to determine the reversiblity of the analyte. Following this exhausive work of recording potentials for a large range of compounds, more sophisticated electrochemical experiments were performed over the next decades. Determinination of mechanisms and the consequences of electron transfer processes upon structure became the subject of interest for electrochemical studies of transition metal complexes.

1.2. Mechanistic Electrochemistry

Before continuing the discussion of the more complex electrochemical experiments from the literature, where structural changes and reactivity occur as a result of redox processes, it is important to describe some notation and terms. In 1961 Testa and Reinmuth introduced a notation to describe the sequence of an electrochemical mechanism. In this 'Testa-Reinmuth' notation, a heterogeneous charge transfer process is labelled as an *E* process and a homogeneous chemical step labelled *C*. The most simple case therefore is an *E* mechanism, where a charge transfer occurs at the electrode upon the analyte, and no other reactivity occurs. The 1-electron oxidation of ferrocene is a good example of this mechanism, but a large number of the previously mentioned analyses were also of compounds that have a simple *E* process. (figure 1.1) Cyclic voltammetry is a powerful technique in determining electrochemical mechanisms. A cyclic voltammogram of a typical *E* process would appear as a reversible wave with a small peak to peak separation and a ratio of peak currents equal to unity.

An important descriptor of an electrochemical system is its reversibility. This term can refer to electrochemical reversibility and chemical reversibility. A redox system is electrochemically reversible when the heterogeneous charge transfer step is fast on the experimental timescale, meaning that it is fast relative to the rate of mass transport. The system is chemically reversible when the analyte is stable after the electron transfer process and can be cycled between the oxidised and reduced state without decomposition or reaction.

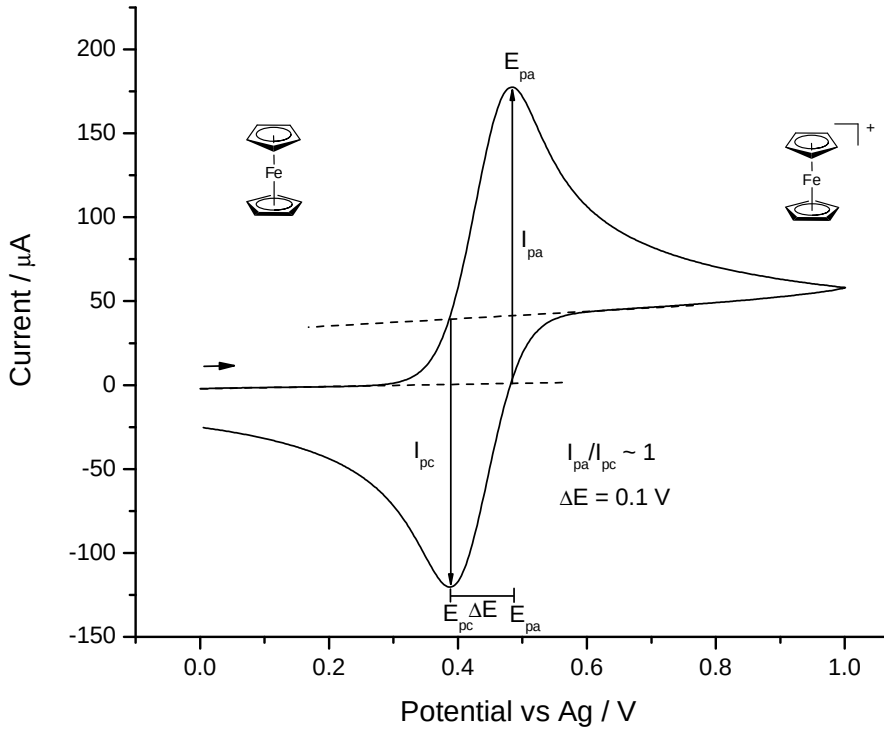

Figure 1.1. Cyclic voltammogram of ferrocene in acetonitrile, showing a quasireversible system with a small peak to peak separation (ΔE) a ratio of peak currents ($\frac{E_{\text{pa}}}{E_{\text{pc}}}$) $\approx$ unity

When a chemical change occurs *after* the charge transfer step, the mechanism is described as *EC*. A simulated voltammogram at varying scan rates of an *EC* mechanism is shown in figure 1.2. In this voltammogram, an analyte (A) is oxidised at 0.5 V, where the oxidised form is consumed by an irreversible chemical reaction. It can be observed that at low scan rates, the back peak (I') has a much lower peak current. This arises from the comsumption of oxidised A. At high scan rates, this chemical step can be out run, therefore at 1000 mV s^{-1}, the ratio of I_{pa} to I_{pc} is $\approx$ unity, similar to the *E* mechanism. Such data is useful to detemine whether

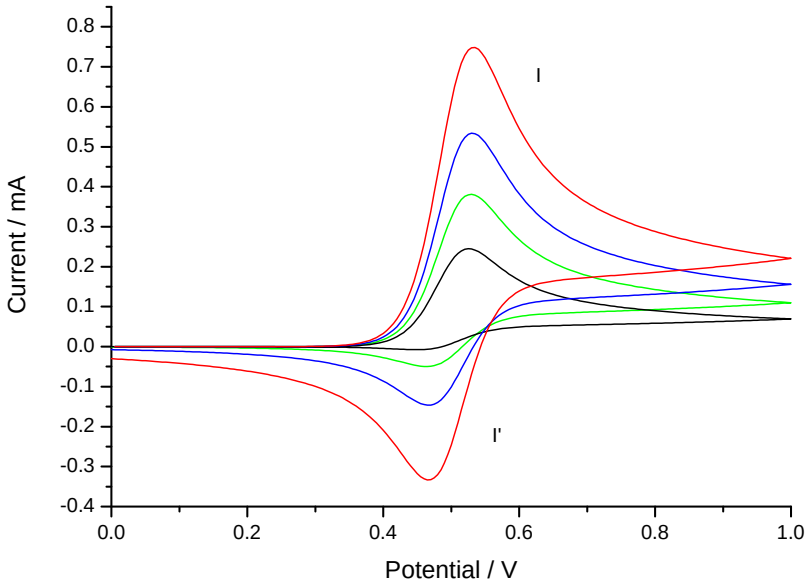

Figure 1.2. Simulated voltammogram of an EC mechanism at varying scan rates

a system is electrochemically and/or chemically reversible. The chemical step could either be intramolecular, such as a hapticity change on a metallocene, or intermolecular such as a ligand exchange induced by oxidation.

The former is exemplified by the electrochemical behaviour of bis(hexamethylbenzene)ruthenium dication, which upon a 2-electron reduction undergoes an η^6 to η^4 hapticity change, where a pair of the benzene carbon atoms are bent away from the ruthenium metal centre. This was one of the first examples of a redox pair differing in hapticity.[11,12]

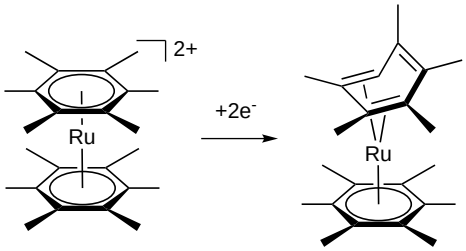

Figure 1.3. Example of an *EC* mechanism, with a structural change as a consequence of an electron transfer

If the product of the chemical step in an *EC* mechanism is electroactive, the mechanism is described as *ECE*. A simulated voltammogram at varying scan rates of an *ECE* mechanism is shown in figure 1.4. In this example, the analyte (A), is oxidised to form B (the E step, oxidation

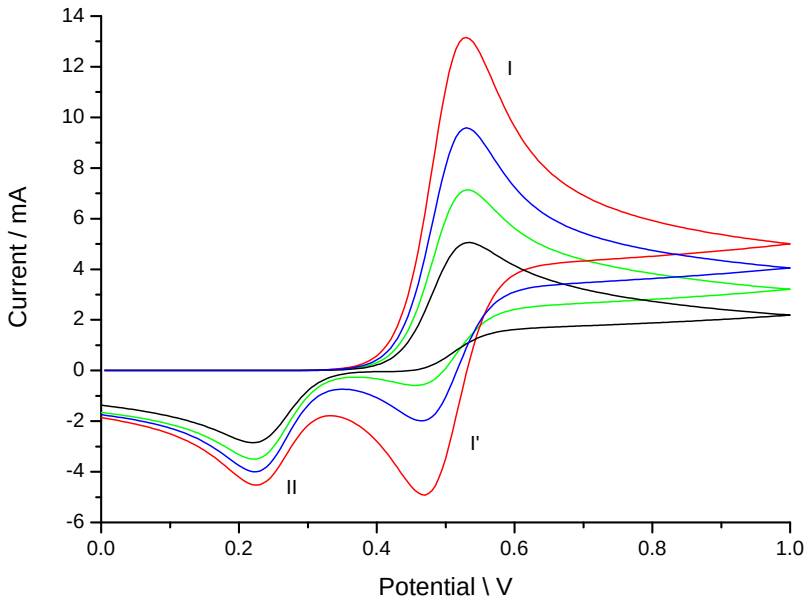

Figure 1.4. Simulated voltammogram of an ECE mechanism at varying scan rates

I). B undergoes a homogeneous chemical reaction (C step) to form an electroactive compound. This compound is then reduced at 0.25 V, giving rise to the second redox wave observed. When experimental data has an appearance similar to this, fitting simulated voltammetry at varying scan rates yields much information about the system. The electrochemical rate constant, k_0 of the first and second E steps the rate of the C step can be determined. An important example of this type of mechanism in organometallic chemistry are the redox induced exchange of metal carbonyls by other donor ligands such as phosphines. This reactivity was discovered by Philip Rieger in 1981, where it was observed that upon reduction of acetylene bridged dicobalt carbonyl complexes in the presence of a phosphine, the cathodic wave associated with the complex at -0.51 V vs Ag/AgCl would disappear in the voltammetry, whilst a new wave would appear at -1.1 V vs Ag/AgCl, corresponding to the phosphine substituted product.[13] The E step is the reduction of the dicobalt complex, the C step is the association of the phosphine and the second E step is the reduction of the phosphine substituted complex.

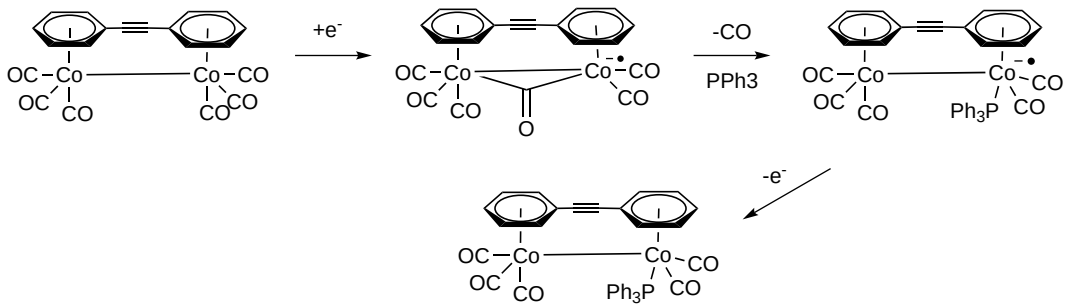

Figure 1.5. Example of an *ECE* mechanism, with an electroactive product formed from a redox induced ligand exchange

1.2.1. 17 and 19 Electron Complexes

An important part of organometallic electrochemistry are the 1-electron reductions and oxidations of 18-electron metallocenes and half sandwich complexes, where electron counts of 17/18/19 are generally reachable. The most obvious of these is the highly reversible ferrocene/ferrocenium redox couple already mentioned, which due to its simplicity is now used as an IUPAC recommended internal reference[14] and has been applied as a molecular redox tag.[15] Ferrocene electrochemistry is not exclusively anodic, it can be reversibly reduced to a 19 electron count electrochemically in 1,2-dimethoxyethane, forming a distorted anion.[16] The voltammetry of indenyl sandwich complexes of ruthenium and osmium has shown that reactive 17-electron radical cationic complexes are formed upon oxidation. The electrogenerated radicals reversibly react with nucleophiles such as MeCN and thf to form bent 19-electron sandwich compounds. These 19-electron products can be oxidised to the corresponding 18-electron dications. In the presence of Cl^- ions, an 18 electron complex is formed, which may be reduced in a 1-electron process.[17]

An important subclass of half sandwich compounds are the carbocyclic metal carbonyl

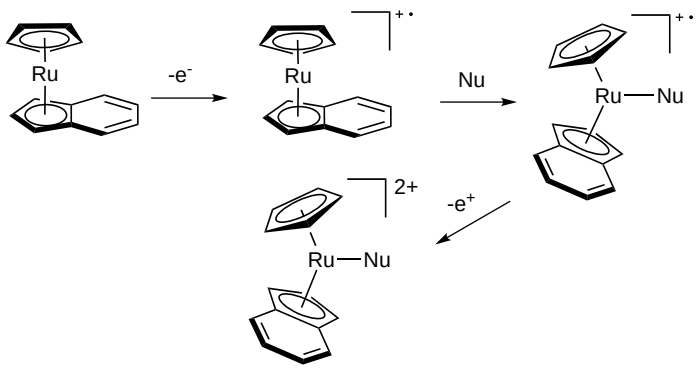

Figure 1.6. The 1-electron oxidation and reactivity of an Ru indenyl complex, Nu = MeCN, thf

complexes, known as 'piano stool' compounds. The application of the redox chemistry of piano stool complexes has generally been slower than that of sandwhich compounds, despite the spectroscopically useful carbonyl ligands. Much of the inital research into half sandwhich complexes had the aim of finding conditions in which to observe the ferrocene like reversible 1-electron oxidation. The findings of the literature are as follows: upon reduction, 19 and occaisonally 20 electron complexes can be obtained and observed spectroscopically. These electron rich compounds can be used in targeted reactions. Upon oxidation, 1-electron transfer processes are common but isolation of the radical products requires benign conditions. More detail of current reseach into piano stool complexes is provided in chapter 5.

1.2.2. Dimerisation

Upon electron transfer involving many half-sandwich tricarbonyl complexes, metal-metal bond formation and cleavage plays an important role in the observed voltammetry. For example, the oxidation of group 6 transition metal (Mo, W) anions of this type leads to the quantitative formation of the neutral dimer. In a non-coordinating solvent such as CH_2Cl_2, the electrogenerated neutral $[MCp(CO)_3]$ is consumed very rapidly on the voltammetric timescale, meaning the system is chemically irreversible.[18] The chromium analog differs due to the weaker nature of the metal-metal bond, leading to more subtle voltammetry. Under standard conditions (1 mmol dm^{-3} $[CpCr(CO)_3]^-$, room temperature, slow scan rates), an electrochemically reversible wave is apparent. With higher concentrations, lower temperatures or faster scan rates, a second wave is apparent at a more negative potential and the peak current of the main reduction decreases. The cause of this is increased formation of the dimeric species in an *EC* mechanism. At faster scan rates the dimerisation can be outrun, whereupon the peak currents for both reductions reflect the equilibrium concentrations.[19] Dimerisations such as these are important to consider if the electrogenerated monomers of half sandwhich complexes are to be used for their reactivity.

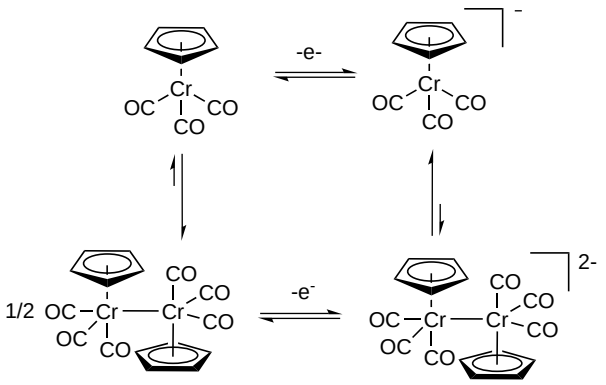

Figure 1.7. Dimerisation of the half-sandwich chromium carbonyl complex η^5-$C_5H_5Cr(CO)_3$]

1.2.3. Electrochemistry with Chemical Redox Agents

The combination of electrochemistry with the use of chemical redox agents has proven to be an advantageous when electron transfer reactions are used for synthetic purposes. Neil Connelly was the primary researcher in this field, starting in the 1970s. His group discovered the suprising result that reaction of the stable paramagnetic chromium complex $[Cr(C_6Me_6)(CO)_2(C_2Ph_2)]$ with nitronium hexafluorophosphate forms the 1-electron oxidation product $[Cr(C_6Me_6)(CO)_2(C_2Ph_2)][PF_6]$ instead of the nitroso coordination complex (see figure 1.8), the discovery having been made with the combination of voltammetry and EPR.[20] This methodology was then applied to various other complexes, such as $[Cr(C_6Me_6)(CO)_2(PPh_3)]$,[21] $[V(Cp)(CO)_2(PPh)_3]$[22] and $[Fe(C_4PH_4)(CO)(POMe_3)_2]$.[23] These 17-electron complexes were not as reactive as was hoped, but the work demonstrated the scope of the availability of 17-electron cations.

An early example of the oxidative activation of an organometallic carbonyl complex is seen with $[Fe(CO)_3(PPh_3)_2]$. Cyclic voltammetry shows that $[Fe(CO)_3(PPh_3)_2]$ undergoes

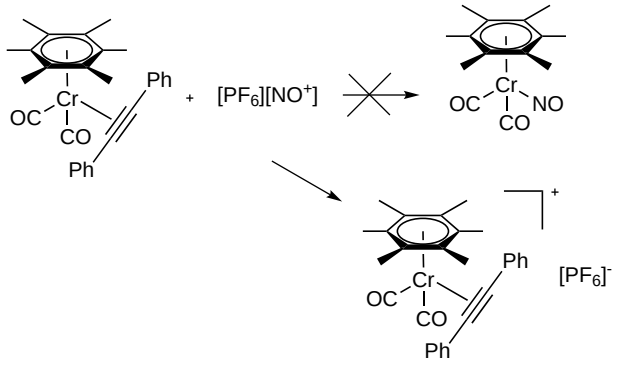

Figure 1.8. The discovery that nitrosium cation is a 1-electron oxidant for half-sandwich complexes

a 1-electron oxidation to form the radical cation $[Fe(CO)_3(PPh_3)_2]^+$. This can be chemically formed by oxidation with $Ag[PF_6]$ or $[N(C_6H_4Br\text{-}p)_3][PF_6]$, with the resulting radical cation reactive to halogens to give $[FeX(CO)_3(PPh)_3][PF_6]$. This yields $[FeX_2(CO)_3(PPh_3)_1]$ where X = I, Br or $[FeX_2(CO)_2(PPh_3)_2]$ where X = Cl. Halide ions react directly with $[Fe(CO)_2(PPh_3)_2]^+$ to give the neutral starting material and the halide coordination products via the radical intermediate $[FeX(CO)_3(PPh_3)_2]$.[24]

1.2.4. Ligand exchange

As we have seen in the work by Reiger and Connelly, electron transfer processes at the electrode can be used to induce a ligand exchange. Since their work, more reports of this type of reactivity have been published. A recent example is the work by Geiger and co-workers on the η^6-arene tricarbonyl complexes of chromium. This work stems from the large amount of interest into Cr-arene tricarbonyl complexes in the literature, where $Cr(CO)_3$ tagged aromatic compounds are widely employed in synthesis. Previous studies on this moiety have shown a 1-electron oxidation product that reacts with the supporting electrolyte medium. In this work, the anodic electrochemical properties of the chromium-arene tricarbonyl complex were investigated using a weakly-coordinating anionic electrolyte, such as $[B(C_6F_5)_4]^-$ or $[B(C_6H_3(CF_3)_2)_4]^-$. The 17-electron radical cation is observed with a much longer lifetime, but is reactive to phosphine donor ligands, undergoing rapid substitution when triphenylphosphine is present in solution. Bulk electrolysis in this inert medium can be used to generate a tractable amount of radical cation for spectroscopic study. Re-reduction of the substituted cation gives high *in situ* yields of the neutral substitution product. This method is an alternative to the more traditional photochemical methods employed to remove metal-carbonyls and introduce donor ligands.[25] At a similar time, Geiger published a report on the unusal oxidatively induced ligand substitution for complexes of the type $[Co(CO)(PPh_3)Cp]$. Upon chemical oxidation of this complex, the di-substituted phosphine complex $[Co(PPh_3)_2Cp]^+$ is afforded, as opposed to the expected radical cation $[Co(CO)(PPh_3)Cp]^{+\cdot}$ Cyclic voltammetry of the monocarbonyl substituent indicated that the product of oxidation is concentration dependent. At low concentrations (10×10^{-4} M), the simple radical cation is the major oxidation product on the voltammetric time scale; at higher concentrations and with a longer reaction time, a mixture of $[CpCo(CO_2)]$

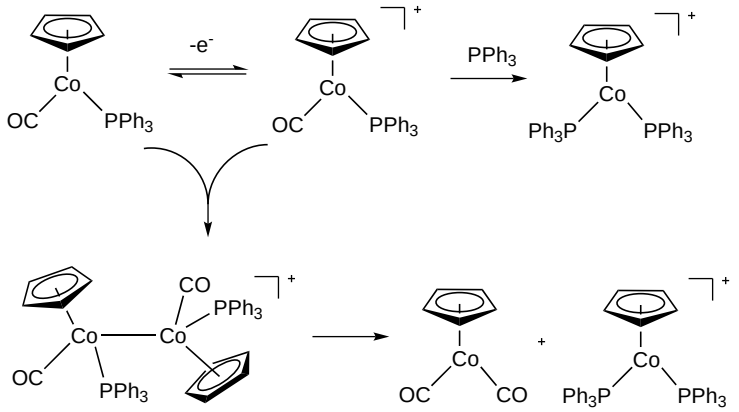

Figure 1.9. The unusual reactivity of oxidised monocarbonyl cobalt half sandwhich complexes

and $[CpCO(PPh_3)_2]^+$ is formed. This work is an important step towards understanding the effect of weak metal-metal interactions on the chemistry of radical sandwhich and half-sandwich complexes.[26]

1.2.5. Electrochemical effects of ligand derivatisation

Modelling the specific effects a ligand has on the half wave potentials of transiton metal complexes has been attempted by various research groups. For example Pickett and Pletcher investigated the relationship between the formal potential E^0 and the stucture for the oxidation of metal carbonyls of the type $[M(CO)_{6-x}L_x]^{y+}$. They discovered that E^0 depends on x and y in the following relationship:

$$E^0 = A + x\frac{dE^0}{dx}_L + 1.48y \tag{1.1}$$

(1.2)

Where A is constant dependent on the solvent and reference potental and $(dE^0/dx)_L$ is a parameter characteristic of the ligand L, defining the shift in potential caused by replacement of a CO ligand by a ligand L. The relationship allows the oxidation potential for hexacoordinate carbonyls and the use of electrochemical measurements to aid in structure characterisation.[27] Similarly, Heath and co-workers discovered that complexes of the type $MX_{(6-n)}(RCN)_n$ have a systematic relationship between the extent of halide ligation and the electrode potentials of the coordinated metal ion. The relationship between n and the electrode potential holds for bromide and chloride, $4d^n$ and $5d^n$ metal ions and many isovalent elements including niobium

and ruthenium. The progressions in LMCT and MLCT band positions are complimentary to the trend in metal-based electrode potentials upon stepwise substitution of halides to nitrile ligands. For the system $[RuX_6]^{2+}$ via $[RuX_{(6-n)}(RCN)_n]^z$ to $[Ru(RCN)_6]^{2+}$, the effect of replacing each halide with a nitrile is a shift in oxidation potential of $+0.6$ V for $Ru^{III/II}$ and $Ru^{IV/III}$, and $+0.45$ V for $Ru^{V/IV}$.[28] The most comprehensive set of parameters of ligand variation are those investigated by Lever and co-workers. For example in 1996 they reported a parametization approach standardised to the $Fe^{(II/III)}$ couple for over 200 π-ligands. The ligand electrochemical parameters based upon the $Fe^{(II/III)}$ couple were correlated with the Hammet σ_p parameter allowing the prediction of the electrochemical potentials of a large number of first row transition metal sandwhich complexes.[29]

1.2.6. Catalysis of organic molecule transformations

The focus so far has been on stoichiometric reactions of electrogenerated products of transition metal compounds. The use of electrochemical methods in catalytic systems can confer advantages, for example removing the need for stoichiometric amounts of chemical redox agents. Care must be taken when referring to catalytic reactions in electrochemistry. The two terms generally used to describe electrochemically catalytic reactions are 'electron transfer chain (ETC) catalysis' and 'redox catalysis'. Astruc reviewed the field of ETC catalysis in 1988, in which these two terms are carefully defined.[30] ETC catalysis is where the rate of a reaction is greatly increased by inclusion of a catalytic amount of a reducing or oxidising agent. For example if the neutral compound A, reacts rapidly in its radical cationic form to produce radical cationic B, which in turn reacts with the starting material to form neutral B, a closed catalytic loop is formed. The compound A can be activated to its radical cationic form with a catalytic amount of an oxidising agent or at an electrode (see scheme 1.1) An example of this type of

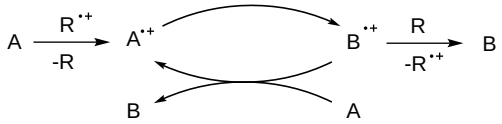

Scheme 1.1 Schematic for a typical electron-chain-transfer catalytic system

catalysis is seen in work by Sochi *et al.* involving the substitution of MeCN by less donating ligands such as PPh_3 in the 18 electron complex $[CpMn(CO_2)(MeCN)]$ The ligand subsitution in this case is initiated by the oxidation of the manganese(I) complex by ferrocenium or at an

electrode.The substitution of the coordinated MeCN ligand with PPh_3 occurs on the oxidised manganese(II) product, which then reacts with the manganese(I) starting material to form the 18-electron phosphine substituted desired product (scheme 1.2).[31] The first promiment work

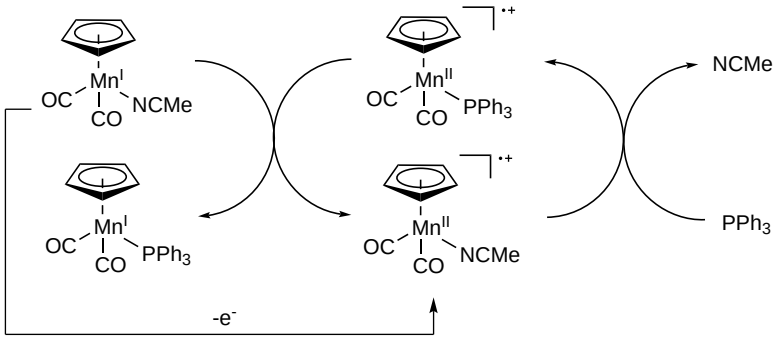

Scheme 1.2 The catalysis of ligand exchange on an 18-electron manganese(I) complex by its oxidised form[31]

in the area of redox catalysis is the investigation by Amatore *et al.* on nickel based biphenyl synthesis in 1988. In this work, a constantly applied reductive potential is used to reduce two nickel intermediates in the synthesis of biphenyl from bromobenzene (see figure 1.10).[32] More recently Jutland and Mosleh have developed this methodology with the formation of biaryls from the cathodic reduction of aryl triflates with a palladium catalyst.[33]

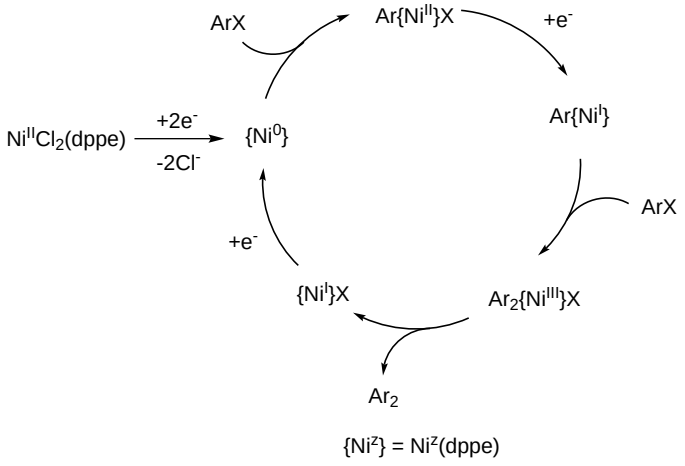

Figure 1.10. Catalytic biphenyl synthesis driven by a contantly applied reductive potential, where dppe = bis(diphenylphosphino)ethane

At a similar time to the prototypical work by Amatore, it was discovered by Meyer *et al.* that the osmium complex *cis*-$[Os(bpy)_2(CO)H][PF_6]$ (where bpy = 2,2'-bipyridine) acts as an electrocatalyst for the reduction of CO_2 in MeCN with $[^nBu_4][PF_6]$ electrolyte. In anhydrous conditions CO is generated, whereas with water present formate is produced..[34]

Much work on CO_2 reduction has been performed by D.L. Dubois and co-workers, in which palladium complexes of tridentate phosphino ligands are active catalysts for the reduction of CO_2 to CO. In addition to this, the importance of producing formate from the CO was investigated, as producing high energy density fuels such as methanol and methane from CO_2 is very desirable. It was found that combining the hydride donor ability of an electrogenerated $[HPt(diphosphene)_2]^+$ complex with rhenium carbonyl complexes such as $CpRe(NO)(CO)(PMe_3)$ lead to the formation of rhenium formyl complexes (see scheme 1.3)

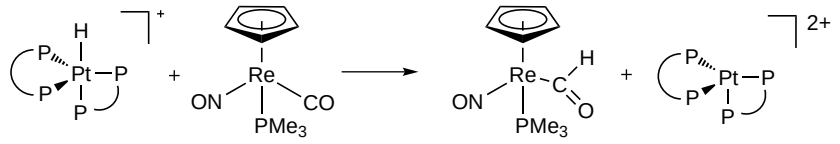

Scheme 1.3 Reaction between electrogenerated Pt hydride and half sandwhich rhenium carbonyl

1.2.7. Mixed-valence compounds

When an electron is removed from an organometallic complex containing two metal centres such as biferrocene, two separate conseqences could occur. A mixed-valance cation with a distinct M^{III} and M^{II} centres may arise, or a fully delocalised cation with two metals in equal oxidation states of apparently half integer value $+2.5$ may result. These extremes are notated as class I and IIIA mixed-valence compounds respectively, in the Robin-Day classification system.[35] Class I compounds contain no metal-metal interactions, have properties of the two metallocene and metallocenium moieties, wherease class IIIA have strong metal-metal interactions with the properties of the metallocene replace by that of a delocalised compound. Any cases intermediate between class I and IIIA are know as class II. Electrochemistry is a useful technique to investigate these type of compounds, with biferrocenyl compounds much studied. The use of electrochemical techniques for studying mixed-valence compounds has many advantages; it is applicable to any redox active metallocenes that are soluble in solvents used for electrochemistry (typically CH_2Cl_2, THF) and the analyte can be the complex in its most stable oxidation state. Early investigations were of biferrocenyl type compounds, for example in 1970 Kaufmann *et al.* investigated the solid-state electronic properties of a mixed-valence biferrocene picrate salt, determining that is has a conductivity of 6 orders of magnitude greater than ferrocenium picrate, showing that the biferrocene has a greater number of charge carriers which have

greater mobility.[36,37] This method has also been applied to bisfulvalenediiron, but the small crystal size of the picrate salt prevents the results being comparable to the bisferrocene.[38] Henrickson and co-workers analysed biferrocene and a series of five bridged biferrocenes with DC polarography.[39]

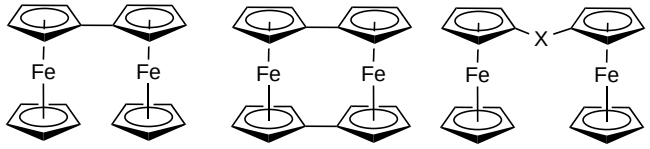

X = CH_2, CH_2-CH_2, $(CH_3)_2CC(CH_3)_2$, Hg, $CH{=}CHC_6H_4CH{=}CH$

Figure 1.11. The biferrocenes investigated by Henrickson

It was found that the the $(CH_3)_2CC(CH_3)_2$, Hg, and CH=CHC,H,CH=CH- bridged biferrocenes exhibited one irreversible two-electron half-wave, suggesting that both iron atoms are oxidised at the same potential, and oxidation of the first iron does not affect the oxidation of the second. The methylene-bridged biferrocene showed two one-electron waves at 0.39 and 0.56 V vs. SCE, that are only partially resolved as two separate waves. Biferrocenylethane has similar polarography, but with the two oxidation waves even closer. The effect of oxidation of one iron atom is more pronounced in the fused biferrocene (0.31 and 0.64 V vs. SCE) and biferrocenylene (0.13 and 0.72 V vs SCE), where the two waves have an increased separation.

More recent research into the electrochemistry of mixed-valence systems includes development of molecular electronics.[40] In terms of sandwich complexes, Geiger *et al.* have used electrochemisty to investigate superphanes containing cyclopentadienyl-cobalt cyclobutyl moieties containing varying alkane bridges, in order to gain more insight into the transition point between delocalised and localised effects in systems with metal-metal interactions.[41]

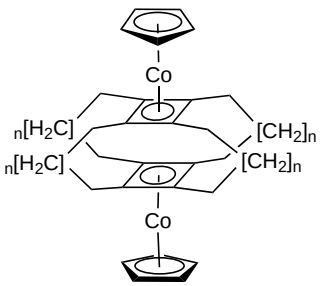

Figure 1.12. The superphane complexes investigated by Geiger, where n = 1, 3, 5

1.3. Electrochemical Techniques and Analysis

In order for a heterogeneous electron transfer reaction to occur in an electrochemical cell, molecules of analyte must be transported to from the bulk solution to the electrode surface. The rate of reaction is limited by one of two steps; the rate at which the analyte is brought to the electrode from bulk solution, or the rate of electron transfer. The former is known as mass transport, of which there are three types: diffusion, migration and convection.

1.3.1. Diffusion

Diffusion is a description of the movement of a chemical species through a solution down a concentration gradient. In electrochemistry, this gradient is created by the consumption of analyte at the electrode by electrolysis. Diffusion acts to oppose the the concentration gradient and is described by Fick's 1st law:

$$j = -D\frac{\partial[A]}{\partial x} \tag{1.3}$$

where j is the flux for the analyte A is mol cm^{-2} s^{-1},$[A]$ is the concentration of the analyte, $\frac{\partial[A]}{\partial x}$ is the concentration gradient towards x, and D is the diffusion coefficient in cm^2 s^{-1}. The diffusion coefficient D is affected by solvent viscosity, temperature and the supporting electrolyte in the cell. How the concentration of the analyte A changes with time is defined by Fick's second law:

$$\frac{\partial[A]}{\partial t} = \frac{\partial[A]^2}{\partial x^2} \tag{1.4}$$

1.3.2. Migration

Migration refers to the electrostatic force acting on a charged particle in the electric field at the interfacial region between the electrode and the solution. The force apparent on the ionic analyte molecule under the external electric field ϕ is given by:

$$Force = \frac{zF}{N_A}\frac{\partial\phi}{\partial x} \tag{1.5}$$

The migratory flux j_M that occurs due to the electric field is proportional to the concentration of the ion, the electric field and the ionic mobility:

$$j_M \propto -u[A]\frac{\partial \phi}{\partial x} \tag{1.6}$$

where $[A]$ is the concentration of the ion, u is the ionic mobility and $\frac{\partial \phi}{\partial x}$ is the potential gradient. A charge transfer process at the electrode will result in a change in the concentration of the ionic species proximal to the electrode, which alters the electrical potential in the solution. This also results in a change in the electric field $\frac{\partial \phi}{\partial x}$. The result of this is a change in the migratory flux, causing the rate of mass transport to and from the electrode during electrolysis to vary. Interpretation of experimental data is therefore difficult, without mitigation of the migration effects. To do this, electrochemical experiments are run in conditions where migration has a negligible effect through use of a supporting electrolyte. The electrolyte, consisting of an ion pair, works by electrolytic ion addition or removal at the electrode/solution interface. This causes a redistribution of the cations and anions of the electrolyte near the electrode surface, to maintain near neutrality. This ensures that the electric field defined by $\frac{\partial \phi}{\partial x}$ cannot build up, and the mass transport effect of equation 1.6 can be neglected.

1.3.3. Convection

Convection is a movement caused by mechanical means, and is split into two types, natural and forced convection. Natural convection is caused by thermal gradients and density differences within the solution. Thermal differences may arise in an electrochemical experiment from a exo- or endo-thermic nature of the process. Density differences are caused by the electrolysis creating concentrations of products at the electrode of a different density to those in bulk solution. The effects of convection are apparent in experiments on the time-scale of 10 to 20 seconds and longer, with macro-electrodes on the millimetre scale. The effects of natural convection are difficult to predict, so forced convection is used on experiments on this time-scale. Forced convection is when convection is deliberately introduced, causing any effects from natural convection to be negligible. This ensures that experiments performed over times scales longer than 10 to 20 seconds are reproducible. Forced convection is usually introduced in a way that has a well-defined hydrodynamic behaviour, thus allowing a quantitative description

of the flow in solution. Concentration changes resulting from movement of solution with a velocity in direction x are given by:

$$\frac{\partial[B]}{\partial t} = -\mu_x \frac{\partial[B]}{\partial x} \tag{1.7}$$

The flux (in one dimension) arising from forced convection is given by:

$$j = cv \tag{1.8}$$

where j is the flux of the analyte, v is the velocity of the solution and c is the concentration of the analyte

1.3.4. Electrode Kinetics

When an analyte arrives at the electrode surface, the electron tranfer reaction that occurs is subject to kinetics as any homogeneous chemical reaction would be. If a reversible heterogeneous one-electron transfer is considered:

$$\mathrm{A} \underset{}{\overset{\pm e}{\rightleftharpoons}} \mathrm{B}$$

the overall current at a given potential is expressed in terms of the oxidatve and reductive currents:

$$I = FA(k_b[B]_0 - k_f[A]_0) \tag{1.9}$$

where A is the electrode area, F is the Faraday constant, $[A]_0$ and $[B]_0$ are the concentrations of the two species at the electrode and k_f and k_b are the rate constants for the forward and backward reactions (in $\mathrm{cm\,s^{-1}}$) Applying transition state theory, these rate constants can be expressed as a function of two parameters, α and k_0, the standard heterogeneous rate constant at the formal potential of the redox couple. The parameter α is the charge transfer coefficient. It is dimensionless, and describes where the transition state of electron transfer reaction lies,

and is usually of a value ≈ 0.5. The rate constants are written as:

$$k_f = k^0 e \left[\frac{-\alpha F(E - E_f^0)}{RT} \right] \tag{1.10}$$

$$k_b = k^0 e \left[\frac{\beta F(E - E_f^0)}{RT} \right] \tag{1.11}$$

The net current at an electrode at a given potential is the sum of the cathodic I_c and anodic I_a components:

$$I = I_c + I_a \tag{1.12}$$

where the cathodic and anodic currents are given by:

$$I_c = -FAk_f[A]_0 \tag{1.13}$$

$$I_a = FAk_b[B]_0 \tag{1.14}$$

The values $[A]_0$ and $[B]_0$ are the concentrations of the compound A and B at the suface of the electrode. Substituting equations 1.13 and 1.14 into 1.12 gives a net current of:

$$I = FA(k_b[B]_0 - k_f[A]_0) \tag{1.15}$$

Substituting the expressions for the rate constants k_f and k_b from equations 1.10 and 1.11 into equation 1.15 gives the Butler-Volmer equation:

$$I = FAk_0 \left[[B]_0 e \left(\frac{(1-\alpha)F\eta}{RT} \right) - [A]_0 e \left(-\frac{\alpha F\eta}{RT} \right) \right] \tag{1.16}$$

This is a fundamental formulation for electrode kinetics. It relates four important parameters: faradaic current, electrode potential and the concentrations of reactant and product. The term

η, is the over potential, given by:

$$\eta = (E - E_0^f) \tag{1.17}$$

1.3.5. Cyclic voltammetry

The most common type of electroanalytical method employed in this work is cyclic voltammetry, in which the current is measured as a function of potential varying with time. In a cyclic voltammogram, the potential is swept from a start potential E_1 to a vertex potential E_2 and back to E_1 (figure 1.13). The resulting current occurs from the reduction or oxidation occuring on the analyte at the electrode.

For the reaction

$$\mathrm{A} \overset{\pm e}{\rightleftharpoons} \mathrm{B}$$

the form of the voltammogram can be predicted in terms of how the current varies with applied potential. The voltammogram will depend on three parameters: The standard electrochemical rate constant k_0 and the formal potential of the redox couple, the diffusion coefficients of A and B and the scan rate υ in $\mathrm{V\,s^{-1}}$ together with the end and start potentials E_1 and E_2. The prediction of the voltammogram requires the solution of the following differential equations, which describe the concentrations of A and B as a function of distance from the electrode x,

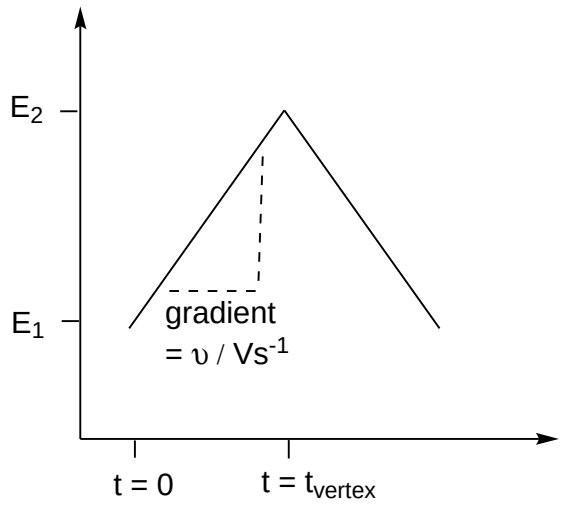

Figure 1.13. The potential applied to the electrode in a cyclic voltammetry experiment

and time t.

$$\frac{\partial[A]}{\partial t} = D_A \frac{\partial[A]^2}{\partial x^2} \tag{1.18}$$

$$\frac{\partial[B]}{\partial t} = D_B \frac{\partial[B]^2}{\partial x^2} \tag{1.19}$$

These equations are coupled via boundary conditions corresponding to a case where only A exists in bulk solution:

$$\begin{aligned}
&t = 0, all\, x, && [A] = [A]_{bulk}, [B] = 0 \\
&t > 0, x \to \infty, && [A] = [A]_{bulk}, [B] = 0 \\
&t > 0, x = 0, && D_A \frac{\partial[A]}{\partial x}_{x=0} = -D_B \frac{\partial[B]}{\partial x}_{x=0,} \\
&t > 0, x = 0, && D_A \frac{\partial[A]}{\partial x}_{x=0} = +k_c[A]_{x=0} - k_a[B]_{x=0,}
\end{aligned}$$

The electrochemical rate constants k_c and k_a are

$$k_c = k^0 e \left[\frac{-\alpha F}{RT} (E - E_f^0(A/B)) \right] \tag{1.20}$$

$$k_c = k^0 e \left[\frac{\beta F}{RT} (E - E_f^0(A/B)) \right] \tag{1.21}$$

where $E_f^0(A/B)$ is the formal potential of the A/B couple and E is the potential applied to the working electrode.

The cyclic voltammetry reported in this work were recorded in inert atmosphere non-aqueous conditions with a typical three electrode system. The working electrode applies a controlled potential to which charge transfer to and from the analyte can occur. The counter electrode completes the cell and supplies the current required to balance the current measured at the working electrode. As it is extremely difficult to keep the potential of the counter electrode constant while it is supplying a varying current, a third reference electrode having a constant potential is used to act a reference for the measurement and control of the working electrode. Therefore the potential is measured between the working electrode and the reference electrode, and the current flows between the working electrode and the counter electrode. The current flow between the working electrode and the reference electrode is negligible.

This set up is shown in figure 1.14 In non-aqeuous work, there are no widely available reference electrodes that provide a thermodynamic reference potential, so a silver wire is used as a *pseudo*-reference electrode, and ferrocene is added to the cell as an internal reference.

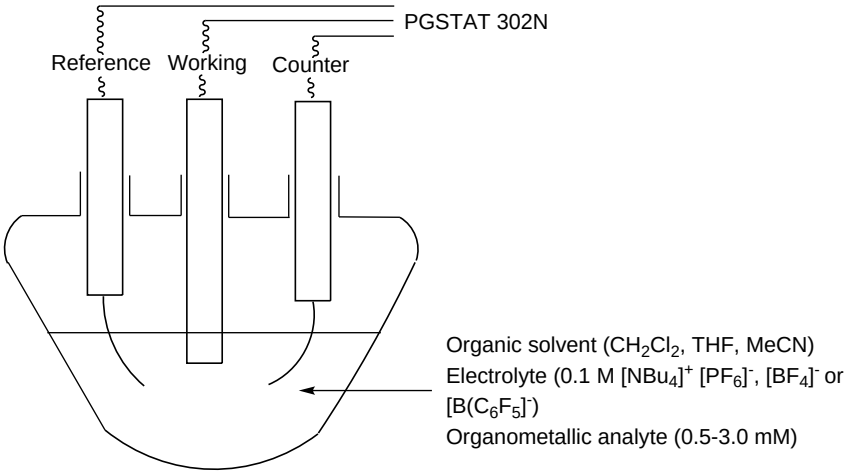

Figure 1.14. The inert atmophere cell with three electrodes employed for the electrochemical measurements recorded

In order characterise electrogenerated compounds, techniques such as spectroelectrochemistry are performed, in which the entirety of the analyte in the cell must be electrolysed. This requires electrodes of a large surface area, so the working electrode consists of carbon felt or platinum gauze (depending on the electrode material required) and the counter electrode is platinum gauze also, to provide the current required. As the counter electrode must use relatively high potentials in non-aqeuous systems, it is separated from the solution containing the working electrode by a fine glass sinter, to prevent impurities generated at high potentials contaminating the bulk sample (see figure 1.15).

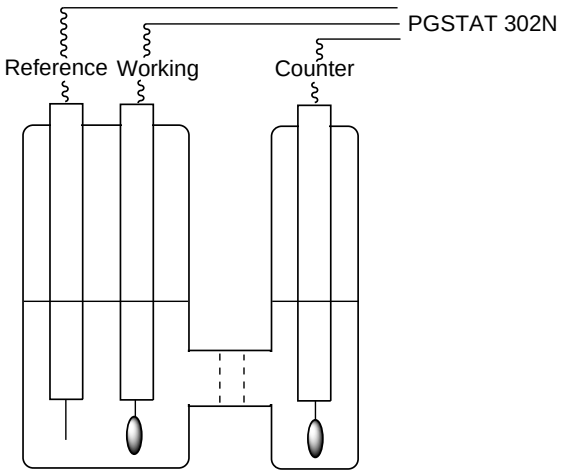

Figure 1.15. The inert atmophere cell employed for bulk electrolysis

1.3.6. Digital Simulation in Electrochemistry

The overall rate of electrolysis in a given system is dependent on the rate of mass transport of electroactive material to the electrode, the rate of the homogeneous reaction and the heterogeneous electron transfer to the electrode. In most cases, a solution of the differential equation describing the rate of an electrochemical reaction cannot be solved, and so a numerical method is instead employed. The electrolyte solution is divided into cubes of discreet volume in which the electrolyte concentration is considered a constant. In the case of linear diffusion, the solution is represented by a series of boxes extending away from the surface of the electrode. The surface is at the centre of the leftmost box (figure 1.16) and each box *b* characterises the solution at the distance $x = (b-1)\Delta x$ from the electrode. If A is the analyte in solution, its concentration in each box is represented by $C_A(b)$, so if enough discreet units are used it can closely represent the continous solution. Δx is a variable, in which the lower Δx is the more refined the model becomes.

Diffusion processes and chemical reactions will change the concentration of A over time, so a large number of discreet time steps, represented by Δt are used. The model then applies the equations describing the mass transport of material to the electrode and the rate of chemical reactions in a form the considers the size of Δt and effects them on the concentration arrays describing the initial system.

The first application determines the concentration of the system at Δt, the second at 2Δt and so on. The smaller Δt is the more the model will approach the real system. Digital

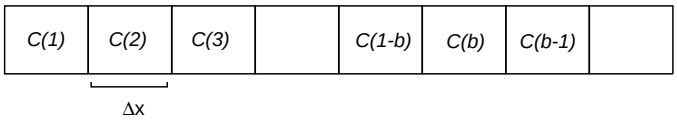

Figure 1.16. Discrete model of the solution adjacent to the electrode

simulations therefor allow treatment of the interplay of diffusion, homogeneous reaction kinetics and convection that accompany heterogeneous electron transfer processes at electrodes of partictilar geometries under a given potential or current perturbation.

In this work, the digital simulation of cyclic voltammetry is performed using the commercial DigiElch™software. The voltammogram produced by the sofware is dependent on thermodynamic and kinetic parameters. These parameters are: the standard oxidation potential E^0, the charge transfer coefficient α, the electron transfer rate coefficient k^0 and the diffusion coefficient D. By varying these parameters (or the input of an experimentally determined value for D) until the simulated voltammogram matches experimental data, a set of these parameters can be determined.

1.4. Surface Bound Electrochemistry

Before discussing the methodologies for the modification of electrodes with organometallic compounds, the structures and properties of the carbon based substrates used will be described. Carbon exists as several morphologies such as graphite, pyrolytic graphite, glassy carbon and carbon nanotubes. All these structures are purely carbon, but have differing properties.

1.4.1. Graphite

In graphite, the carbon exists as fused hexagonal rings, stacked in an alternating arrangement (see figure 1.17). Graphite is a conductor due to the aromaticity of the carbon planes. The resistivity is anisotropic however, with the least resistivity in the plane of the carbon sheets (4.1 $\times 10^{-5}$ Ω cm) and much greater resistivity perpendicular to the sheets (1.7 $\times 10^{-1}$ Ω cm).[42]

The two main forms of graphite used in electrochemical applications are graphite powder, consisting of irregularly sized micropartices, and 'pyrolytic' graphite. Pyrolytic graphite is synthesised from the decomposition of hydrocarbon gases at high temperature over an iron surface. At temperatures above 1200 °C ordering of the graphite sheets occurs, and annealing

at over 3800 °C with high pressure applied along the carbon plane yields highly ordered pyrolytic graphite (HOPG). The resulting graphite crystals have two faces. The face along the plane of the hexagonal sheets is known as the basal plane, and the face perpendicular to this known as the edge-plane. Cutting a HOPG crystal in a direction parallel to the carbon sheets reveals the basal plane, wherease cutting perpendicular to this reveals the edge plane. This allows the preparation of either basal-plane pyrolytic graphite (bppg) or edge-plane pyrolytic graphite (eppg) electrodes respectively.

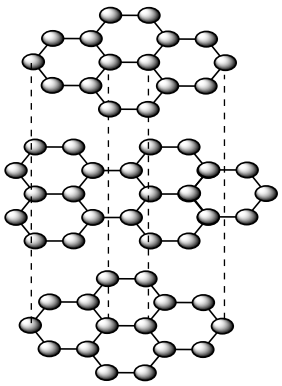

Figure 1.17. Representation of the crystal structure of graphite

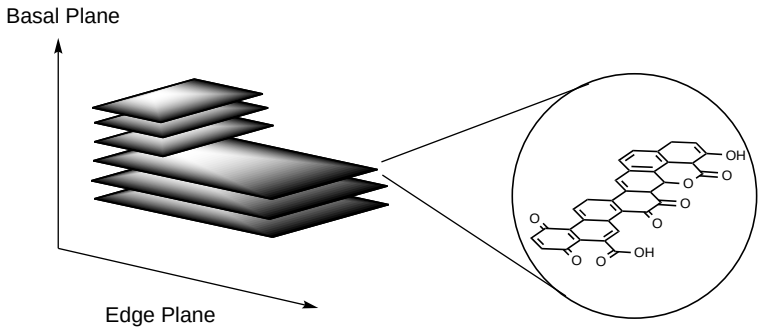

Figure 1.18. Schematic of pyrolytic graphite, with functional groups found on edge planes

The bppg electrode consists of layers of hexagonal carbon atoms parallel to the electrode surface, with a distance between each layer of 3.35 Å.[43] Defects occur, where the edge plane is exposed in the form of a step (figure 1.18). When chemical modification of an electrode is performed, the reactivity of the basal-plane versus the edge plane must be considered. A freshly cut edge plane will react with atmospheric water and oxygen, forming a variety of functional groups on the edges of the carbon sheets (figure 1.18). The edge-plane is functionalised with a range of oxygen containing groups, such as hydroxyl, carboxyl and quinonlyl groups. In contrast, the basal plane is a layer of sp^2 hybridised carbon atoms in a hexagonal arrangement.

This is important when the considering methods for the chemical modification of electrodes, as the functional groups are exploited to form covalant surface attachments.

1.4.2. Glassy carbon electrodes

Glassy carbon is formed from the heating of polyacrylonitrile or polyermic formaldehyde or phenol mixtures at temperatures from 1000 to 3000 °C under high pressure.[42] The process results in a structure of intertwined graphite ribbons (see figure 1.19). While heteroatoms such as nitrogen and oxygen are expelled during this process, the edge planes are decorated with similar functional groups as seen with graphite itself, as XPS studies have shown.[44]

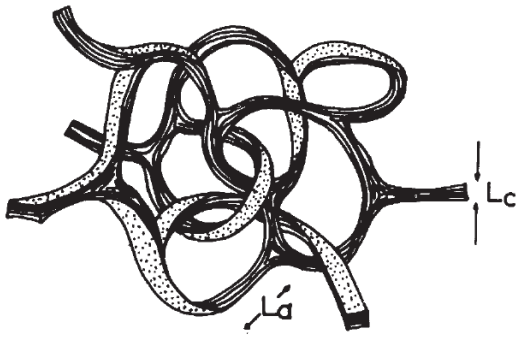

Figure 1.19. Schematic of the structure of a glassy carbon electrode

The conductivity of glassy carbon is approximately $\frac{1}{4}$ of that of randomly ordered graphite powder, but is still sufficient to allow glassy carbon to act as a conductor.[42] This is likely due to the smaller regions of order in glassy carbon. In terms of physical properties, glassy carbon is harder than graphite and impermeable to liquids or gases. The properties are dependent on the pressure and temperature used during manufacture, and are specified by the manufacturer. The structure was suggested by Harris and Tsang, where they proposed that glassy carbon consists of curved fragments of graphite sheets, explaining the low reactivity and chemical inertness of glassy carbon.[45] Glassy carbon electrodes were first successfully utilised by Zittel and Miller in 1965 for the detection of $Ce^{III/IV}$, Fe^{II}, Cr^{VI} ions among others in an aqeuous system.[46] They reported a wider potential window and and a greater ease of fabrication compared to the other carbon based electrodes such as carbon paste and pyrolytic graphite. Glassy carbon electrodes are now available as a rod sealed in a insulating tube, and are used the most common commercially available carbon based working electrode.

1.4.3. Carbon nanotubes

Carbon nanotubes (CNTs) are an allotrope of carbon in which hexagonal carbon sheets are rolled up into nanoscale tube structures. They were brought into the awareness of the scientific community by a combination of Iijima's discovery of multi-wallled carbon nanotubes on arc-burned graphite rods in 1991[47] and the prediction by Minlap, Dunmire and White that a single-walled nanotube would have similar conductivity to a metal. However nanotubes had benn observed much earlier; carbon fibres with parallel stacks of carbon sheets were reported as early as 1976.[48]

CNTs are prepared via several methods, such as chemical vapour deposition (CVD) and arc discharge. The CVD method uses a nano scale metal catalyst to break down hydrocarbon gases, resulting in the tubes growing on the tips of the metal structures. Arc discharge produces graphite vapour by passing a current between two graphite electrodes in a helium atmosphere. The condenation of graphite results in carbon nanotubes forming on the reaction chamber walls and on the cathode. Carbon nanotubes are classified into two subclasses, single walled (SWCNTs) and multi-wall (MWCNTs), shown in figure 1.20.

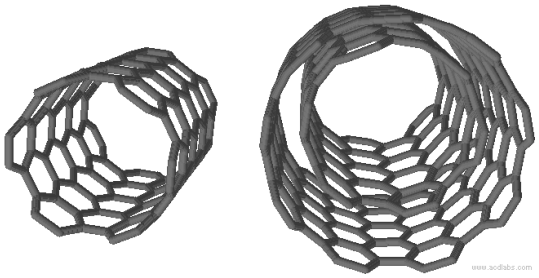

Figure 1.20. Schematic of a single wall (left) and a multiwalled CNT (right)

SWCNTs consist of a single sheet of carbon rolled into a nanotube structure, with a diameter from 0.2 to 2 mm, with lengths up to a several centimeters.[49] MWCNTs are formed of concentric nanotubes and consequently their diameter can reach 100 mm.[50] Nanotubes, like HOPG and glassy carbon, contain the two distinct basal-plane and edge plane environments, with the sides of the tube basal-plane like and tube ends edge-plane like, with the same functional groups as the edge-plane of graphite.

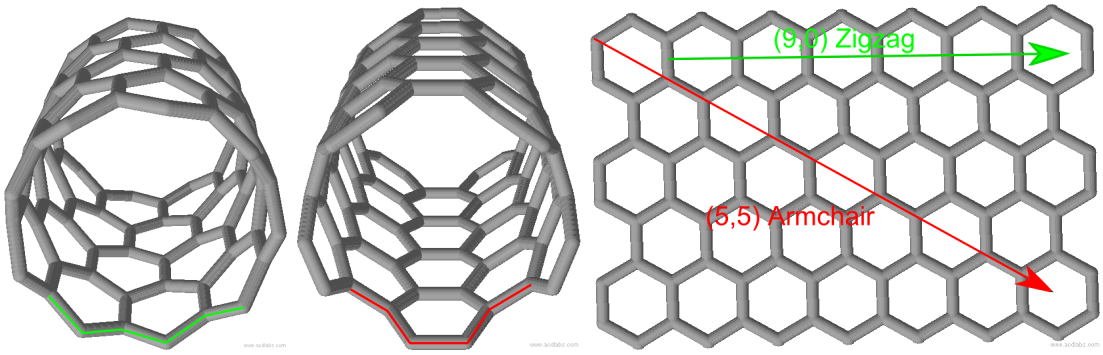

Figure 1.21. The forms of nanotubes, defined by their roll up vector

SWCNTs are formed from the rolling up of a graphite sheet, and the direction of which this folding occurs results in a different geometry of nanotube, for example zigzag and armchair (figure 1.21). These different geometries results in nanotubes with varying mechanical, chemical and electrical properties.[50] MWCNTs have differing morphologies, such as 'hollow-tube', 'bamboo' and 'herringbone', shown in figure 1.22.[51] In the case of bamboo and herringbone, the plane of the graphite sheets are angled with regard to the axis of nanotube, resulting in a higher proportion of edge-plane sites accessible. The morphology is determined by the conditions of preparation used.

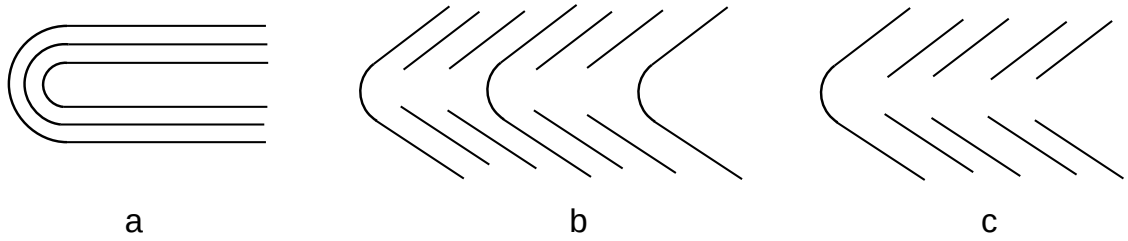

Figure 1.22. Three morphologies of MWCNTs. a) hollow tube, b) bamboo, c) herringbone.

1.4.4. Modification methods

The modification of electrode surfaces is generally achieved via the same methods as for bulk materials, with the added advantage that electrochemical techniques can be employed. While polymer coatings are the most common surface modifications used, here the procedures for attaching small molecules to surfaces will be the focus. There are seveal methods currently employed to attach small molecules to surfaces, including Self Assembling Monolayer (SAM) formation using gold-sulfur interactions,[52] siloxane chemistry,[53,54] electrochemical oxidation of

amines[55] and reduction of diazonium salts.[56] SAM methods have the advantage that they are generally reproducible and form well-organised surfaces.

The gold-sulfur method involves an organic substrate containing a thiol moiety interacting with a gold surface via the affinity of sulfur to gold. These bonds are weak however at only 20 $kJ\,mol^{-1}$,[57] and gold surfaces or nanoparticles must be employed. Siloxanes have seen wide use for SAM formation, forming strong bonds to surfaces, but the surface or modifier must be silicon based, limiting its scope. An alternatve method is the oxidation of amines, which forms strong covalent bonds to glassy carbon surfaces via the attack of the radical cation formed upon oxidation. This method however is limited by the number of substrates suitable for the process. Attaching organometallics to surfaces is much less common than simple organic substrates, but the gold-sulfur[58–60] and siloxane[61–63] methods have been employed for metal containing substrates. Alternatively, the organometallic can be applied to a surface incorporated into an immobilised polymer or paste.

1.4.5. Diazonium salt reduction

A powerful method of attaching small molecules to electrodes is via the reduction of diazonium salts. The method for this was elucidated by Pinsen and Saveant in 1992,[56] where they describe the mechanism in which an aryl diazonium salt is reduced at a glassy carbon electrode to form a radical species which attacks the electrode surface. The mechanism is described as concerted, with simultaneous electron transfer and dinitrogen cleavage.[64] This is advantageous as the radical is formed in close proximity to the surface to be modified. The radical formation occurs at the low potential of ca 0.2 to -0.2 V vs SCE (for example benzenediazonium tetrafluoroborate reduced at -0.16 V vs SCE), preventing further reduction of the radical to an anion, which occurs during reduction of aryl halides.[65] Additionally, the modest reduction potential gives this method large scope in terms of functional group tolerance. Analysis of the surface modification is achieved by performing cyclic voltammetry in a solution of electrolyte only, showing the surface bound wave of any functional groups on the bound species. These modified electrodes are stable to strong acid and basic condtions, and to sonication in various solvents with only mechanical polishing appears to remove the surface bound species. This is further evidence of the strong covalent nature of the surface attachment, as apposed to physisorption or ionic

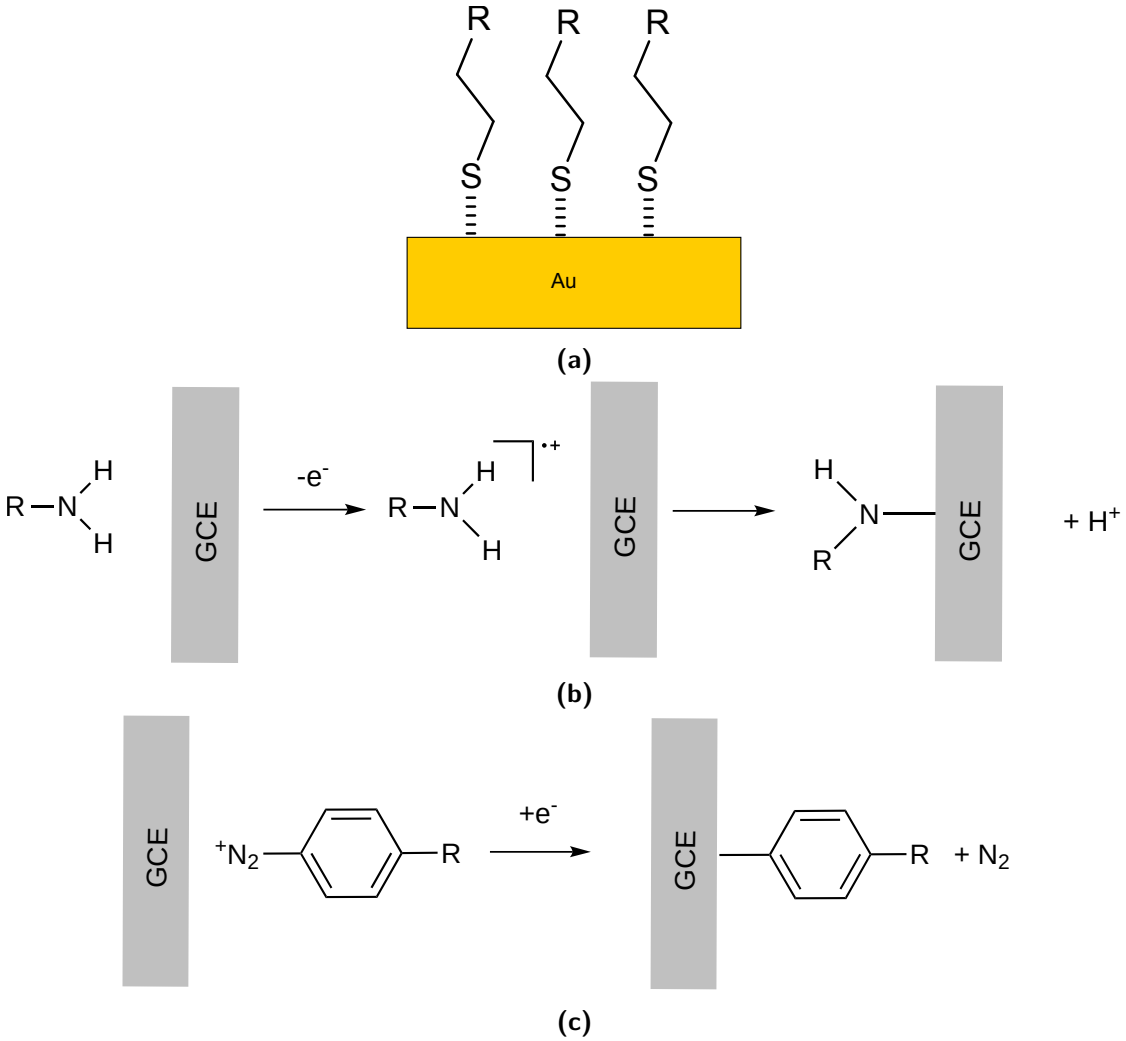

Figure 1.23. Methods for modifying a surface via a covalent bond, **a)** a gold-thiol SAM, **b)** Surface modification by oxidation of an amine, **c)** Surface modification by reduction of a diazonium salt

interactions..[57] The resilient nature of surface modifications of this type is important for the various uses these modified electrodes may have, such as electrocatalysis, sensing or corrosion resistance.

Surface modification using this method is relatively facile, with an organic solution of diazonium salt in millimolar concentration with a standard non-aqeuous electrolyte such as $[NBu_4][PF_6]$ prepared. An electrode cleaned with mechanical polishing and sonication is then inserted into the solution and held at the correct reduction potential, either by multiple cyclic voltammetric scans or with a chronoamperometric technique. After sonication of the modified electrode in an appropriate solvent, it is inserted into a solution containing only electrolyte and surface bound waves resulting from any electroactive groups on the surface bound species used

as evidence of modification. In lieu of an electroactive group, passivation of the electrode can be studied with an electroactive analyte present. Other surface characterisation techniques will be discussed later.

A recent example of the diazonium method being successfully used to prepare an electrode modified with an organometallic species is that by Geiger *et al*.[66] In this work, previously prepared amine derivatives of cymantrene[67] and cobaltocene[68] are treated with hydrochloric acid, $NaNO_2$ and then $[NBu_4][PF_6]$ to form the diazonium salts. The reductions are then performed by cyclic voltammetry or chronoamperometry and the voltammetry is then run in a fresh cell of appropriate electrolyte to observe the surface bound redox processes.

1.4.6. Lithium alkyne salt oxidation

A recent addition to the literature for the modifcation of electrodes with organometallic compounds employs the oxidation chemistry of lithium alkynyl groups.[69] The relatively high acidity of the alkynyl proton allows formation of a lithium salt with standard reagents (such as *n*-BuLi in THF). The oxidation of the lithium salf affords a radical upon liberation of the lithium cation. This radical is reactive towards atoms on a glassy carbon electrode surface.

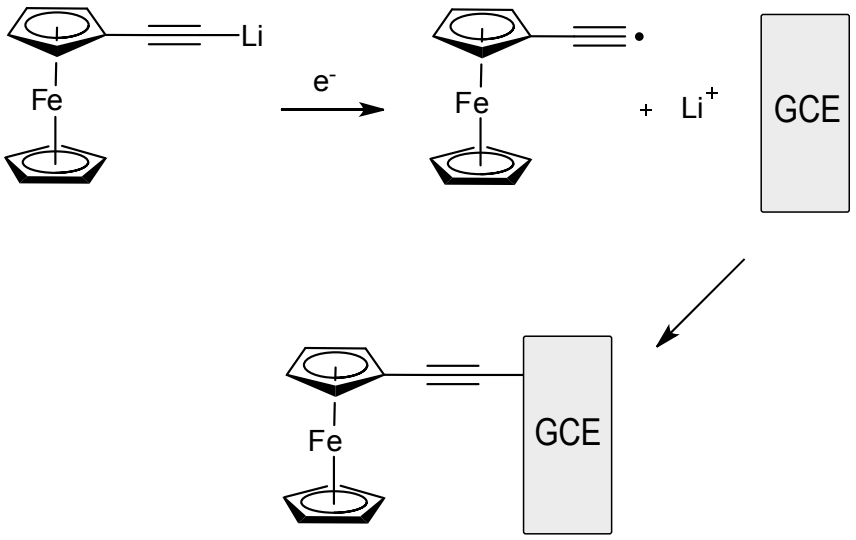

Scheme 1.4 The reaction of organometallic alkynyl lithium salts with a GCE upon oxidation

The oxidation of arylacetates ($R-CH_2COO^-$) in acetonitrile has been successfully used to chemically modify GC and HOPG electrodes by Savéant *et al*, where a variety of organic groups were attached to the carbon electrode, such as pheny, 4-nitrophenyl, 4-dimethylaminophenyl

and 1-naphthyl.[70] Holding a glassy carbon electron at a high potential (2.0 V vs SCE) in a solution of 1°aliphatic alcohol, causes the gradual passivation of the electrode. It has been proposed by Ohmori and co-workers than a covalently bound layer of alkyl groups is formed on the electrode. This is evidenced by the effect of the length of the aliphatic chain on the alcohol used on the electrode kinetics of $[Fe(CN)_6]^{-}_{3}$, where longer chains have a greater resistance consistent with a greater insulating layer between the analyte and the electrode. This modification method has been used on many alcohols, from methanol to diols and glycols.[71]

1.4.7. Exploitation of CNT edge plane defects

In additon to the covalent modification of electrodes, the functional groups present on edge-plane defects on CNTs have been exploited to attach compounds via a covalent bond. Carbodiimides have been used in this way, for example Wong *et al.* functionalised CNTs for use as probe tips for such applications as atomic force microscopy (AFM) via reaction of carbodiimides with edge plane carboxyl groups to selectively form amides.[72] Simple esterification of the edge-plane carboxyls with a compound containing a hydroxyl group has been successfully used to modify CNTs. This method was used by Li *et al.* to attach hydroxy-functionalised porphyrins to CNTs, in order to prepare a nanoscale photoactive material as an alternative to the more commonly used dye-functionalised nanoparticles.[73] Reaction of the edge plane carboxyls with thionyl chloride to afford surface bound acyl chloride, then subsequent reaction with an amine is also an effective method for attaching a compound to a CNT. Riggs *et al.* prepared polymer bound CNTs in this way, with treatment of acidified CNTs with $SOCl_2$, then mixing with propionylethylenimine-*co*-ethylenimine, forming a highly luminescent nanomaterial.[74] A summary of edge-plane defect chemistry is shown in scheme 1.5

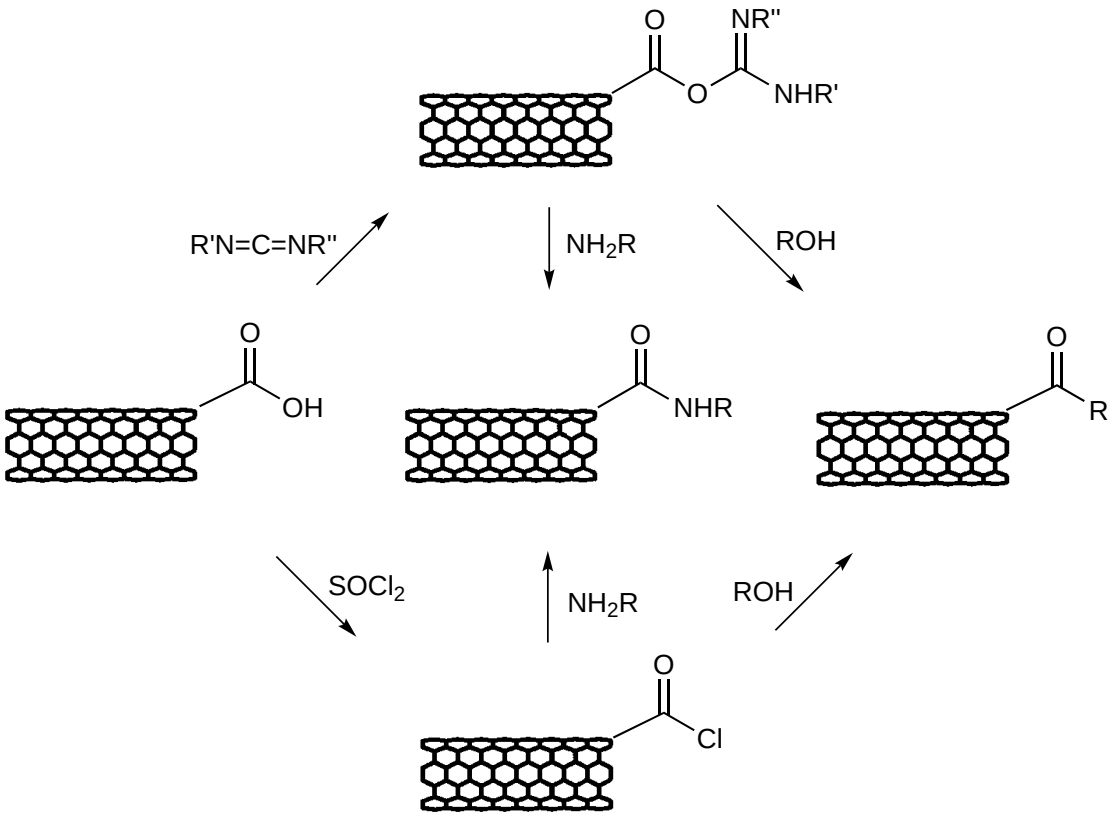

Scheme 1.5 An overview of the methods of edge-plane defect chemistry

1.5. Modification with Non-heterocyclic Carbenes

A distinct disadvantage of the methods for surface modification summarised so far is the locations on the graphitic surface that become modified. These mainly rely on the reactivity of functional groups on the edge-plane of graphitic surfaces. To obtain an improved surface coverage, a method that forms a colvant bond to the basal-plane, consisting of mainly sp^2 hybrised carbon atoms, would be desirable. In this regard, the in-situ formation of carbenes or radicals is a promising method for surface modification. The use of 1,3-dipolar cycloadditions on CNT sidewalls has been successfully employed for nanotube modification. Callegari *et al.* used the in-situ formation of an azomethine ylide from the condensation of an amino acid and an aldehyde to attach ferrocene to a SWCNT. This was used as an amperometric biosensor for glucose.[75]

Hu *et al.* has modified basal-plane of a CNT via the thermal decomposition of a dichlorocarbene, to add a dichloromethylene moiety attached via a cyclopropyl group. This

improves the solubility of CNTs in organic solvents such as THF and chlorobenzene, which is advantageous for further solution phase oganic chemistry of CNTs.[76]

Sidewall functionalisation of CNTs has also been achieved by the decomposition of organic peroxides, in which the release of CO_2 forms an organic radical than can attack the basal plane. Peng *et al* has employed this method to decorate a SWCNT with benzoyl and lauroyl peroxides.[77]

The in-situ formation of nitrenes is a effective methodology for attachment of molecules to CNT sidewalls. The thermal decomposition of organic azides results in a nitrene, which undergoes a [2+1] cycloaddition with the sp^2 hybridised carbon atoms on the CNT sidewall. This results in the organic bound to the CNT via an aziridine group.[78]

In terms of organometallics, Lobach *et al*. have used the chromium radical species resulting from the homolytic bond cleavage from the dimer of the complex η^5-$C_5Me_5Cr(CO)_2$ to covalenty modify the CNT basal plane.[79]

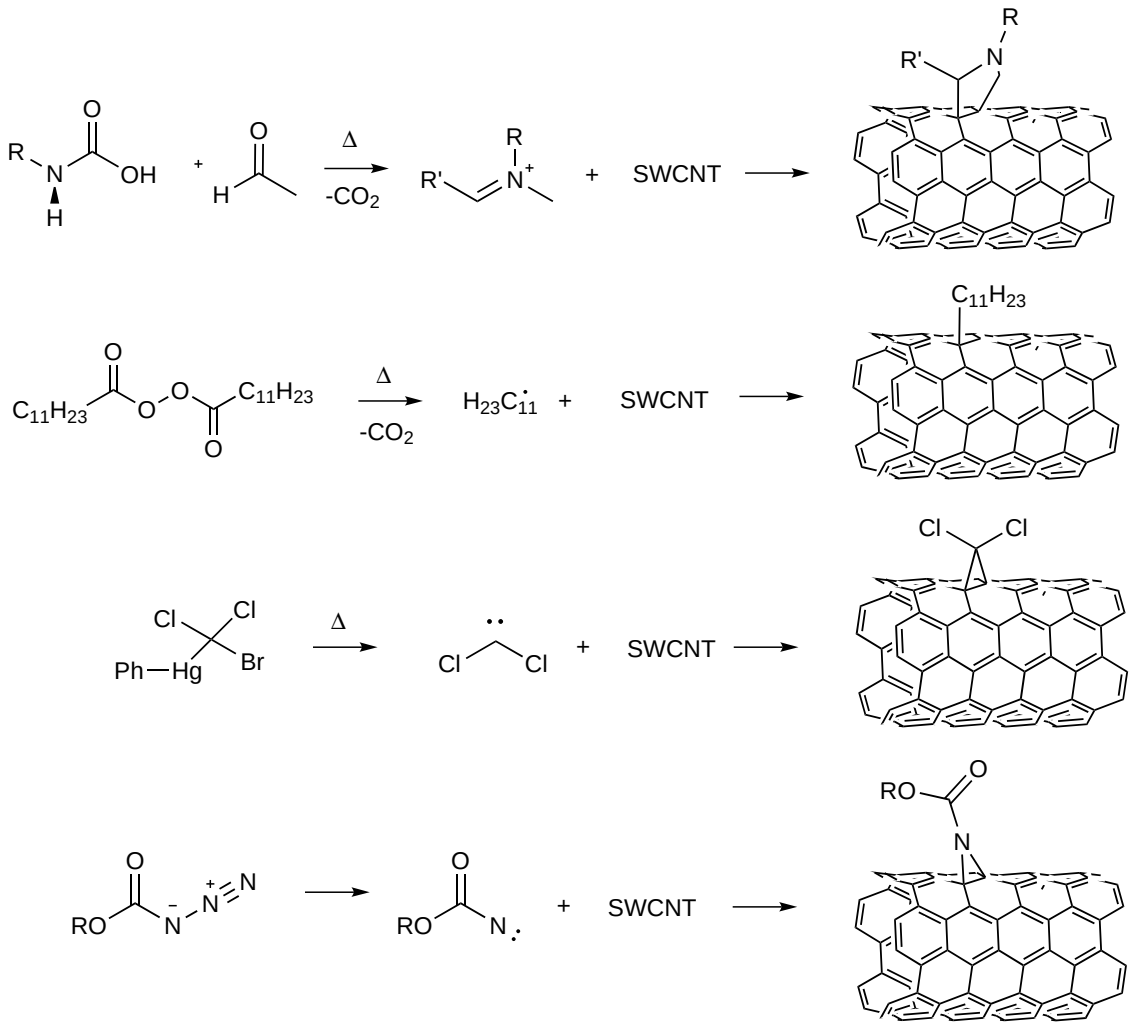

Scheme 1.6 Summary of the methods used to covalently modify the basal-plane of CNTS

1.5.1. Diazirines as carbene precursors for surface modification

Diazirines are also a very promising substrate for surface modification. A diazirine consists of an azo group bound across an sp^3 hybridized carbon, and are known to form carbenes upon release of dinitrogen when exposed to light and heat.[80] The resulting carbenes can insert into the sp^2 hybrised carbon atoms of graphite edge plane, form a cyclopropyl group, similar to the nitrenes above. For a detalied discussion of diazirines, see chapter 5 in which the use of diazirine chemistry for the attachment of group VII organometallics is investigated.

1.6. Surface Characterisation Techniques

The most immediate method to determine the presence of a surface bound electroactive species is via cyclic voltammetry. After the modifation process, there are two parameters of cyclic voltammetry that are specific to waves corresponding to heterogeneous electroactive species. The first is the peak to peak separation; surface bound waves tend to have a small peak to peak separation, compared to the 59 mV separation predicted for a perfectly reversible solution phase system. The waveform is also symmetric for surface bound systems. Secondly, as surface bound waves are assumed not be under diffusion control, a linear relationship between peak current (i_p) and scan rate (ν). Therefore plots of peak currents vs. scan rate should appear linear, especially when compared to a plot versus the square root of scan rate ($\nu^{1/2}$), proof of a diffusion controlled process from the Randles-Sevcik equation.[81]

1.6.1. X-ray Photoelectron Spectroscopy

More direct evidence of a surface absorbed species can be obtained from X-ray Photoelectron Spectroscopy (XPS). XPS is a surface analysis technique based on the photoelectric effect. Irradiation of a surface with radiation above a threshold frequency μ_c, provides sufficient energy to remove an electron from the surface. The minimum potential energy required is known as the work function: ϕ Light is quantised in units of $h\nu$, where h is the Planck constant, so at the threshold frequency, the energies of the incident photon $h\nu$ and the emitted electron $e\phi$ are equal. An increase in the frequency of the incident radiation causes the emitted electrons to have an excess of kinetic energy (E_k) which is quantised and represents the binding energy E_B of the bound electronic state of the electron within the sample:

$$E_k = h\nu - E_B - e\phi \tag{1.22}$$

(1.23)

therefore:

$$E_B = h\nu - (E_k + e\phi) \tag{1.24}$$

At very high incident radiation frequencies, the kinetic energy of the emitted electron reaches a maximum value, which reflects the emission from the Fermi level of the sample.

$$E_k^{max} = h\nu - e\phi \tag{1.25}$$

(1.26)

Upon irradiation of a sample with X-rays, the kinetic energy spectrum of the emitted photons gives a direct indication of the electronic structure of the atoms in the sample surface. Ultra-high vacuum (UHV) conditions are employed during an XPS analysis, to prevent scattering or absorption of the emitted electrons by atmospheric gases. XPS results are presented as a graph of binding energy versus electron count. In order to achieve a linear measurement of binding energies to allow multi-element detection, a deflection element is used which applies a certain potential to the entrance of the analyser, allowing only photons possessing at least the pass energy to enter. By varying this potential, electrons of different kinetic energies can pass, leading to a scan over a range of binding energies. The binding energies are calculated from equation 1.24, as the incident energy of radiation and the surface work function are both known.

The electronic structure therefore the binding energy of each element is unique, allowing detection of a specific element on a samples surface.

Having introduced the background and techniques of organometallic electrochemistry, its application to new areas will now be explored, beginning with the electrochemistry of Gold(II)/(III) pincer complexes.

References

(1) K. Mann, C. Barnes, *Electrochemical Reactions in Non-aqueous systems*, New York, 1970.

(2) J. A. Page and G. Wilkinson, *J. Am. Chem. Soc.*, 1952, **74**, 6149–6150.

(3) T. Kuwana, D. E. Bublitz and G. Hoh, *J. Am. Chem. Soc.*, 1960, **82**, 5811–5817.

(4) D. E. Walker, R. N. Adams and A. L. Juliard, *Anal. Chem.*, 1960, **32**, 1526–1528.

(5) H. Hennig and O. Gürtler, *J. Organomet. Chem.*, 1968, **11**, 307–316.

(6) G. L. K. Hoh, W. E. McEwen and J. Kleinberg, *J. Am. Chem. Soc.*, 1961, **83**, 3949–3953.

(7) R. E. Dessy, F. E. Stary, R. B. King and M. Waldrop, *J. Am. Chem. Soc.*, 1966, **88**, 471–476.

(8) R. E. Dessy, R. B. King and M. Waldrop, *J. Am. Chem. Soc.*, 1966, **88**, 5112–5117.

(9) R. E. Dessy and R. L. Pohl, *J. Am. Chem. Soc.*, 1968, **90**, 1995–2001.

(10) R. E. Dessy, R. L. Kornmann, C. Smith and R. Haytor, *J. Am. Chem. Soc.*, 1968, **90**, 2001–2004.

(11) M. Y. Darensbourg and E. L. Muetterties, *J. Am. Chem. Soc.*, 1978, **100**, 7425–7428.

(12) E. O. F. Und and C. Elschenbroich, *Chemische Berichte*, 1970, **103**, 162–172.

(13) G. J. Bezems, P. H. Rieger and S. Visco, *J. Chem. Soc., Chem. Commun.*, 1981, 265–266.

(14) G. Gritzner and J. Kuta, *Electrochim. Acta*, 1984, **29**, 869–873.

(15) D. R. van Staveren and N. Metzler-Nolte, *Chem. Rev.*, 2004, **104**, 5931–5986.

(16) N. Ito, T. Saji and S. Aoyagui, *J. Organomet. Chem.*, 1983, **247**, 301–305.

(17) S. Kukharenko, V. Strelets, A. Kudinov, A. Kreidlin, M. Peterleitner, L. Denisovich and M. Rybinskaya, *J. Organomet. Chem.*, 1996, **519**, 1–5.

(18) K. M. Kadish, D. A. Lacombe and J. E. Anderson, *Inorg. Chem.*, 1986, **25**, 2246–2250.

(19) T. C. Richards, W. E. Geiger and M. C. Baird, *Organometallics*, 1994, **13**, 4494–4500.

(20) N. G. Connelly, *Chem. Soc. Rev.*, 1989, **18**, 153–185.

(21) N. G. Connelly, Z. Demidowicz and R. L. Kelly, *J. Chem. Soc., Dalton Trans.*, 1975, 2335–2340.

(22) N. G. Connelly and M. D. Kitchen, *J. Chem. Soc., Dalton Trans.*, 1976, 2165–2168.

(23) N. G. Connelly, R. L. Kelly and M. W. Whiteley, *J. Chem. Soc., Dalton Trans.*, 1981, 34–39.

(24) P. K. Baker, N. G. Connelly, B. M. R. Jones, J. P. Maher and K. R. Somers, *J. Chem. Soc., Dalton Trans.*, 1980, 579–585.

(25) N. Camire Ohrenberg, L. M. Paradee, R. J. DeWitte, D. Chong and W. E. Geiger, *Organometallics*, 2010, **29**, 3179–3186.

(26) A. Nafady and W. E. Geiger, *Organometallics*, 2010, **29**, 4276–4281.

(27) C. J. Pickett and D. Pletcher, *J. Organomet. Chem.*, 1975, **102**, 327–333.

(28) C. M. Duff and G. A. Heath, *Inorg. Chem.*, 1991, **30**, 2528–2535.

(29) S. Lu, V. V. Strelets, M. F. Ryan, W. J. Pietro and A. B. P. Lever, *Inorg. Chem.*, 1996, **35**, 1013–1023.

(30) D. Astruc, *Angew. Chem., Int. Ed. Engl.*, 1988, **27**, 643–660.

(31) D. Astruc, *Organometallic Chemistry and Catalysis*, ed. D. Astruc, Springer-Verlag Berlin Heidelberg 2007, 2007, pp. 127–130.

(32) C. Amatore and A. Jutand, *Organometallics*, 1988, **7**, 2203–2214.

(33) A. Jutand and A. Mosleh, *J. Org. Chem.*, 1997, **62**, 261–274.

(34) M. R. M. Bruce, E. Megehee, B. P. Sullivan, H. Thorp, T. R. O'Toole, A. Downard and T. J. Meyer, *Organometallics*, 1988, **7**, 238–240.

(35) M. B. Robin and P. Day, in *Advances in Inorganic Chemistry and Radiochemistry*, Academic Press, 1968, vol. Volume 10, pp. 247–422.

(36) D. O. Cowan and F. Kaufman, *J. Am. Chem. Soc.*, 1970, **92**, 6198–6204.

(37) D. O. Cowan and F. Kaufman, *J. Am. Chem. Soc.*, 1970, **92**, 219–220.

(38) U. T. Mueller-Westerhoff and P. Eilbracht, *J. Am. Chem. Soc.*, 1972, **94**, 9272–9274.

(39) W. H. Morrison, S. Krogsrud and D. N. Hendrickson, *Inorg. Chem.*, 1973, **12**, 1998–2004.

(40) J.-P. Launay, *Chem. Soc. Rev.*, 2001, **30**, 386–397.

(41) M. E. Stoll, S. R. Lovelace, W. E. Geiger, H. Schimanke, I. Hyla-Kryspin and R. Gleiter, *J. Am. Chem. Soc.*, 1999, **121**, 9343–9351.

(42) A. Moore, *Chemistry and Physics of Carbon*, ed. P. A. Walker, P. L; Throwers, New York, 1991, p. 233.

(43) H. Chang and A. J. Bard, *Langmuir*, 1991, **7**, 1143–1153.

(44) R. I. R. Blyth, H. Buqa, F. P. Netzer, M. G. Ramsey, J. O. Besenhard, P. Golob and M. Winter, *Appl. Surf. Sci.*, 2000, **167**, 99–106.

(45) P. J. F. Harris, *Philos. Mag.*, 2004, **84**, 3159–3167.

(46) H. E. Zittel and F. J. Miller, *Anal. Chem.*, 1965, **37**, 200–203.

(47) S. Iijima, *Nature*, 1991, **354**, 56.

(48) A. Oberlin, M. Endo and T. Koyama, *J. Cryst. Growth*, 1976, **32**, 335–349.

(49) H. W. Zhu, *Science*, 2002, **296**, 884–886.

(50) G. D. M. S. Saito, R.; Dresselhaus, *Physical Propeties of Carbon Nanotubes: Theory and Applications*, Imperial College Press, 1998.

(51) M. Monthioux, L. Noé, L. Dussault, J. C. Dupin, N. Latorre, T. Ubieto, E. Romeo, C. Royo, A. Monzón and C. Guimon, *J. Mater. Chem.*, 2007, **17**, 4611.

(52) C. Vericat, M. E. Vela, G. Benitez, P. Carro and R. C. Salvarezza, *Chem. Soc. Rev.*, 2010, **39**, 1805–1834.

(53) M. R. Linford and C. E. D. Chidsey, *J. Am. Chem. Soc.*, 1993, **115**, 12631–12632.

(54) M. R. Linford, P. Fenter, P. M. Eisenberger and C. E. D. Chidsey, *J. Am. Chem. Soc.*, 1995, **117**, 3145–3155.

(55) R. S. Deinhammer, M. Ho, J. W. Anderegg and M. D. Porter, *Langmuir*, 1994, **10**, 1306–1313.

(56) M. Delamar, R. Hitmi, J. Pinson and J. M. Saveant, *J. Am. Chem. Soc.*, 1992, **114**, 5883–5884.

(57) J. Pinson and F. Podvorica, *Chem. Soc. Rev.*, 2005, **34**, 429.

(58) J. F. Smalley, H. O. Finklea, C. E. D. Chidsey, M. R. Linford, S. E. Creager, J. P. Ferraris, K. Chalfant, T. Zawodzinsk, S. W. Feldberg and M. D. Newton, *J. Am. Chem. Soc.*, 2003, **125**, 2004–2013.

(59) L. Wei, H. Tiznado, G. Liu, K. Padmaja, J. S. Lindsey, F. Zaera and D. F. Bocian, *J. Phys. Chem. B*, 2005, **109**, 23963–23971.

(60) T.-Y. Dong, C. Huang, C.-P. Chen and M.-C. Lin, *J. Organomet. Chem.*, 2007, **692**, 5147–5155.

(61) E. Le Roux, M. Chabanas, A. Baudouin, A. de Mallmann, C. Copéret, E. A. Quadrelli, J. Thivolle-Cazat, J.-M. Basset, W. Lukens, A. Lesage, L. Emsley and G. J. Sunley, *J. Am. Chem. Soc.*, 2004, **126**, 13391–13399.

(62) A. Sakthivel, J. Zhao, M. Hanzlik, A. S. T. Chiang, W. A. Herrmann and F. E. Kühn, *Adv. Synth. Catal.*, 2005, **347**, 473–483.

(63) A. Sakthivel, M. Abrantes, A. S. Chiang and F. E. Kühn, *J. Organomet. Chem.*, 2006, **691**, 1007–1011.

(64) C. P. Andrieux and J. Pinson, *J. Am. Chem. Soc.*, 2003, **125**, 14801–14806.

(65) C. Amatore, J. Chaussard, J. Pinson, J. M. Saveant and A. Thiebault, *J. Am. Chem. Soc.*, 1979, **101**, 6012–6020.

(66) D. R. Laws, J. Sheats, A. L. Rheingold and W. E. Geiger, *Langmuir*, 2010, **26**, 15010–15021.

(67) T. C. Holovics, S. F. Deplazes, M. Toriyama, D. R. Powell, G. H. Lushington and M. V. Barybin, *Organometallics*, 2004, **23**, 2927–2938.

(68) J. E. Sheats and M. D. Rausch, *J. Org. Chem.*, 1970, **35**, 3245–3249.

(69) M. V. Sheridan, K. Lam and W. E. Geiger, *J. Am. Chem. Soc.*, 2013, **135**, 2939–2942.

(70) C. P. Andrieux, F. Gonzalez and J.-M. Savéant, *J. Am. Chem. Soc.*, 1997, **119**, 4292–4300.

(71) H. Maeda, Y., Y. Yamauchi, M. Hosoe, T.-X. Li, E. Yamaguchi, M. Kasamatsu and H. Ohmori, *Chem. Pharm. Bull.*, 1994, **42**, 1870–1873.

(72) S. S. Wong, E. Joselevich, A. T. Woolley, C. L. Cheung and C. M. Lieber, *Nature*, 1998, **394**, 52–55.

(73) H. Li, R. B. Martin, B. A. Harruff, R. A. Carino, L. F. Allard and Y.-P. Sun, *Adv. Mater.*, 2004, **16**, 896–900.

(74) J. E. Riggs, Z. Guo, D. L. Carroll and Y.-P. Sun, *J. Am. Chem. Soc.*, 2000, **122**, 5879–5880.

(75) A. Callegari, S. Cosnier, M. Marcaccio, D. Paolucci, F. Paolucci, V. Georgakilas, N. Tagmatarchis, E. Vázquez and M. Prato, *J. Mater. Chem.*, 2004, **14**, 807–810.

(76) H. Hu, B. Zhao, M. A. Hamon, K. Kamaras, M. E. Itkis and R. C. Haddon, *J. Am. Chem. Soc.*, 2003, **125**, 14893–14900.

(77) H. Peng, P. Reverdy, V. N. Khabashesku and J. L. Margrave, *Chem. Commun.*, 2003, 362–363.

(78) M. Holzinger, O. Vostrowsky, A. Hirsch, F. Hennrich, M. Kappes, R. Weiss and F. Jellen, *Angew. Chem., Int. Ed.*, 2001, **40**, 400–4005.

(79) A. S. Lobach, R. G. Gasanov, E. D. Obraztsova, A. N. Shchegolikhin and V. I. Sokolov, *Fullerenes, Nanotubes and Carbon Nanostructures*, 2005, **13**, 287–297.

(80) M. T. H. Liu, *Chem. Soc. Rev.*, 1982, **11**, 127–140.

(81) J. Randles, *Trans. Faraday. Soc.*, 1948, **44**, 327.

2. Electrochemistry of gold(III) and gold(II) pincer complexes: determination of the Au^{II}-Au^{II} bond energy

The results contained in this chapter have been published in the journal Chemistry Communications.[1]

2.1. Introduction to the organometallic chemistry of gold

Recently, there has been much interest in gold chemistry due to it's versatility in homogeneous catalysis and as a catalyst precursor, with many gold carbon-carbon and carbon-heteroatom bond forming reactions reported.[2] Gold compounds are most commonly found in the $+1$ or $+3$ oxidation state.[3] The chemistry of gold(I) is the most developed by some margin.[4] The most common gold(I) compounds are linear two coordinate complexes of the generic form [AuXL], where L is a neutral donor ligand such as a phosphine, amine, isocyanine or carbene among others, and X is a monoanionic species such as a halide, alkyl or aryl ligand. Gold(I) compounds have received renewed interest from their propensity to form oligomers and in some cases even multidimensional polymers, via gold(I)-gold(I) 'aurophilic' interactions.[5] An important class of gold(I) compounds are the organometallic gold(I) complexes formed with alkynyl and carbene ligands; the chemistry of N-heterocyclic carbene (NHC) containing gold compounds used in the catalysis of organic reactions is particularly well developed.[6] For example, Nolan *et al.* have used gold(I) NHC complexes for the cycloisomerisation of an enyne,[7] and Hermann *et al.* have used NHC gold(I) acetates to catalyse the hydration of 3-hexyne.[8]

The chemistry of gold(III) is not as well developed than that of gold(I), but gold(III) will form stable coordination compounds with carbon, phosphorus, nitrogen, sulfur and

oxygen donor ligands. In terms of organogold(III) complexes, alkyl gold complexes exist with the general formula $[AuR_4]^-$, $[AuR_3L]$, $[AuR_2X_2]^-$ or $[AuR_2L_2]^+$, where X is a halogen, L is a donor ligand and R is an aryl or alkyl ligand. Mixed compounds of the type $[AuR_nX_{3-n}L]$ or $[AR_nR'_{3-n}L]$ also exist. Aryl gold(III) compounds are more numerous than alkyl complexes, and their synthesis from the activation of aromatic C-H bonds has been known since the 1930s. The auration of aromatics such as benzene or toluene by gold(III) chloride in an inert solvent to give the corresponding gold aromatic dichloride readily occurs. In the presence of other donor ligands, compounds of the type $[AuRCl_2L]$ are formed.[9] Several gold(III) catalysed organic reactions have been reported in the literature. In 1991, Utimoto and co-workers used sodium tetrachloroaurate to catalyse the transformation of unactivated alkynes into ketones and acetals.[10] In 2000, Hashami *et al*. reported the selective cross cycloisomerisation/dimerisation of terminal allenyl ketones and α,β-unsaturated alkenes with $AuCl_3$ in acetonitrile.[11] Cyclometallated complexes containing a nitrogen donor ligand can be prepared by reacting pyridine derivatives with gold(III) chloride under reflux conditions.[12–14] For example, 2-phenylpyridine reacts with $[HAuCl_4]$ or $Na[AuCl_4]$ in warm acetonitrile to form a cyclometallated gold(III) complex of 2-benzyl pyridine (figure 2.1, compound **a**).[15] For complexes where this route is unsuccessful, organomercury reagents can be employed as arylating agents, a method which has been employed to synthesise bis[2-(dimethylamino)methylphenyl] gold(III) compounds (figure 2.1, compound **b**).[16] This method has also been used with azobenzene (figure 2.1, compound **c**) and N,N'-dimethylbenzene among others.[17,18] Complexes of this type have been used in carbon-carbon bond forming reactions to form biaryls via a reductive elimination step.[19]

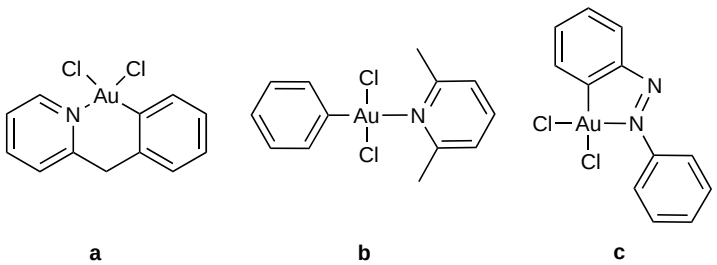

Figure 2.1. Examples of cyclometallated gold(III) compounds

Gold(II) compounds are relatively scarce in the literature when compared to gold(I) and gold(III), especially when the gold(II) compound is mononuclear. This is attributed to

the instability of the odd electron in the d^9 configuration of Au(II). An authentic gold(II) mononuclear centre may be detected by means of its paramagnetism, with a hyperfine four line EPR signal which arises from the nuclear spin of ^{197}Au (I=3/2). This method of detection was employed by Herring *et al.* in 1992, where an Au^{2+} species was observed in partially reduced $Au(SO_3F)_3$.[20] More recently, Bartlett and co-workers have synthesised and characterised gold(II) fluoro compounds, from the dissolution of gold with fluorine gas in the medium of anhydrous hydrofluoric acid, acidfied with SbF_5. This produced the gold(II) species $Au^{II}(SbF_5)_2Au^{II}Au^{III}F_4)_2$.[21] The majority of the remaining examples in the literature contain S-donor ligands, which are non-innocent according to DFT calculations and EPR simulations, but there exist in the literature several examples of gold(II) mononuclear complexes in the gas phase with N and O-donor ligands, such as CO_2, acetonitrile, tetrahydrofurn and pyridine among others.[22,23] The formation of a gold-gold bond in a dinuclear gold(II) compound gives extra stability against disproportionation, therefore gold(II) compounds with an Au_2^{4+} core are more numerous than their mononuclear counterparts. A bimetallic gold(II) sulfate (figure 2.1, **a**) has been prepared from the evaporation of $Au(OH)_3$ in concentrated sulfuric acid (scheme 2.1, **a**).[24] A widely used, convenient route to a binuclear gold(II) complex is the oxidative addition of a halogen to a gold(I) precursor. This method has been employed with thiolates and amidinates (scheme 2.1, **b** and **c** respectively) among others .[25,26]

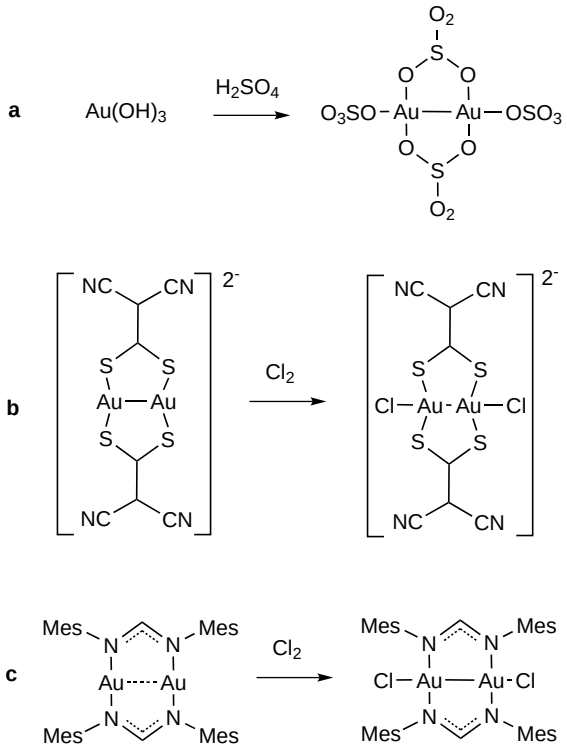

Scheme 2.1 Examples of homobridged gold(II) complexes

The most common gold(II) dinuclear bridged complexes are prepared from bis-ylide ligands, where complexes of the type $[Au_2\{\mu\text{-}(CH_2)_2PR_2\}_2]$ are found to be good substrates for gold(II) formation *via* oxidation with halogens or alkyl halides. Haloalkanes also form gold(II) compounds upon addition to the bis-yilde precursor.[27] The ligands either side of the gold-gold bond do not have to be identical. Heterobridged gold(II) dinuclear complexes have also been reported, prepared *via* oxidation of the corresponding heterobridged gold(I) precursor.[28] The mixed precursors are prepared by reacting two difference homobridged gold(I) complexes, *via* a ligand exchange reaction.[29] Not all gold(II) complexes require bridging ligands, there exist a small number of unsupported Au^{II}-Au^{II} compounds, for example the chelating phosphino napthalene ligand has been used to successfully prepare an unsupported gold(II) complex (figure 2.2, **a**); the chelating (quinolin-8-ylthio) ligand has yielded a similar complex. Only one example of a non-chelating gold(II) unsupported complex exists; $[Au_2(C_6F_6)_4(tht)_2]$ which has been prepared *via* reaction of [Au(C6F5)(tht)] and $[Au(C_6F_5)_3(tht)$ (where tht = tetrahydrothiophene).[30–32]

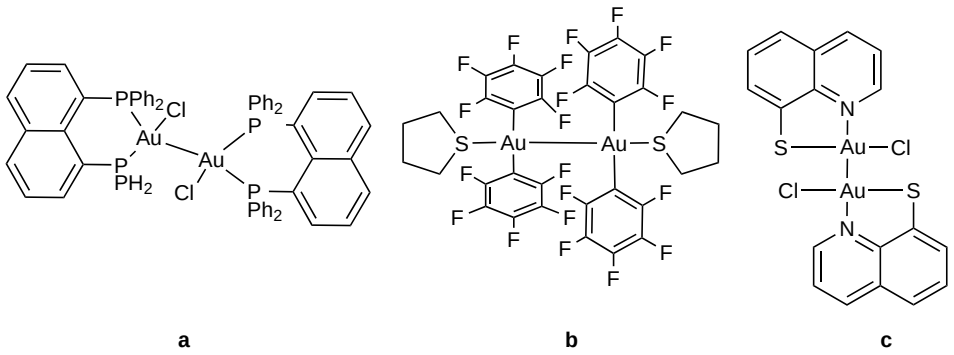

Figure 2.2. Examples of unsupported gold(II) complexes

2.2. Electrochemistry of organogold compounds

Reports detailing the electrochemical characterisation of organogold complexes are relatively scarce, likely due to the propensity of organogold complexes to form complex mixtures from the decomposition of reactive electrogenerated intermediates. The few notable examples include cyclic voltammetric analysis of heterocylic gold(I) and gold(III) carbene complexes[33] by Kuhlkamp *et al.* and the work by Jamin and Iwamoto *et al.* showing the inactivity of gold(III) porphyrin clusters.[34] In 2001, Sanna *et al.*[35] reported the preparation and electroreduction of cyclometallated N-C and N-N-C gold(III) complexes, in which N-C and N-C-C are 2-benzylpyridine and 6-benzyl-2,2'-bipyridine respectively. (figure 2.3, **a** and **b** respectively) They report reduction potentials in the range of -0.9 to -1.2 V vs. ferrocene, showing complex decomposition of the electrogenerated species which afforded elemental gold and various gold by-products. An example of electrochemical analysis of a complex containing the cyclometallated C-N-C ligand are the alkynyl gold(III) complexes prepared by Yam *et al* in which they report C-N-C ligand centred reductions with potentials in the region of -2.1 V vs. $Cp_2Fe^{0/+}$ (figure 2.3, **c**).[36]

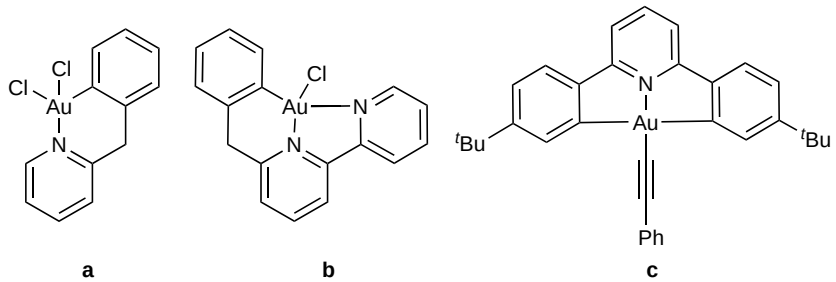

Figure 2.3. The gold(III) cyclometallated complexes that have been previously electrochemically characterised

2.3. Gold pincer complexes

As described in section 2.1, there is substantial interest in organic transformations where a gold(III) species acts as a catalyst or a catalyst precursor. This lead the Bochmann group in 2013 to investigate the reactivity of well defined gold(III) compounds in detail. The thermal stability and resistance to reduction of cyclometallated gold(III) compounds led the group to focus on using the 'pincer' backbone of a doubly cyclometalated 2,6-bis(4'-tert-butylphenyl)pyridine ligand to prepare the cyclometallated gold(III) chloride **1** as a starting material. The difficulty of removing chloride from gold centres, in which certain reactions lead to decomposition and formation of colloidal gold led to the preparation of the cyclometallated gold(III) hydroxide **2**, a versatile starting material, able to activate C-H and N-H bonds. While the auration of aromatic compounds is well developed, the hydroxide **2** is able to aurate the less reactive pentafluorobenzene.[37] Both gold(I) and gold(III) hydrides have been postulated as intermediates in numerous organic transformations, such as homogeneously catalyzed hydrogenations, hydrosilylations, dehydrogen-ative alcohol silylations and hydroborations. This led the group to develop the system further and synthesize the first thermally stable gold(III) hydride,[38] derived from the cyclometallated hydroxide. This family of C-N-C cyclometallated gold(III) complexes are ultimately prepared by *via* the organomercury method (see section 2.1). The 2,6-bis(4'-tert-butylphenyl)pyridine ligand coordinates to mercury(II) acetate and the acetate ligands are exchanged for a chloride *via* addition of two equivalents of lithium chloride. Potassium tetrachloroaurate is then added to form the cyclometallated gold(III) chloride product (see scheme 2.2). The gold(III) pincer chloride can then be transformed to the corresponding hydroxide *via* reaction with CsOH, and the hydride is then derived from the hydroxide by reaction with the superhydride $Li[HBEt_3]$

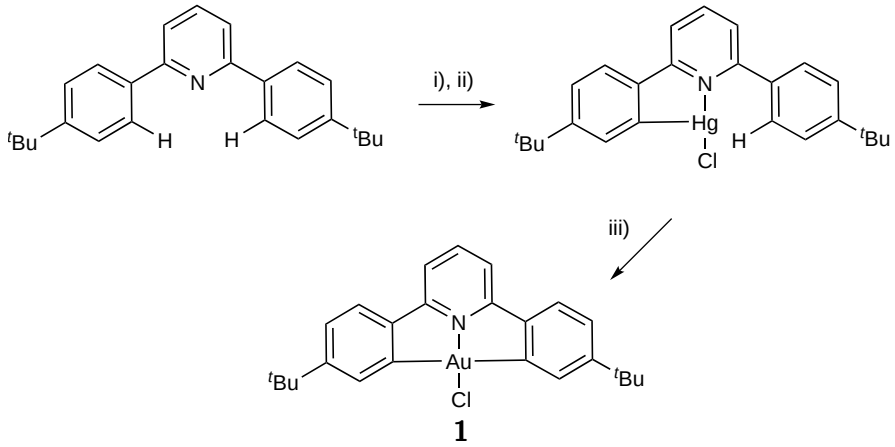

Scheme 2.2 Reagents and conditions: i) Hg(II)OAc, EtOH, reflux, 24h ii) 2LiCl, reflux, 15 min, iii) $KAuCl_4$, MeCN, reflux 24h

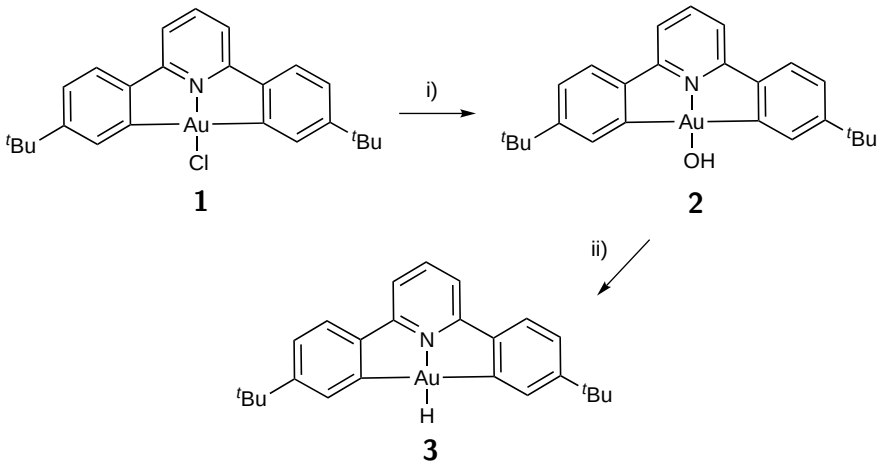

Scheme 2.3 Reagents and conditions: i) CsOH, toluene/THF/H_2O, ii) Li[$HBEt_3$], -78 °C, toluene

2.4. Gold(II) chemistry

As discussed above, the chemistry of organogold complexes is dominated by compounds in the I and III oxidation states and most current gold(II) compounds posses a binuclear metallic centre (Au_2^{4+}) supported by bridging ligands. Without these bridging ligands, the gold(II) complex will tend to disproportionate into gold(I) and gold(III) species.[39–41] The reverse reaction however is possible, with the formation of a bimetallic gold(II) centre from gold(I) and gold(III) during catalytic carbon-carbon bond forming catalysis.[41] As stated, the examples of stable gold(II) bimetallic complexes without supporting ligands are uncommon.[30–32] For example Zopes *et al.* have recently reported the photochemical self-oxidation of a silver salt of gold(II)trifluoromethyl complex.[42] Recently Xiong and Pykko have shown that unsupported gold(II)-gold(II) bonds are theoretically allowed in the complexes of this type (with the

generalised structure $X_4Au_2(py)_2$, where X = H, F, Cl, Br, I or CF_3) and estimated using DFT calculations the bond energy was determined to be 200 kJ mol^{-1}, depending on the ligands..[43] The gold(II) complex $Au^{II}(CF_3)_2$.py spontaneously forms gold(I) and gold(III) products via a disproportion reaction. This is not the case in compounds containing the cyclometallated C-N-C pincer based on the 2,6-bis(4'-tert-butylphenyl)pyridine ligand. Bochmann *et al.* have recently reported that the gold(III) pincer hydride can undergo a reductive condensation in the presence of the hydroxide analogue to form a novel unsupported gold(II) binuclear complex, that is stable to disproportionation. It is this unusual chemical stability that lead the author to investigate the gold-gold bond in this complex in some detail via electrochemical methods.

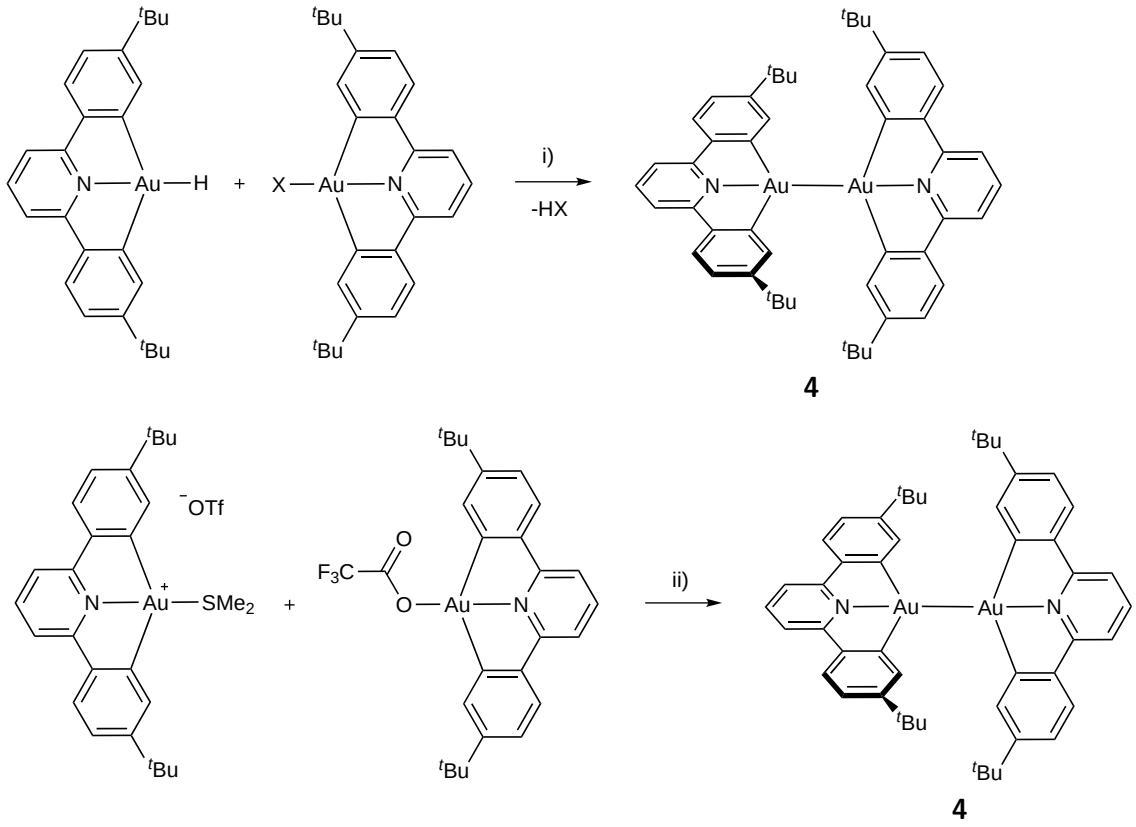

Figure 2.4. Chemical formation of gold(II) dimer, i) stir in dark for 24h; ii) cobaltocenium

2.5. Electrochemical characterisation of Gold(III) hydroxide, hydride and chloride complexes

Authentic samples of **1**, **2**, **3** and **4** prepared by D. Rosca of the Bochmann group were electrochemically characterised by cyclic voltammetry, performed using a glassy carbon

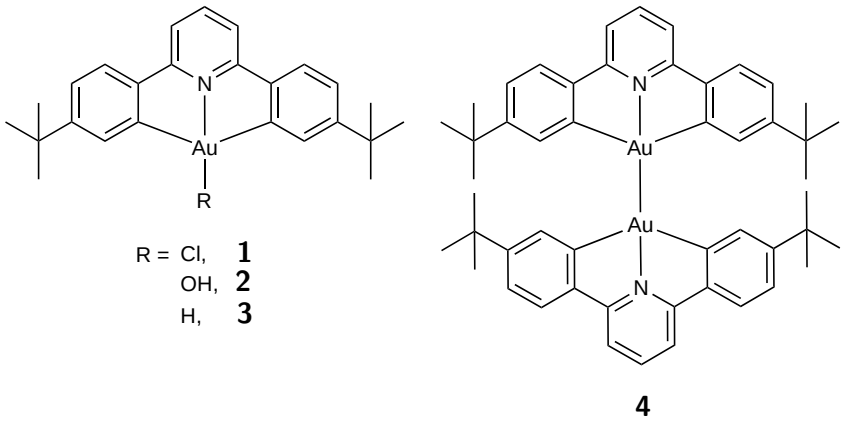

Figure 2.5. The gold pincer complexes under investigation.

electrode, with CH_2Cl_2 as the non-coordinating aprotic solvent and $[^nBu_4N][B(C_6F_5)_4]$ as the supporting electrolye. Survey scans were performed by scanning from 0 V vs the Ag *pseudo* reference electrode into the cathodic region up to the solvent window, then scanning up to the anodic solvent limit, recording all waves that occur within the window of -2.7 to +2.4 V vs ferrocene. The survey scans were carried out at 100 $mV\,s^{-1}$. This is after performing the same scans of a solution of electrolyte in the absence of an analyte. The weakly coordinating electrolyte was chosen for the electrochemical analysis of these complexes to prevent possible reaction of the electrogenerated products, some of which are radical in nature. No test was performed with the more traditional non-aqueous electrolytes containing the $[BF_4]$ and $[PF_6]$ anions. In the case of the gold(III) hydroxide complex **2**, two reduction waves are observed at the potentials of, -2.39 and -2.66 V vs. $Cp_2Fe^{0/+}$ respectively. (figure 2.6) A small, poorly defined reduction wave at -2.09 V is observed as a shoulder on the main reduction wave and likely corresponds to some trace impurity arising during the synthesis of **2**. At 100 $mV\,s^{-1}$ there appeared to be no corresponding oxidation waves, either from scanning the whole cathodic region or scanning to potentials just after each reduction sequentially. This indicates that all three reductions observed are either chemically or electrochemically irreversible on this time-scale. In the anodic region, an oxidation at 0.59 V is observed (labelled oxidation II). After scanning each reduction sequentially including the anodic region in each scan, it was determined that this oxidation only occurs after first scanning the cathodic region past the reduction wave labelled I. When scanning in the anodic region only, no oxidation potential is observed. It can therefore be assumed that an electroactive product is formed from reduction I in this case **2**.

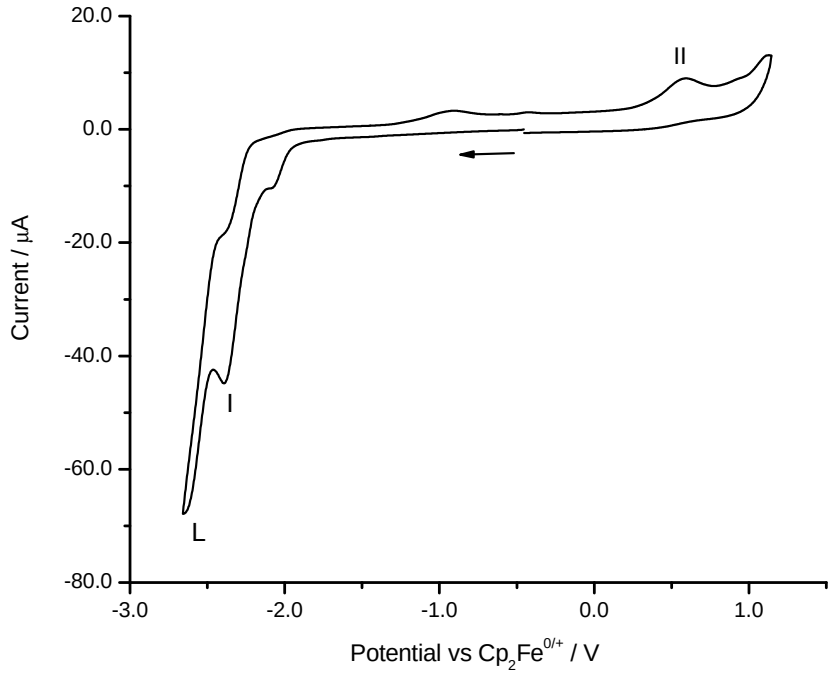

Figure 2.6. Full range cyclic voltammogram of **2** in CH_2Cl_2 (1.5 mmol dm^{-3}, 50 mmol dm^{-3} [^{n}Bu$_4$N][B(C$_6$F$_5$)$_4$]) at a scan rate of 100 mV s^{-1}.

In the voltammetry of the hydride **3** three reduction waves are observed (figure 2.7, with peak potentials at -2.00 V, -2.25 V and -2.60 V vs. $Cp_2Fe^{0/+}$ respectively. The reduction I, at -2.00 V is initially assumed to be the metal centred reduction of Au(III) to Au(II). The second reduction (labelled D, figure 2.7) is speculated to be the reduction of a bridged complex of the type LAuII-H-AuIIIL formed upon reduction of **3**. Such reductions are only observed for the hydride **3** and chloride **1** derivatives, but not seen for hydroxide **2**. The third reduction at -2.60 V again corresponds to ligand based multi-electron processes, on the basis that this reduction occurs at very similar potentials for all **1**, **2**, **3** and **4** As was the case with **2**, no corresponding oxidation waves are observed upon reversing the scan direction from the solvent window or sequentially after each reduction potential, indicating that each reduction exhibits electrochemically or chemically irreversible behaviour. The same irreversible oxidation wave at +0.59 V vc $Cp_2Fe^{0/+}$ is observed with **3** as it was with **2** and again this oxidation wave is only observed after first scanning the potential beyond the first reduction wave at -2.00 V. As a control to assess the possibility of chloride abstraction from the CH_2Cl_2 solvent used in the voltammetry, the gold(III) chloride **1** was electrochemically characterised. The results

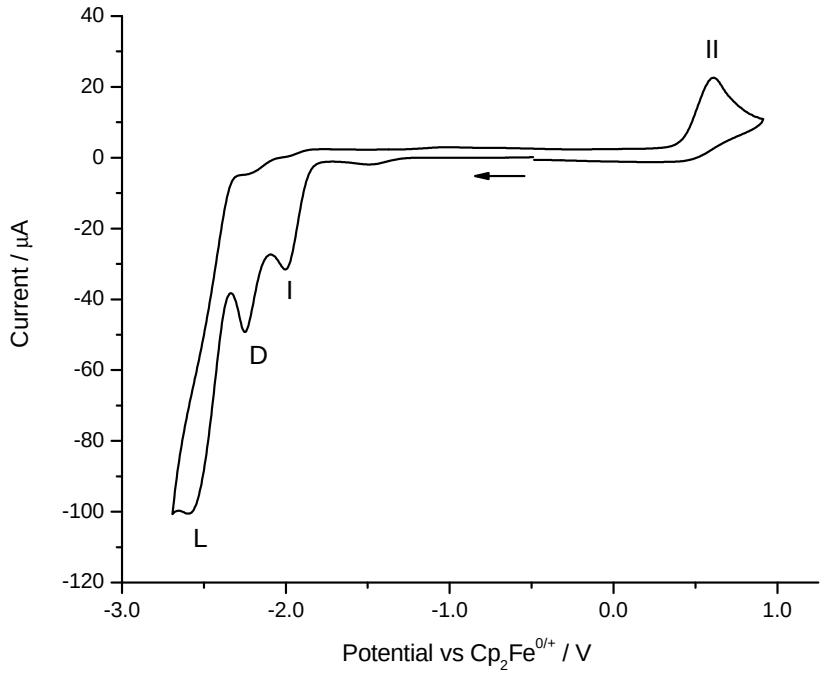

Figure 2.7. Full range cyclic voltammogram of **3** in CH_2Cl_2 (1.5 mM, 0.05 M $[^nBu_4N][B(C_6F_5)_4]$) at a scan rate of 100 $mV\,s^{-1}$

observed are very similar to those of the hydride **3**, with reduction potentials at -1.85, -2.10 and -2.45 V vs. $Cp_2Fe^{0/+}$ (figure 2.7). The least negative reduction potential (labelled I) is assigned again as the metal centred reduction, as with the hydroxide and hydride. The second reduction (labelled D) is assigned, by analogy to the hydride, as the reduction of the chloride bridged product (vide *infra*). Again the multi-electron reduction of the pincer scaffold (labelled L) is observed at the most negative potential.

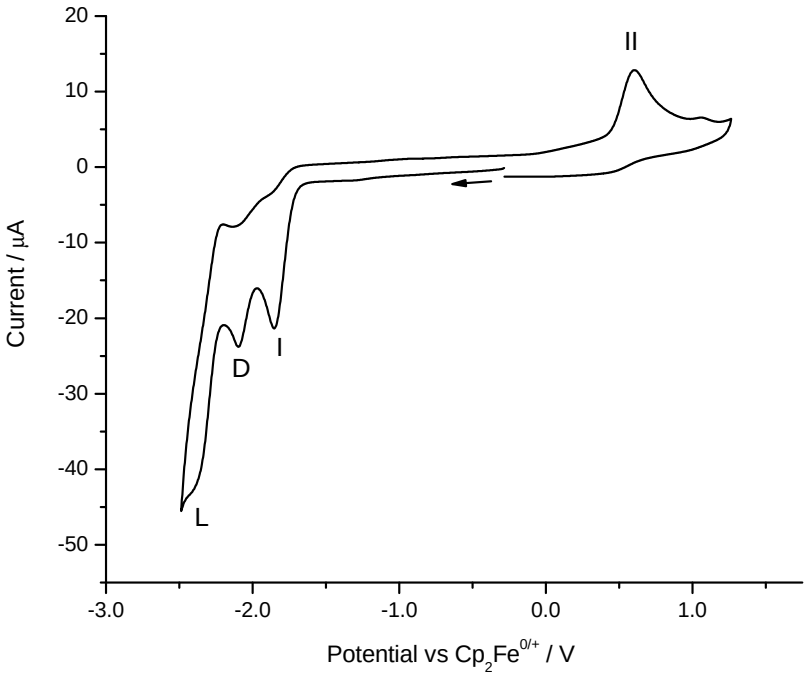

Figure 2.8. Full range cyclic voltammogram of **1** in CH_2Cl_2 (1.5 mmol dm^{-3}, 0.05 M [^{n}Bu$_4$N][B(C$_6$F$_5$)$_4$]) at a scan rate of 100 mV s^{-1}

An authentic sample of the dimer **4** was voltammetrically characterised, to determine if the reduction products of **2**, **4** and **1** dimerise in solution. The dimer **4** shows the multi-electron reduction of the ligand at - 2.63 V vs $Cp_2Fe^{0/+}$, as well as an irreversible oxidation wave at +0.59 V vs $Cp_2Fe^{0/+}$, due to the direct oxidation of **4** at the electrode. A second oxidation wave (labelled III) is also observed at + 0.97 V vs. $Cp_2Fe^{0/+}$s, that is not seen in the case of **2** or **3**, which only appears after the ligand-based reduction (L) has occurred. We therefore assign this to the oxidation product of ligand decomposition.

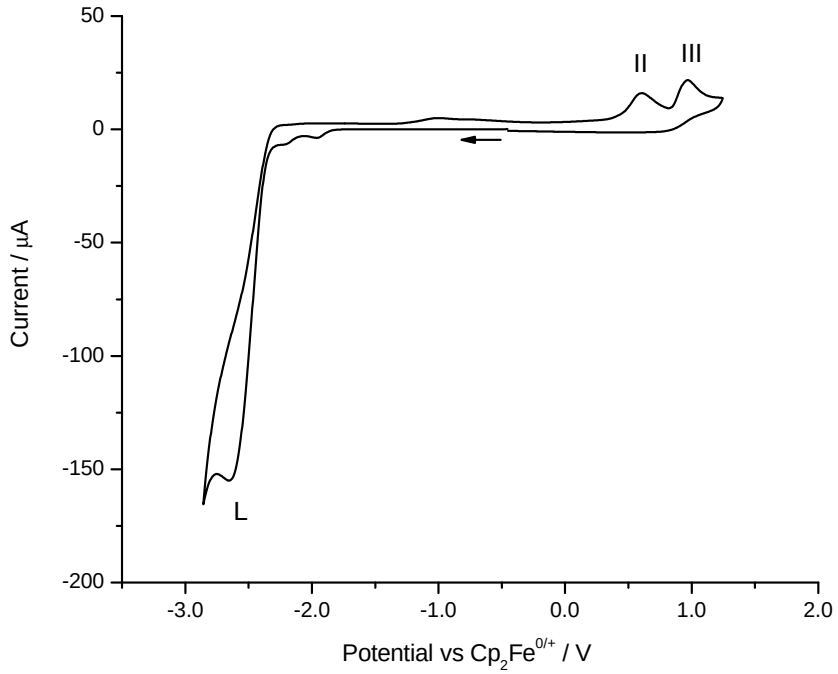

Figure 2.9. Full range cyclic voltammogram of **4** in CH_2Cl_2 (1.5 mmol dm^{-3}, 0.05 M [^{n}Bu$_4$N][B(C$_6$F$_5$)$_4$]) at a scan rate of 100 mV s^{-1}

The summary of the electron transfer processes postulated from these survey scans is in scheme 2.4, where I is the initial reduction of the Au^{III} metal centre, followed by a chemical formation of the bridged intermediate. This is followed by the reduction of the intermediate bridged dimer (electrochemical process D), which then spontaneously forms a molecule of the Au^{II} dimer.

$$LAu^{III}X + e^- \longrightarrow LAu^{II\bullet} + X^- \quad (I)$$

$$LAu^{II\bullet} + XAu^{III}L \longrightarrow LAu^{II}\text{-}X\text{-}Au^{III}L$$

$$LAu^{II}\text{-}X\text{-}Au^{III}L + e^- \longrightarrow LAu^{II}\text{-}X\text{-}Au^{II}L \quad (D)$$

$$LAu^{II}\text{-}X\text{-}Au^{II}L \longrightarrow LAu^{II}\text{-}Au^{II}L + X^-$$

Scheme 2.4 Electron transfer steps for I and D, where X = H, Cl.

More insight into the mechanisms governing the redox behaviour of **2**, **3**, **1** and **4** can be found upon recording cyclic voltammetry at varying scan rates. Therefore for each complex, the voltammetry over the regions of interest was recorded at scan rates from 50 to 1000 $mV\,s^{-1}$.

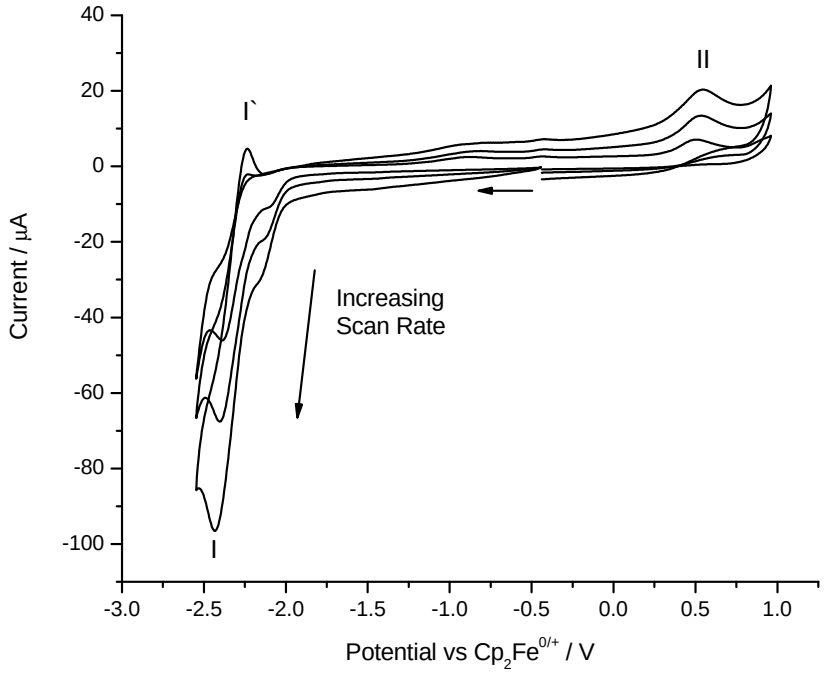

Figure 2.10. Cyclic voltammogram of **2** in CH_2Cl_2 (1.5 $mmol\,dm^{-3}$, 0.05 M $[^nBu_4N][B(C_6F_5)_4]$) at scan rates of 100, 300 and 750 $mV\,s^{-1}$

In the case of **2**, at scan rates greater than 100 $mV\,s^{-1}$ a corresponding oxidation wave for the Au^{III} to Au^{II} reduction (labelled I, figure 2.6) at 2.39 V vs $Cp_2Fe^{0/+}$ can be observed. This suggests that following the initial heterogeneous quasi-reversible electron transfer, an irreversible chemical step involving the cleavage of the Au-OH bond occurs, forming a Au(II) radical. This is suspected to be followed by the formation of the Au(II) dimer. As the scan rate is increased, the kinetics of the follow-up chemical steps begin to be outrun on the voltammetric time-scale, such that a fraction of the Au^{II} intermediate is subsequently re-oxidized to the parent $LAu^{III}OH$ complex before the Au–OH bond is cleaved and dimerisation can occur. The oxidation at 0.59 V, which is assigned to oxidation of the gold(II) dimer, is observed at the comparatively high scan rate of 1 $V\,s^{-1}$. This suggests a high rate of dimerisation of the LAu^{II} intermediates.

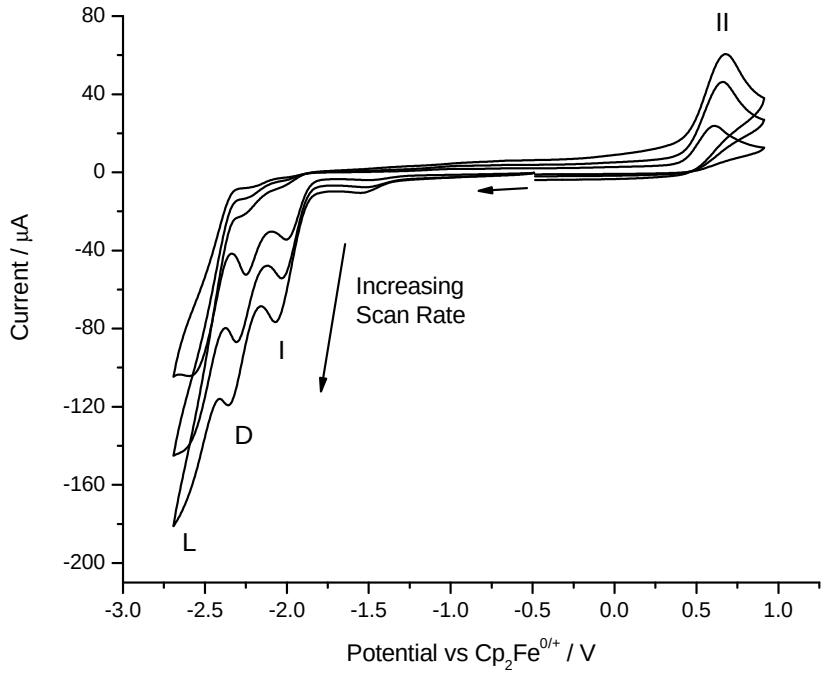

Figure 2.11. Cyclic voltammogram of **3** in CH_2Cl_2 (1.5 mmol dm^{-3}, 0.05 M [^{n}Bu$_4$N][B(C$_6$F$_5$)$_4$]) at a scan rates of 100, 300 and 750 mV s^{-1}

In contrast to the behaviour of the hydroxide **2**, no back peaks are observed in the cathodic region up to a scan rate of 1 V s^{-1}. This suggests that the gold(II) hydride bond is broken more rapidly than the gold(II) hydroxide bond, such that the follow-up homogeneous chemical step are not being outrun on the voltammetric time-scale. The faster cleavage of the hydride compared to hydroxide is in contrast to the Au-X bond energies of the parent gold(III) complexes in which the Au^{III}-OH bond is weaker than the Au^{III}-H bond (279 vs. 317 kJ mol^{-1}). The standard potentials vary from the observed reduction potentials due to the effect of the follow-up chemical steps, thus requiring the use of digital mechanistic simulations in these more complex cases. The energy difference between the hydride and hydroxide may be explained by different reduction pathways for the two species. DFT calculations (performed by Dr. Joseph Wright) (see section 2.8) show that reaction of [LAu^{III}-X] with a [LAu^{II}] fragment to give a [LAu-X-AuL] intermediate is exothermic by 49 kJ mol^{-1} in the case where X = H. This species has a roughly symmetrical Au-H-Au core which is retained on reduction. In contrast, when X = OH reaction of two fragments does not give a molecular intermediate structure: the second

gold fragment associates only weakly with the oxygen atom (Au-O distance 2.487 Å, from DFT calculations, see section 2.8)

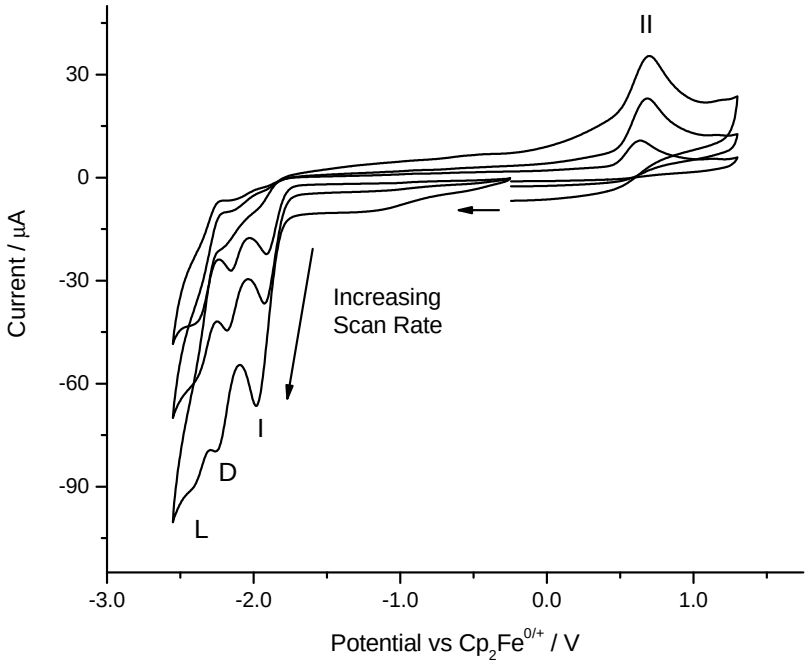

Figure 2.12. Cyclic voltammogram of **1** in CH_2Cl_2 (1.5 mmol dm^{-3}, 0.05 M [^{n}Bu$_4$N][B(C$_6$F$_5$)$_4$]) at a scan rates of 100, 300 and 750 mV s^{-1}

The behaviour of the chloride **1** is very similar to that of the hydride, with all reductions appearing irreversbile at all scan rates recorded, meaning that the follow-up homogeneous steps for the chloirde are not being out run on the voltammetric time-scale. In all cases the oxidation of **4** (+0.59 V vs. $Cp_2Fe^{0/+}$) is irreversible at all scan rates recorded (figure 2.13). This would suggest that the product of the oxidation of the Au^{II} dimer is unstable and likely undergoes rapid follow–up chemistry, probably involving cleavage of the Au^{II}–Au^{II} bond to form redox inactive products. There was no evidence for detectable amounts of a mixed-valence radical cation intermediate $[LAu^{II}\text{-}Au^{III}(L)]^+$ in the oxidation process.

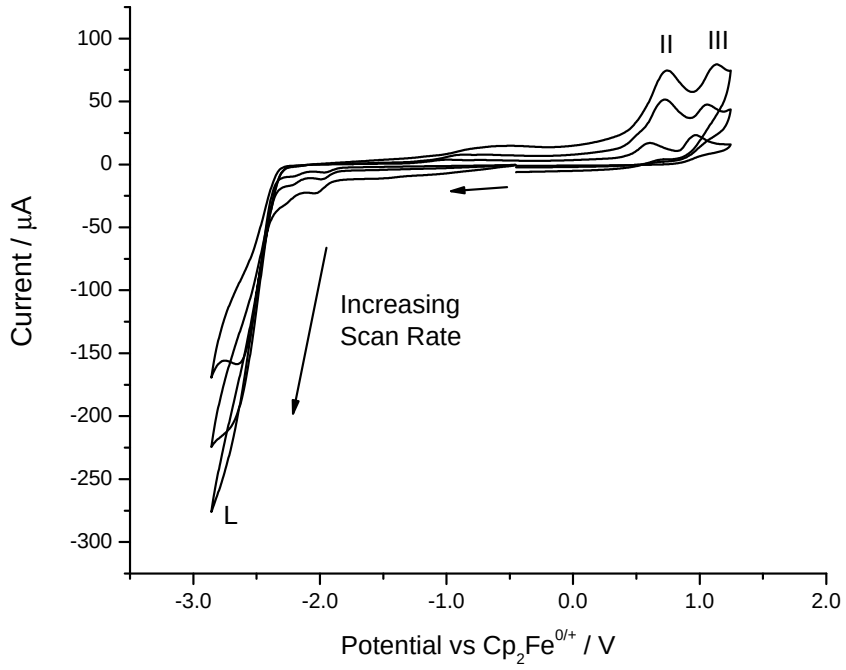

Figure 2.13. Cyclic voltammogram of **4** in CH_2Cl_2 (1.5 mmol dm^{-3}, 0.05 M [^{n}Bu$_4$N][B(C$_6$F$_5$)$_4$]) at a scan rates of 100, 300 and 750 mV s^{-1}

2.6. Electrochemical Simulations

Digital electrochemical simulations were performed for the reduction of **2** and the oxidation of **4** (figures 2.14 and 2.15 respectively). Digital simulation of cyclic voltammograms provide access to thermodynamic and kinetic parameters not measurable by experiment alone. The methods behind digital simulation are described in introduction in section 1.3.6. The best fit after simulating several mechanisms supports the steps seen in 2.4. Each Au^{III} centre undergoes a 1-electron reduction (E step) concomitant with the cleavage of the Au-X bond (where X = H, OH). The resulting Au^{II} radicals then undergo a rapid dimerisation to form compound **4** (C step). This dimer is electroactive and can be oxidised (E step) at a positive potential vs ferrocene. The product of this oxidation is not currently known, but deduced from its irreversibility it can be postulated that it involves cleavage of the Au^{II}-Au^{II} bond. Bochmann *et al.* have previously determined that the gold(II) pincer complex **4** is resistant to disproportionation, and including any disproportionation steps in the electrochemical mechanism provides a poor fit with experimental data. The globally optimised

parameters determined from the simulation can be seen in table 2.1. This includes the formal potential (E^0), charge transfer coefficient (α), standard electron transfer coefficient (k^0) and the diffusion coefficient (D_0).

Table 2.1. Simulated parameters of the reduction of **2** and **3** and the oxidation of **4**

Parameter	$Au^{III}OH$	$Au^{III}H$	Au^{II}-Au^{II}
E^0 / V vs $Cp_2Fe^{0/+}$	-2.30	-1.91	0.6
α	0.3	0.35	0.6
k^0 / 10^{-3} cms^{-1}	5.4	2.0	68
D_0 / 10^{-5} cm^2s^{-1}	1.51	1.60	0.7

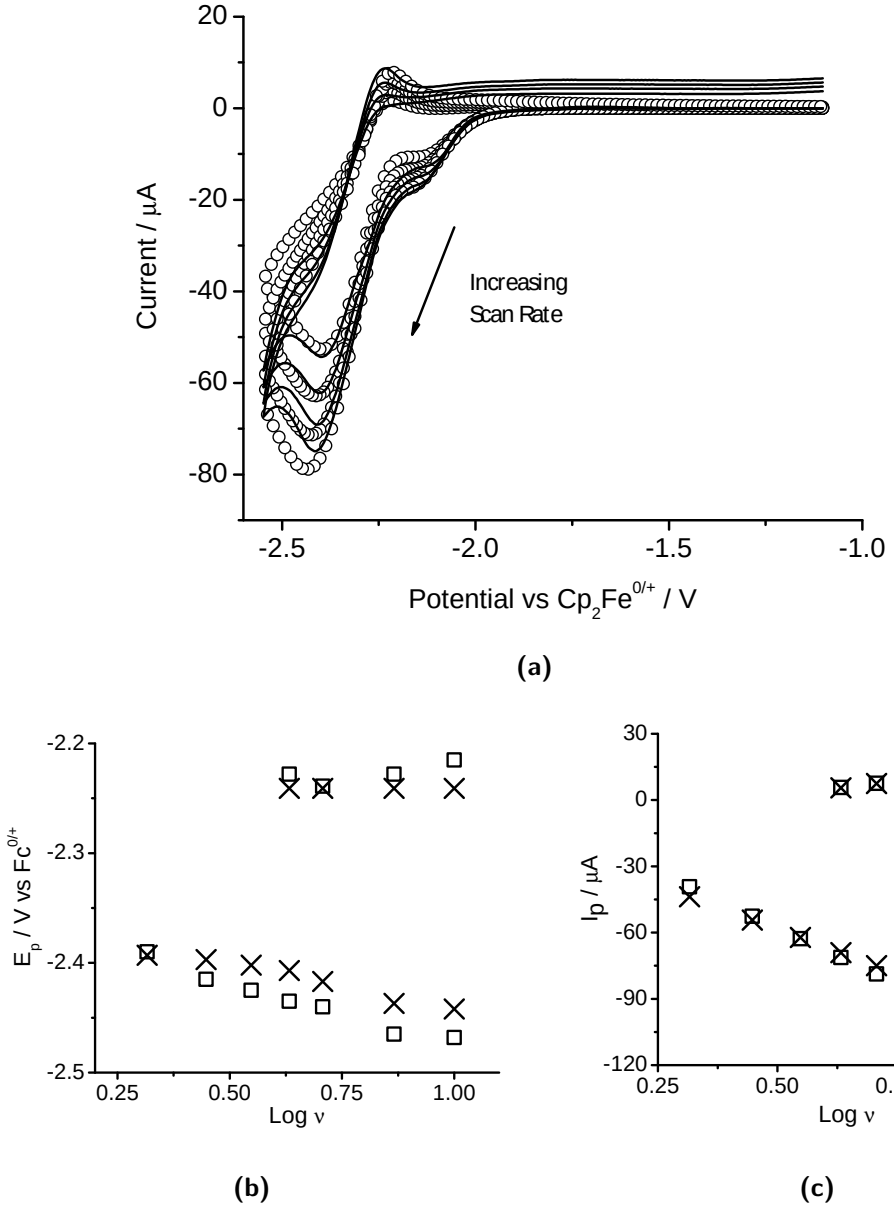

Figure 2.14. **a)**, Experimental (solid line) and simulated (open circle) voltammogram of the cathodic voltammetry of **2**, 1.5 mmol dm^{-3} in CH_2Cl_2 with 0.5 mol dm^{-3} [^{n}Bu$_4$N][B(C$_6$F$_5$)$_4$] as supporting electrolyte. **b)** and **c)**: plot comparing simulated (open squares) with experimental (crosses) peak potential (E_p) and peak current (I_p) respectively

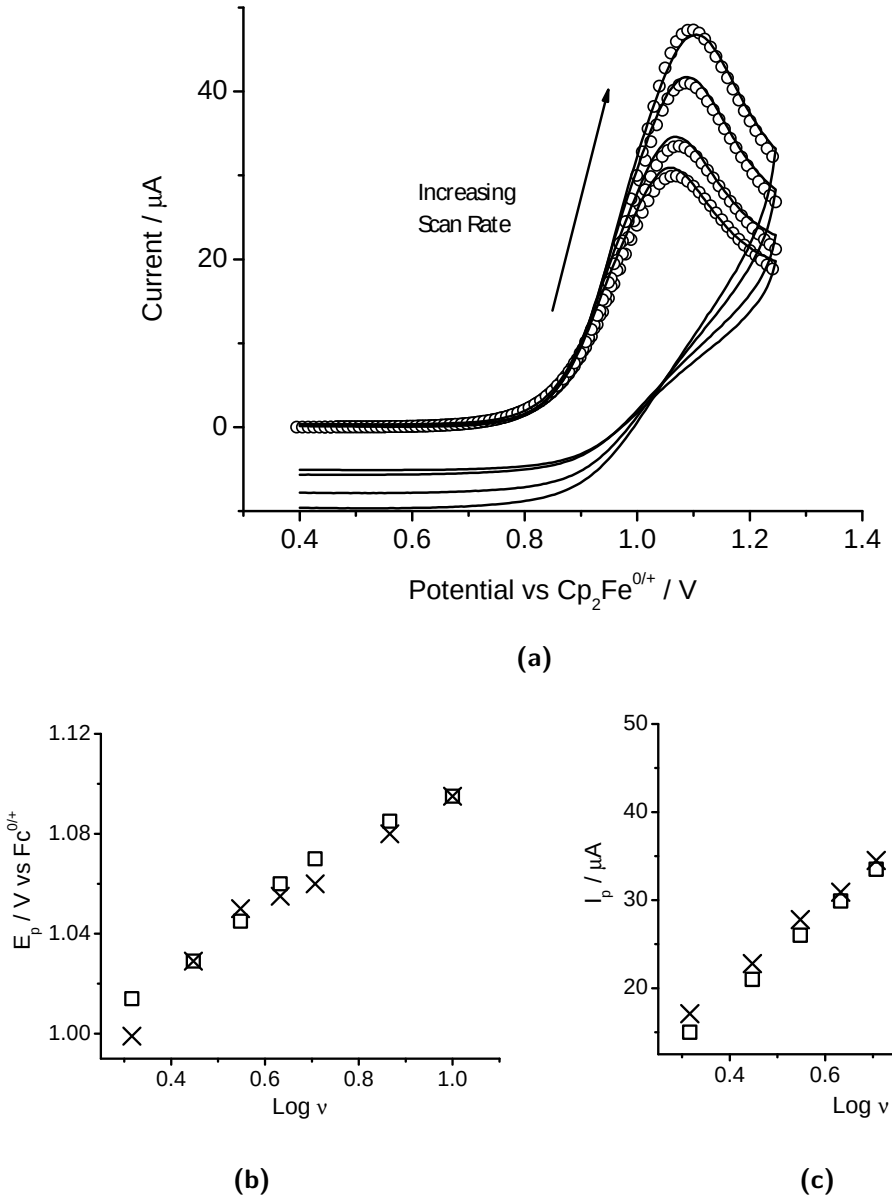

Figure 2.15. **a)**, Experimental (solid line) and simulated (open circle) voltammogram of the anodic voltammetry of **4**, 1.5 mmol dm^{-3} in CH_2Cl_2 with 0.5 mol dm^{-3} [^{n}Bu$_4$N][B(C$_6$F$_5$)$_4$] as supporting electrolyte. **b)** and **c)**, plots comparing simulated (open squares) with experimental (crosses) peak potential (E_p) and peak current (I_p) respectively

2.7. Thermodynamic Cycle of Reductive Condensation

The combination of the reductive condensation of **2** in the presence of **3** and the known potentials of hydride and hydroxide oxidation allows the construction of a Hess cycle to determine the bond dissociation energy of the gold-gold bond in **4**. Using the relationship in equation 2.1, where F = 96.485 kJ mol^{-1} (Faraday's constant), the potentials can be expressed as a Gibb's free energy in kJ mol^{-1}.

$$\Delta G = -FE \tag{2.1}$$

Figure 2.5 shows the relationship between the products of reduction I for the hydride and hydroxide, water and the resulting dimer. Using the formal potentials in equation 2.1 it is possible to determine that the dissociation energy of the gold(II)-gold(II) bond is 198 kJ mol^{-1}. This is reassuringly close to the value calculated for the unbridged gold(II) compounds investigated by Xiong and Pykko, described in section 2.4

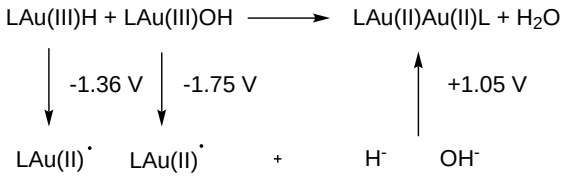

Scheme 2.5 Relationship between **3**, **2**, **4** and water

$$\Delta G = 96.485(-1.36 - 1.75 + 1.05)$$

$$\Delta G = 198 \text{kJ mol}^{-1}$$

Similarly, the same relationship can be utilised to determine the bond energy difference between the gold(III) hydroxide and gold(III) hydride bonds in **2** and **3** respectively, giving a ΔG of *ca.*

19 kJ mol^{-1}. This value is close to that calculated with DFT.

$$\Delta G = \frac{-F(-1.36 + 1.75)}{2}$$

$$\Delta G = \frac{-F \times 0.39}{2}$$

$$\Delta G = \frac{-96.485 \times 0.39}{2}$$

$$\Delta G = 18.81 \text{kJ mol}^{-1}$$

2.8. DFT Calculations

To confirm the results determined from electrochemical simulation, density functional theory calculations were performed by Dr Joseph Wright (figure 2.16). The NMe_4+ ion was used to balance the charges on the reduced products, giving the overall reaction in scheme 2.6. The six steps postulated for the electrochemical pathway upon reduction are summarised in scheme 2.7 with the relative energies in table 2.2 What can be determined from these results

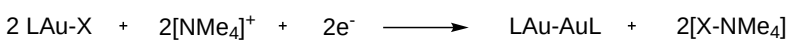

Scheme 2.6 Overall reaction in DFT analysis

A) $2LAu^{\cdot}X + 2[NMe_4]^+$

B) $[LAu\text{-}X\cdots NMe_4] + LAu\text{-}X + [NMe_4]^+$

C) $LAu^{\cdot} + [X\cdots NMe4] + LAu^{\cdot}X + [NMe_4]^+$

D) $LAu\text{-}X\text{-}AuL + [X\cdots NMe_4] + [NMe_4]^+$

E) $[LAu\text{-}X\text{-}AuL\cdots NMe_4] + [X\cdots NMe_4]$

F) $LAu\text{-}AuL + 2[X\cdots NMe_4]$

Scheme 2.7 The 6 electrochemical and chemical reaction steps upon gold(III) pincer reduction

Table 2.2. Relative energies of electrochemical steps in $kJ\,mol^{-1}$

Step	Au-OH	Au-H
A	0	0
B	-410	-444
C	-169	-475
D	-217	-495
E	-740	-1054
F	-563	-1174

is that the final step (formation of the Au(II)-Au(II) dimer in step F) is exothermic relative to E, where X = OH but not where X = H. Therefore the second reduction follows through to the dimer where X = OH. When allowing for a cation, reduction in both H and OH cases goes through to the Au-Au dimer as a low energy species. The DFT calculations also show that the loss of X^- is endothermic, when X = H (steps B to C and E to F are both 'up hill', see figure 2.16). This is to be expected as a free hydride ion should be of much higher energy than a free hydroxide ion. Even accounting for the energetic differences between the H and

OH pathways, the lack of a 'bridge' structure in the OH case is more likely the cause of the observed reduction behaviour.

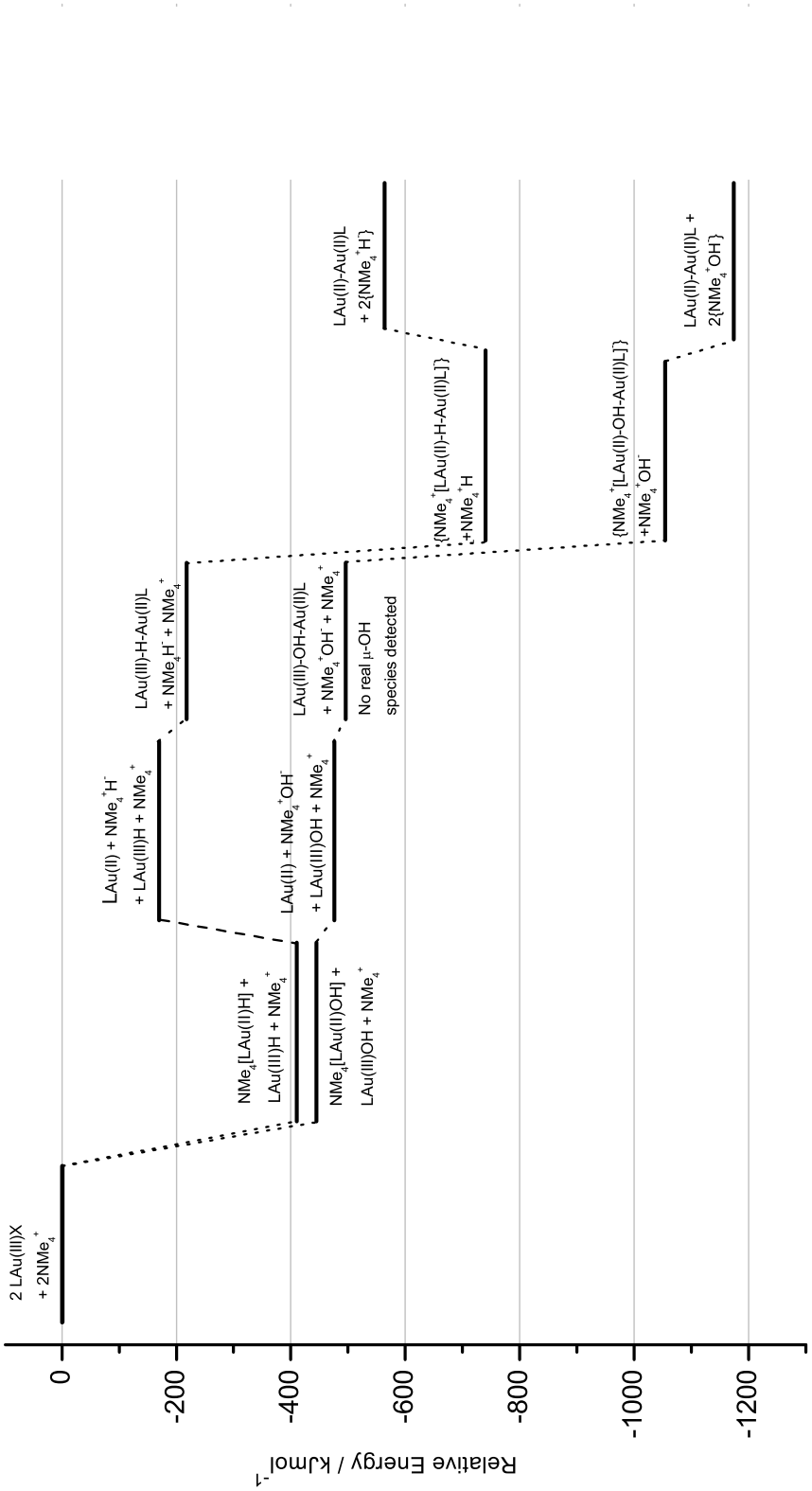

Figure 2.16. DFT energies of the products from stages A-F

2.9. Conclusions

To summarise the work carried out, the unusual stability of the unsupported gold(II)-gold(II) bond in bimetallic complexes based on the 2,6-bis(4'-tert-butylphenyl)pyridine 'pincer' backbone was investigated by electrochemical methods. The cyclic voltammetry shows that upon reduction of gold(III) pincer hydrides and hydroxides, one of the chemical steps that occurs is the formation of the gold(II) bimetallic complex. This was determined by recording cyclic voltammetry of an authentic sample of the gold(II) dimer, showing an oxidation wave at 0.59 V vs $Cp_2Fe^{0/+}$, a wave that is present in the voltammograms of the hydride and hydroxide. Using digital simulation, the reduction potentials of the hydride and hydroxide along with the oxidation potential of the dimer were determined, allowing the construction of a Hess cycle, from which the bond energy of the gold-gold bond in the dimer and the difference of the Au-OH and Au-H bond energies. This is the first example of the determination of a gold(II) bond energy by experimental electrochemical methods, where the bond energy of the Au^{II}-Au^{II} bond in the gold(II) pincer dimer **4** was determined to be 198 kJ mol^{-1} These data were supported by DFT calculations, which also resolved the counter-intuitive result that the hydride reduction is more facile than the reduction of the hydroxide.

Having demonstrated the power of organometallic electrochemistry to elucidate mechanistic and thermodynamic for metal-centred redox reactions of organometallic complexes, attention is now turned to complexes containing a redox inactive metal centre, where instead the ligand framework exhibits redox activity.

References

(1) T. Dann, D.-A. Roșca, J. A. Wright, G. G. Wildgoose and M. Bochmann, *Chem. Commun.*, 2013, **49**, 10169–10171.

(2) L.-P. Liu and G. B. Hammond, *Chem. Soc. Rev.*, 2012, **41**, 3129–3139.

(3) M. Gimeno and A. Laguna, in *Comprehensive Coordination Chemistry II*, ed. Editors-in-Chief: J. A. McCleverty and T. J. Meyer, Pergamon, Oxford, 2003, pp. 911–1145.

(4) M. Gimeno, *Modern Supramolecular Gold Chemistry: Gold-Metal Interactions and Applications*, ed. A. Laguna, Wiley-VCH Verlag GmbH & Co. KGaA, Weinheim, 2008.

(5) H. Schmidbaur, *Gold Bull*, 2000, **33**, 3–10.

(6) A. S. K. Hashmi, *Chem. Rev.*, 2007, **107**, 3180–3211.

(7) N. Marion, P. d. Frémont, G. Lemière, E. D. Stevens, L. Fensterbank, M. Malacria and S. P. Nolan, *Chem. Commun.*, 2006, 2048–2050.

(8) S. K. Schneider, W. A. Herrmann and E. Herdtweck, *Z. Anorg. Allg. Chem.*, 2003, **629**, 2363–2370.

(9) Y. Fuchita, Y. Utsunomiya and M. Yasutake, *J. Chem. Soc., Dalton Trans.*, 2001, 2330–2334.

(10) Y. Fukuda and K. Utimoto, *J. Org. Chem.*, 1991, **56**, 3729–3731.

(11) A. S. K. Hashmi, L. Schwarz, J.-H. Choi and T. M. Frost, *Angew. Chem., Int. Ed.*, 2000, **39**, 2285–2288.

(12) Y. Fuchita, H. Ieda, Y. Tsunemune, J. Kinoshita-Nagaoka and H. Kawano, *J. Chem. Soc., Dalton Trans.*, 1998, 791–796.

(13) E. C. Constable, R. P. G. Henney, P. R. Raithby and L. R. Sousa, *Angew Chem , Int Ed*, 1991, **30**, 1363–1364.

(14) M. A. Cinellu, A. Zucca, S. Stoccoro, G. Minghetti, M. Manassero and M. Sansoni, *J. Chem. Soc., Dalton Trans.*, 1995, 2865–2872.

(15) E. C. Constable and T. A. Leese, *J. Organomet. Chem.*, 1989, **363**, 419–424.

(16) J. Vicente, M. D. Bermúdez, M. J. Sánchez-Santano and J. Payá, *Inorg. Chim. Acta*, 1990, **174**, 53–56.

(17) J. Vicente, M. Chicote and M. Bermúdez, *Inorg. Chim. Acta*, 1982, **63**, 35–39.

(18) J. Vicente, M. Chicote and M. Bermúdez, *J. Organomet. Chem.*, 1984, **268**, 191–195.

(19) J. Vicente, M. Dolores Bermudez and J. Escribano, *Organometallics*, 1991, **10**, 3380–3384.

(20) F. G. Herring, G. Hwang, K. C. Lee, F. Mistry, P. S. Phillips, H. Willner and F. Aubke, *J. Am. Chem. Soc.*, 1992, **114**, 1271–1277.

(21) S. H. Elder, G. M. Lucier, F. J. Hollander and N. Bartlett, *J. Am. Chem. Soc.*, 1997, **119**, 1020–1026.

(22) N. R. Walker, R. R. Wright, P. E. Barran and A. J. Stace, *Organometallics*, 1999, **18**, 3569–3571.

(23) N. R. Walker, R. R. Wright, P. E. Barran, J. N. Murrell and A. J. Stace, *J. Am. Chem. Soc.*, 2001, **123**, 4223–4227.

(24) M. S. Wickleder, *Z. Anorg. Allg. Chem.*, 2001, **627**, 2112–2114.

(25) M. N. I. Khan, J. P. Fackler, C. King, J. C. Wang and S. Wang, *Inorg. Chem.*, 1988, **27**, 1672–1673.

(26) H. E. Abdou, A. A. Mohamed and J. P. Fackler, *Inorg. Chem.*, 2007, **46**, 9692–9699.

(27) H. Murray and J. P. Fackler Jr., *Inorg. Chim. Acta*, 1986, **115**, 207–209.

(28) M. Bardaji, M. C. Gimeno, P. G. Jones, A. Laguna and M. Laguna, *Organometallics*, 1994, **13**, 3415–3419.

(29) M. Bardají, N. G. Connelly, M. C. Gimeno, J. Jiménez, P. G. Jones, A. Laguna and M. Laguna, *J. Chem. Soc., Dalton Trans.*, 1994, 1163–1167.

(30) V. W.-W. Yam, S. W.-K. Choi and K.-K. Cheung, *Chem. Commun.*, 1996, 1173–1174.

(31) V. W.-W. Yam, C.-K. Li, C.-L. Chan and K.-K. Cheung, *Inorg. Chem.*, 2001, **40**, 7054–7058.

(32) J. Coetzee, W. F. Gabrielli, K. Coetzee, O. Schuster, S. D. Nogai, S. Cronje and H. G. Raubenheimer, *Angew. Chem. Int. Ed*, 2007, **46**, 2497–2500.

(33) P. Kühlkamp, H. G. Raubenheimer, J. S. Field and M. Desmet, *J. Organomet. Chem.*, 1998, **552**, 69–74.

(34) M. Jamin and R. Iwamoto, *Inorg. Chim. Acta*, 1978, **27**, 135–143.

(35) G. Sanna, M. I. Pilo, N. Spano, G. Minghetti, M. A. Cinellu, A. Zucca and R. Seeber, *J. Organomet. Chem.*, 2001, **622**, 47–53.

(36) K. M.-C. Wong, L.-L. Hung, W. H. Lam, N. Zhu and V. W.-W. Yam, *J. Am. Chem. Soc.*, 2007, **129**, 4350–4365.

(37) D.-A. Roșca, D. A. Smith and M. Bochmann, *Chem. Commun.*, 2012, **48**, 7247–7249.

(38) D.-A. Rosca, D. A. Smith, D. L. Hughes and M. Bochmann, *Angew. Chem. Int. Ed.*, 2012, **51**, 10643–10646.

(39) A. Laguna and M. Laguna, *Coord. Chem. Rev.*, 1999, **193–195**, 837–856.

(40) A. A. Mohamed, H. E. Abdou and J. P. Fackler Jr., *Coord. Chem. Rev.*, 2010, **254**, 1253–1259.

(41) E. Tkatchouk, N. P. Mankad, D. Benitez, W. A. Goddard and F. D. Toste, *J. Am. Chem. Soc.*, 2011, **133**, 14293–14300.

(42) D. Zopes, C. Hegemann, W. Tyrra and S. Mathur, *Chem. Commun.*, 2012, **48**, 8805–8807.

(43) X.-G. Xiong and P. Pyykkö, *Chem. Commun.*, 2013, **49**, 2103–2105.

3. Bis(formanzanate) zinc compounds: electrochemical characterisation of redox non innocent ligands

The work contained in this chapter has been published in Angewante Chemie.[1]

3.1. Introduction to redox non-innocent ligands

As has been discussed with gold organometallic compounds, metal-centered redox reactions are important for many reactions involving bond formation and cleavage. Recently howerer, there has been much attention on redox processes that instead take place on the ligand framework of transition metal complexes.[2] The idea that ligands are involved in electron transfer reactions has been around since the 1960s, where metal dithiolate complexes were characterised by polarography and cyclic voltammetry.[3] It was discovered that the redox non-innocence of the dithiolate ligands was obscuring the true oxidation state of the metal centre (see figure 3.1). This work lead to dithiolenes and dioxolenes becoming the most studied class of redox non-innocent ligands. More recently however, α-diimines[4] and bis(imino)pyridines[5–7] have been the focus of much work in this field.

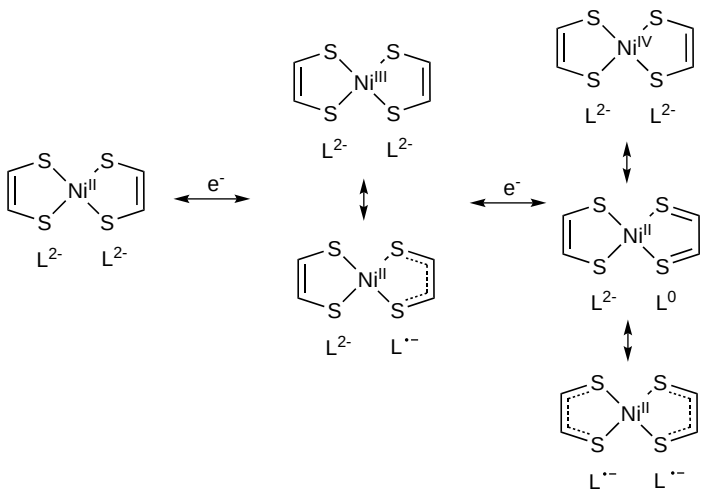

Figure 3.1. The electron transfer series of a nickel dithiolate, showing redox non-innonce of the ligand

To determine the redox-non innocence of a ligand, crystallographic analysis can be used, where unusual bond lengths of the ligand are evidence that it has undergone reduction or oxidation. For example, Patra *et al*, using X-ray structure analysis showed that in $[Ru(acac)_2L]$ (where L = iminoquinone) the C-C intra-ring, C-N and C-O bond distances indicate a consistent Ru(III) system upon which the ligands account for the majority of the redox activity.[8] In this system metal centred redox processes also occur (see figure 3.2)

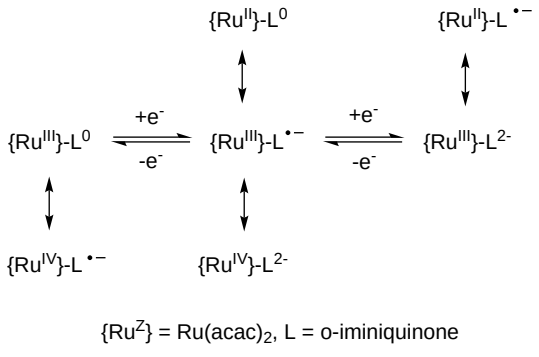

Figure 3.2. Redox-non innocence of a ruthenium iminoquinone with acac ligands

β-diketiminates (figure 3.3, a) are a class of compounds that are widely used as ligands for a large variety of metals, and are considered to be stable and not involved in redox chemistry. Recently it has been discovered that some examples of β-diketiminates[9] are redox non-innocent, where the ligands were reduced to be metal bound di- and trianions.[10–12] For example, the reduction of the ytterbium β-diketiminate $[YbL_2]$ where L = $\{N(SiMe_3)C(Ph)\}_2CH^-$ with ytterbium-napthalene affords the trinuclear complex $[YbL_3.THF]$, with one terminal monoanionic β-diketiminate and two doubly reduced bridging trianion ligands. Compounds with

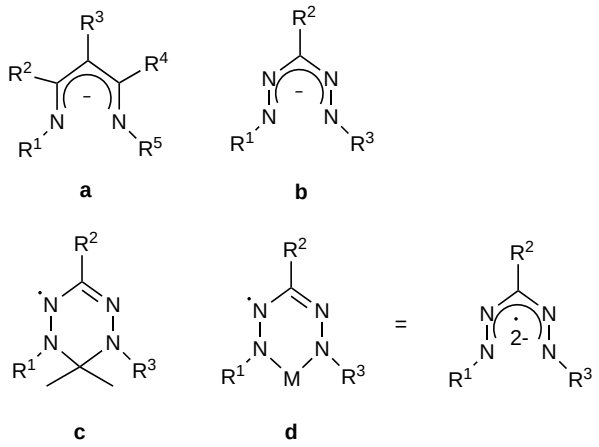

Figure 3.3. a) β-diketiminate b) formazanate c) vedazyl radical d) 'metalloverdazyl'

reduced β-diketiminate tend to be unstable however, giving them only limited applications.[13–16] A much less studied but close analogue of the β-diketiminates ligands are formazanate ligands (formally 1,2,4,5-tetraazapentadienyls). The stability of the 6-membered radical heterocycles derived from formazans (known as verdazyls, figure 3.3, c) prompted the investigation of formazanate ligands (figure 3.3, b) by Otten *et al.* in collaboration with the Wildgoose group and the author. Therefore zinc(II) complexes with formazanate ligands were electrochemically characterised by cyclic voltammetry, with the thermodynamic and kinetic paramters of the redox processes obtained by digital simulation of the resultant voltammograms. Note that the zinc(II) metal centre is redox inactive at all potentials studied.

3.2. Synthesis of bis(formazanate) zinc compounds

Bis(formazanate) zinc complexes are prepared by the protonolysis of neutral ligand precursors. In the case of the formazan **5**, the successful preparation of the zinc complex can be determined from a colour change from red to intense blue. The formazan **7** also has a facile reaction with Me_2Zn, but requires heating overnight to get full conversion (see scheme 3.1). The compounds characterised herein were prepared by Dr Edwin Otten and Mu-Chieh Chang at the University of Groningen (Netherlands) and electrochemically characterised at the University of East Anglia in collaboration with the author. X-Ray quality crystals were grown of compound **7**, and crystallographic analysis shows the full delocalisation of the formazanate ligand by the equivalent N-N and C-N bond lengths in the ligand backbone (see table 3.1).

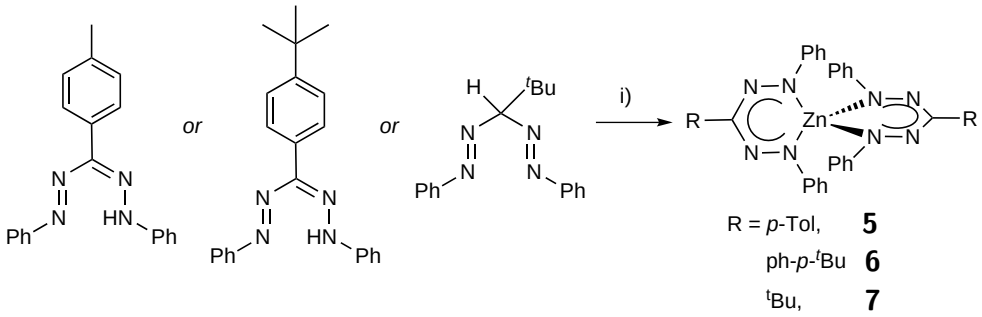

Scheme 3.1 Reagents and conditions: i) Me_2Zn, toluene

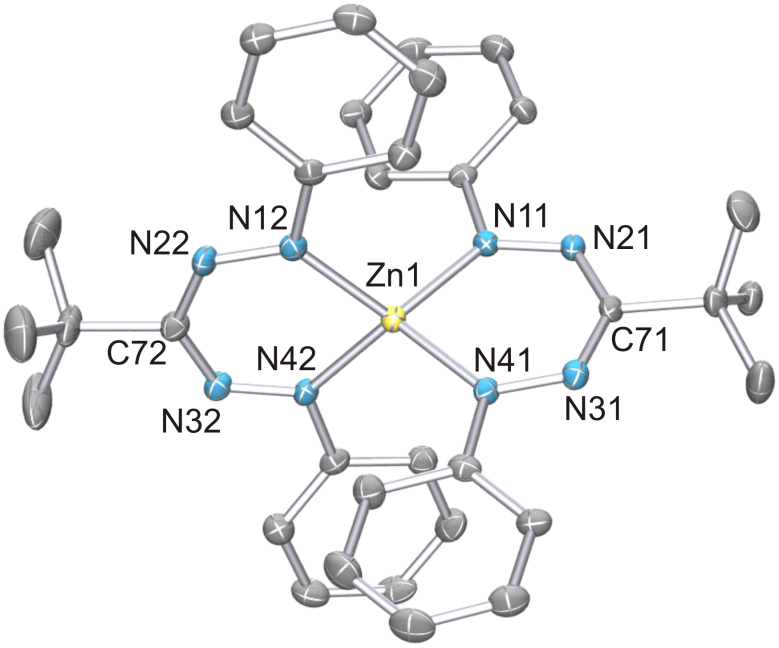

Figure 3.4. Molecular structure of compound **7**

Table 3.1. Selected bond lengths in **7**

Bond	Length Å
Zn(1)-N(11)	1.9824(17)
Zn(1)-N(41)	1.9822(18)
Zn(1)-N(12)	1.9902(17)
Zn(1)-N(42)	1.9769(18)
N(11)-N(21)	1.310(2)
N(32)-N(41)	1.307(2)
N(12)-N(22)	1.307(2)
N(32)-N(42)	1.309(2)

3.3. Cylic Voltammetric Analysis

Cyclic voltammetry was used to evaluate the redox chemistry of the formazanate complexes **5**, **6** and **7** in THF solution with weakly coordinating $[^nBu_4N][B(C_6F_5)_4]$ as the supporting electrolyte. In the case of **5**, scanning in a reductive direction the CV shows two quasi-reversible, single-electron redox processes at -1.3 and -1.6 V vs $Cp_2Fe^{0/+}$, labelled system I/I' and II/II' respectively (figure 3.5) These quasi-reversible reductive peaks are stable over at least 30 redox cycles. The cyclic voltammetry of formazanate **6** appears to be very similar to that of **5**. Two quasi-reversbile reduction waves are observed, and the voltammetry is stable to 30 repeats scans. The reduction waves of **6** are at -1.5 and -1.86 V vs $Cp_2Fe^{0/+}$. The cyclic voltammetry of formazanate **7** again has an appearance similar to that of **5** and **6**, with two quasi-reversible reducion waves observed, which are also stable to 30 repeat cycles. The two waves for **7** are at the most negative potentials of -1.61 and 1.87 V vs $Cp_2Fe^{0/+}$ respectively. In all cases, the reductions are shown to be sequential and independent by reversing the scan after peak I

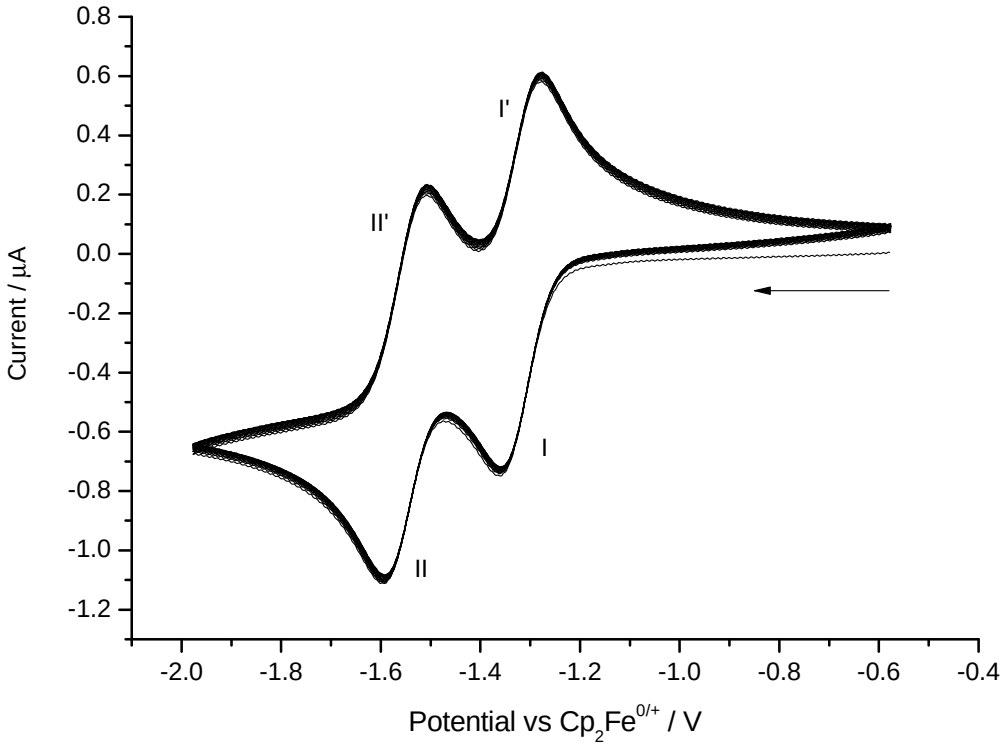

Figure 3.5. Thirty repeat cyclic voltammograms of a 2.5 mM solution of **5** in THF with $[^nBu_4N][B(C_6F_5)_4]$ electrolyte recorded at 100 mV s^{-1}

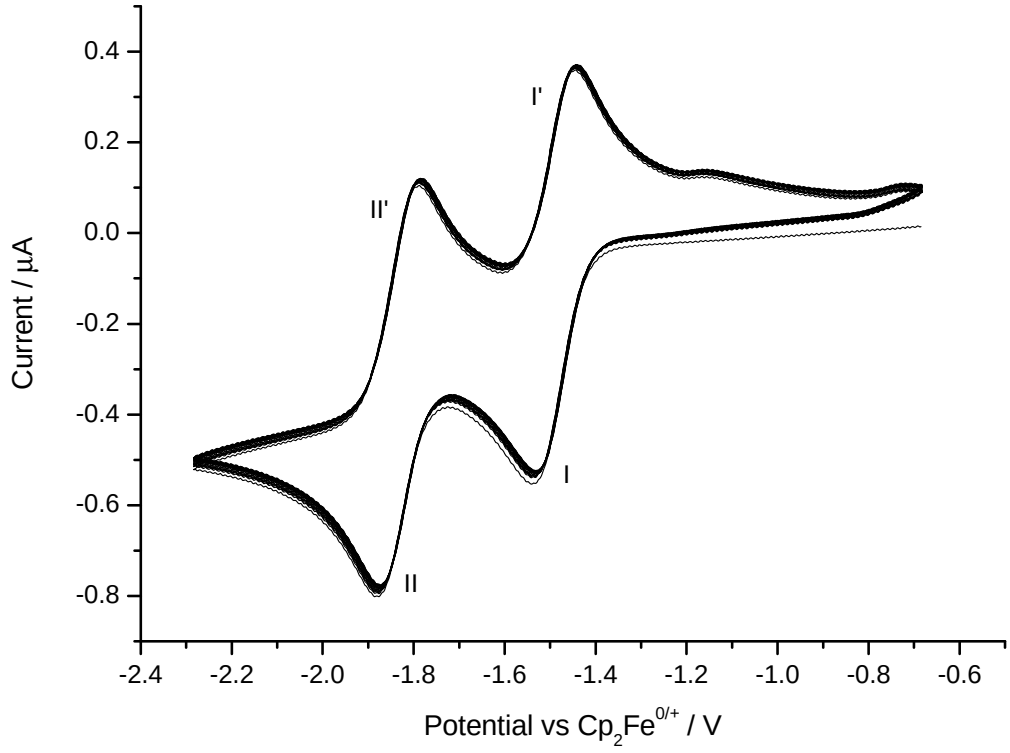

Figure 3.6. Thirty repeat cyclic voltammograms of a 2.5 mM solution of **6** in THF with $[^nBu_4N][B(C_6F_5)_4]$ electrolyte recorded at 100 mV s^{-1}

but before peak II, as the oxidation I' is still observed. When the scan rate is varied from 100 mV s^{-1} to 1000 mV s^{-1}, both processes for **5** and **7** had a linear relationship between the peak current and the square root of the scan rate, indicating solution phase diffusion-controlled redox processes. To obtain thermodynamic and kinetic parameters for the redox processes observed, digital simulation of cyclic voltammetry was performed. Excellent fits were obtained between the experimental and simulated voltammograms (see figures 3.8 and 3.9) where an *EE* mechanism was applied, yielding values for formal potentials, E^0, and electron transfer rate coefficients, k^0.These values are listed in table 3.2. Charge transfer coefficients (α) for all processes were 0.5 $\pm$ 0.02.

The formal potentials determined by simulation make it clear that the replacement of an inductively electron withdrawing *p*-tolyl group with an electron donating ^{t}-butyl group has the expected effect of a more negative reduction potential, with the ^{t}-butyl reduction potential at the more negative -1.57 vs. -1.31 V vs $Cp_2Fe^{0/+}$ for the *p*-tolyl (see table 3.2 The cyclic

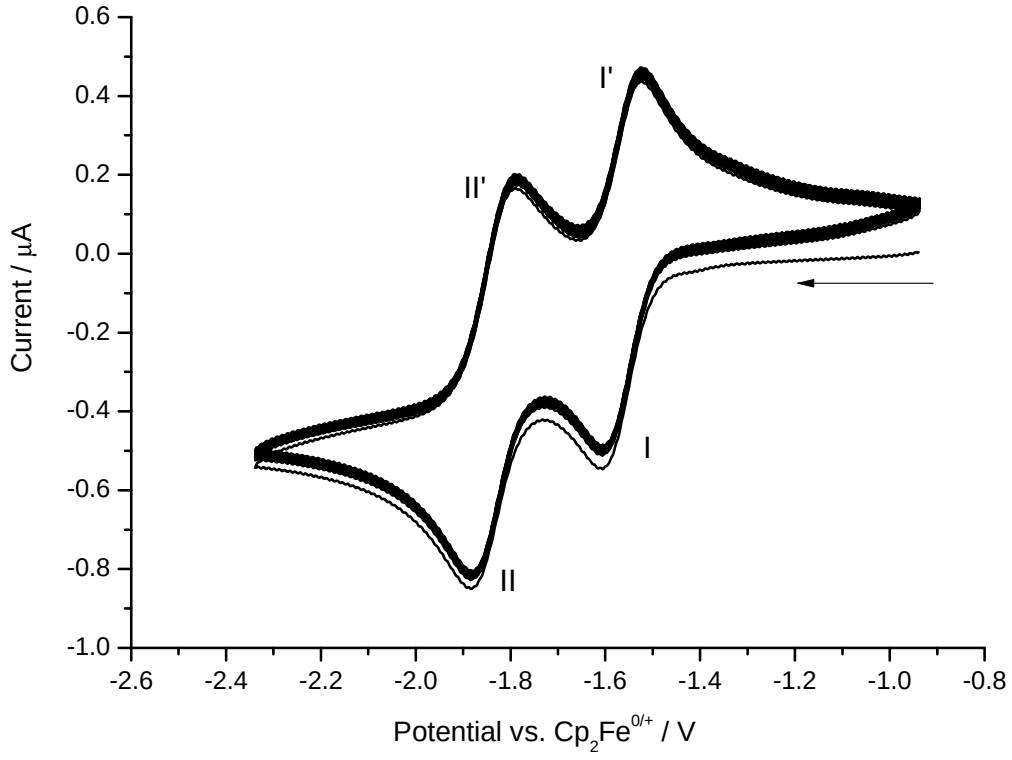

Figure 3.7. Thirty repeat cyclic voltammograms of a 2.5 mM solution of **7** in THF with $[^{n}Bu_4N][B(C_6F_5)_4]$ electrolyte recorded at 100 mV s^{-1}

voltammetry also indicates that the singly reduced radical and double reduced anionic forms of **5** and **7** are synthetically accessible. In 2007, Hicks and co-workers showed that formazans react with boryl triacetate to form boratetraazines, which can be reduced in a 1-electron transfer process to borataverdazyl radical anions.[17] Interestingly the one electron reductions for the zinc formazanates **5** and **7** occur at a more negative potential than the reduction of the boratetraazines. This is likely to be due to the different lewis acidities of the zinc(II) and boron centres in addition to the delocalisation across the bis-formazanate ligands in the zinc complexes.

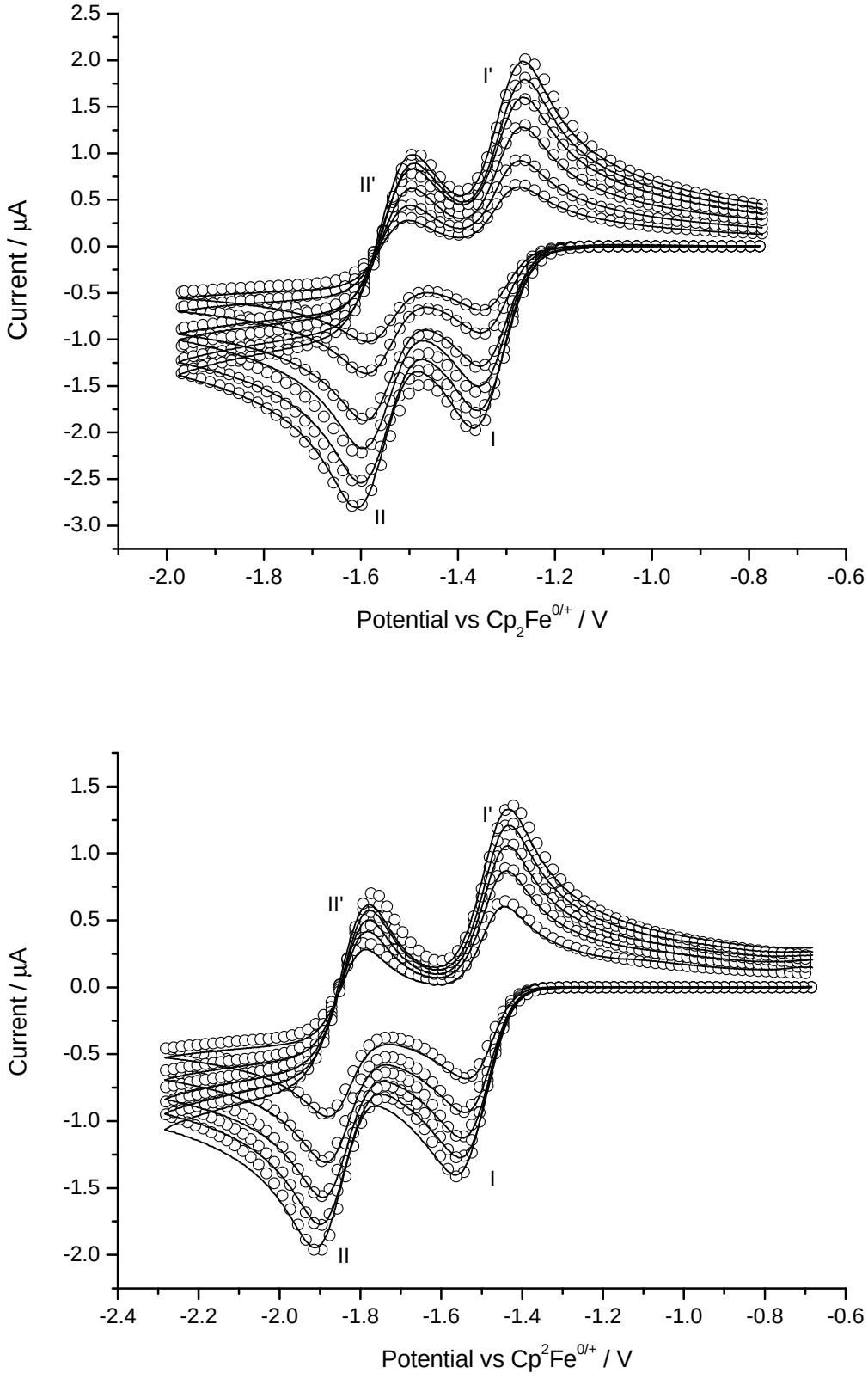

Figure 3.8. A comparison of experimental (solid line) vs. simulated data (open circles) for a 2.5 mM solution of **5** (top) and **6** (bottom) in THF with $[^nBu_4N][B(C_6F_5)_4]$ electrolyte recorded at 100, 200, 400, 600, 800, and 1000 $mV\,s^{-1}$

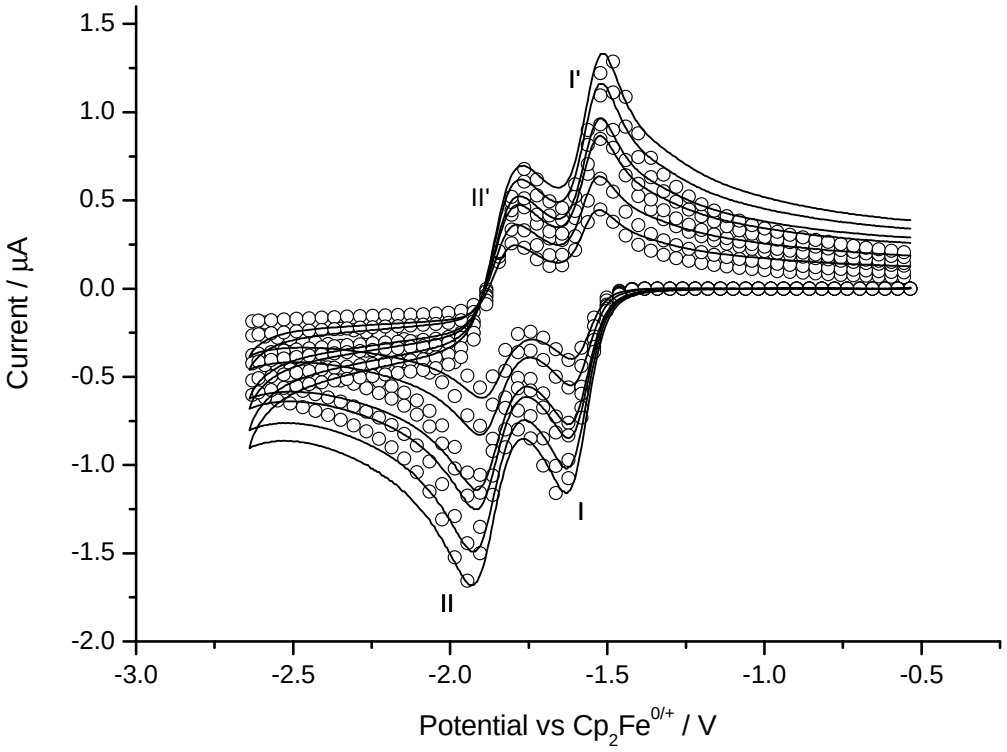

Figure 3.9. A comparison of experimental (solid line) vs. simulated data (open circles) for a 2.5 mM solution of **7** in THF with $[^{n}Bu_4N][B(C_6F_5)_4]$ electrolyte recorded at 100, 200, 400, 600, 800, and 1000 mV s^{-1}

Table 3.2. Simulated parameters of the reduction of compounds **5** **6** and **7**

Compound **5**	E^0 / V vs $Cp_2Fe^{0/+}$	k^0 / $\times 10^{-2}$cm s^{-1}
System I/I'	-1.31 ± 0.01	1.25 ± 0.05
System II/II'	-1.55 ± 0.01	0.9 ± 0.05
Compound **6**		
System I/I'	-1.49 ± 0.01	0.67 ± 0.05
System II/II'	-1.84 ± 0.02	0.63 ± 0.05
Compound **7**		
System I/I'	-1.57 ± 0.01	1.30 ± 0.05
System II/II'	-1.86 ± 0.02	0.75 ± 0.05

3.3.1. Chemical reduction of zinc formazante compounds

The cyclic voltammetry indicates that the singly reduced radical and doubly reduced dianion form of **5** and **7** are synthetically accessible. Therefore in this collaboration the products of the chemical reduction of the zinc formazanate compounds were prepared and characterised by Edwin Otten and Mu-Chieh Chang. Their findings are summarised here. Initially compounds **5** and **7** with 1 equivalent of sodium amalgam in THF (figure 3.10). This resulted in the radical species $[Na(THF)_3][\{PhNNC(R)NNPh\}_2Zn]$ (R = *p*-tolyl, **8**; R = ^{t}Bu, **9**), which were both crystallised by slow diffusion of hexane into a THF solution. The compounds **8** and **9** are NMR silent but give rise to broad signals in EPR spectroscopy (g-value $\approx$ 2) in THF and frozen solution, in which no hyperfine splitting was observed. In the molecular structures of **8** and **9**, it is observed that the tetrahedral zinc formazanate radical anion interacts with a $Na(THF)_3^+$ cation through either one (**8**) or two (**9**) nitrogen atoms (figure 3.11). Close inspection of the parameters within the formazanate backbone shows that there are two distinc ligands in the zinc formazanate radical anion. One of the formazanates is similar to the neutral precursor, wherease the formazanate that binds to the sodium cation has a shorter Zn-N bond, with elongated N-N bond lengths. Therefore the zinc formazanate radical anion can be described as a Zn^{2+} cation coordinated by a monoanionic formazanate and a reduced dianionic formazanate. The dianionic formazanate can be considered an inoganic analogue of the verdazyl radical. The electrostatic interaction of one of the formazanates to the $Na(THF)_3^+$ cation likely localizes

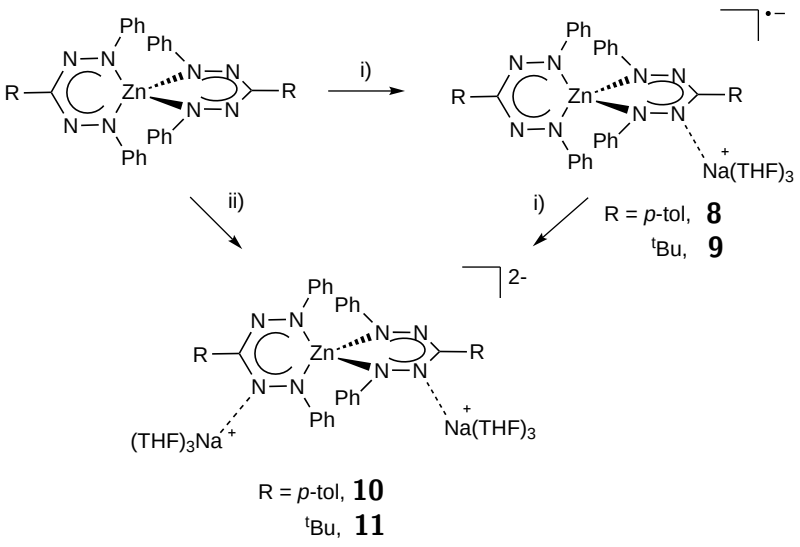

Figure 3.10. Synthesis of mono and dianionic zinc formazanates. Reagents and conditions: i) 1 Eq Na(Hg), THF, ii) 2 Eq Na(Hg), THF.

Table 3.3. Selected Bond Lengths in **8** and **9**

Bond	**8** x = 1		**9** x = 2	
Zn(1)-N(1x)	2.0226(15)	1.9542(15)	1.9857(16)	1.9447(16)
Zn(1)-N(4x)	2.0272(15)	1.9625(15)	2.0207(16)	1.9657(16)
N(1x)-N(2x)	1.299(2)	1.357(2)	1.313(2)	1.360(2)
N(3x)-N(4x)	1.308(2)	1.364(2)	1.295(2)	1.370(2)

the additional negative charge, giving rise to the two ligand based redox states. This is comparable to what is observed for species such as $[\{PhB(\mu\text{-}NtBu)_2\}_2M]$ (where M = Al, Ga)[18] and $(\beta\text{-diketiminate})_2Al$. In the case of the neutral radical species, the unpaired electron is delocalized over the spirocyclic structure, wherease in the radical $[\{PhB\mu\text{-}NtBu)_2\}_2M]$ (where M = Mg, Zn)[19]

The cyclic voltammetry of **5** and **7** indicates that adding two equivalents of sodium amalgam will afford the dianionic zinc formazanate complexes in the form $[Na(THF)_3]_2[\{PhNNC(R)NNPh\}_2Zn]$ (R = *p*-tolyl, **10**; R = ^{t}Bu, **11**). An X-ray quality crystal of **11** was characterised to give the molecular structure. It contains two sodium cations that both interact with two N-atoms of each formazanate ligand. The presence of an additional electron in both formazante ligands is evidenced by the similar bond lengths observed in each (Table 3.4). Specifically, all N-N bonds in **11** are elongated in comparison to those in the neutral precursor (average bond lengths in Å:1.308(4) for neutral **7**,1.304(3) and 1.365(3) for the neutral and Na coordinated ligand in the singly reduced **9** respectively, and 1.367(4) for both ligands in the diradical **11**)

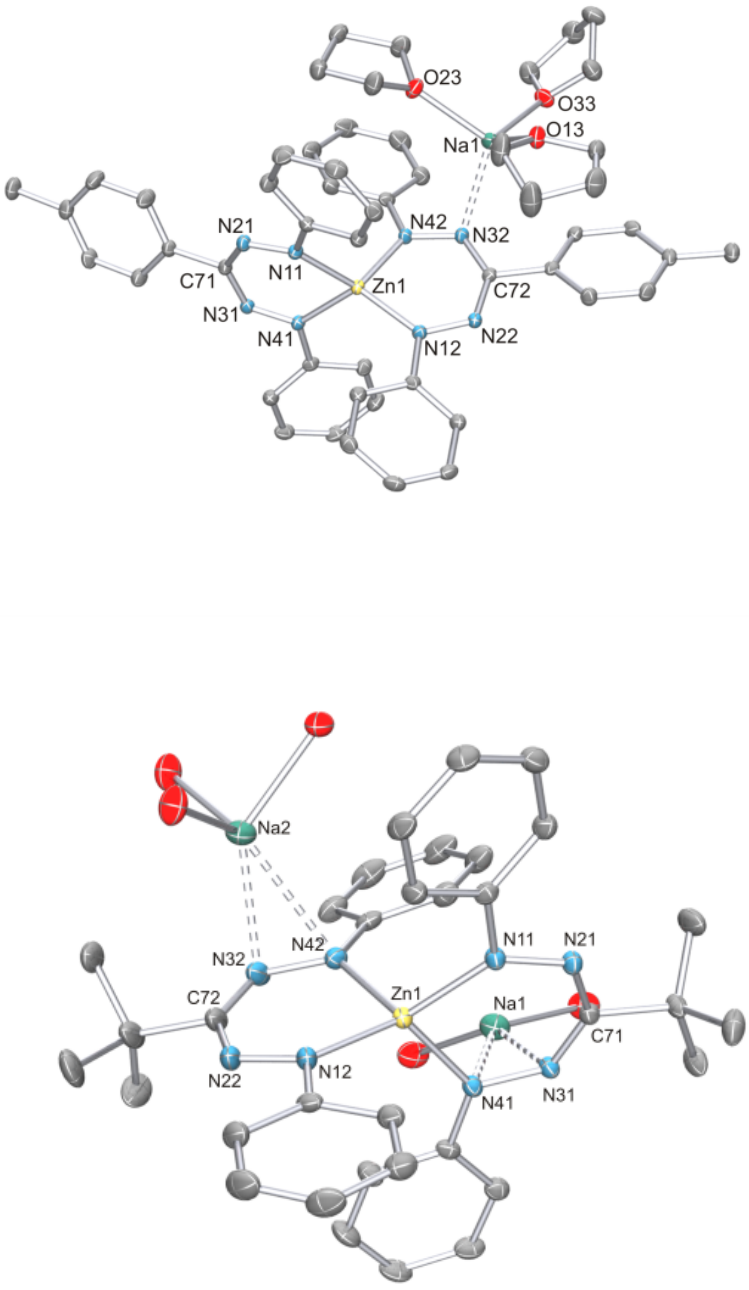

Figure 3.11. Molecular structure of **8** and **9** showing 50% probability ellipsoids. The hydrogen atoms are omitted for clarity.

Table 3.4. Selected Bond Lengths in **11**

	(x = 1)	(x = 2)
Zn(1)-N(1x)	1.9793(14)	1.9696(14)
Zn(1)-N(4x)	1.9839(14)	1.9952(15)
N(1x)-N(2x)	1.359(2)	1.355(2)
N(3x)- N(4x)	1.376(2)	1.378(2)

3.3.2. DFT calculations

DFT calculations (performed by Martin Lutz at Utrecht University) were carried out to examine the electronic structure of the complexes described here. The crystallographically determined bond lengths and angles are reproduced accurately by (unrestricted) B3LYP/6-31G(d) calculations using Gaussian09 starting from the X-ray coordinates. However, geometry optimization of the 'free' radical anions in **5** at the UB3LYP/6-31G(d) level of theory resulted in structures in which the SOMO is delocalized over both ligands. For example, in $\mathbf{5}_{calc}$ the diagnostic N-N bond lengths are all equivalent at $\approx$ 1.322 Å, in between the short radical formazanate (average: 1.304 Å) and long N-N bonds in the dianionic fragment (average 1.361 Å) observed experimentally. When the countercation $[Na(THF)_3]^+$ that is present in the crystal structure determination is included in the computations, the unpaired electron is localized (see figure 3.12 for $\mathbf{5}_{calc}$). This is in agreement with the experimental data and suggests that electrostatic effects are responsible for this localization. The calculated hyperfine interactions with the ^{14}N nuclei are small in $\mathbf{5}_{calc}$ (< 2.1 G), which likely accounts for the broad, featureless EPR signals observed experimentally.

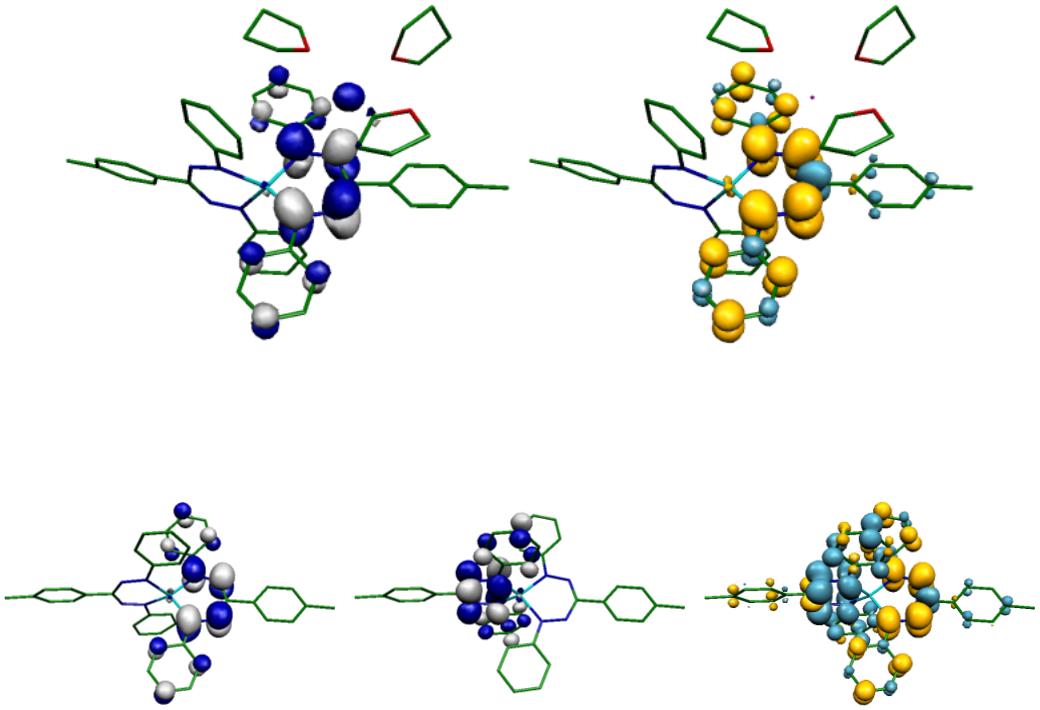

Figure 3.12. SOMO (left) and spin density plot (right) for $\mathbf{8}_{calc}$ (top); the two ligand-centered SOMOs for the BS(1,1) solution (left) and spin density plot (right) for$\mathbf{10}_{calc}$ (bottom)

For the diradicals **10** and **11**, geometry optimizations of the zinc formazanate fragment in the absence of countercations converges at structures that have two (virtually) identical dianionic formazanate ligands with elongated N-N bond lengths of $\approx$ 1.346 Å, which is somewhat shorter than those observed experimentally for **11** (average 1.367 Å). DFT calculations of singlet and triplet states in compounds **10** and **11** suggest that the triplet is favoured by 14-16 kcalmol^{-1} for both UB3LYP and UM06 calculations, but a broken-symmetry (BS)21 singlet diradical solution was found to have approximately equal energy as the triplet. For this BS(1,1) solution, the two ligand-based unpaired electron spins are antiferromagnetically coupled with J_{calcd} = -7.9 cm^{-1} to give a singlet diradical ground state.

3.4. Conclusion

In summary, formazanate compounds have been used as redox non-innocent ligands for zinc complexes, in place of the less stable β-diketiminates. These complexes have been

electrochemically characterised by cyclic voltammetry, showing remarkably facile reduction to a radical anion (-1.31 V where R = *p*-tolyl, -1,49 V where R = Ph-*p*-^{t}Bu and -1.57 V where R = ^{t}Bu) and further reduction to a dianion, (-1.55 V where R = *p*-tolyl, -1,84 V where R = Ph-*p*-^{t}Bu and -1.86 V where R = ^{t}Bu) in which both reductions are reversible. This allowed the radical anion and dianionic compounds to be accessible synthetically by reduction with 1 or 2 equivalents of sodium amalgam respectively. Simulation of the cyclic voltammetry recorded for these compounds yielded optimised values of formal potentials, E^0, and electron transfer rate constants, k^0. Crystal structures and DFT calculations indicated that upon reduction, the once equivalent formazanate ligands in the bis(formazanate) system become distinct, due to the coordination of the nitrogen atom(s) to the sodium THF adduct.

Having elucidated mechanistic information for gold(II)/(III) complexes, and investigated redox non-innocence in zinc(II) formazanate complexes, the powerful combination of organometallic synthesis and electrochemistry will now be used to explore surface bound electrocatalysts based on novel group VII 'piano stool' complexes.

References

(1) C. Mu-Cheih, T. B. Dann, D. P. Day, M. Lutz, E. Otten and G. G. Wildgoose, *Angew. Chem. Int. Ed*, 2014, DOI: 10.1002/anie.201309948.

(2) P. J. Chirik and K. Wieghardt, *Science*, 2010, **327**, 794–795.

(3) M. D. Ward and J. A. McCleverty, *J. Chem. Soc., Dalton Trans.*, 2002, 275–288.

(4) H. Tsurugi, T. Saito, H. Tanahashi, J. Arnold and K. Mashima, *J. Am. Chem. Soc.*, 2011, **133**, 18673–18683.

(5) S. C. Bart, K. Chłopek, E. Bill, M. W. Bouwkamp, E. Lobkovsky, F. Neese, K. Wieghardt and P. J. Chirik, *J. Am. Chem. Soc.*, 2006, **128**, 13901–13912.

(6) J. M. Darmon, S. C. E. Stieber, K. T. Sylvester, I. Fernández, E. Lobkovsky, S. P. Semproni, E. Bill, K. Wieghardt, S. DeBeer and P. J. Chirik, *J. Am. Chem. Soc.*, 2012, **134**, 17125–17137.

(7) A. M. Tondreau, S. C. E. Stieber, C. Milsmann, E. Lobkovsky, T. Weyhermüller, S. P. Semproni and P. J. Chirik, *Inorg. Chem.*, 2013, **52**, 635–646.

(8) S. Patra, B. Sarkar, S. M. Mobin, W. Kaim and G. K. Lahiri, *Inorg. Chem.*, 2003, **42**, 6469–6473.

(9) L. Bourget-Merle, M. F. Lappert and J. R. Severn, *Chem. Rev.*, 2002, **102**, 3031–3066.

(10) A. G. Avent, A. V. Khvostov, P. B. Hitchcock and M. F. Lappert, *Chem. Commun.*, 2002, 1410–1411.

(11) O. Eisenstein, P. B. Hitchcock, A. V. Khvostov, M. F. Lappert, L. Maron, L. Perrin and A. V. Protchenko, *J. Am. Chem. Soc.*, 2003, **125**, 10790–10791.

(12) A. G. Avent, P. B. Hitchcock, A. V. Khvostov, M. F. Lappert and A. V. Protchenko, *Dalton Trans.*, 2004, 2272–2280.

(13) F. Basuli, U. J. Kilgore, D. Brown, J. C. Huffman and D. J. Mindiola, *Organometallics*, 2004, **23**, 6166–6175.

(14) H. Hamaki, N. Takeda and N. Tokitoh, *Organometallics*, 2006, **25**, 2457–2464.

(15) G. Bai, P. Wei and D. W. Stephan, *Organometallics*, 2006, **25**, 2649–2655.

(16) N. C. Tomson, J. Arnold and R. G. Bergman, *Organometallics*, 2010, **29**, 5010–5025.

(17) J. B. Gilroy, M. J. Ferguson, R. McDonald, B. O. Patrick and R. G. Hicks, *Chem. Commun.*, 2006, 126–128.

(18) J. Moilanen, J. Borau-Garcia, R. Roesler and H. M. Tuononen, *Chem. Commun.*, 2012, **48**, 8949–8951.

(19) T. Chivers, D. J. Eisler, C. Fedorchuk, G. Schatte, H. M. Tuononen and R. T. Boeré, *Inorg. Chem.*, 2006, **45**, 2119–2131.

4. Cymantrene and cyrhetrene–triazole "Click" Products: Structural Characterization and Electrochemical Properties

Parts of this chapter are published in organometallics.[1]

4.1. Introduction to cymantrene

The complex cyclopentadienyl manganese(I) tricarbonyl, known as cymantrene as reference to ferrocene, is one of the most studied organometallic species after ferrocene itself[2] and remains an intense area of study. It was first prepared by Wilkinson and co-workers in 1955 by the reaction of carbon monoxide with a mixture of sodium cyclopentadienide and manganous bromide.[3] The products were characterised by IR spectroscopy, via the metal-carbonyl spectroscopic handles.[4] More modern approaches to the synthesis of cymantrene include reduction of a mixture of manganese(II) dichloride and cyclopentadiene by metallic manganese or magnesium in the presence of $TiCl_4$ or $Ti(OBu)_4$, following a carbonylation with carbon monoxide. Cymantrene is an 18 electron complex where the manganese atom has a d^6 configuration and an oxidation state of $+1$. It can be considered to have pseudooctahedral geometry with the cyclopentadienyl ligand occupying 3 coordination sites, with 3 sites occupied by the carbonyl ligands. The inital synthetic work on cymantrene constituted the replacement of a hydrogen on the cyclopentadienyl ring for a functional group, via the electrophilic aromatic substitution methodology traditionally utilised for benzene and ferrocene. Other reactivity that has been performed on the cyclopentadienyl ring includes acylation, alkylation

and phosphorlyation reactions via Friedel Crafts methodology, and sulfonation, metallation and chloromethylation. Following on from this, the coordination of main group ligands to the manganese via electron donating elements and synthetic work on indene analogues of cymantrene were performed.[5] More recent examples of work on cymantrene include water splitting by photochemical loss of a carbonyl ligand by Kee *et al* and the photochemical formation of cymantrene alkane complexes by Perutz *et al*.[6,7] Cymantrene has found wide use in biochemistry, with its incorporation into antimalarial compounds such as chloroquine[8] and as a redox tag for proteins.[9]

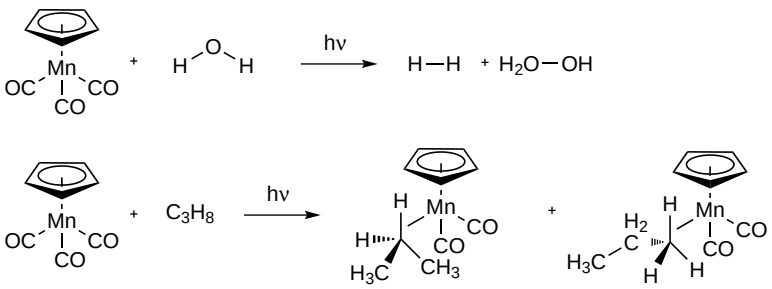

Figure 4.1. Examples of recently published work on cymantrene, top: water splitting, bottom: alkane coordination

4.2. Redox Chemistry

Of particular interest with cymantrene is its very well defined redox chemistry. Geiger was the first to report the anodic one electron oxidation of cymantrene and characterise the radical cation product.[10] The key to studying the nature of the 17 electron product of cymantrene oxidation is in the careful choice of solvent and electrolyte. Geiger determined that the very poor lifetime of the cymantrene radical cation compared with ferrocenium was due to reactivity with the traditional electrolytes used in non-aqueous electrochemistry, namely $[BF_4]$ and $[PF_6]$ anions. Previously it was thought that removing an electron from cymantrene would weaken the Mn-CO and Mn-Cp bonds, causing decomposition. If cymantrene is oxidised in the non-coordinating medium of CH_2Cl_2 solvent and $[^nBu_4N][B(C_6F_5)_4]$ as the electrolyte, the radical cation persists long enough that bulk electrolysis may be utilised to obtain a sample to be analysed by NMR, IR, UV-vis and ESR. Cymantrene has been electrochemically characterised in previous studies,[11–13] where it has been determined that the oxidation is a one electron process. Also, at lower temperatures, the voltammetry appears partially reversible allowing

ligand substitution reactions. Previous attempts made at characterising the radical cation spectroscopically were unsuccessful due to electrode passivation effects and decomposition on the synthetic time scale.

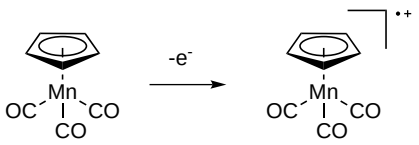

Figure 4.2. The electrochemical oxidation of cymantrene to form the radical cation

4.3. Ligand Exchange - Replacing the Carbonyls

The most immediate way of controlling at what potential the manganese(I) is oxidised is by exchanging the carbonyl ligands with other donor ligands. Upon irradiation of a sufficient duration the carbonyl ligands are labile, becoming released as carbon monoxide, leaving a vacant site. In the presence of triphenylphosphine, the irradiation of cymantrene in cyclohexane yields the product $[CpMn(CO)_2PPh_3]$. Cyclic voltammetry of this compound shows an oxidation potential that has a relative value 300 mV more negative than that of the parent cymantrene. This is to be expected from electronic effects. The ligand exchange can also be promoted electrochemically, with the carbonyl ligands on oxidised cymantrene more labile. In the presence of the phosphite $P(OPh_3)$, oxidation of cymantrene results in the formation of $[CpMn(CO)_2\{P(OPh)_3\}]$.

4.4. Cyrhetrene

The third row piano stool complex cyclopentadienyl rhenium(I) tricarbonyl draws much attention, within applications such as labelling of oestrogen receptors,[14] protein[15] and peptide[16] labelling, IR probes[17] and photochemistry[18–21] for example. The chemistry for the addition of substituents to the cyclopentadienyl ring of cyrhetrene is well developed, with the classical method of deprotonation following by addition of an electrophile used successfully in numerous examples. It is due to the high stability of cyrhetrene that it has found much use in the field of biomedical imaging, but the classical methods of attaching side groups are incompatible with the peptides, proteins and steroids requiring attachment.[22] This has lead to much development

in the field of rhenium and technetium organometallic synthesis. For the purposes of this research however, the classical methods are suitable.

4.5. Redox Chemistry

Due to the importance of dileptic organometallic compounds containing carbonyl ligands alongside cyclopentadienyl or arene ligands, the redox properties of cyrhetrene have been investigated in the literature. The oxidation of cyrhetrene is also of interest due to the isoelectronic nature of the cyrhetrene cation to tungsten and molybdenum analogues, which have well developed chemistry. It was found that in similar non-coordinating environments as those used for the successful analysis of the cymantrene oxidation products (see section 4.2), cyrhetrene shows a partially reversible oxidation at 1.16 V vs ferrocene. Interestingly, the radical products of this oxidation are present as both the more thermodynamically stable dimers and monomers in appreciable amounts (figure 4.3). The dimeric species is interesting as it is the first isolated dimeric piano stool complex with a weak metal-metal bond that has a charge. The dicationic dimer is also useful as it releases the rather powerful oxidising agent $[ReCp(CO)_3]_2^+$.[23] In addition to this, it has been discovered that the cyrhetrene oxidation product acts as an

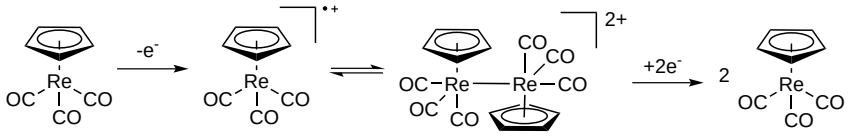

Figure 4.3. The electrochemical oxidation and dimerisation of cyrhetrene

electron transfer mediator between the electrode and small molecules containing unactivated C-H bonds. In the presence of a cyclic alkene such as cyclopentene, the cyrhetrene once oxidised at the electrode will undergo an electron transfer from the carbon-carbon double bond in the alkene, causing the alkene to become a radical. There is a subsequent sequence of reactivity (see figure 4.4), which results in the corresponding cycloaddition products. The product of cycloaddition depends on the cyclic olefin present in solution. Geiger and co-workers tested this reactivity with the C_5 through C_7 cyclic olefins.

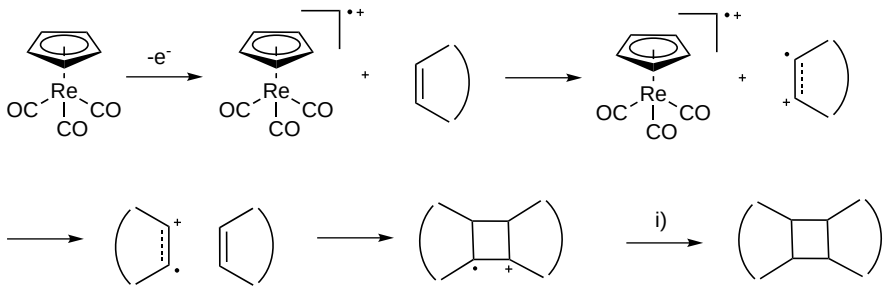

Figure 4.4. Proposed mechanism of cycloaddition from oxidation products of cyclic alkenes, i) an electron donor, either cyrhetrene or neutral olefin

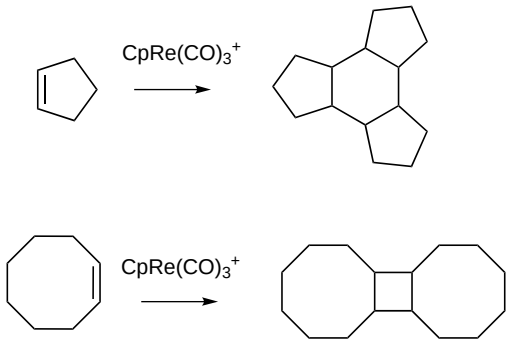

Figure 4.5. Cylcoaddition products from cyclopentene and cis-cyclooctene

4.6. Surface bound organometallic chemistry

As the primary goal of this work is to achieve a surface bound organometallic catalyst, a search of the recent literature was performed to determine the current most effective methodologies for attaching organometallics to graphitic surfaces. The methods of covalent surface attachment are summarised in section 1.4. Of note immediately was the work by Geiger and co workers on the attachment of cobaltocene and cymantrene directly to the electrode surface via use of the reduction of diazonium salts. As discussed in section 1.4, the concerted mechanism for the generation of a radical proximal to the electrode and its attack of the surface was first developed by Pinson and Saveant in 1992.[24] With the preparation of amino substituted cymantrene[10] and the formation of organometallic diazonium salts[25] published in the literature, it was possible to achieve the formation of the surface bound organometallic species with this methodology. With this system, Geiger has also reported the process of exchanging ligands on the surface bound cymantrene. When the surface bound cymantrene is oxidised, the carbonyl ligands become more labile, allowing coordination of phosphites such as $P(OPh)_3$ Also of note is the 'lithium alkyne oxidation' methodology, also developed by Geiger *et al*, where the oxidation of

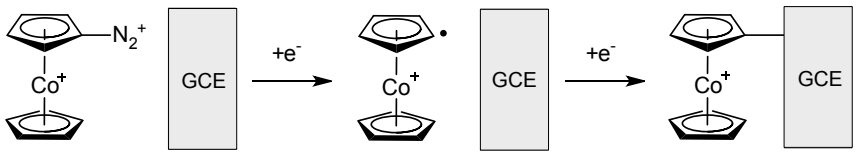

Figure 4.6. Attachment of cobaltocenium to GCE via diazonium reduction

lithium alkynyl salts on the cyclopentadienyl ring of ferrocene, cobaltocene and cymantrene forms a radical, which can attack the surface of carbon and precious metal electrodes (see section 1.4.6)

4.7. Introduction to triazole chemistry

The name triazole refers to one of two isomers of a chemical compound with the formula $C_2H_3N_3$, consisting of a five membered ring with two carbon atoms and three nitrogen atoms. Triazoles were originally prepared via the azide-alkyne Huisgen cycloadditon, a reaction discovered by Otto Dimroth in the early 20th century but fully realised by German chemist Rolf Huisgen in the 1960s.[26] In this reaction, an azide reacts with an alkyne to afford a mixture of a 1,4 and 1,5 cycloaddition products. The first successful attempt to introduce regioselectivity

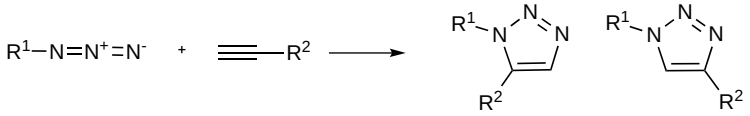

Scheme 4.1 The Huisgen 1,3 dipolar cycloaddition, showing a lack of regioselectivity

employed a copper catalyst in a variant of the Huisgen cycloaddition, published by Sharpless in 2002.[27] A copper(I) catalyst successfully binds terminal azides and alkynes to process only the 1,4-disubstituted 1,2,3-triazole products. This reaction satisfies the criteria for a 'click' reaction, with a robust tolerance of reaction conditions (such as pH) and a huge scope arising from the functional group tolerance of the catalytic process. Copper (I) salts such as copper iodide and copper triflate can be used in acetonitrile solvent with a nitrogen base to generate the 1,4 cycloaddition product in exclusivity without the need for a reducing agent, however under these conditions more side products such as bis triazoles and 5-hydroxytriazoles are produced.

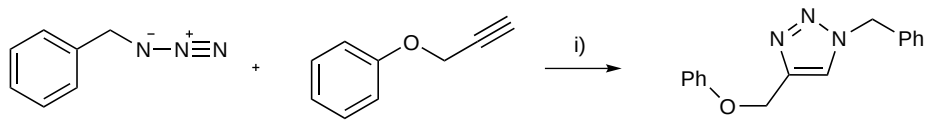

Scheme 4.2 An example of the Cu(I) catalysed regiogselective triazole formation

The postulated catalytic cycle for this organic reaction is shown in figure 4.7 The Cu(I) catalysed Huisgen cycloaddition has many applications. It has been widely applied in medicinal chemistry, due to the relative inertness of the azide and alkyne functional groups to those typically found in biological molecules. The azide and alkynes are referred to as 'bioorthogonal' groups.[28] For example, the Huisgen 1,3 cycloaddition has been used for the rapid synthesis of fifty triazole analogs of vancomycin for use against bacterial strains resistant to this antibiotic.[29] Steroid mimics have also been synthesised using this reactivity. Starting from diepoxides a tricyclic molecule resembling the ring skeleton of a steroid can be prepared in a one pot synthesis with three high yielding steps.[30] The 'click' reaction can be used in conjunction with coordination to transition metal complexes. Recently, 2-pyridyl-1,2,3-triazole ligands have been used to form a variety of new transition metal complexes. For example, Crowley *et al.* prepared a series of $[RuCl(CO)_{(}3)]$ complexes of 1,2,3-triazole-pyridine, and characterised their spectroscopic and electronic properties. It was determined that the 1,2,3-triazole moiety acts as an insulator in this case, allowing a wide range of functionalisation of the pyridyl ring without altering the photophysical properties of the complex (figure 4.8, a).[31] The functionalised

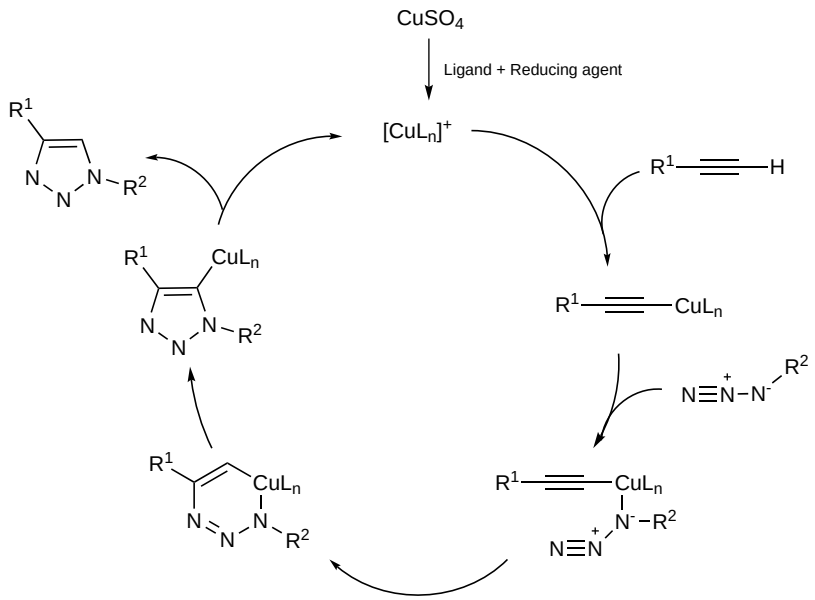

Figure 4.7. Postulated copper catalysed mechanism of the regioselective 1,3 cycloaddition

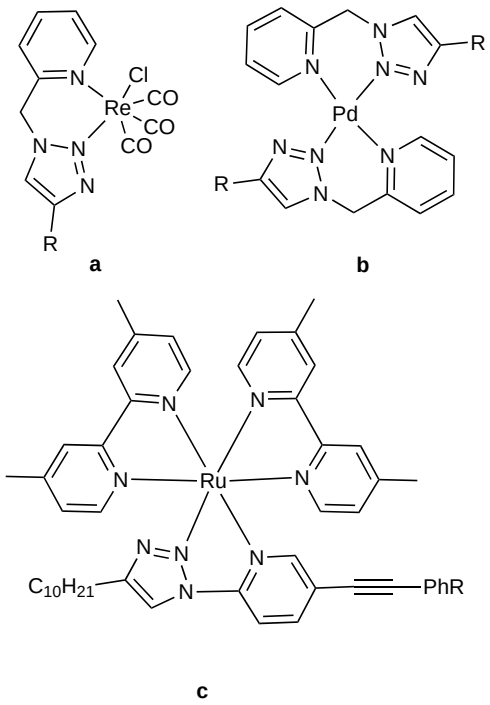

Figure 4.8. Examples of coordination complexes of 2-pyridyl-1,2,3-triazole ligands

2-pyridyl-1,2,3-triazole ligands have also been shown to readily form palladium(II) complexes, where the molecular structures indicate that the formation and stability of these complexes is unaffected by the steric effects of substituents on the periphery of the ligand scaffold. (figure 4.8, b).[32] This type of ligand has also been used as an alternative to the widely used bipyridine (bpy) ligand. Gonazalez *et al*. recently prepared a ruthenium complex containing the 2-pyridyl-1,2,3-triazoe ligand with various phenylacetylene moieties in the 5 position of the pyridine. It was shown that the nature of these groups has a large effect on the electronic properties of these ligands, and that contrary to other studies, the pyridyl-triazole ligands in this case gave luminescence at room temperature.[33] (figure 4.8, c)

Schweinfurth *et al*. has reported the use of new tripodal triazole ligands in coordinating to various transition metals such as Ni(II),[34] Co(II) and Fe(II).[35] These complexes have shown to act as catalysts for polymerisation and oligomerisation reactions, and are an important class of compounds for studying the fundamental geometric and electronic properties of d^3 coordination compounds.[36]

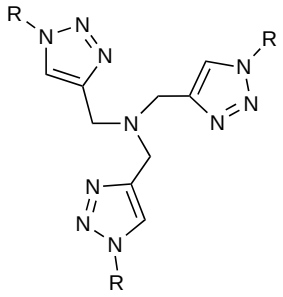

Figure 4.9. The tripodal triazole ligand used by Schweinfurth

4.8. Organometallic triazole chemistry

Triazole moieties have been used in organometallic chemistry, a recent example being reported by Molina *et al.* on ferrocenyl triazoles.[37] In this work, a series of monosubstitued and disubstituted ferrocene triazole derivatives were prepared via the copper catalysed click methodology discussed above. These compounds were assessed for the sensing of anions such as F^-, AcO^- and $H_2PO_4^-$. The method of detection is a large cathodic shift of the ferrocenyl redox couple in the presence of the anions. The 1,2,3-triazole moiety contains two binding sites, the sp^2 hybridised nitrogen atom and the C-H group, which is highly polarised from the electronegativity of the nitrogen atoms. The nitrogen atom coordinates to metal cations (Li^+, Na^+, K^+, Mg^{2+}, Ca^{2+}, Ni^{2+}, Cu^{2+}, Zn^{2+},Cd^{2+}, Hg^{2+}, and Pd^{2+}), where as the C-H group can associate with anions (F^-, Cl^-, Br^-,AcO^-, NO_3^-, HSO_4^-, $H_2PO_4^-$ and $HP_2O_7^{3-}$).

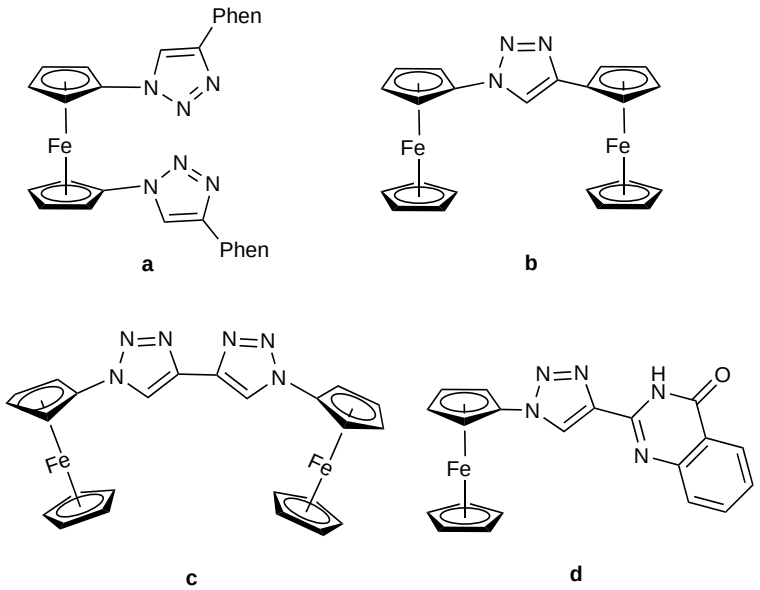

Figure 4.10. Examples of ferrocenyl triazoles prepared by Molina *et al.*

Astruc and co-workers have successfully developed ferrocenyl triazole dendrimers that sense both oxo anion and metal cations.[38] The solution phase cyclic voltammetry of the ferrocenyl dendrimers recorded in CH_2Cl_2 shows a fully reversible oxidation, but upon addition of a salt of an oxo anion ($H_2PO_4^-$ or ATP_2^+) or transition metal cation (Cu^+, Cu_2^+, Pd_2^+ or Pt_2^+) a new wave appears. The addition of oxo anions causes a new wave at a less positive potential than the dendrimer, whereas the transition metal cations cause the new wave to be observed at a more positive potential. This is an example of a system which has 'strong redox recognition' according to the Echegoyen–Kaifer model, where a less strong recognition would only cause a shift in redox potential.[39] Organometallic triazoles have been successfully employed as catalysts. For example the ruthenium complexes of the general structure [(η^6-arene)RuCl(N,N)] (where N,N is a κ^2 bis(triazolyl)borate) prepared by Kumar *et al.*[40] Complexes of this type were discovered to be effective catalysts for transfer hydrogenation of aryl ketones with a base co-catalyst.

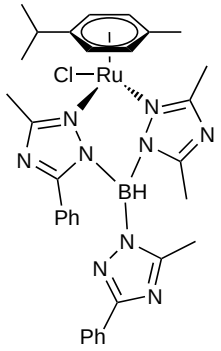

Figure 4.11. Ruthenium triazolyl hydrogenation catalyst

4.9. Synthesis and characterisation of cymantrene triazole derivatives

To determine the most efficient method for modifying carbon surfaces with organometallics, several modification procedures were contrasted. As discussed in section 1.4 Geiger has successfully attached sandwich compounds to glassy carbon electrode surfaces by use of diazonium salts, where the complex is bound directly via its cyclopentadienyl ring.[41] As the utility of this method has been seen multiple times, it was used initially to attach the novel cymantrene triazoles prepared (*vide infra*) to the electrode to investigate their surface

electrochemistry. There are two synthetic routes to triazole derivatised cymantrene complexes. The cyclopentadienyl ring could be derivatised with a pendant alkyne, and reacted with an aryl-azide. Alternatively the azide derivative of cymantrene couple be prepared used with phenylacetylene derivatives. Geiger has introduced cymantrene derivatised with a pendant alkyne for surface attachment,[42] whilst cymantrene azide preparations have been reported by Holovics[43] and Sunkel[44] with good yields. The goal here is to modify graphitic surfaces with cymantrene triazoles, via performing '*in situ*' click reactions where the surface has been previously modified by reduction of an aryl diazonium salt (see section 4.14.3). With this in mind, the latter method seems preferable, since aryl-alkyne diazonium salts are more stable and more easily handled than aryl-azide diazoniums.

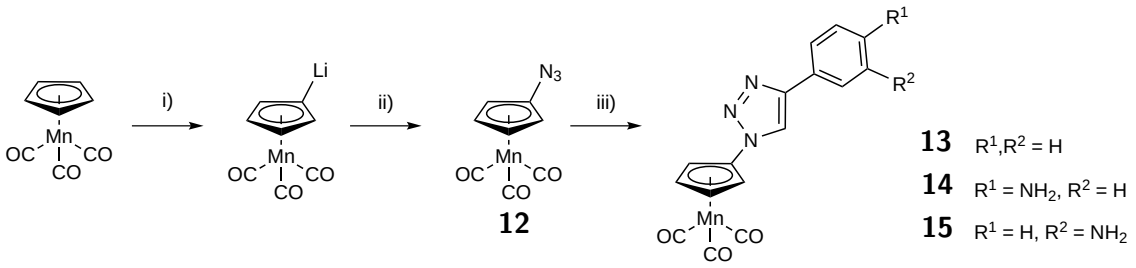

Scheme 4.3 Reagents and conditions: i) *n*-BuLi, THF, -78 °C; ii) TsN_3 THF, -78 °C; iii) phenylacetylene / ethynylaniline, $Cu(OAc) \cdot H_2O$, CH_3CN.

Initially, the cymantrene azide **12** was prepared using the method from Holovics, achieving a yield of 75%. **12** was then used without further purification in the preparation of **13**, the simplest 'cymantrene phenyl click'. This was synthesised using the azide/alkyne cycloaddition conditions of Hu *et al.*[45] Forming **13** from **12** required 2 hours under these mild conditions. Purification was achieved by silica gel chromatography in a petroleum ether acetone eluent system to give excellent purity and a good yield. This complex according to a survey of the literature is novel, so full structural characterisation is required to ensure **13** had been isolated. ^{1}H NMR shows good evidence of a successful preparation via the diagnostic proton shifts in the cyclopentadienyl and phenyl rings. A characteristic splitting of the proton environments in the cyclopentadiene is observed, with singlet from the starting material split into two equivalent triplets at δ4.8 and 5.5 ppm by the introduction of the triazole moiety. The proton environments of the phenyl ring of **13** have been investigated by 2D COSY NMR spectroscopy, showing coupling between signals of the correct integration in the aromatic region. A shift associated with the triazole is observed at 7.99 ppm, which does not undergo coupling.

A phenylalkyne substrate bearing an unprotected amine functional group has been used successfully in many literatures reports with the 1,4-CuAAC reaction.[46,47] As our aim is to prepare a cymantrene modified electrode with a 'linker' acting as a spacer, adding an amine functionality to the amine, via the use of 4-ethynylaniline allows access to the phenyl diazonium moiety required for surface modification. Therefore the preparation of the 1,4-disubstituted triazole **14** was attempted under similar conditions to those used to synthesise **13** Purfication by silica gel column chromatography afforded the product **14** as a fine yellow poweder in 88% yield. Unfortunately, under all conditions attempted, no single crystals of X-ray quality could be grown, therefore crystallographic analysis of **14** could not be performed. Characterisation by ^{1}H NMR, ^{13}C NMR and IR spectroscopy were used to confirm successful preparation of **14**

The 1,4-disubstituted triazole **15** containing an amine moiety at the *meta*-position of the phenyl ring was synthesized in a much lower yield than that observed for **14** Purification via silica gel column chromatography, afforded **15** as a dark yellow oil. X-ray quality single crystals were formed of **15** by slow evaporation of CH_2Cl_2 and petroleum ether, appearing as colourless shards, allowing crystallographic analysis. (see section 4.9.0.1) The UV-vis spectra of the parent molecule, [$CpMn(CO)_3$], can be directly compared with click-product **13**, and it is observed that in both cases, MLCT bands occur around the region of 330-340 nm. These absorptions can be attributed to an MLCT band, based on systems that are closely related to the triazole derivatised cymantrenes.[48,49]

One of the advantages of using 'piano stool' complexes is the sharp infra-red absorption of the carbonyl ligands, providing a useful spectroscopic handle. The infra-red spectral data collected for compounds **12**, **13**, **14** and **15** with band assignments, are tabulated below (table 4.1)

Table 4.1. νcm^{-1} bands for cymantrene and **12**, **13**, **14** and **15**

Complex	ν(C≡O)		ν(C=C) triazole
	Sym	Asym	
$CpMn(CO)_3$	2014	1905	n/a
12	2016	1910	n/a
13	2024	1959, 1936, 1918	1533
14	2022	1940,1910	1622, 1566, 1540
15	2022	1928	1614, 1592, 1530

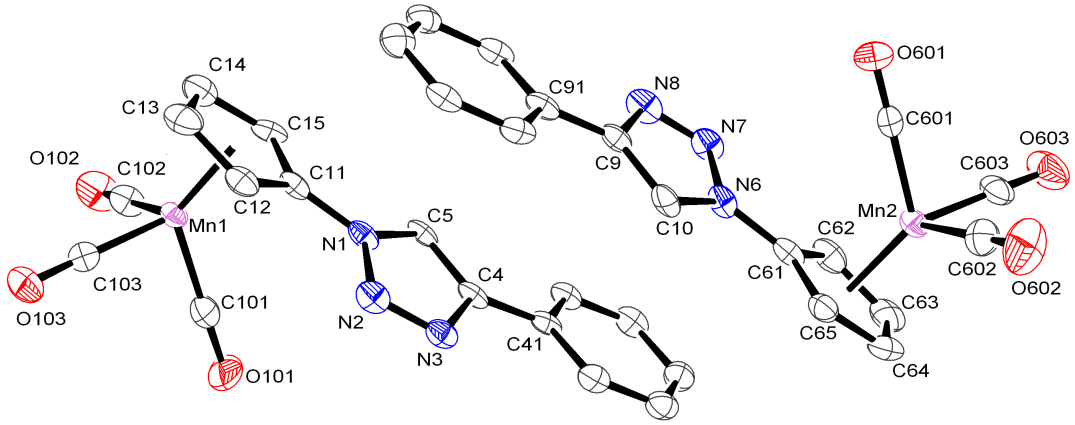

Figure 4.12. The two independent molecules in single crystals of compound **13**. Thermal ellipsoids are shown at the 50% probability level. Mean Mn-C(carbonyl) and Mn-C(cyclopentadienyl) bond lengths are 1.796(6) and 2.147(13) Å.

4.9.0.1. Crystallographic analysis

X-ray crystallography quality crystals of **13** were grown via slow crystallisation from petroleum ether and dichloromethane, to give colourless plates. The structure confirms the presence of a 1,4-disubstituted triazole, and an intact cymantrene moiety, with the manganese atoms observed to be coordinated by three carbonyl ligands. The asymmetric unit contains two molecules of **13**, lying adjacent at 3.4 Å apart, related by a pseudo inversion centre.

The three rings of each triazole-cyclopentadienyl structure are approximately coplanar, with the normal to the triazole ring rotated 14.0(3)° from the normal to the cyclopentadienyl ring, and 12.2(2)° from that to the phenyl ring in the first ligand, and correspondingly, 12.9(3)° and 10.6(3)° in the second molecule.

The triazole ligands of the molecules of Mn(1) and Mn(2) overlap with N(6) above the centre of the neighbouring phenyl ring, and N(1) below the opposite phenyl ring. The overlaps of the next ligands are more offset, with the normals of adjacent triazole rings 17.0(2)° apart. The alignment of these ligands can be seen in the packing diagram, figure 4.12. The mean Mn-C(carbonyl) bond lengths in **13** are observed to be 1.7696 Å; by comparison, the known Mn-C(carbonyl) bond lengths for the literature value of the parent cymantrene is similar, at 1.797(4) Å, reported in a study by Borrisova *et al.*[50] The mean Mn-C(cyclopentadienyl) bonds lengths of **13** are also very similar to the literature value, with the value for **13** at 2.147(4) Å and the parent cymantrene 2.145(5) Å.

Analysis of the crystal structure of **15** shows the manganese atom lies 1.774(2) Å from the

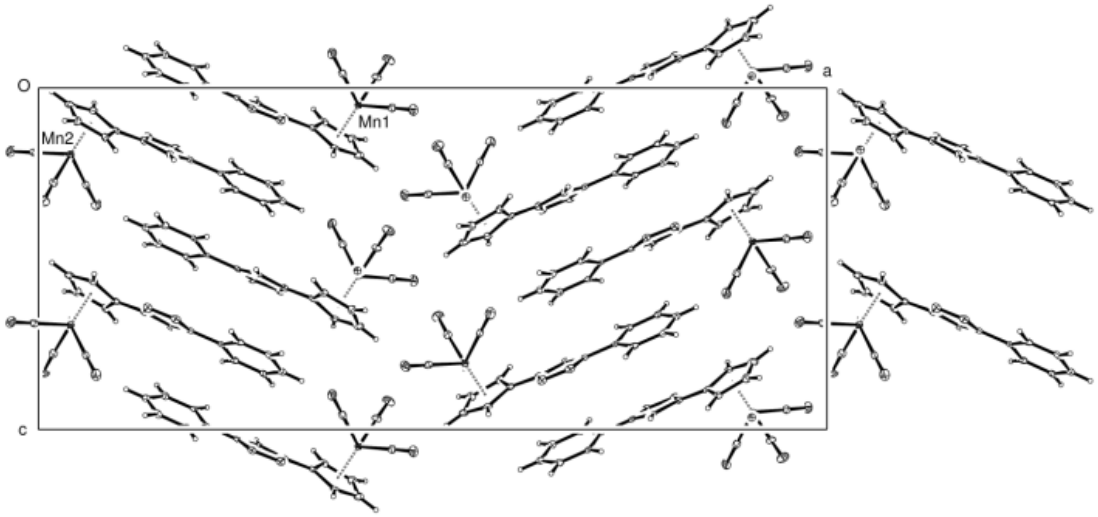

Figure 4.13. The crystal packing of **13**, viewed down the short b axis.

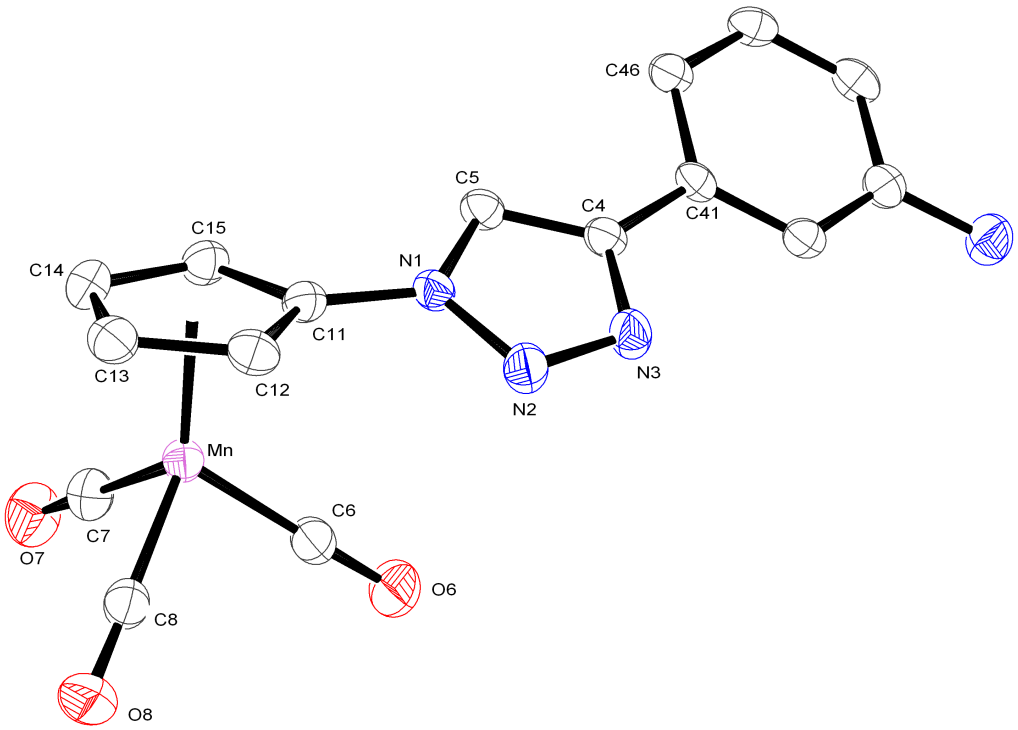

Figure 4.14. Molecular structure of **15**, Thermal ellipsoids are drawn at the 50% probability level.

	13A		**13B**		**15**	
Mn-Cp	Mn1-C11	2.159(5)	Mn2-C61	2.164(5)	Mn-C11	2.158(3)
	Mn1-C12	2.152(5)	Mn2-C62	2.156(6)	Mn-C12	2.155(3)
	Mn1-C13	2.148(5)	Mn2-C63	2.136(5)	Mn-C13	2.133(3)
	Mn1-C14	2.125(6)	Mn2-C64	2.131(5)	Mn-C14	2.125(3)
	Mn1-C15	2.156(5)	Mn2-C65	2.143(5)	Mn-C15	2.152(3)
$Mn\text{-}C_{carbonyl}$	Mn1-C101	1.786(6)	Mn2-C601	1.797(5)	Mn-C6	1.801(3)
	Mn1-C102	1.801(6)	Mn2-C602	1.792(6)	Mn-C7	1.802(3)
	Mn1-C103	1.802(5)	Mn2-C603	1.798(6)	Mn-C8	1.784(3)
$C{=}O_{carbonyl}$	C101-O101	1.144(7)	C601-O601	1.142(7)	C6-O6	1.150(4)
	C102-O102	1.138(7)	C602-O602	1.128(7)	C7-O7	1.149(4)
	C103-O103	1.154(7)	C603-O603	1.130(7)	C8-O8	1.152(4)

Table 4.2. Selected bond lengths (Å) for compounds **13** and **15**

mean-plane of the cyclopentadienyl ring atoms (figure 4.14), and the three carbonyl ligands are arranged in an almost tripodal pattern on the opposite side of the metal; the mean OC–Mn–CO angle is 91.7°. The three rings form a progression in orientation by rotation; about the C(11)–N(1) bond, the normals to the Cp and triazole rings are 26.0(2)° apart and the corresponding rotation about the C(4)–C(41) bond is 16.2(2)° in the same direction (figure 4.14). There are no close contacts of the amino group, and nothing close enough to indicate any hydrogen bonding interactions. There are π···π interactions between offset overlapping of phenyl rings *ca.* 3.45 Å apart, around centres of symmetry (figure 4.15). The parallel alignments of pairs of triazole rings are further apart, at *ca.* 3.63 Å. The closest intermolecular contact is of a triazole C(12)–H(12) group pointing to the edge of a phenyl ring with H(12)···C(46') 2.78 Å.

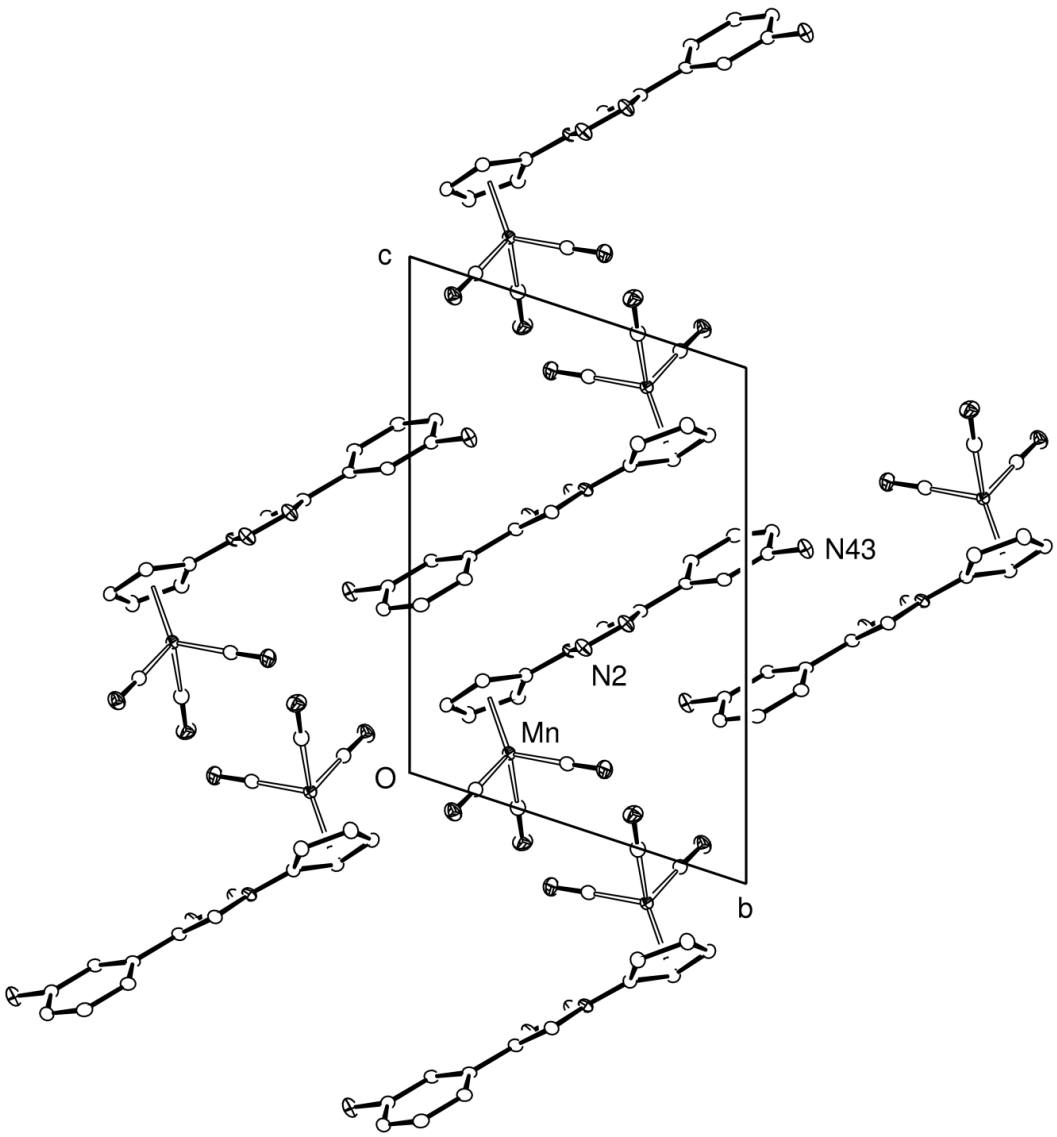

Figure 4.15. Crystal packing of molecules of **15**, viewing along the αaxis

The bond lengths of the triazole ligands in compounds **13** and **15** are comparable to those reported for known crystal data for the free triazole ligand, reported by Elguero *et al.*[51] The average bonds lengths for the cymantrene triazole complexes **13** and **15** can be seen in table 4.3. Interestingly, there are two differences between the cymantrene triazoles and the free ligand. The bond length N3-C4 in the free triazole is 0.04-0.05 Å shorter than the two manganese triazoles. A similar difference is observed for the N1-N2 bond length, where the free triazole is ca. 0.04 Å shorter than in complexes **13** and **15**.

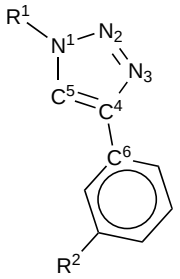

13 $R^1 = CpMn(CO)_3$, $R^2 = H$
15 $R^1 = CpMn(CO)_3$, $R^2 = NH_2$
16 $R^1 = H$, $R^2 = H$

Figure 4.16. Atom labels for the triazole moiety

Table 4.3. Mean bond lengths in Å for compounds **13**, **15** and free triazole **16**. Esd are given in parentheses.

Bond	Compound		
	13	**15**	**16**
N1-N2	1.356(3)	1,353(4)	1.315(3)
N2-N3	1.325(7)	1.311(4)	1.321(3)
N3-C4	1.383(6)	1.371(4)	1.332(3)
C4-C5	1.384(7)	1.375(4)	1.386(3)
C5-N1	1.341(6)	1.358(4)	1.325(3)
C4-C6	1.476(7)	1.417(4)	1.472(3)

4.10. Cyclic voltammetric characterisation

The cymantrene triazole derivatives **13**, **14** and **15** were analysed by cyclic voltammetry in CH_2Cl_2 solvent and $[^nBu_4N][B(C_6F_5)_4]$ as the supporting electrolyte. This WCA electrolyte was used because group VII piano stool compounds are known to passivate GC and platinum electrodes when oxidised in the presence of traditional electrolytes with $[PF_6]$ and $[BF_4]$ anions. In the cyclic voltammogram of **13** two partially reversible oxidations at $+1.4$ and $+1.7$ V vs $Cp_2Fe^{0/+}$ are observed. By comparison to the organic triazole 1,4-diphenyltriazole, the first wave is assigned as the cymantrene/cymantrene$^+$ redox couple and the second wave assigned

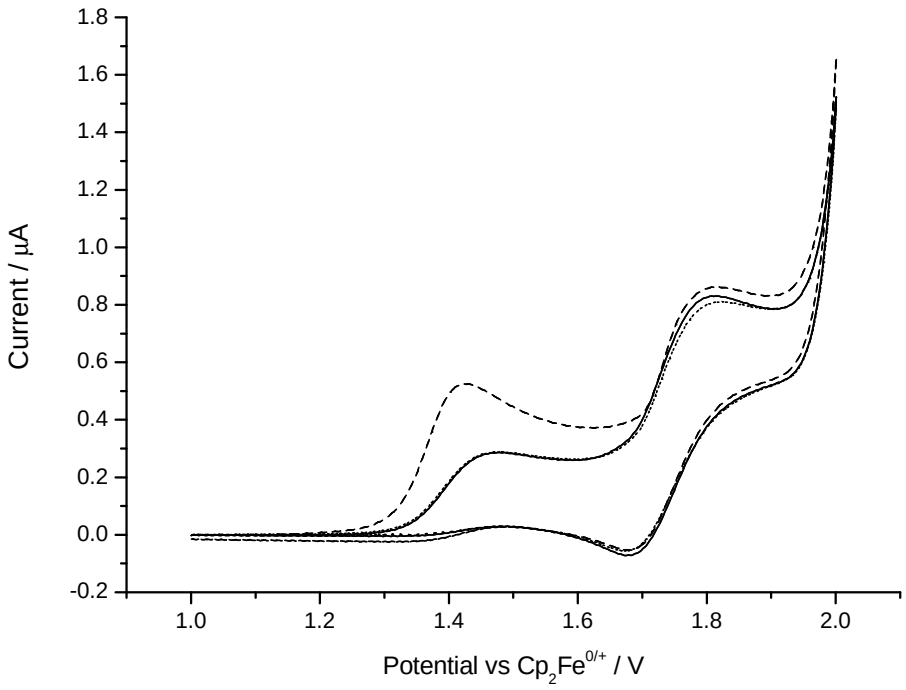

Figure 4.17. Cyclic voltammogram recorded for 2 mM **13** in CH_2Cl_2 at a scan rate of 100 mV s^{-1} (ii) Oxidation between +1 and +2 V vs $Cp_2Fe^{0/+}$, (Where bold line = 1st scan, dotted line = 5th scan, dashed line = 10th scan).

to the triazole/triazolium couple. Extending the window into the cathodic region reveals a reduction with surface adsorbed character at 0.315 v vs $Cp_2Fe^{0/+}$ and an eletrochemically and chemically quasi-reversible wave at *ca.* -1.375 V vs $Cp_2Fe^{0/+}$. These cathodic waves are only observed if scan range includes the cymantrene redox couple. Upon repeat scans of the oxidation waves only, the peak current of the cymantrene wave decreases steadily until the 10^{th} scan. Inclusion of the cathodic waves in the scan range restores the peak current of the cymantrene oxidation wave, which is then stable to the 20^{th} scan.

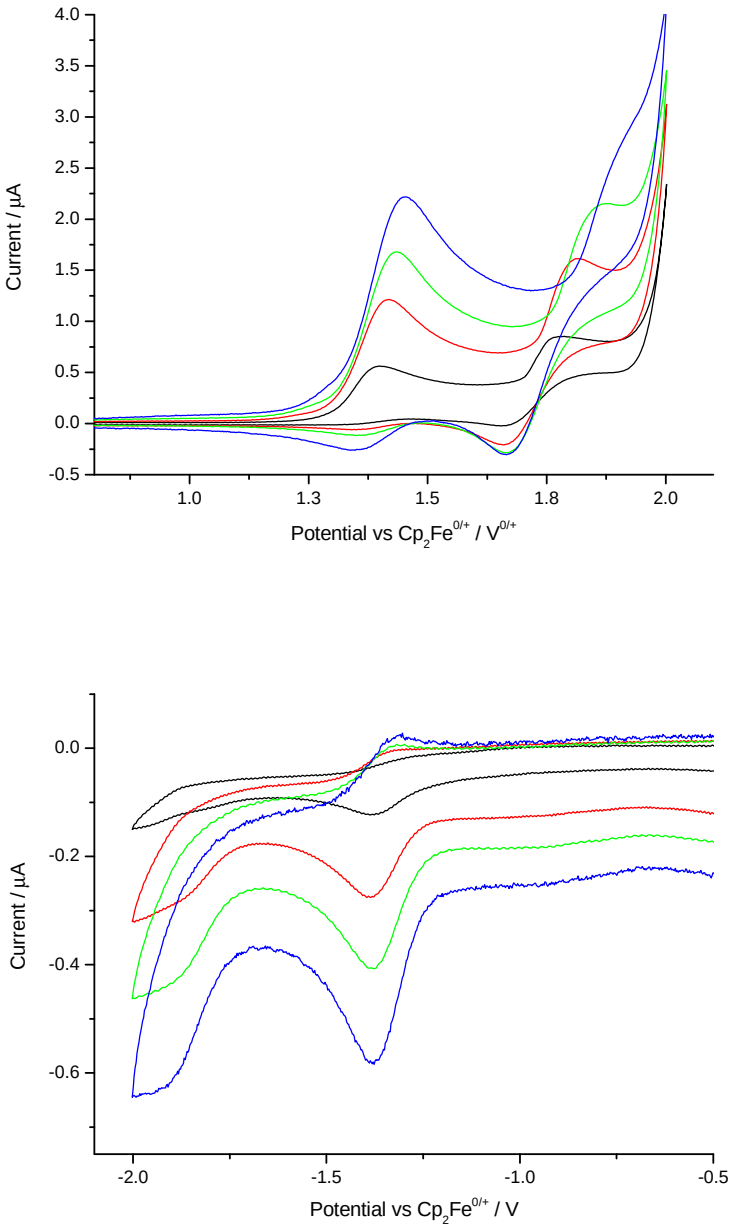

Figure 4.18. The oxidative (top) and reductive (bottom) cyclic voltammetry of 2mM **13** in CH_2Cl_2 with 0.5 M $[^nBu_4N][B(C_6F_5)_4]$ as supporting electrolyte (where blue = 2000 $mV\,s^{-1}$; green = 1000 $mV\,s^{-1}$; red = 500 $mV\,s^{-1}$; black = 100 $mV\,s^{-1}$)

In order to examine the intermediates formed during the complex redox chemistry of the triazole-modified cymantrene derivatives, in situ infra–red spectroelectrochemistry was performed. The electrode, housed in a glass cell was held adjacent to the ATR-IR window of the spectrometer to allow IR characterization of species formed immediately adjacent to the electrode surface. Initailly, the experimental set up was tested by characterising the spectroelectrochemistry of the metal-carbonyl absorbances of cymantrene. As expected, the asymmmetric and symmetric stretching modes of the manganese carbonyl bonds were observed to shift upwards by ca 100 cm^{-1}, replicating the work previously performed on cymantrene by Geiger *et al*. A 2 mM solution of **13** was oxidised by bulk electrolysis, with the potential held at +1.55 V vs $Cp_2Fe^{0/+}$ and IR spectra recorded periodically. After 30 minutes, the electrolysis was observed to be complete, with a dark red solution formed from the yellow starting material. It was observed in the IR spectra (see figure 4.19) that the absorbance of the symmetrical stretch at 2030 cm^{-1} decreases in intensity during the electrolysis, with a shift by 10 cm^{-1} gradually forming a new spectral peak at 2040 cm^{-1} The asymmetric carbonyl stretch absorbance was also observed to increase by 10-20 cm^{-1}, which became two broad partially resolved peaks at 1956 and 1965 cm^{-1}. The C=C stretch at 1533 cm^{-1}, assigned to the triazole moiety, was observed to increase in intensity during the electrolysis. Increasing the potential to +2.0 V vs $Cp_2Fe^{0/+}$, beyond the second oxidation wave causes the symmetrical carbonyl stretch absorbance to shift higher by 10-15 cm^{-1}. After 40 minutes at this potential, decomposition of the system is observed, with the solution becoming brown in colour and the electrode becoming fouled.

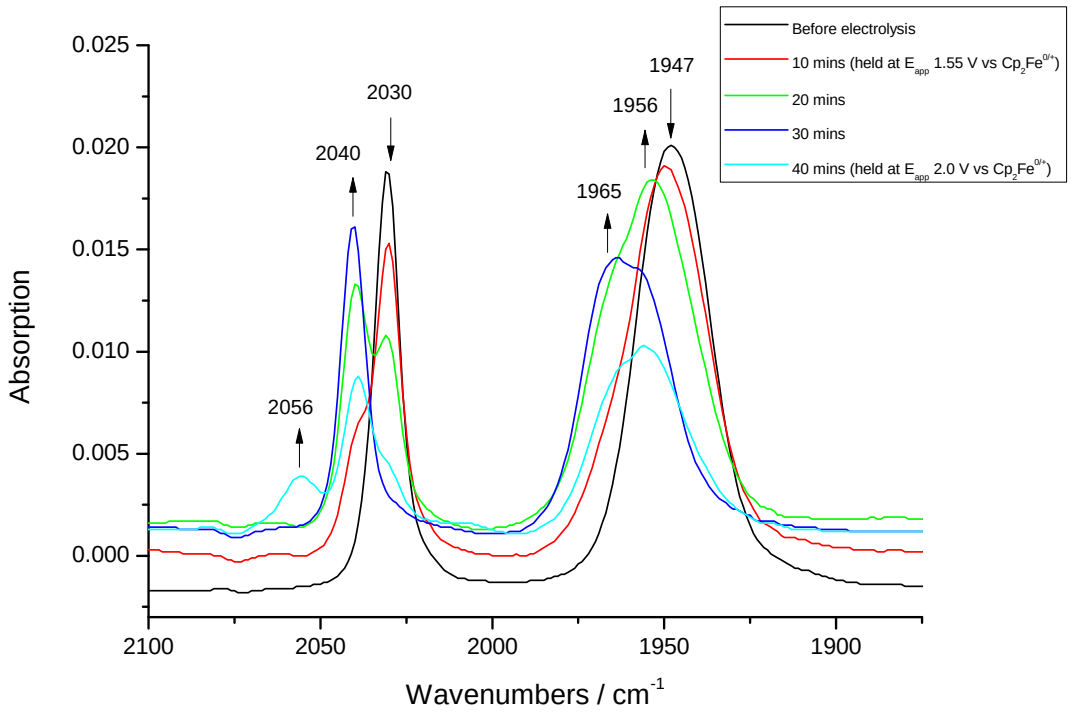

Figure 4.19. In situ IR spectroelectrochemistry of a bulk solution of 2 mM **13** in CH_2Cl_2 and 0.1 M $[^nBu_4N][B(C_6F_5)_4]$ at 293 K recorded during bulk electrolysis at $E_{app} = 1.55$ V.

The size of the shift in the metal carbonyl IR absorption bands is smaller than those reported for the parent cymantrene oxidation product. In order to investigate the possibility that a dimerisation is occurring, DFT calculations were performed. The neutral **13** and its oxidised radical cation form were modelled in gas phase and in dichloromethane using a solvent continuum model, in order to establish the form of the HOMO, LUMO and SOMO, the spin density in the radical cation and to predict the IR absorbances of the neutral and oxidised forms. Comparison of the predicted IR spectra of **13** and $\mathbf{13}^+$ (see figure 4.20) shows that the symmetric and asymmetric metal-carbonyl stretches are predicted to shift to higher wave numbers by ca. 100 cm^{-1}, similar to what is observed for cymantrene itself, whose cation is by comparison long lived and stable in solution.[10] This is not what is observed experimentally however, and the explanation for this difference is seen in the form of the SOMO and relative spin density of the radical cation of **13** Geiger reported that the cymantrene radical cation, the distribution of the spin density between the manganese metal centre and the cyclopentadienyl ligand is 50% on each respectively. In the case of the radical cation of **13**, 67% of the spin

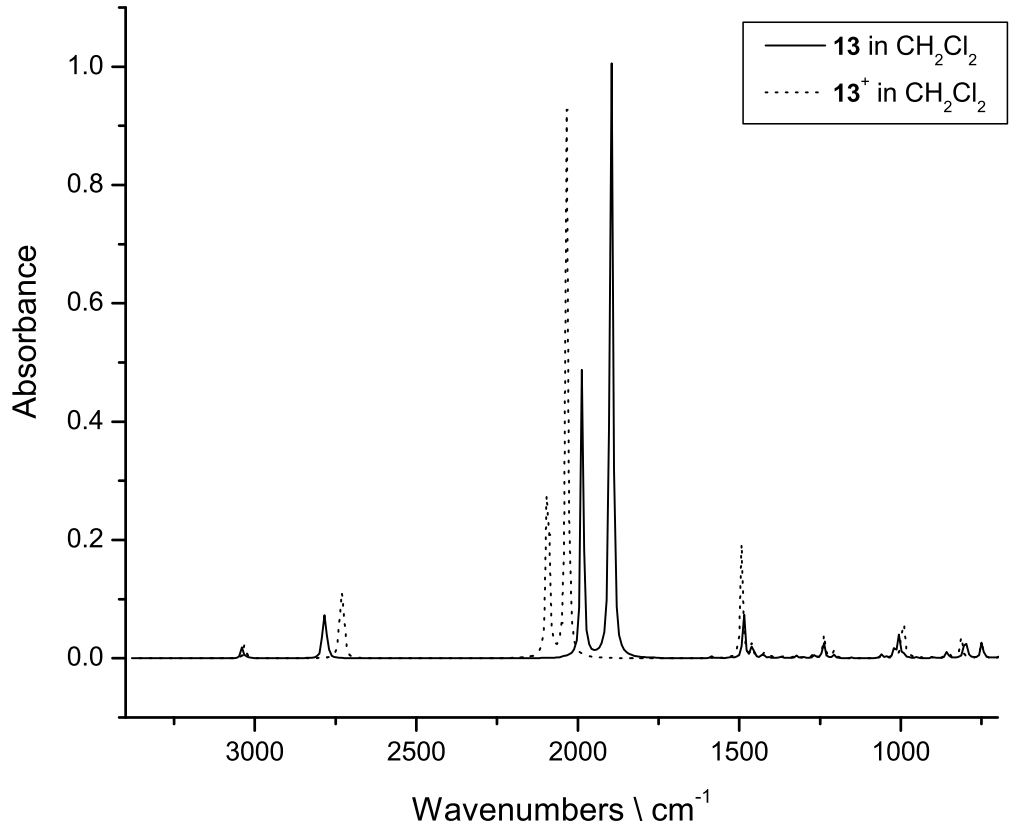

Figure 4.20. Predicted IR spectrum of **13** (solid line) and its oxidised form (dotted line)

density resides on the metal in gas phase. When modelled in CH_2Cl_2 however, 97% of the spin density is seen to be residing on the metal centre. Additionally, a large accessible orbital lobe is apparent between the metal-carbonyl groups opposite the pendant triazole moeity (figure 4.21) It is therefore feasible that, unlikne the parent cymantrene, the electrogenerated radical cation of **13** undergoes rapid dimerisation in solution via the formation of a manganese-manganese bond, leading to the metal-carbonyl stretches to that which are observed experimentally. Note that no evidence for bridging–carbonyl groups is observable. Also note that DFT calculations predict an increase in intensity of the triazole C=C stretch, consistent with that observed experimentally.

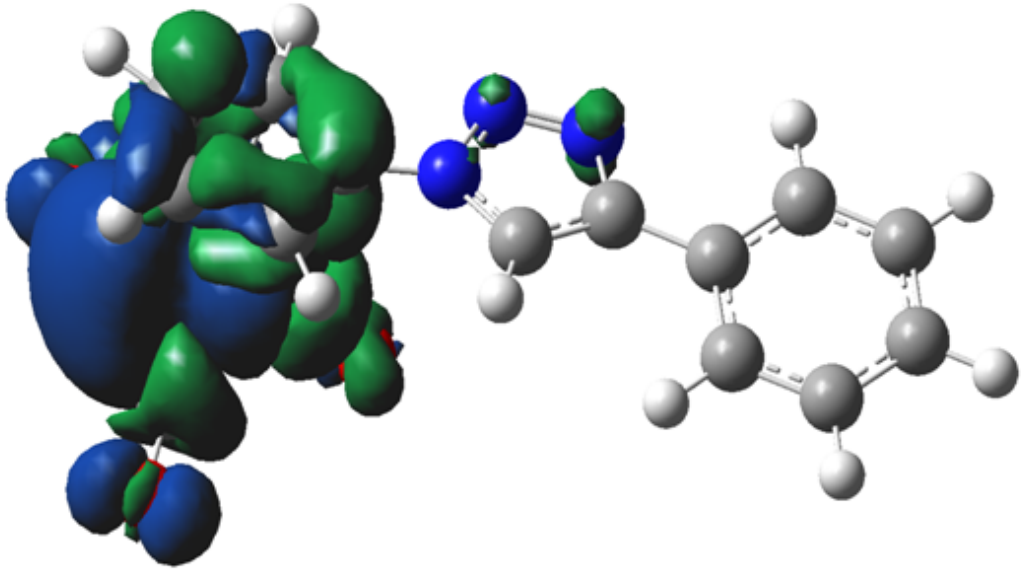

Figure 4.21. DFT calculated spin density diagram for the SOMO of cationic $\mathbf{13}^{+}$ in CH_2Cl_2. In the solvent the spin density on the Mn metal centre corresponds to 97% in solvent.

In the characterisation of the redox chemistry of cymantrene, Geiger reported that the electrogenerated cymantrene radical cation underwent decomposition to produce unidentified redox active produts, with reduction potentials at -0.48 and -1.35 V vs $Cp_2Fe^{0/+}$, and a surface adsorbed species that lead to passivation of the working electrode.[10] A similar behaviour is observed for **13**, except that with insight from the voltammetry of **13** and **14** and the results of DFT calculations and spectroelectrochemistry, it can be tentatively proposed that there is some degree of dimerisation of the radical cation of **13** to form a dimeric dication on the electrode surface. The dimer is electroactive and is reduced at approximately -0.315 V to form $\mathbf{13}^{2+}$, which desorbs and fragments upon further reduction at approximately -1.375 V to regenerate the cymantrene triazole parent **13**. (scheme 4.4)

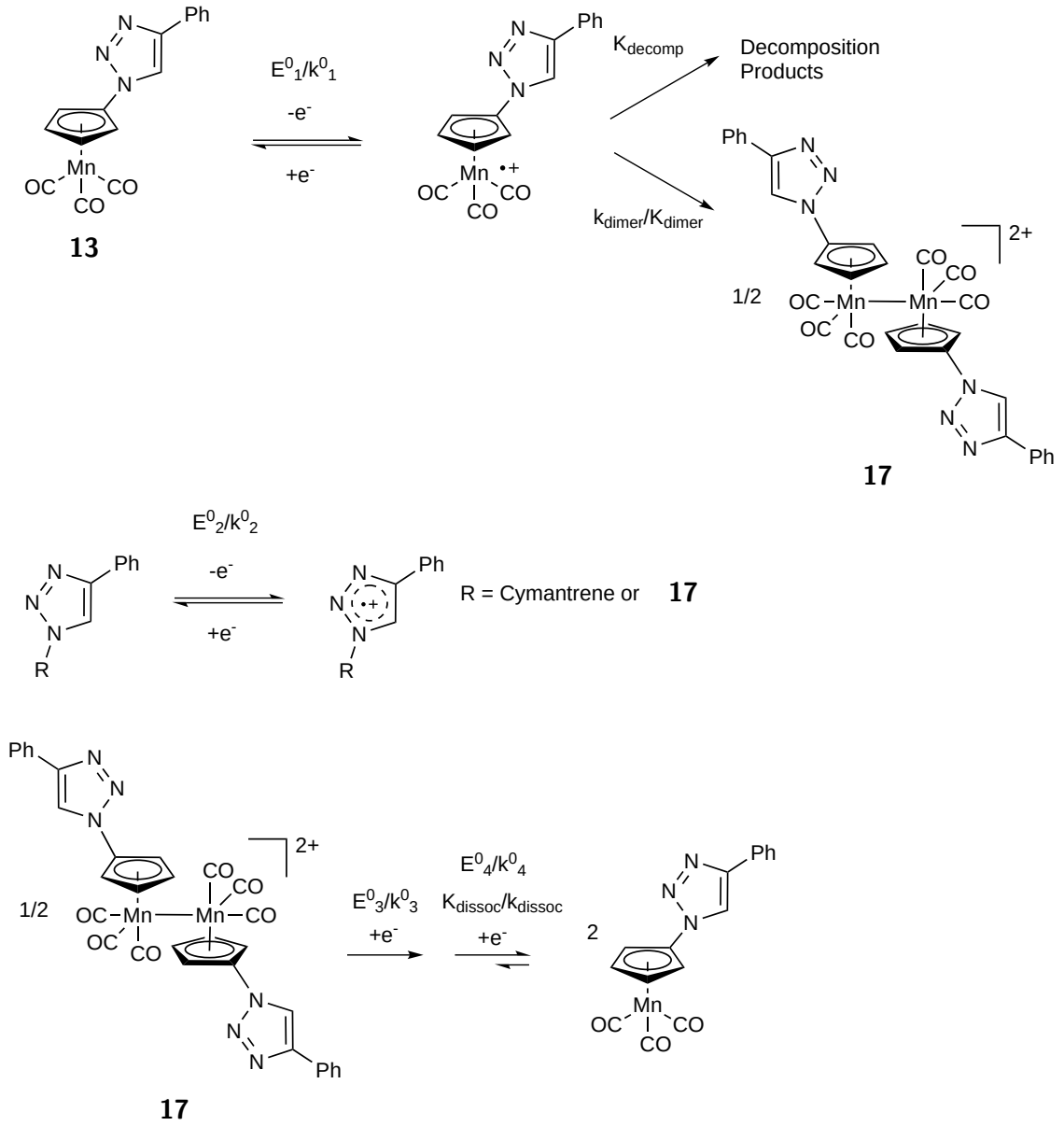

Scheme 4.4 The proposed mechanism and parameters used in the digital simulation of the voltammetry of **13**

Digital simulation of the observed voltammetry of **13** at varying scan rates (figure 4.22) is consistent with our proposed mechanism in scheme 4.4, producing an excellent fit between simulation and experiment. Attempts to fit the simulation to experimental data using a wide variety of other plausible mechanisms, gave much poorer fits outside our confidence value of 95% s.d. Each parameter in the simulation was globally optimized; the simulation converged to a set of values that produced fit to within 95% s.d., across each and every scan rate studied and for each redox peak position, shape and height. Each individual parameter was then varied separately and manually until the simulation no longer produced a satisfactory fit over all redox processes at all scan rates studied, to produce error bounds or minimum lower limiting values. These globally optimized parameters for the redox process and subsequent dimerization processes are given in Table 4.4. Note that in the case of **13** surface fouling prevented us from quantitatively simulating the triazole/triazolium redox wave using a diffusion-only simulation model.

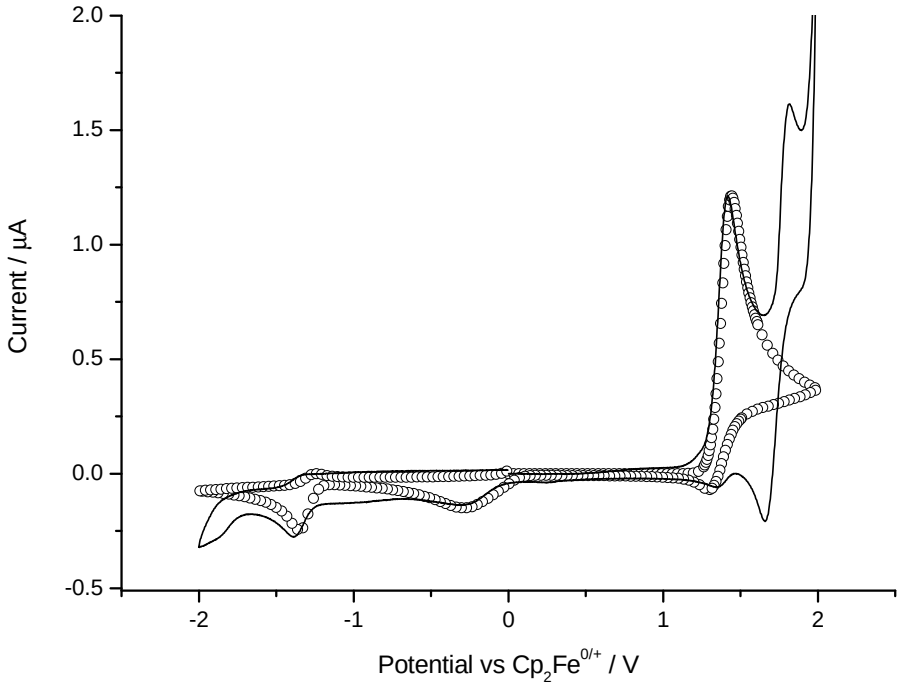

Figure 4.22. A comparison of experimental (solid line) vs. simulated data (open circles) for **13** (2 mM, in CH_2Cl_2) at a scan rate of 1 $V\,s^{-1}$. Note no attempt to model the triazole/triazolium redox process has been made due to complex adsorption processes

The solution phase electrochemistry of **14** is more informative than for **13**, as there is no electrode passivation. Again, upon first scanning in an oxidative direction we observe two clear oxidations at ca +1.20 V and +1.63 V vs. $Cp_2Fe^{0/+}$, which is again assigned to the oxidation of the cymantrene moiety and the 4-aminophenyl-derivatised triazole ring respectively (Figure 4.23). Both oxidation potentials appear to be shifted by –200 mV and –145 mV compared to those in **13** and both appear to be more reversible than is the case for **13** at higher scan rates, with corresponding reduction waves observed for both processes. However the reduction wave corresponding to the radical cation of **14** is approximately half the area (charge) of the oxidation wave when scanned at 2 $V s^{-1}$. If the reverse scan is extended into more negative potentials then a clear reduction wave of area again approximately half that of the oxidation of **14** is observed at -0.625 V vs ferrocene. The voltammetric behaviour of **14** is strikingly similar to that reported by Geiger for the rhenium analogue, cyrhetrene $[CpRe(CO)_3]$,[52] save for the presence of the triazole/triazolium redox couple. Upon oxidation the cyrhetrene radical cation also undergoes rapid dimersiation, with the dimer reduced at more negative potentials than the parent cyrhetrene. Unlike **13**, complex **14** shows no evidence of surface adsorption onto the electrode, allowing us to fully simulate all redox processes (Figure 4.24), again invoking the formation of a dimer, with excellent fit between theory and experiment over the scan rates studied (Scheme 4.5).

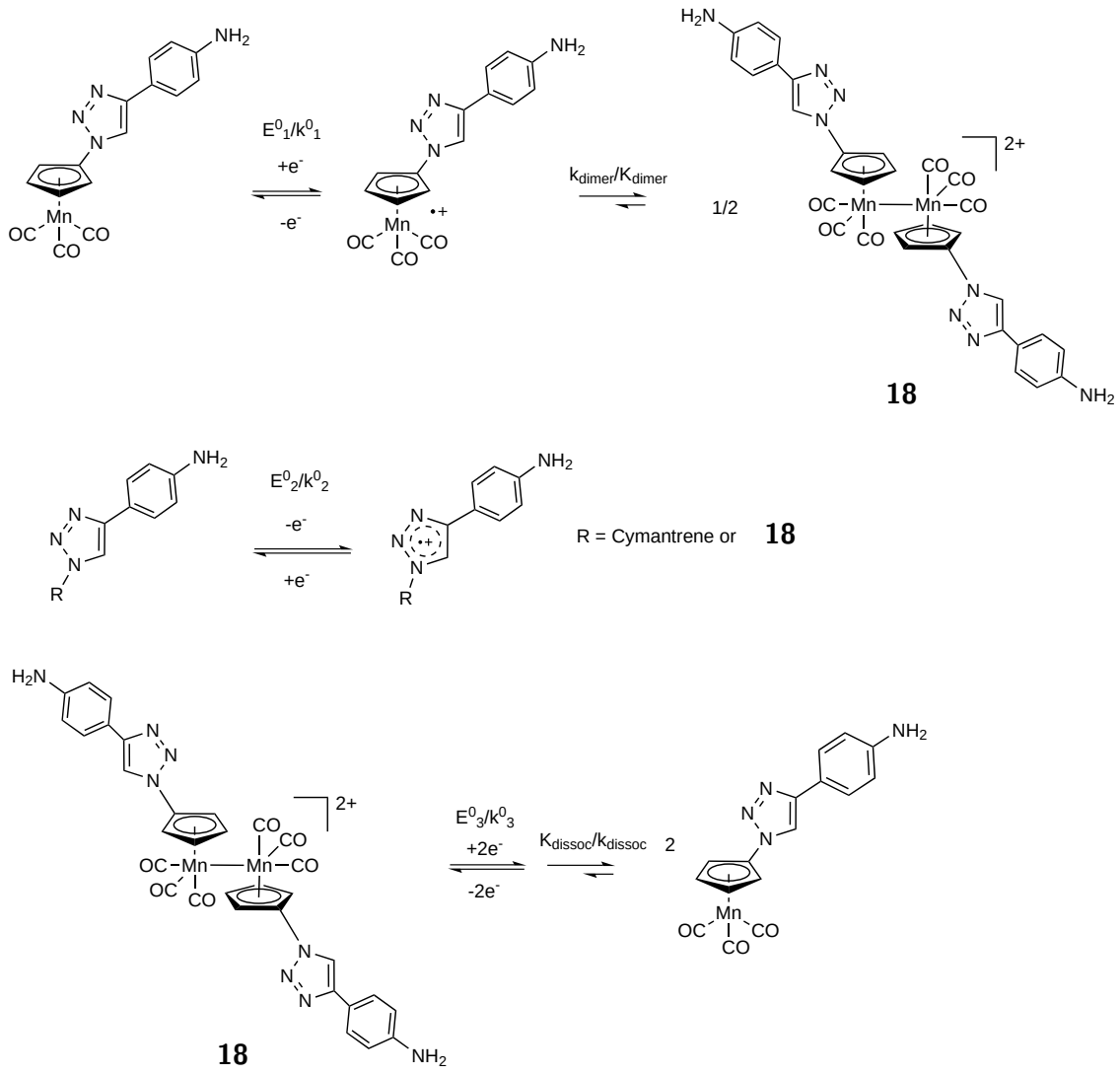

Scheme 4.5 The proposed mechanism and parameters used in the digital simulation of the voltammetry of **14**

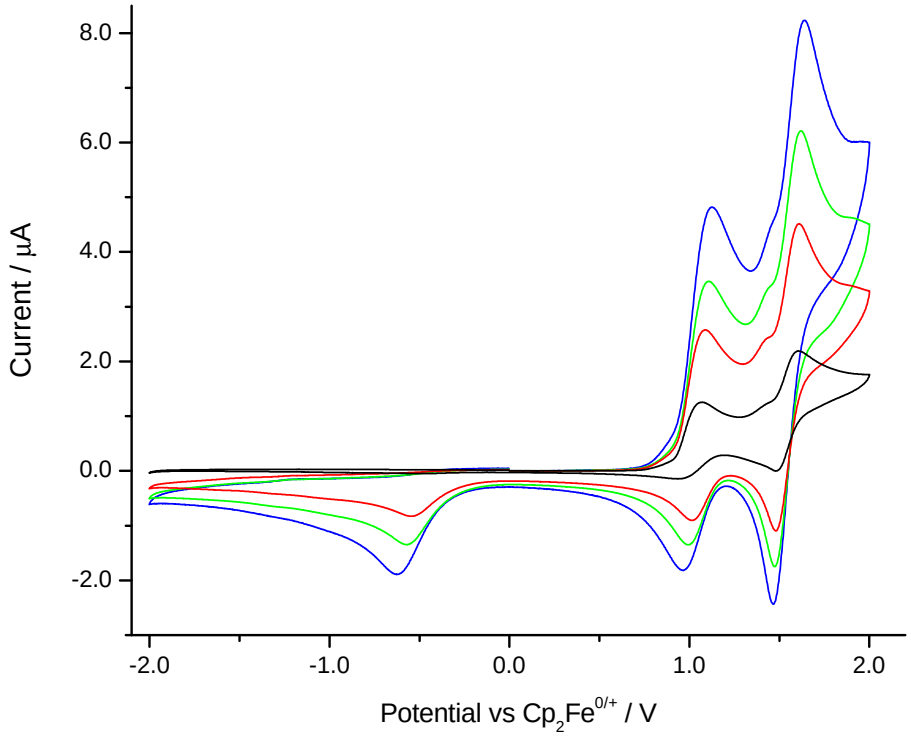

Figure 4.23. Cyclic voltammogram recorded for 2 mM **14** in CH_2Cl_2 at varied scan rates; blue = 2000 $mV\,s^{-1}$; green = 1000 $mV\,s^{-1}$; red = 500 $mV\,s^{-1}$; black = 100 $mV\,s^{-1}$

.

The globally optimized redox parameters obtained from the simulations as well as the equilibrium constant, K_{dimer}, and rate of dimerisation, k_{dimer}, of **14** are included in Table 4.4. The values of K_{dimer} and k_{dimer} are, respectively, 25 and 3.3 times smaller than those reported by Geiger for cyrhetrene.[52] This likely reflects the tendency of first–row d-block metals, such as Mn, not to form metal-metal bonds as readily as their third–row metal counterparts, e.g. Re (although we cannot preclude the possibility that dimerisation of the radical cations of **13** and **14** and occurs via other routes than through metal–metal bonding). We attribute both the shift to less positive redox potentials of **14** compared to **13** and the increased reversibility (chemical stability of the radical cation of **14**) of the redox processes to the resonance stabilization and electron donating character of the 4-amino phenyl moiety on the triazole ring.

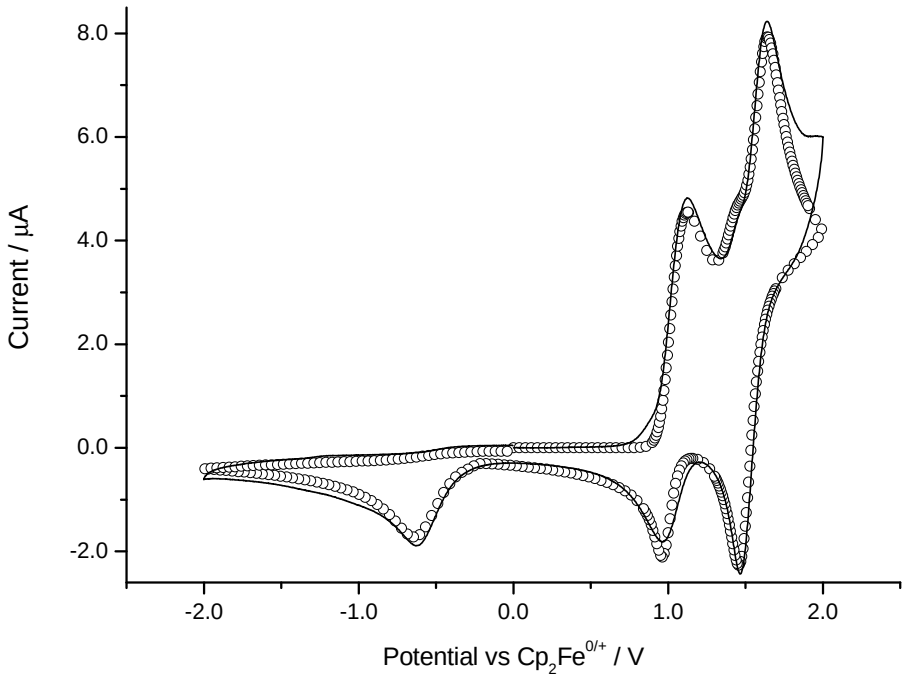

Figure 4.24. A comparison of experimental (solid line) vs. simulated data (open circles) for **14** (2 mM, in CH_2Cl_2) at a scan rate of 2 $V\,s^{-1}$.

Table 4.4. Redox parameters, associated chemical equilibria and rate constants determined from digital simulation of CVs for compounds **13** and **14**

		Compound **13**	Compound **14**
Standard Potential E^0 / V vs $Cp_2Fe^{0/+}$	E_1	1.37 ± 0.04	1.00 ± 0.02
	E_2	not simulated	1.55 ± 0.01
	E_3	-0.025 ± 0.005	-0.40 ± 0.02
	E_4	-1.30 ± 0.01	-
Electron Transfer Rate Constant k^0 / cm^{-1}	k_1	8.0 ± 0.2	13 ± 1
	k_2	n/a	8.0 ± 0.1
	k_3	1.0 ± 0.5	2.1 ± 0.1
	k_4	10 ±	-
Charge Transfer Coefficient α	α_1	0.50 ± 0.05	0.65 ± 0.05
	α_2	not simulated	0.55 ± 0.01
	α_3	0.20 ± 0.05	0.20 ± 0.05
	α_4	0.50 ± 0.05	-
Chemical Step Parameters	K_{dimer} / $mol^{-1}dm^3$	1.0 ± 0.1 $\times 10^6$	4.0 ± 0.2 $\times 10^4$
	k_{dimer} / $mol^{-1}dm^3s^{-1}$	1.0 ± 0.2 $\times 10^4$	3.00 ± 0.05 $\times 10^3$
	K_{decomp} / s^{-1}	5 ± 1 $\times 10^5$	
	K_{dissoc} / $mol^{-1}dm^3$	8.65×10^{63}	4×10^{43}
	k_{dissoc} / $moldm^3s^{-1}$	1.6 ± 0.2	1×10^9

The voltammetric characterization of **15** shows two oxidation processes at +1.25 V and +1.55 V vs $Cp_2Fe^{0/+}$ (figure 4.25). Again, we can assign the first oxidation to the cymantrene moiety. Neither oxidation process appears to be chemically nor electrochemically reversible with broad, ill-defined redox waves observed in the reverse scan. The voltammetry is not reproducible upon repeated scans. This is consistent with the second oxidation wave being due to oxidation of the 3-aminophenyl moiety and/or separately the triazole ring which leads to polymerization and fouling of the electrode surface. This is likely due to the *meta* amino group being unable to take part in resonance stabilization and electron donation into the triazole ring to stabilize the radical cation intermediate, unlike the case of **14**, and lends further support to our interpretation of the voltammetry of **14**. The electrode fouling prevents any meaningful attempt at digital simulation of the voltammetric data for **15**.

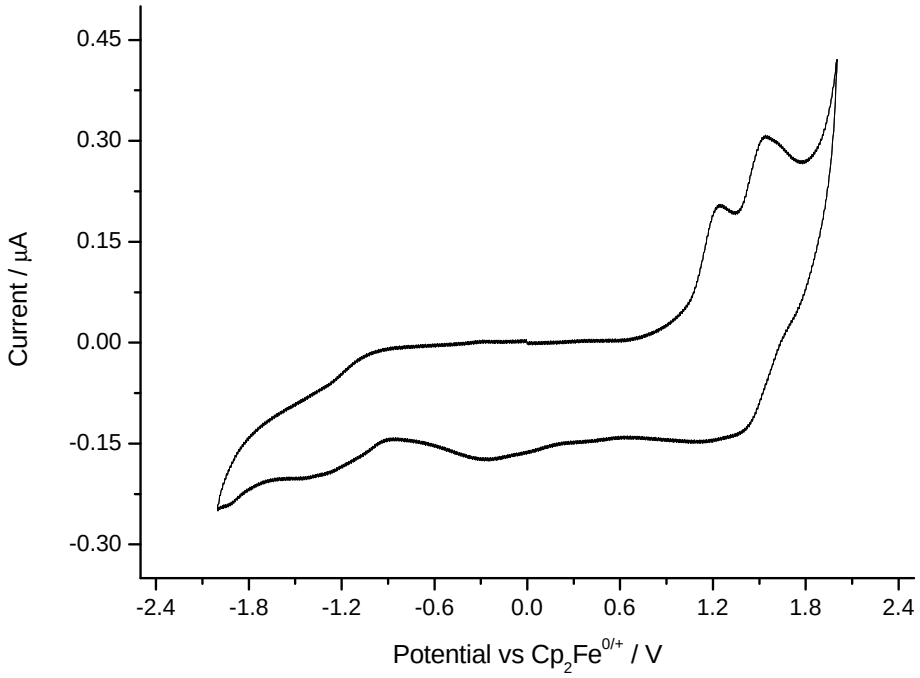

Figure 4.25. Cyclic voltammetry of **15** recorded at 100 $mV\,s^{-1}$ in CH_2Cl_2 with $[^nBu_4N][B(C_6F_5)_4]$ as supporting electrolyte

4.11. Synthesis and characterisation of cyrhetrene triazole complexes

Owing to the success of the preparation of **13**, **14** and **15**, the 1,4-copper catalysed azide-alkyne 'click' reaction was applied to cyhretrene [$CpRe(CO)_3$], utilising similar conditions to those used for the cymantrene derivatives. The preparation of **19** was achieved with a good yield as an

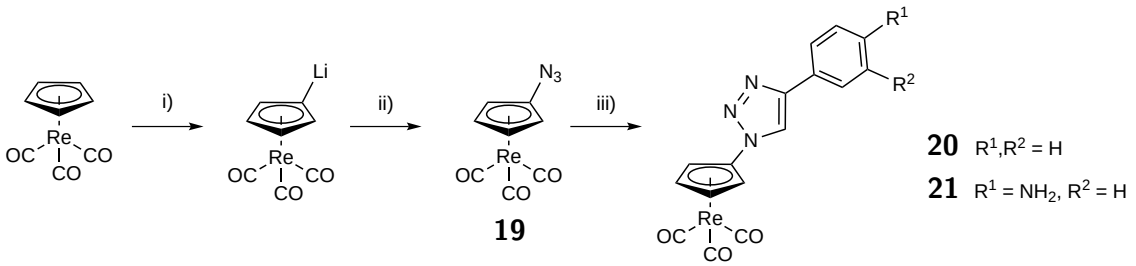

Scheme 4.6 Reagents and conditions: i) *n*-BuLi, THF, -78 °C; ii) TsN_3 THF, -78 °C; iii) phenylacetylene / ethynylaniline, $Cu(OAc) \cdot H_2O$, CH_3CN.

off white solid, after purification with silica gel chromatography. The structure was confirmed by ^1H and ^{13}C NMR and IR spectroscopy. The synthesis of **20** from **19** utilised modified

conditions as proposed by Hu *et al.*, (as used for **13**) affording a white crystalline solid in good yield and high purity after silica gel chromatography. (scheme 4.6). The ^{1}H NMR spectrum of **20** allows assignment of protons in characteristic environments in the complex, confirming the successful preparation of the 'click' triazole product. The cyclopentadienyl protons form two triplets integrating to two protons each, at chemical shifts of δ5.6 and 6.5 ppm, confirming the derivatisation of the Cp ring. ^{1}H COSY NMR experiments show the coupling of the protons on the phenyl substituent attached to the triazole moiety, in the aromatic region of δ 7.3-8.0 ppm. The chemical shift that integrates to 1 at δ 8.86 ppm is assigned as the proton as the 5-position of the triazole moiety.

The UV-vis spectra of the 'click' product **20** is comparable to the parent complex [η^5-$C_5H_5Re(CO)_3$]. In both cases the MLCT bands occur in the region of 250-280 nm. This assignment is based upon related cyrhetrene systems.[48] As per the cymantrenyl systems, the carbonyl ligands in **20** and **21** are a useful spectroscopic label, with symmetric and asymmetric stretches. Additionally, C=C stretches in the region of 1500-1600 cm^{-1} are observed for complexes **20** and **21**, which are assigned by reference to the literature.[53] The stretches are tabulated below. (table 4.5)

Table 4.5. νcm^{-1} bands for cyrhetrene and **19**, **20** and **21**

Complex	ν(C≡O)		ν(C=C) triazole
	Sym	Asym	
$CpRe(CO)_3$	2014	1888	n/a
19	2019	1907	n/a
20	2021	1949, 1927, 1907	1530
21	2025	1939, 1908, 1897	1621, 1565, 1498

4.12. Crystallographic analysis of triazole derivatised cyrhetrene

X-ray quality crystals were grown of compound **20** allowing crystallographic analysis of this complex. The resulting structure confirms the successful preparation of compound **20**, with the 1,4-triazole moiety visible and three carbonyl ligands coordinated to the rhenium centre. Similar to the manganese complex **13**, two molecules are present in the unit cell, denoted A and B in the molecular structure. Selected bond lengths are presented in table 4.6.

No x-ray quality single crystals of **21** could be grown under all the conditions attempted.

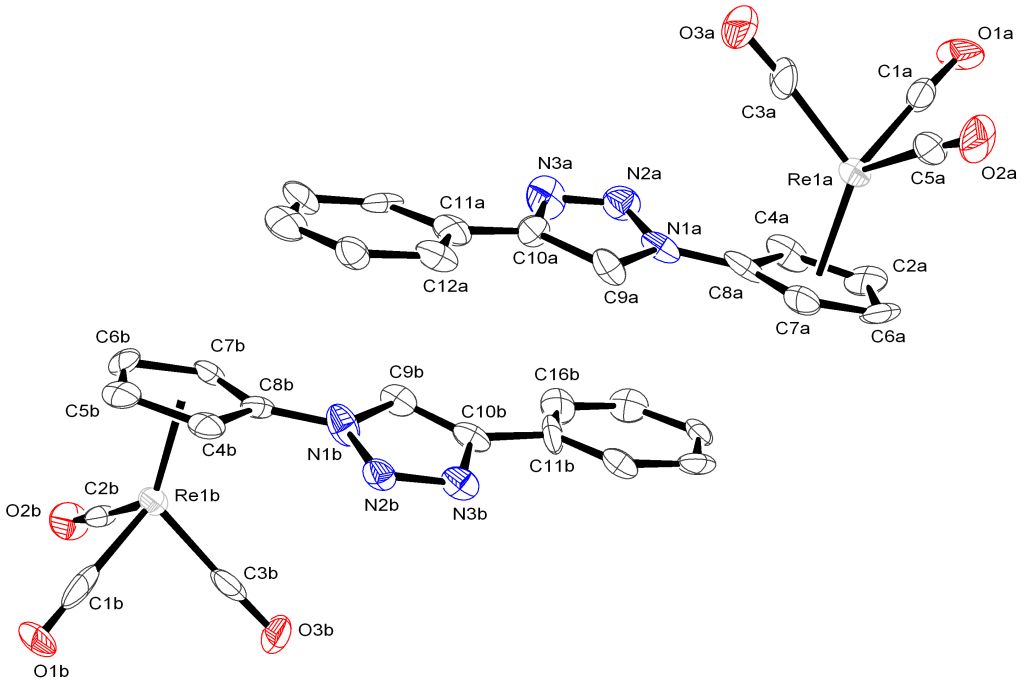

Figure 4.26. Molecular structure of compound **20**, showing the two molecules of the unit cell. Thermal ellipsoids are drawn at the 50% probability level.

Table 4.6. Selected bond lengths of the two molecules of **20** in the asymmetic unit

Bond	**20**A		**20**B	
Mn-Cp	Re1A-C8A	2.34(2)	Re1B-C8B	2.33(2)
	Re1A-C4A	2.30(2)	Re1B-C4B	2.33(2)
	Re1A-C5A	2.275(19)	Re2B-C5B	2.31(2)
	Re1A-C6A	2.30(2)	Re2B-C6B	2.30(2)
	Re1A-C7A	2.28(2)	Re1B-C7B	2.29(2)
$Mn\text{-}C_{carbonyl}$	Re1A-C3A	1.95(3)	Re1B-C3B	1.89(3)
	Re1A-C1A	1.95(3)	Re1B-C1B	1.93(4)
	Re1A-C2A	1.93(3)	Re1B-C2B	1.93(3)
$C{=}O_{carbonyl}$	C3A-O3A	1.11(3)	C3B-O3B	1.17(4)
	C1A-O1A	1.11(3)	C1B-O1B	1.14(4)
	C2A-O2A	1.11(3)	C2B-O2B	1.15(4)

4.13. Electrochemical characterisation of cyrhetrene triazole derivatives

Compounds **20** and **21** were electrochemically analysed by cyclic voltammetry, performed in CH_2Cl_2 solvent with $[^nBu_4N][B(C_6F_5)_4]$ as the supporting electrolyte. The only feature observed in the voltammetry of **20** was an irreversible oxidation at ca. 1.2 V vs $Cp_2Fe^{0/+}$. The wave is stable to repeat scans, (figure 4.27 bottom) but is irreversble at all scan rates recorded (figure 4.27 top). Analysis of the cyclic voltammetry of compound **21** shows an irreversible oxidation at 0.68 V vs $Cp_2Fe^{0/+}$, which similarly to the voltammetry of compound **20** is irreversible at all scan rates recorded. The oxidation waves in the voltammetry for both **20** and **21** are assigned to the oxidation of the triazole moiety to a triazolium, which occurs at a less positive potential than any electron transfer at the metal centre. This is in stark contrast to that observed for the cymantrene triazole derivatives reported above. The fast *EC* mechanism observed for the cyrhetrene triazole derivatives means that they are not suitable candidates for used in a heterogeneous context with more optimisation of electrochemical conditions.

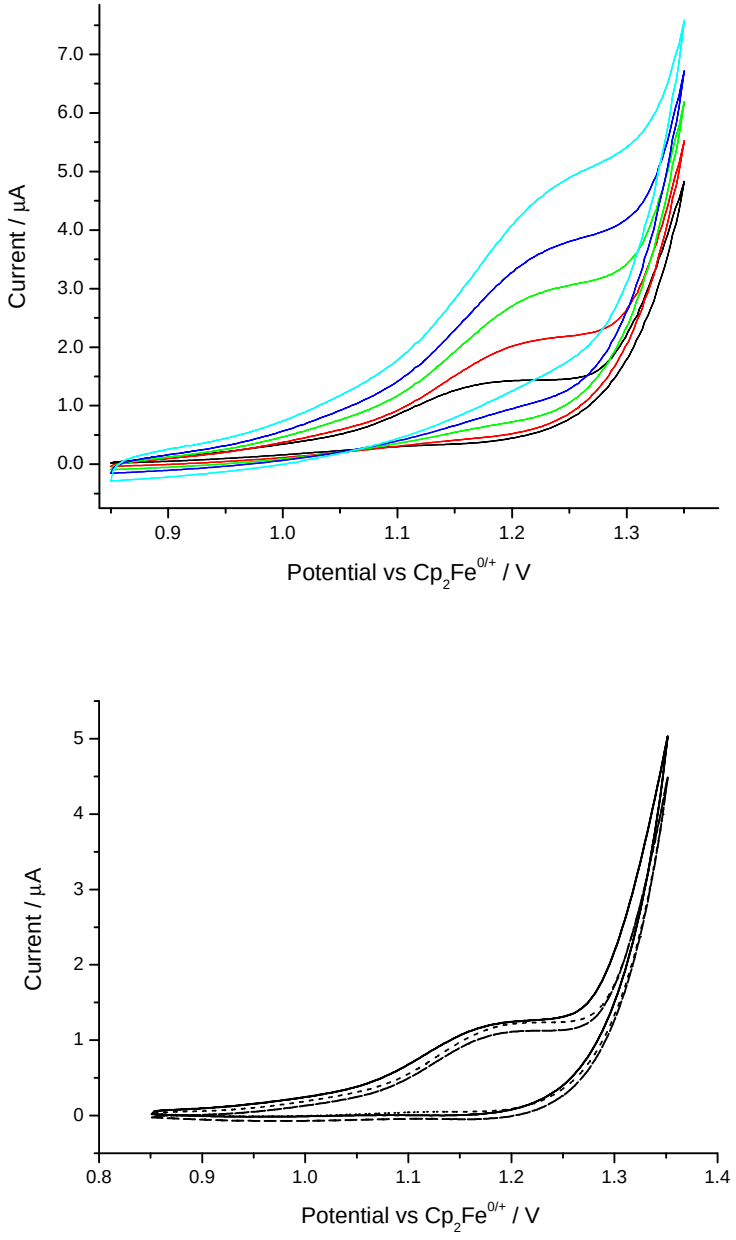

Figure 4.27. Top: Cyclic voltammogram recorded for 2 mM **20** in CH_2Cl_2 at varied scan rates; light blue = 1000 mV s^{-1} blue = 600 mV s^{-1} ; green = 400 mV s^{-1}; red = 200 mV s^{-1}; black = 100 mV s^{-1}. Bottom: repeat scans at 100 mV s^{-1} (line): 1st scan, (dots) 5th scan, (dashes): 10th scan.

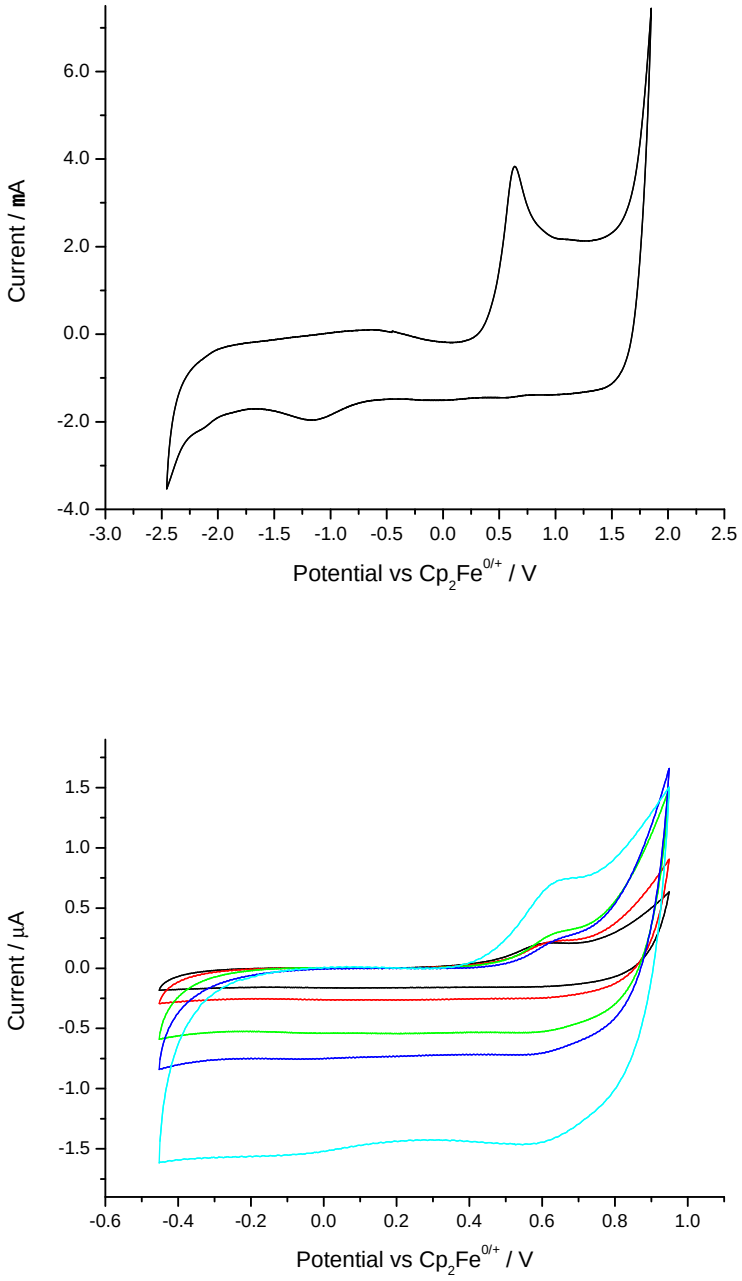

Figure 4.28. Top: Cyclic voltammogram recorded for 2 mM **21** in CH_2Cl_2 with $[^nBu_4N][B(C_6F_5)_4]$ as supporting electrolyte. Bottom: Cyclic voltammetry at varied scan rates; light blue = 1000 mV s^{-1} blue = 600 mV s^{-1}; green = 400 mV s^{-1}; red = 200 mV s^{-1}; black = 100 mV s^{-1}

4.14. Surface bound electrochemistry

4.14.1. Triazole derivatised phenyldiazonium reduction method

To investigate the surface bound electrochemistry of the novel compound **15**, the first method employed was surface attachment via reduction of the diazonium salt. The amino functional group on the phenyl ring of **14** was transformed to a diazonium salt with $NaNO_2$ in 6 M HCl. A salt metathesis with ammonium hexafluorophosphate then yielded the phosphate salt. A solution of **22** was then made up in dichloroethane and $[^nBu_4N][PF_6]$ electrolyte. The diazonium salt was then reduced by successive scans into the cathodic region up to -1.0 V vs Ag. The reduction potential observed in the cyclic voltammetry disappears, presumably as the electrode becomes coated in a monolayer of **14**. The modified electrode was then sonicated in various solvents (CH_2Cl_2, acetone) to remove any physisorbed compound, leaving only that which is chemisorbed on the surface.

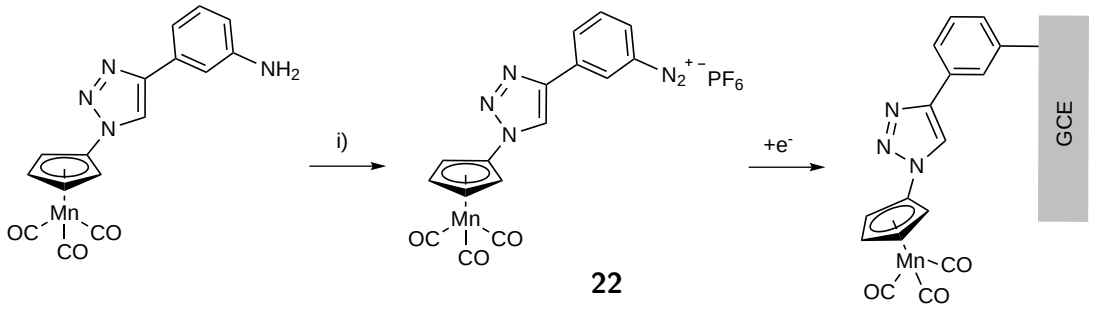

Figure 4.29. Reagents and conditions: i) $NaNO_2$, 6 M HCl, $[NH_4][PF_6]$

Cyclic voltammetry of the modified GCE in a solution of $CH_2Cl_2$with $[^nBu_4N][B(C_6F_5)_4]$ showed an oxidation at ca. 1.5 V vs $Cp_2Fe^{0/+}$. The wave was not stable to repeat scans however, and diminishes with each cycle.

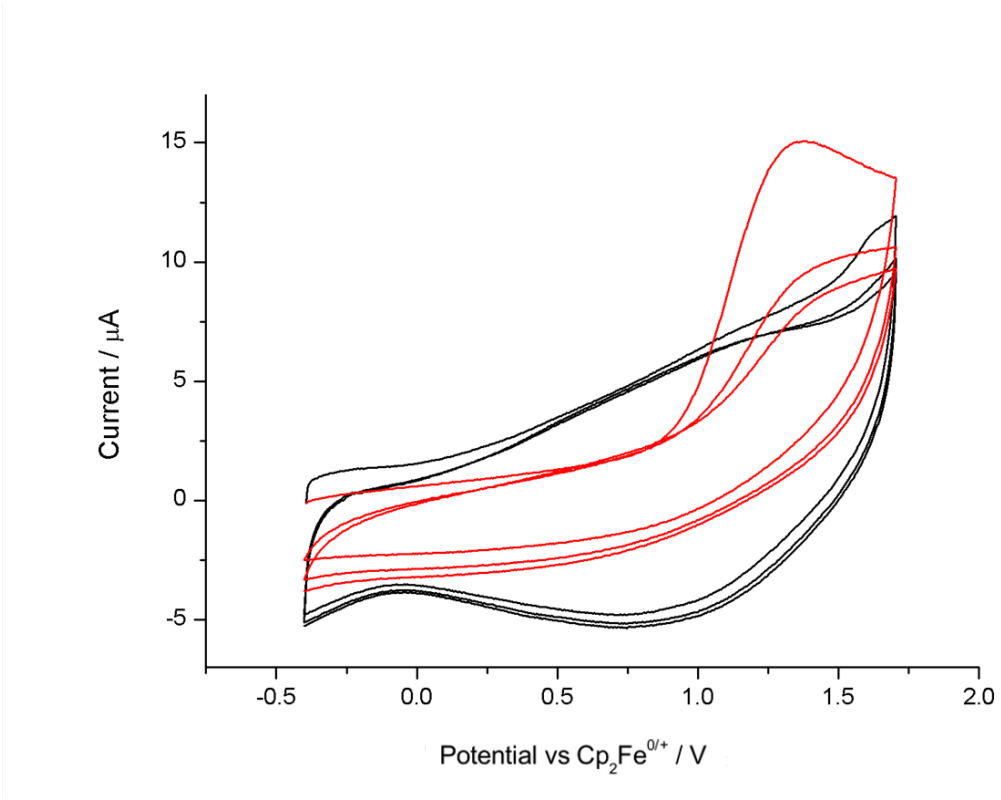

Figure 4.30. (Black) CV of unmodified GCE in CH_2Cl_2 with 0.05 M $[^nBu_4N][B(C_6F_5)_4]$ electrolyte at scan rate of 2000 mV s^{-1}, first 3 scans. (Red) CV of surface bound **15** in CH_2Cl_2 with 0.05 M $[^nBu_4N][B(C_6F_5)_4]$ electrolyte at scan rate of 2000 mV s^{-1}, first 3 scans.

4.14.2. Surface coverage estimation

To quantify the efficacy of the surface modification methods, the surface coverage of the organometallic species is estimated from the cyclic voltammetry of the modified electrodes. The area of the GCE is known from calibration with a standard solution of ferrocene in MeCN, using the Randles-Sevcik relationship between scan rate and peak current of the ferrocene oxidation. The integral of the voltammogram of the surface bound species, divided by the scan rate gives the charge. Faraday's first law of electrolysis (equation 4.1) is then invoked:

$$\Gamma = \frac{Q}{nFA} \tag{4.1}$$

where Q is charge, n is the number of electrons involved in the process, F is Faraday's constant (96485 C mol^{-1}), A is the area of the electrode in cm^2 and Γ is the surface concentration in mol cm^{-2}. This gives an estimation of Γ. Further to this, using dimensions from the crystal data, the area required for each molecule on the surface can be estimated. This gives an upper

limit for the amount of compound expected for a theoretical complete monolayer. The ratio of Γ and the theoretical maximum (equation 4.2) gives a fraction of surface coverage, Θ, which allows different modification methods to be contrasted.

$$\Theta = \frac{\Gamma}{\Gamma_{\text{min}}} \tag{4.2}$$

Using this method the surface coverage obtained via reduction of the diazonium triazole cymantrene derivatives can be estimated. At a scan rate of 2000 $\text{mV}\,\text{s}^{-1}$ (the scan rate necessary to observe a wave for the surface bound product in this case), the peak area corresponds to a charge of 3.07 $\times 10^{-7}$ C. Equation 4.1 gives a value of Γ at 4.97 $\times 10^{-11}$ $\text{mol}\,\text{cm}^{-2}$.

$$\Gamma = \frac{3.07 \times 10^{-7}}{96485 \times 0.064}$$
$$\Gamma = 4.97 \times 10^{-11} \text{mol}\,\text{cm}^{-2}$$

Using Avogadro's number and the area occupied by one molecule of phenyl-triazole derivatised cymantrene as 99.2 Å^2

$$\Gamma_{\text{min}} = \frac{1}{a_{\text{max}} \times 6.0221 \times 10^{23}}$$
$$\Gamma_{\text{min}} = \frac{1}{99.2 \times 10^{-19} \times 6.0221 \times 10^{23}}$$
$$\Gamma_{\text{min}} = 2 \times 10^{-10} \text{mol}\,\text{cm}^{-2}$$

4.14.3. Electrode surface 1,3-CuAAC of cymantrene azide

Modification of a glassy carbon electrode was also attempted via 'in situ' click chemistry, where the electrode was first modified with 4-ethynylaniline using the reduction of the diazonium salt. The electrode was then immersed into the solution typical of copper catalysed click chemistry, with Cu(I).OAc and cymantrene azide. It was hoped that a cycloaddition would occur on the alkyne functional groups now on the electrode, however upon testing for the oxidation of

cymantrene on a electrode that had this treatment, no oxidation waves were seen in the cyclic voltammetry. Therefore this method of electrode modification will require more optimisation to yield a significant surface coverage of cymantrene on the electrode.

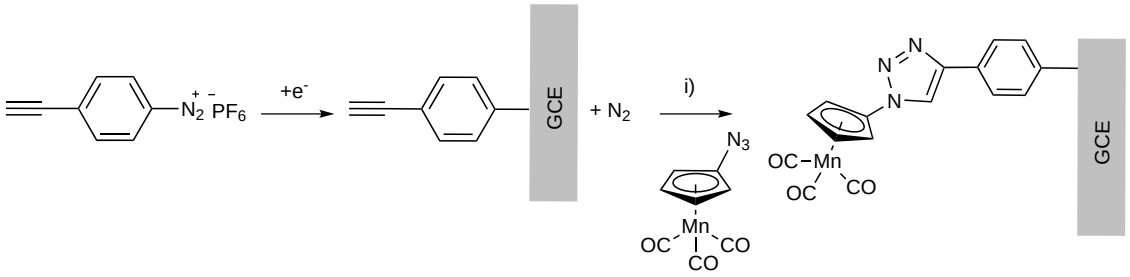

Figure 4.31. 'In situ' formation of triazole derivatised cymantrene at the GCE

4.15. Conclusions

The synthesis of the novel triazole derivatised cymantrene complexes **13**, **14** and **15** has been achieved in good yield, with full structural characterisation performed. The 'click' reaction reaction is unaffected by the addition of a *para* or *meta* amine group into the phenyl ring at the 4-position of the triazole structure. The electron donating effects of the amine groups in **14** and **15** has an effect of the redox properties of the cymantrene metal centre and triazole ring. This behaviour is rationalised by the resonance stabilisation of the triazolium intermediate and a decrease in the magnitude of electron-withdrawing effect of the triazole ring on the cyclopentadienyl ring. The amine group in **15** has been transformed to a diazonium salt, which was electro-grafted onto a GCE to show a surface bound redox wave. With further optimisation, this technique could be employed for the heterogeneous electrocatalytic activation of small molecules. Using the successful preparations of the cymantrene triazole derivatives as a starting point, similar cyrhetrene triazoles were prepared using the 1-3-CuAAC methodology with good yields. These compounds were structurally and electrochemically characterised, showing that in this case of both **20** and **21**, the only feature observed in cyclic voltammetry is the chemically irreversible oxidation of the triazole moiety. Have prepared and fully characterised triazole derivatised cymantrene and cyrhetrene, the electroactive nature of the triazole moeity has necessitated an alternative method of

(2) D. A. Sweigart, J. A. Reingold and S. U. Son, in *Comprehensive Organometallic Chemistry III*, Elsevier, 2007, pp. 761–813.

(3) T. Piper, F. Cotton and G. Wilkinson, *J. Inorg. Nucl. Chem.*, 1955, **1**, 165–174.

(4) F. Cotton, A. Liehr and G. Wilkinson, *J. Inorg. Nucl. Chem.*, 1955, **1**, 175–186.

(5) A. G. Ginzburg, *Russ. Chem. Rev.*, 1993, **62**, 1025.

(6) J. W. Kee, Y. Y. Tan, B. H. G. Swennehuis, A. A. Bengali and W. Y. Fan, *Oraganometallics*, 2011, **30**, 2154–2159.

(7) J. A. Calladine, S. B. Duckett, M. W. George, S. L. Matthews, R. N. Perutz, O. Torres and K. Q. Vuong, *J. Am. Chem. Soc.*, 2011, **133**, 2303–2310.

(8) L. Glans, W. Hu, C. Jöst, C. de Kock, P. J. Smith, M. Haukka, H. Bruhn, U. Schatzschneider and E. Norlander, *Dalton Trans*, 2012, **41**, 6443–6450.

(9) M. Hromadová, M. Salmain, R. Sokolová, L. Popišil and G. Jaouen, *J. Organomet. Chem.*, 2003, **668**, 17–24.

(10) D. R. Laws, D. Chong, K. Nash, A. L. Rheingold and W. E. Geiger, *J. Am. Chem. Soc.*, 2008, **130**, 9859–9870.

(11) C. J. Pickett and D. Pletcher, *J. Chem. Soc., Dalton Trans.*, 1976, 636–638.

(12) Y. Huang, C. C. Neto, K. A. Pevear, M. M. Banaszak Holl, D. A. Sweigart and Y. K. Chung, *Inorg. Chim. Acta*, 1994, **226**, 53–60.

(13) C. G. Atwood, W. E. Geiger and T. E. Bitterwolf, *Journal of Electroanalytical Chemistry*, 1995, **397**, 279–285.

(14) E. S. Mull, V. J. Sattigeri, A. L. Rodriguez and J. A. Katzenellenbogen, *Bioorg. Med. Chem.*, 2002, **10**, 1381–1398.

(15) H.-J. Pietzsch, A. Gupta, M. Reisgys, A. Drews, S. Seifert, R. Syhre, H. Spies, R. Alberto, U. Abram, P. A. Schubiger and B. Johannsen, *Bioconjugate Chem.*, 2000, **11**, 414–424.

(16) T. W. Spradau and J. A. Katzenellenbogen, *Bioconjugate Chem.*, 1998, **9**, 765–772.

(17) J.-M. Heldt, N. Fischer-Durand, M. Salmain, A. Vessières and G. Jaouen, *J. Organomet. Chem.*, 2004, **689**, 4775–4782.

(18) H. Yang, M. C. Asplund, K. T. Kotz, M. J. Wilkens, H. Frei and C. B. Harris, *J. Am. Chem. Soc.*, 1998, **120**, 10154–10165.

(19) R. G. Bergman, T. R. Cundari, A. M. Gillespie, T. B. Gunnoe, W. D. Harman, T. R. Klinckman, M. D. Temple and D. P. White, *Organometallics*, 2003, **22**, 2331–2337.

(20) D. J. Lawes, S. Geftakis and G. E. Ball, *J. Am. Chem. Soc.*, 2005, **127**, 4134–4135.

(21) D. J. Lawes, T. A. Darwish, T. Clark, J. B. Harper and G. E. Ball, *J. Am. Chem. Soc*, 2006, **45**, 4486–4490.

(22) C. Romão and B. Royo, in *Comprehensive Organometallic Chemistry III*, Elsevier, Oxford, 2007, pp. 855–960.

(23) D. Chong, A. Nafady, P. J. Costa, M. J. Calhorda and W. E. Geiger, *J. Am. Chem. Soc.*, 2005, **127**, 15676–15677.

(24) M. Delamar, R. Hitmi, J. Pinson and J. M. Saveant, *J. Am. Chem. Soc.*, 1992, **114**, 5883–5884.

(25) J. E. Sheats and M. D. Rausch, *J. Org. Chem.*, 1970, **35**, 3245–3249.

(26) R. Huisgen, *Proc. Chem. Soc.*, 1961, 357–396.

(27) V. V. Rostovtsev, L. G. Green, V. V. Fokin and K. B. Sharpless, *Angew. Chem., Int. Ed.*, 2002, **41**, 2596–2599.

(28) H. C. Kolb and K. B. Sharpless, *Drug Discov. Today*, 2003, **8**, PMID: 14678739, 1128–1137.

(29) F.-L. Cui, J. Fan, J.-P. Li and Z.-D. Hu, *Bioorganic & Medicinal Chemistry*, 2004, **12**, 151–157.

(30) H. C. Kolb, M. G. Finn and K. B. Sharpless, *Angew. Chem., Int. Ed.*, 2001, **40**, 2004–2021.

(31) C. B. Anderson, A. B. S. Elliott, C. J. McAdam, K. C. Gordon and J. D. Crowley, *Organometallics*, 2013, **32**, 788–797.

(32) K. J. Kilpin, E. L. Gavey, C. J. McAdam, C. B. Anderson, S. J. Lind, C. C. Keep, K. C. Gordon and J. D. Crowley, *Inorg. Chem.*, 2011, **50**, 6334–6346.

(33) B. Happ, D. Escudero, M. D. Hager, C. Friebe, A. Winter, H. Görls, E. Altuntaş, L. González and U. S. Schubert, *J. Org. Chem.*, 2010, **75**, 4025–4038.

(34) D. Schweinfurth, J. Krzystek, I. Schapiro, S. Demeshko, J. Klein, J. Telser, A. Ozarowski, C.-Y. Su, F. Meyer, M. Atanasov, F. Neese and B. Sarkar, *Inorg. Chem.*, 2013, **52**, 6880–6892.

(35) D. Schweinfurth, S. Demeshko, M. M. Khusniyarov, S. Dechert, V. Gurram, M. R. Buchmeiser, F. Meyer and B. Sarkar, *Inorg. Chem.*, 2012, **51**, 7592–7597.

(36) D. Schweinfurth, F. Weisser, D. Bubrin, L. Bogani and B. Sarkar, *Inorg. Chem.*, 2011, **50**, 6114–6121.

(37) T. Romero, R. A. Orenes, A. Tárraga and P. Molina, *Organometallics*, 2013, **32**, 5740–5753.

(38) C. Ornelas, J. Ruiz Aranzaes, E. Cloutet, S. Alves and D. Astruc, *Angew. Chem.*, 2007, **119**, 890–895.

(39) S. R. Miller, D. A. Gustowski, Z. H. Chen, G. W. Gokel, L. Echegoyen and A. E. Kaifer, *Anal. Chem.*, 1988, **60**, 2021–2024.

(40) M. Kumar, J. DePasquale, N. J. White, M. Zeller and E. T. Papish, *Organometallics*, 2013, **32**, 2135–2144.

(41) D. R. Laws, J. Sheats, A. L. Rheingold and W. E. Geiger, *Langmuir*, 2010, **26**, 15010–15021.

(42) M. V. Sheridan, K. Lam and W. E. Geiger, *J. Am. Chem. Soc.*, 2013, **135**, 2939–2942.

(43) T. C. Holovics, S. F. Deplazes, M. Toriyama, D. R. Powell, G. H. Lushington and M. V. Barybin, *Organometallics*, 2004, **23**, 2927–2938.

(44) K. Sünkel, U. Birk, S. Soheili, C. Stramm and R. Teuber, *J. Organomet. Chem.*, 2000, **599**, 247–255.

(45) Y. Liu, X. Wang, J. Xu, Q. Zhang, Y. Zhao and Y. Hu, *Tetrahedron*, 2011, **67**, 6294–6299.

(46) I. Carvalho, P. Andrade, V. L. Campo, P. M. M. Guedes, R. Sesti-Costa, J. S. Silva, S. Schenkman, S. Dedola, L. Hill, M. Rejzek, S. A. Nepogodiev and R. A. Field, *Bioorganic & Medicinal Chemistry*, 2010, **18**, 2412–2427.

(47) T. Hirano, H. Kubo, T. Shiraishi, K. Hiromoto, T. Fujiwara and H. Kagechika, *Tetrahedron Lett.*, 2012, **53**, 5916–5919.

(48) R. T. Lundquist and M. Cais, *J. Org. Chem.*, 1962, **27**, 1167–1172.

(49) M. L. Lage, D. Curiel, I. Fernández, M. J. Mancheño, M. Gómez-Gallego, P. Molina and M. A. Sierra, *Organometallics*, 2011, **30**, 1794–1803.

(50) A. O. Borissova, M. Y. Antipin and K. A. Lyssenko, *J. Phys. Chem. A*, 2009, **113**, 10845–10851.

(51) J.-L. M. Abboud, C. Foces-Foces, R. Notario, R. E. Trifonov, A. P. Volovodenko, V. A. Ostrovskii, I. Alkorta and J. Elguero, *Eur. J. Org. Chem.*, 2001, **2001**, 3013–3024.

(52) D. Chong, D. R. Laws, A. Nafady, P. J. Costa, A. L. Rheingold, M. J. Calhorda and W. E. Geiger, *J. Am. Chem. Soc.*, 2008, **130**, 2692–2703.

(53) E. J. Yoo, M. Ahlquist, S. H. Kim, I. Bae, V. V. Fokin, K. B. Sharpless and S. Chang, *Angewandte Chemie International Edition*, 2007, **46**, 1730–1733.

5. Diazirine derivatised cymantrene and cyrhetrene: structural and electrochemical characterisation

5.1. Using carbene forming diazirines for organometallic electrode modification

Diazirines are a promising substrate for carbon surface modification. A diazirine consists of an azo group bound across an sp^3 hybridized carbon, and are known to form carbenes upon release of dinitrogen when exposed to light and heat.[1] These carbenes are extremely reactive with a lack of chemoselectivity, however the diazirine precursor is relatively stable, and therefore synthetically very useful.[2,3] Diazirine, alkyl diazirine and 3-halodiazirines were first prepared in the early 1960s,[4–6] however the chemical utility of these was relatively limited, due to the rather unstable nature of 3-halodiazirines, and the propensity of intra and intermolecular reactions of alkyl diazirines.[7,8] For example, diethyl-diazirine thermally decomposes to result in formation of *cis* and *trans*-2-pentenes and ethylcyclopropane from a 1,3-hydride migration process ((b) in figure 5.1). Similarly, arylalkyl diazirines undergo intramolecular rearrangements to yield cyclopropanes, and a significant amount of the azine decomposition product (c) in figure 5.1)

A much more synthetically useful class of diazirine carbene precursors are the 3-aryl-3-(trifluoromethyl)diazirines, first reported by Brunner and co-workers in the 1980s. They are very promising photo-activated linkers, satisfying the main requirements of photo-activated compounds; the stability prior to photolysis, the rapidity of the photolysis and high reactivity of the photogenerated species. The 3-aryl-3-(trifluoromethyl)diazirines are much stabilised compared with the alkyl and halodiazirines previously mentioned, which are

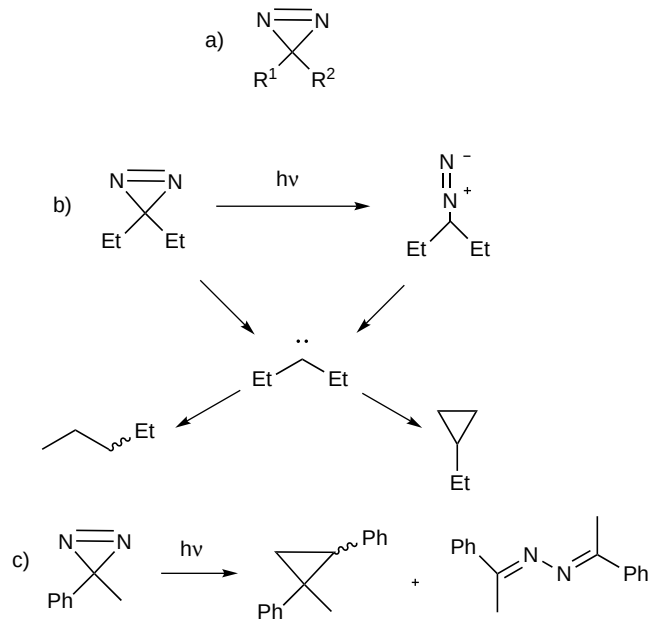

Figure 5.1. a) General structure of a diazirine, b) intramolecular reactivity of dialkyl diazirine, c) intramolecular reaction of phenyl diazirine

explosive. 3-(trifluoromethyl)3-phenyldiazirine is stable in methanol containing 1M HCl or NaOH for up to 2 hours, and stable up to 75 °C for 30 minutes if kept in the dark. They are also relatively facile to synthesise, with an overall yield of 60 % from the 2,2,2-trifluoroacetophenone starting material. The photolysis of this diazirine, despite its chemical stability, yields a carbene reactive enough to insert into the C-H bond on cyclohexane (figure 5.2).[9] A major use of these

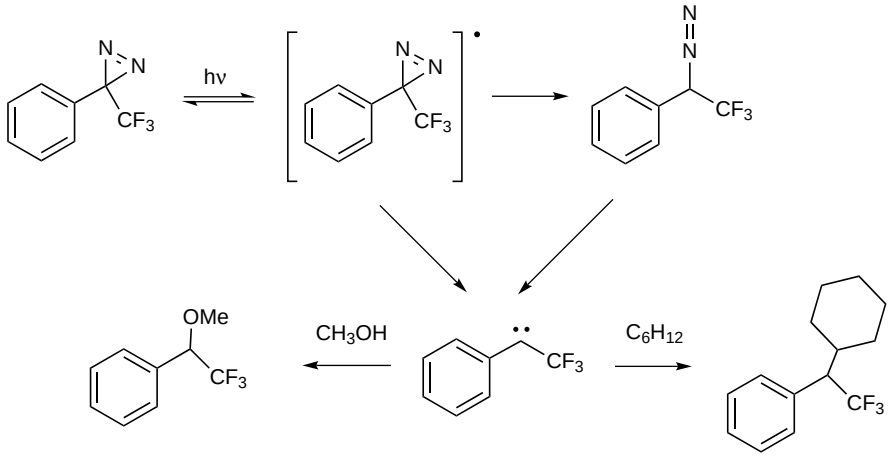

Figure 5.2. Reactivity of 3-aryl-3-trifluoromethyldiazirine with methanol and cyclohexane

reagents is for photoaffinity labelling (PAL) in biological applications, which enables study of a protein substrate binding site via formation of a covalent bond between the protein and it's substrate. This field has been reviewed extensively by Blencowe and Hayes.[10] The Hayes group,

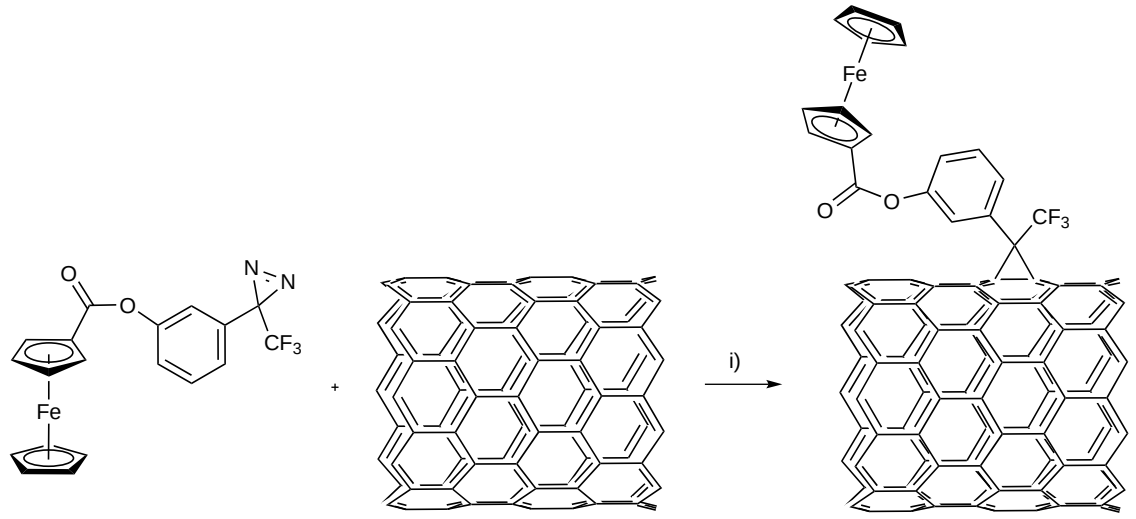

Figure 5.3. Surface modification with diazirine derivatised ferrocene. Reagents and conditions: i) hν, 24 H

among others have used diazirine methodology for a wide range of applications in materials chemistry. Notably, they have used the carbene produced upon diazirine photolysis to label nylon with a fluorescent probe.[11] Previously in the Wildgoose group, 3-aryl-3-trifluoromethyl diazirine has been successfully used to attach ferrocene to graphitic surfaces, including a GCE and MWCNTs. The ferrocene was derivatised with the diazirine moiety via an ester linkage to the cyclopentadienyl ring (figure 5.3. Treatment with UV light formed the carbene upon loss of dinitrogen, which formed a covalent attachment to the carbon surface. This presence of surface bound ferrocene was evidenced by cyclic voltammetry after washing the surface, and X-ray Photoelectron Spectroscopy (XPS). The surface coverage calculated from this method was high, due to the mechanism of the surface modification process. Due to this success, and the electroactive nature of the triazole linker discussed in the previous chapter, the author attempted to attach cymantrene to a graphitic surface via the same methodology. This lead to the synthesis and characterisation of 3-[3-(trifluoromethyl)diazirin-3-yl]phenyl cymantrene monocarboxylate, referred to as 'cymantrene diazirine', via the preparation of a carboxylic acid derivatised cymantrene.

5.2. Preparation and characterisation of cymantrene derivatives

The electronic effects of any side groups on the cyclopentadienyl ring of sandwich complexes are a major factor in determining the oxidation potential of the half-sandwich complex. This is

observed with the amino-cymantrene and the permethylated cymantrene derivatives,[12] where the oxidation potential is shifted from 0.91 V to 0.62 and 0.64 V respectively. This effect must be considered, as our final goal is the surface bound heterogeneous catalytic system, where the 'linker' is attaching the complex to the electrode via the cyclopentadienyl ring. To this end, the intermediate cymantrene derivatives were analysed by solution phase voltammetry, to determine the oxidation potential we expect for the surface bound species, and ensure the side groups used are compatible with the radical cation produced upon oxidation of the core cymantrene moiety.

5.2.1. Preparation and characterisation of η^5-methylcarboxylate cyclopentadienyl tricarbonyl manganese(I)

The 3-aryl-3-trifluoromethyl-diazirine is attached to cymantrene via an ester linkage, so the electrochemical properties of an ester modified cymantrene must be determined before the surface based electrochemistry is attempted. To this end, cymantrene methyl ester **23** was prepared by the formation of the lithium salt of cymantrene with Schlosser's base[13] and the addition of methyl chloroformate as the electrophile (scheme 5.1). The product from this reaction can be purified by crystallisation from hexane, affording a sample of sufficient purity for electrochemical analysis. The successful preparation of **23** was initially determined by ^{1}H NMR, where a diagnostic splitting of the cyclopentadienyl protons into two triplets at δ 5.44 and 4.79 ppm indicate a substituent on the ring, with a singlet at δ 3.81 ppm showing the presence of a methoxy group. IR spectroscopy was used to confirm that the manganese tricarbonyl core was intact, showing the metal carbonyl stretches at 2023 and 1914 cm^{-1}, and the carbonyl stretch from the ester at 1722 cm^{-1}. Purity was assessed by elemental analysis. The direct cyclic voltammetry of **23** was performed in CH_2Cl_2 using

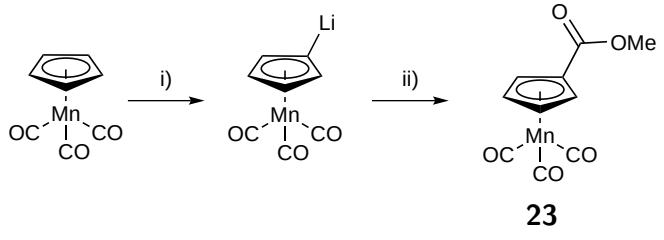

23

Scheme 5.1 Reagents and conditions: i) KO ^{t}Bu 0.1 Eq, ^{t}BuLi, -78 °C, THF; ii) $ClCO_2Me$

0.1 mol dm^{-3} [^{n}Bu$_4$N][B(C$_6$F$_5$)$_4$] as the supporting electrolyte, due to the nucleophilicity of

traditional electrolytes towards organometallic radical cations. Initially a survey voltammogram was recorded by scanning from 0 V vs Ag to the oxidative edge of the window, then reversing and scanning the cathodic region up to the reductive solvent limit. The voltammetry is remarkably similar to that of the parent cymantrene, with the reversible oxidation potential at a more anodic 1.1 V vs $Cp_2Fe^{0/+}$ compared to 0.91 V (figure 5.4). The voltammetry is reversible at all scan rates, showing that the radical cations produced upon oxidation do not react with intermolecularly with ester moieties at an appreciable rate (figure 5.5). A small poorly defined cathodic wave was however observed at 0.16 V, that is presumably a trace of decomposition product. The results suggest that the an ester linkage is compatible with the principle of using electrogenerated radical species to activate C-H bonds, and that the ester itself does not consume the radical.

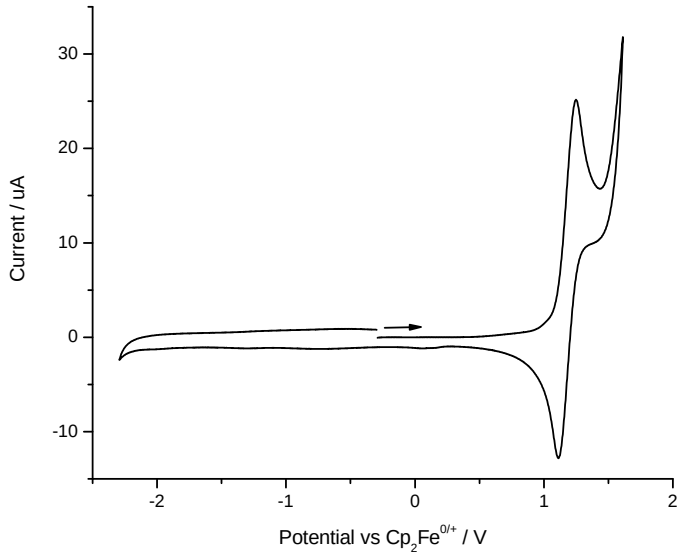

Figure 5.4. Full range cyclic voltammogram of **23** in CH_2Cl_2 (2.0 mmol dm^{-3}, 0.05 M [^{n}Bu$_4$N][B(C$_6$F$_5$)$_4$]) at a scan rate of 100 mV s^{-1}

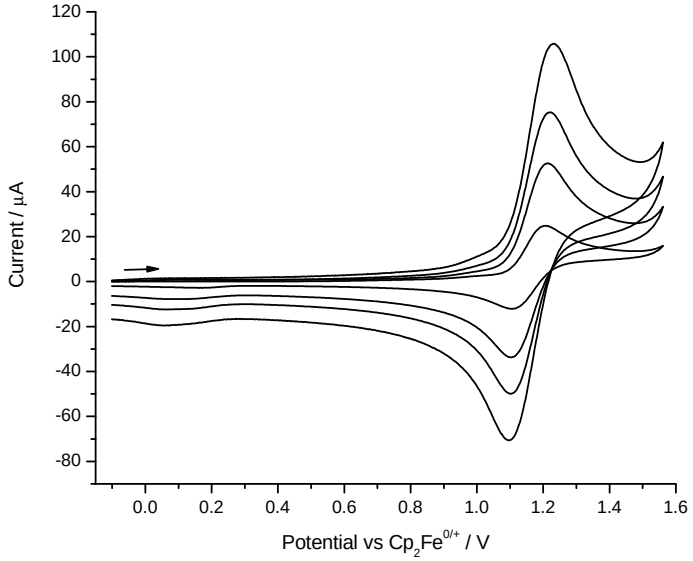

Figure 5.5. Cyclic voltammogram of **23** in CH_2Cl_2 (2.0 mmol dm^{-3}, 0.05 M [^{n}Bu$_4$N][B(C$_6$F$_5$)$_4$]) at scan rates of 100, 500, 1000 and 2000 mV s^{-1}

5.2.2. Preparation and characterisation of η^5-[carboxyl]cyclopentadienyl tricarbonyl manganese(I)

To form the diazirine derivatised cymantrene product used to modify the GCE, the hydroxy-3-aryl-3-trifluoromethyl-diazirine was reacted with the carboxylic acid derivatised cymantrene to form an ester linkage, via the methodology of Steglich (see section 5.2.3). To prepare the carboxylic acid derivative of cymantrene, two synthetic routes were compared. Initially, the methylcarboxylate cymantrene was hydrolysed with ethanolic KOH, then extracted from an acidified aqueous solution, to yield the product as a yellow powder. Purification can be achieved with recrystallisation from methanol and petroleum ether to afford pale yellow crystals. In the second method, the lithium salt was again prepared by Schlosser's base, but with carbon dioxide used as the electrophile. This yields a lithium carboxylate salt of the cymantrene, which can be acidified with an acid work up in mild $HCl_{(aq)}$ and extracted with diethyl ether (scheme 5.2). The product was then purified by recrystallisation from ethanol and hexane, yielding pale yellow crystals. Successful preparation of **24** was determined by the presence of two triplets in the ^{1}H NMR spectrum at, diagnostic of a functional group on the cyclopentadienyl ring. The metal carbonyl stretches at 2030 and 1946 cm^{-1} and carboxylic

acid C=O stretch at 1730 cm^{-1} observed in the IR spectrum confirmed that the manganese tricabonyl fragment was intact and the presence of the acid. The overall yields from both methods are similar, but the latter method involving the direct carbonylation with CO_2 is simpler.

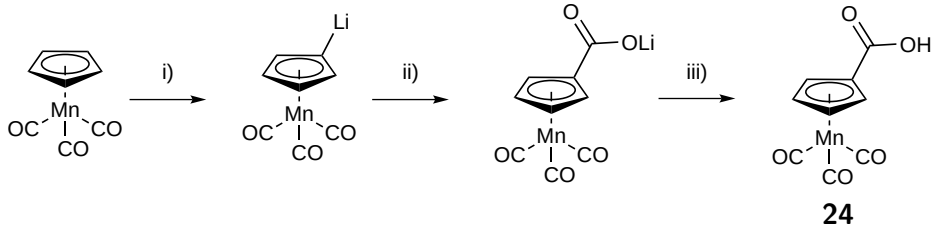

Scheme 5.2 Reagents and conditions: i) KOtBu 0.1 Eq, ^{t}BuLi, -78 °C, THF;, ii) CO_2(g); iii) HCl(aq), 0.1 M

5.2.3. Preparation and characterisation of 3-[3-(Trifluoromethyl)diazirin-3-yl]phenyl cymantrene monocarboxylate

The diazirine derivative of cymantrene was prepared by reaction of the cymantrene carboxylic acid (above) with 3-(trifluoromethyl)-3-(3-hydroxyphenyl)diazirine **27**. The diazirine was prepared by a modified literature procedure,[2] in which a Swern oxidation was used in place of silver oxide for the oxidation of the diaziridine **25** to the diazirine **26**.[14] This was due to the poor yields achieved when using silver oxide, and the extra step incurred from the preparation of the silver oxide reagent. The Swern oxidation is a much more facile one pot reaction, which involves the formation of dimethylchlorosulfonium chloride, driven by the release of CO_2 and CO.

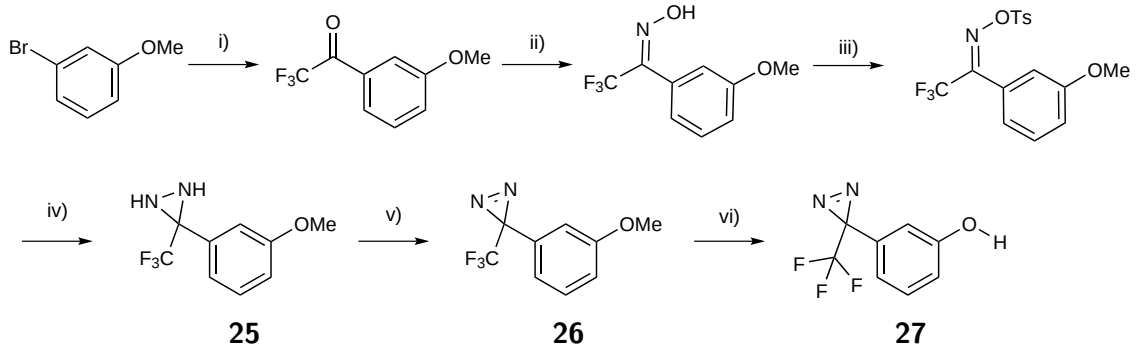

Scheme 5.3 Reagents and conditions: i) ^{n}BuLi, CF_3CO_2Me, -78 °C, THF; ii) $NH_2OH \cdot HCl$, EtOH; iii) Tosyl chloride, DMAP, DCC, NEt_3, CH_2Cl_2 iv) NH_3(l), CH_2Cl_2; v) Oxalyl chloride, DMSO, NEt_3, CH_2Cl_2, -78 °C; vi) BBr_3, CH_2Cl_2, rt.

The diazirine linker **27** was then coupled with cymantrene carboxylic acid **24** via the use of Steglich esterification, in which N-N'-dicyclohexylcarbodiimide (DCC) is the mediator and a catalytic amount of dimethylaminopyridine (DMAP) is used to prevent side reactions. The product was purified by column chromatography and crystallised from petroleum ether and dichloromethane. Complex **28** (scheme 5.4) is a novel compound, so full characterisation including multinuclear NMR and crystallographic analysis was recorded for this product for evidence of its successful preparation and elucidation of its properties. The ^{1}H NMR spectrum

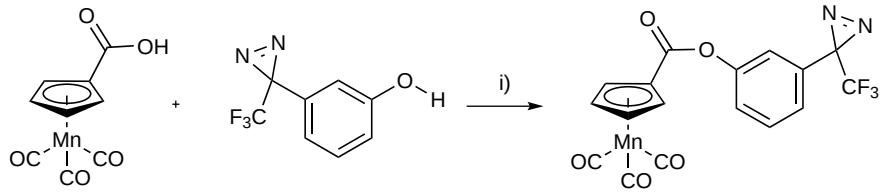

28

Scheme 5.4 Reagents and conditions: i) DCC, DMAP, CH_2Cl_2, rt, 12h

of **28** contains the diagnostic split cyclopentadienyl protons, in this case at δ 5.61 and 4.92 ppm. The product has other useful spectroscopic labels; the meta-substituted phenyl ring from **27** has a characteristic pattern of splitting that is preserved in **28**, with a triplet at δ7.54 ppm and a series of multiplets at 7.23, 7.09 and 6.99 ppm. A 2D COSY NMR spectrum was recorded to determine the source of the splitting in order to give more weight to the previous assignments. As expected, the cyclopentadienyl protons are coupled together, and the aromatic protons are coupled in a series of multiplets (figure 5.6).

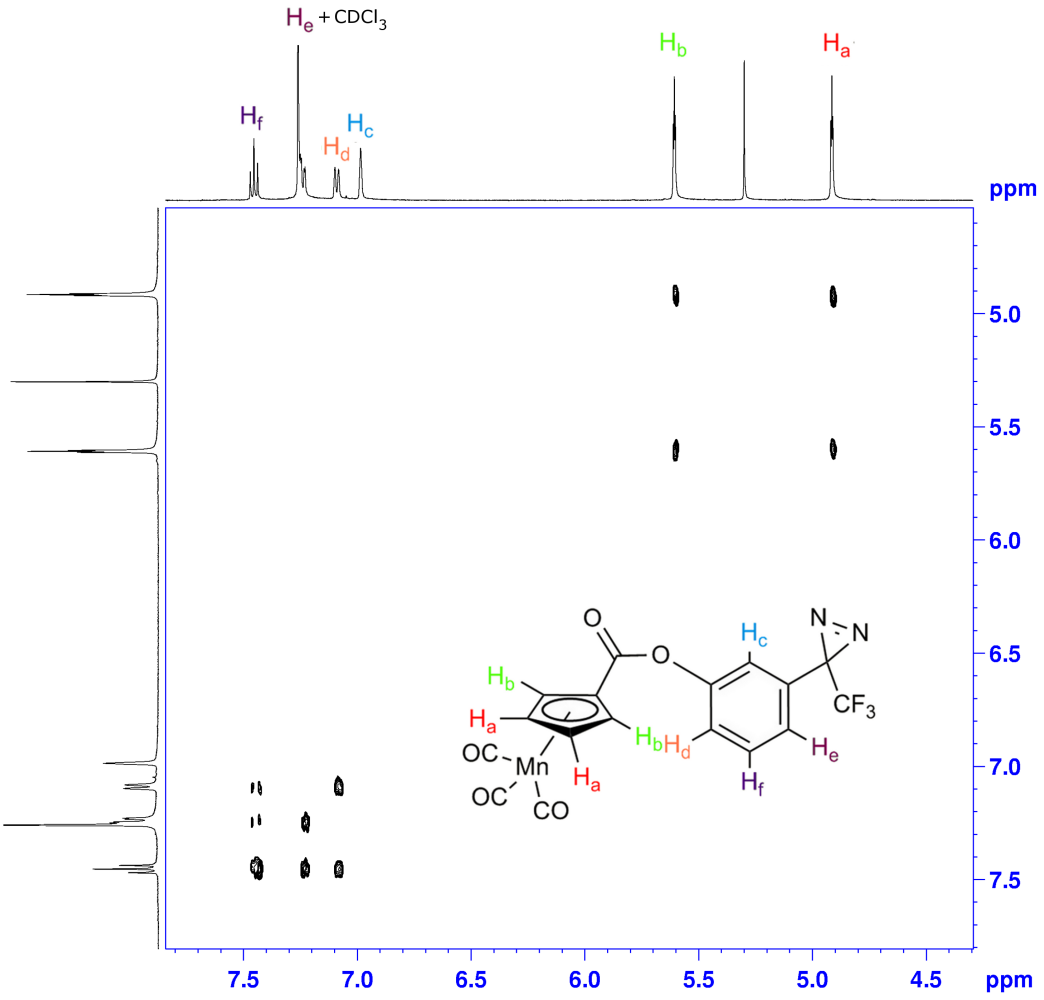

Figure 5.6. COSY ^{1}H NMR of **28**

A 2D HSQC NMR was recorded to aid the assignment of the carbon atoms bonded to protons in **28**, shown in figure 5.7. The ^{13}C chemical shifts associated with the carbonyl ligands could not be observed in the spectrum, and the chemical shift at 133 ppm is assigned as the carbon atom of the trifluoromethyl group. The trifluoromethyl group is an especially useful spectroscopic handle, indicating the preservation of the light sensitive diazirine functional group with a ^{19}F NMR chemical shift of -65.14 ppm (*c.f* -65.6 for the parent diazirine **27**). Under ambient light, **28** is liable to dimerise into the azine **29**, the formation of which can be detected through the ^{19}F NMR spectrum.

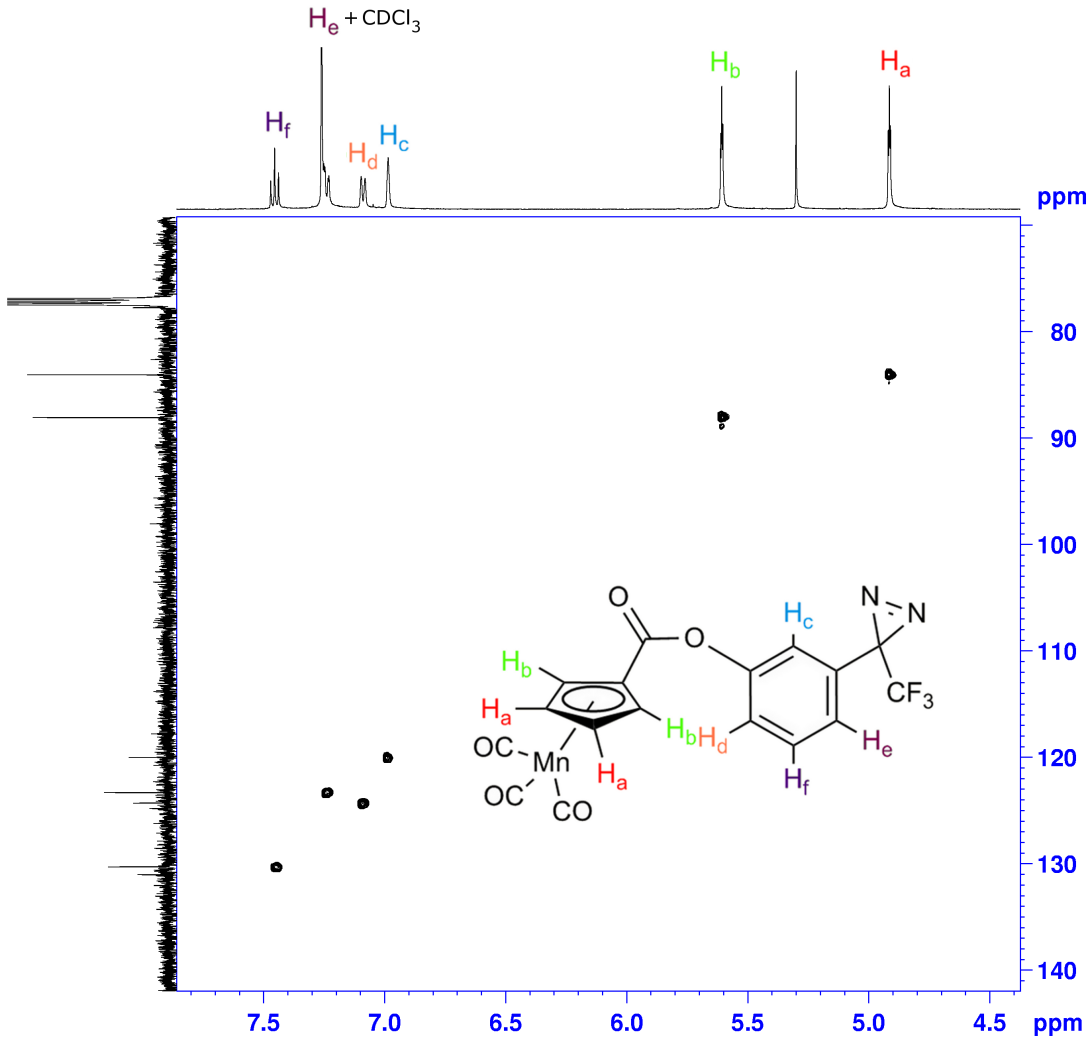

Figure 5.7. HSQC ^{13}C and ^{1H} NMR of **28**

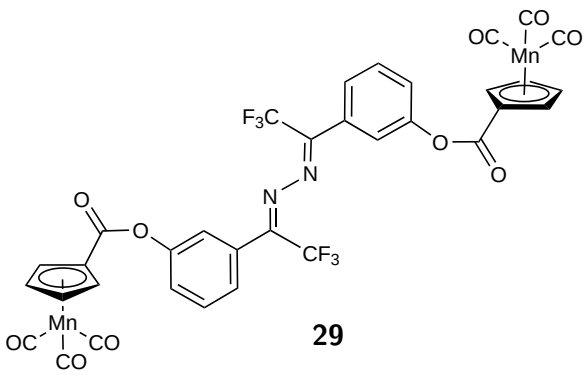

29

Figure 5.8. Azine formed upon photochemical dimerisation of diazirine

5.2.3.1. Crystallographic analysis

A single crystal of **28** was obtained by evaporation of a petroleum ether dichloromethane mixture. The structure was collected and solved by Dr. Robin Blagg. The asymmetric unit contains one molecule of **28**. The structure confirms the presence of the diazirine moiety in the meta position of the phenyl ring. The intact cymantrene moiety is also confirmed, with three manganese carbonyl bonds observed. Of immediate note is the non-planarity of the cyclopentadienyl ring with the phenyl ring, they are offset by 68 °along the C8-C10 axis. We can presume from this observation that there is no conjugation throughout the whole system in the crystal structure. A comparison of bond lengths of cymantrene[15] and a 3-aryl-3-trifluoromethyl diazirine[16] from literature sources is summarised in table 5.1

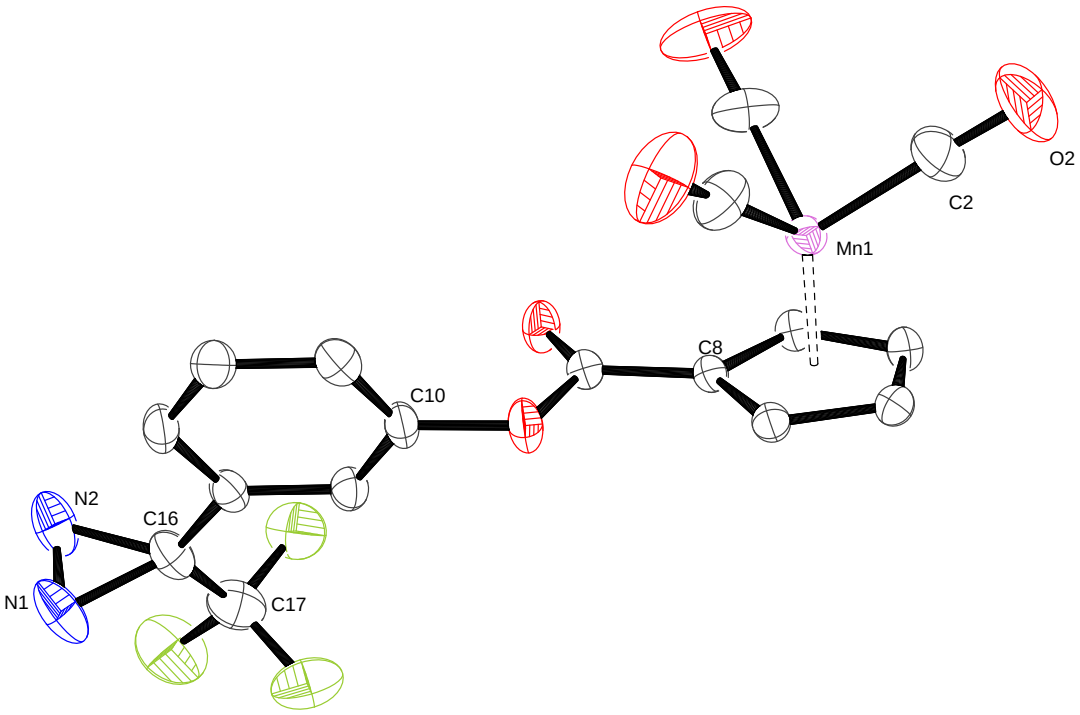

Figure 5.9. Molecular structure of **28**, Thermal ellipsoids shown at 50% probability level, Mean Mn-C (carbonyl) and Mn-C(cp) bond lengths are 1.793(3) and 2.138(15) Å, protons removed for clarity

Table 5.1. Bond lengths of **28**, cymantrene and 3-aryl-3trifluoromethyl diazirine

Bond	Cymantrene	Cymantrene diazirine **28**	3-aryl-3trifluoromethyl diazirine
Mn-C	1.799(6)	1.793(4)	-
C=O	1.154(1)	1.144(6)	-
N=N	-	1.232(3)	1.299(8)

Compound **28** was characterised by cyclic voltammetry, first in order to determine at what potential the surface bound oxidation will occur, and as an alternative method to determine the presence of the diazirine in the bulk sample from its reduction. Therefore the direct cyclic voltammetry of **28** was recorded in CH_2Cl_2 solvent with $[^nBu_4N][B(C_6F_5)_4]$ as the supporting electrolyte. Initially, the potential was scanned from 0 V vs Ag up to the anodic solvent window to determine the oxidation potential of **28**. The scanning direction was then reversed and the potential drawn up to the reductive solvent limit. Reassuringly, a reversible oxidation was observed at 1.17 V vs $Cp_2Fe^{0/+}$ (oxidation I/I' figure 5.10) which is assigned as the manganese centred oxidation and formation of the radical cation, as reported for the parent cymantrene and various derivatives..[12] In the cathodic region, a relatively poorly defined reduction is observed (reduction II, figure 5.10), which is assigned as the reduction of the diazirine moiety, from previous studies.[17] Multiple scans in this region cause passivation of the GCE, noticed from the diminishing peak current of the oxidation upon successive scans. Polishing the electrode and sonication in acetone and CH_2Cl_2 causes the oxidation to reappear. Scans limited in potential to only the oxidative region do not cause electrode passivation. The anodic voltammetry of

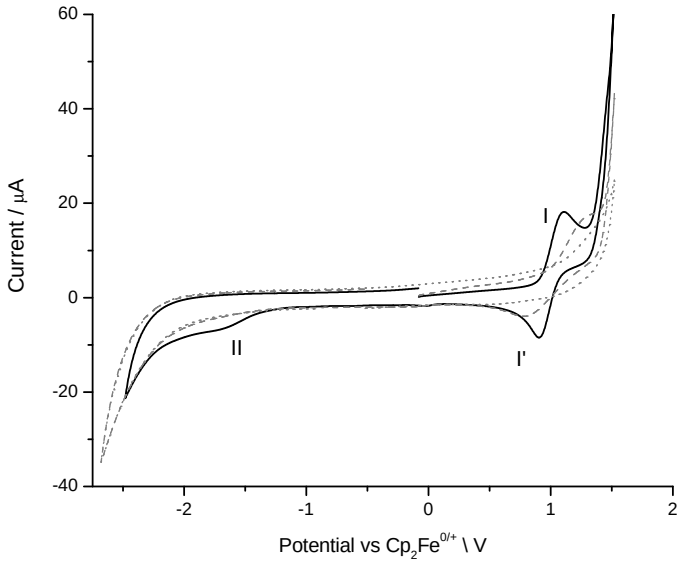

Figure 5.10. Full range cyclic voltammogram of **28** in CH_2Cl_2 (2.0 mmol dm^{-3}, 0.05 M $[^nBu_4N][B(C_6F_5)_4]$) at a scan rate of 100 mV s^{-1}, showing passivation effects upon subsequent scans into the cathodic region

28 is remarkably similar to that of the ester **23**, where a fully reversible wave is observed at

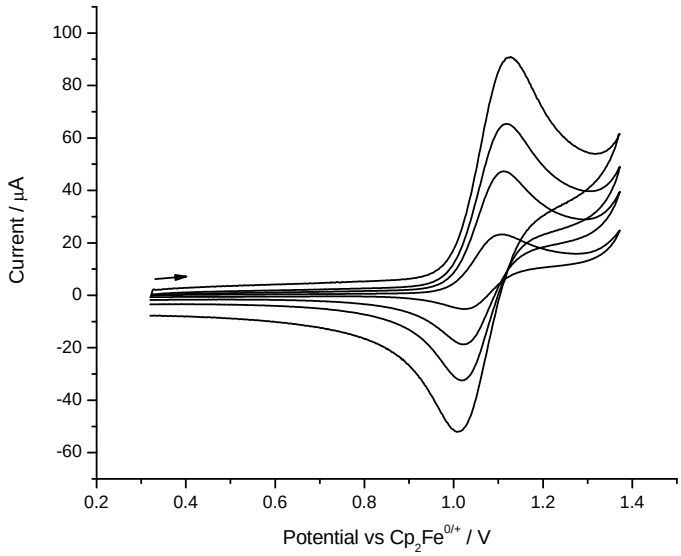

Figure 5.11. Cyclic voltammogram of **28** in CH_2Cl_2 (2.0 mmol dm^{-3}, 0.05 M [^{n}Bu$_4$N][B(C$_6$F$_5$)$_4$]) at scan rates of 100, 500, 1000 and 2000 mV s^{-1}

all scan rates recorded. No dimerisations or electrogenerated products are observed, indicating that the cymantrene radical cation does not attack the phenyl moiety intermolecularly.

5.3. Cyrhetrene derivatives

5.3.1. Cyrhetrene carboxylic acid

The cyrhetrene analogue of **24** was prepared using the same methodology as for the cymantrene, reassuringly with the same results. ^{1}H NMR spectroscopy showed two triplets, this time at a more downfield 6.01 and 5.37 ppm. In the IR spectrum, the stretches for the rhenium carbonyls and the carboxylic acid can be observed at 2028, 1912 and 1676 cm^{-1} respectively.

5.3.2. Cyrhetrene diazirine

The cyrhetrene analogue of **28** was prepared in the same way, with a Steglich esterification with **27**, in the presence of DCC and a catalytic amount of DMAP (figure 5.12). The yield was lower than with cymantrene, but this is likely due to the smaller scale the reaction was performed on. Full characterisation data for **30** was gathered.

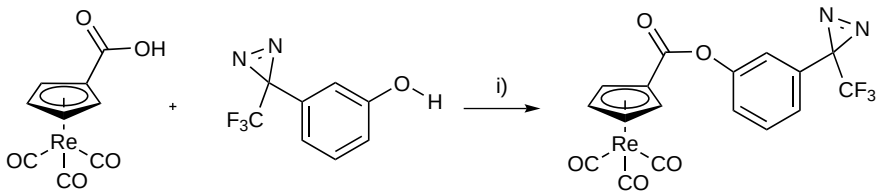

30

Figure 5.12. Reagents and conditions: i) DCC, DMAP, CH_2Cl_2, rt, 12h

Similarly to the manganese analogue **28**, the ^1H NMR shows the two cyclopentadienyl environments, and the multiplets associated with the phenyl moiety. COSY NMR shows the relationship between these environments (figure 5.13). The FTIR spectrum again shows the carbonyl stretches of the metal-carbonyl ligands and the carbonyl of the ester linkage at 2033, 1941 and 1745 cm^{-1} respectively.

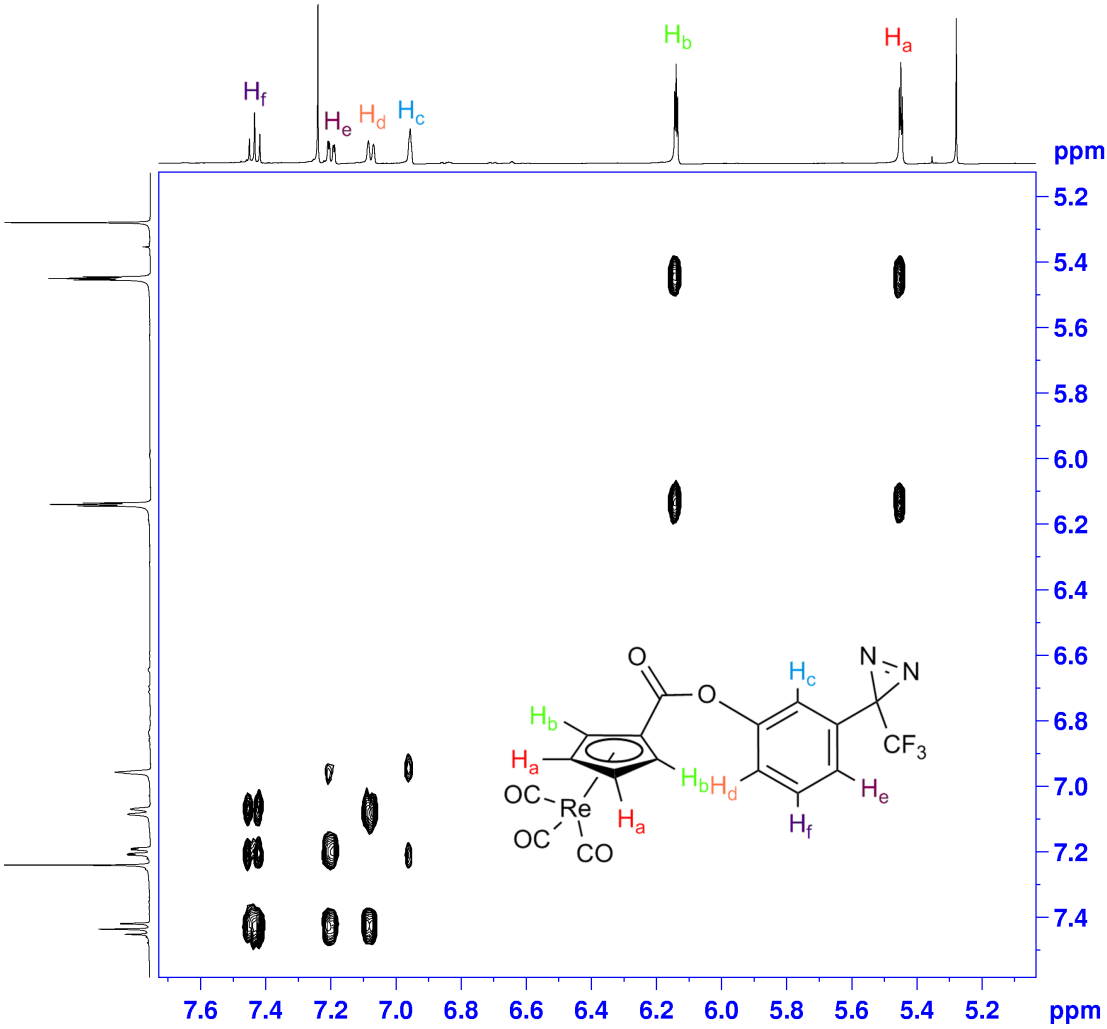

Figure 5.13. COSY NMR of compound **30**

5.3.3. Cyclic voltammetric characterisation

The solution phase cyclic voltammetry of **30** has, as expected large differences than that of the cymantrene containing **28**. An irreversible oxidation is observed at 1.27 V vs $Cp_2Fe^{0/+}$, and is assigned as the oxidation of cyrhetrene core to a radical cation. The chemically irreversible nature is likely due to the abstraction of a chloride from the CH_2Cl_2 solvent the voltammetry was recorded in. This behaviour is stongly suggestive of catalytic EC' mechanism whereby the solvent is the substrate. This is effect reduces the solvent window to the potential of complex **30**. This effect was seen with the parent cyrhetrene complex investigated by Geiger *et al.*.[18] A reduction wave is observed at ca. -1.7 V vs $Cp_2Fe^{0/+}$, and is assigned as the reduction of

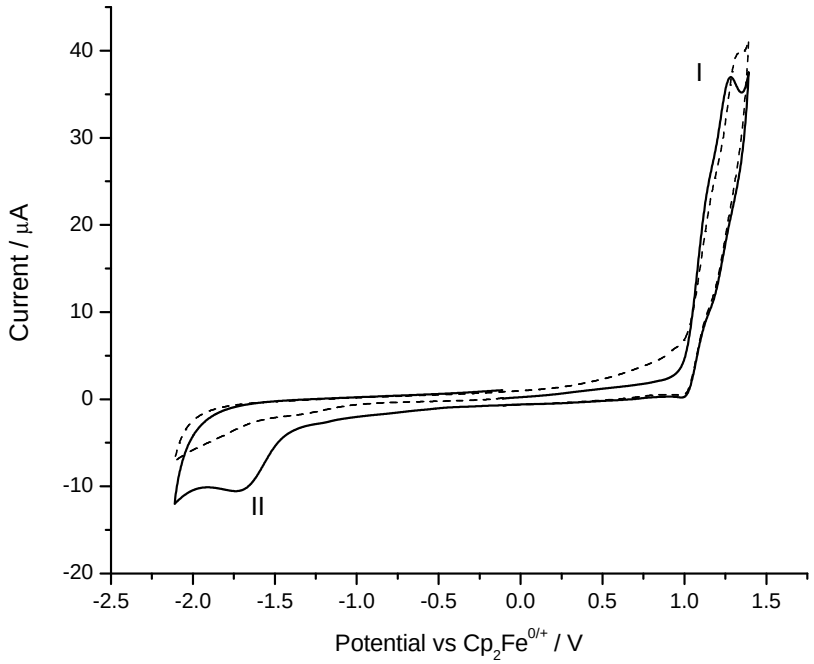

Figure 5.14. Full range cyclic voltammogram of **30** in CH_2Cl_2 (2.0 mmol dm^{-3}, 0.05 M [^{n}Bu$_4$N][B(C$_6$F$_5$)$_4$]) at a scan rate of 100 mV s^{-1}, showing the oxidation of the rhenium metal centre (oxidation I) and reduction of the diazirine moiety (reduction II), showing passivation upon scanning the cathodic region, (solid line): 1st scan, (dashed line): 2nd scan.

the diazirine moiety to a radical anion, as seen in the voltammetry of **28**, evidenced by the passivation observed upon including this region in the scan range.

5.4. Surface Bound Electrochemistry

5.4.1. Modification with cymantrene derivatives - diazirine method

Initially, to determine the efficacy of the diazirine modification method, the GCE modification was attempted directly. A solution of diazirine derivatised cymantrene **28** in CH_2Cl_2 was drop cast onto the electrode surface and the solvent left to evaporate. Once dry, the electrode, sealed under a N_2 atmosphere was treated with UV light for 1.5 hours at a distance of 5 cm from the light source and at 25 °C. Following this, the electrode was washed and sonicated in acetone and CH_2Cl_2. The cyclic voltammetry was then recorded in a cell of CH_2Cl_2 and [^{n}Bu$_4$N][B(C$_6$F$_5$)$_4$] with no solution phase analyte present.

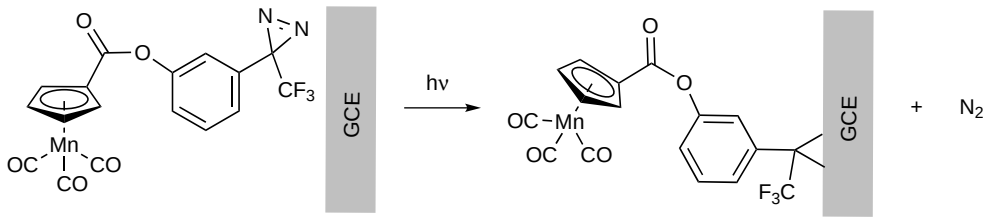

Figure 5.15. Modification of the GCE via diazirine photolysis

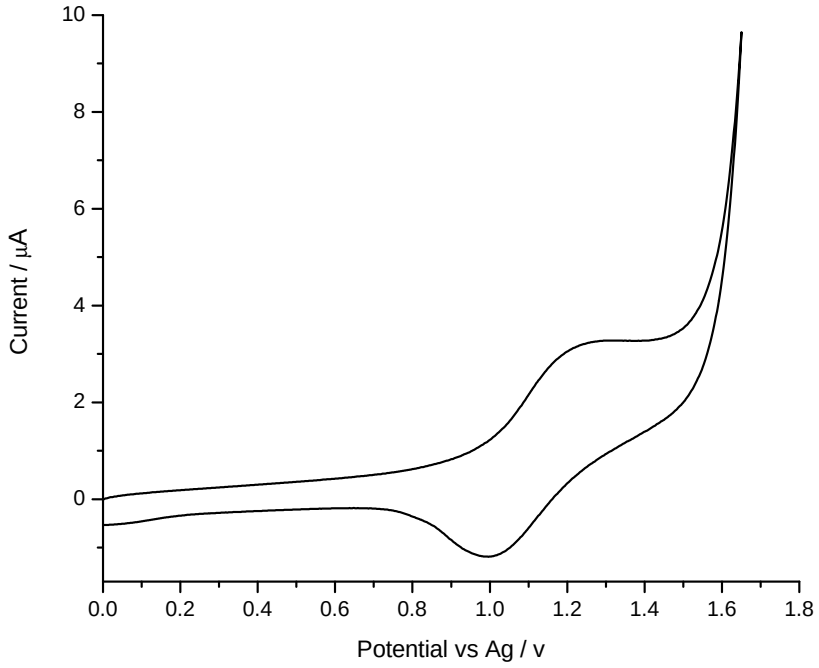

Figure 5.16. Cyclic voltammogram of surface bound **28** recorded at 100 mV s^{-1} in CH_2Cl_2 with [^{n}Bu$_4$N][B(C$_6$F$_5$)$_4$] as supporting electrolyte.

In the voltammetry of the electrode modified with **28**, a reversible oxidation was observed in an initial survey scan at 100 mV s^{-1}. To determine that this wave is surface bound, the wave was scanned at various scan rates, and the Randles-Sevcik relationship invoked. For a solution phase oxidation wave, the peak current is proportional to the square root of the scan rate (see equation 5.1)

$$i_{\mathrm{p}} = (2.69 \times 10^5) n^{3/2} A C D^{1/2} \nu^{1/2} \tag{5.1}$$

In an system with reversible electrode kinetics, the peak current of a surface bound wave is directly proportional to the scan rate. This is due to the non-diffusion controlled nature of the current associated with a Faradaic process occurring at a modified electrode. Analysis of

the peak current versus the scan rate behaviour exhibits a linear dependence confirming the surface bound nature of the redox process.

5.4.2. Characterisation with X-ray Photoelectron Spectroscopy

X-ray Photoelectron Spectroscopy (XPS) characterisation was performed on samples of graphite and hollow-tube MWCNTs that had undergone the same treatment, irradiation and work up process as the glassy carbon electrode, in order to reinforce the results from the cyclic voltammetry. The electron binding energies of fluorine and manganese were used as spectroscopic handles, as they are unique to the compound **28** used for surface modification. A survey spectrum was run for each material (CNT and graphite), followed by repeat scans over each region of interest. For both the ht-MWCNT and graphite sample, the survey scan showed peaks corresponding to C1s, F1s and O1s binding energies, with a signal corresponding to the Mn2p binding energy visible for the graphite sample. The F1s and Mn2p signals are good evidence for sucessful surface modification.The peak corresponding to the N1s binding energy would be expected at 400 eV,[19] but no signals are visible in this region of the survey spectrum indicating that any unreacted diazirine was washed off during the work up process. The peaks corresponding to the F1s and Mn2p binding energies were fitted with a mixed Gaussian Lorentzian function using a non-linear analysis.

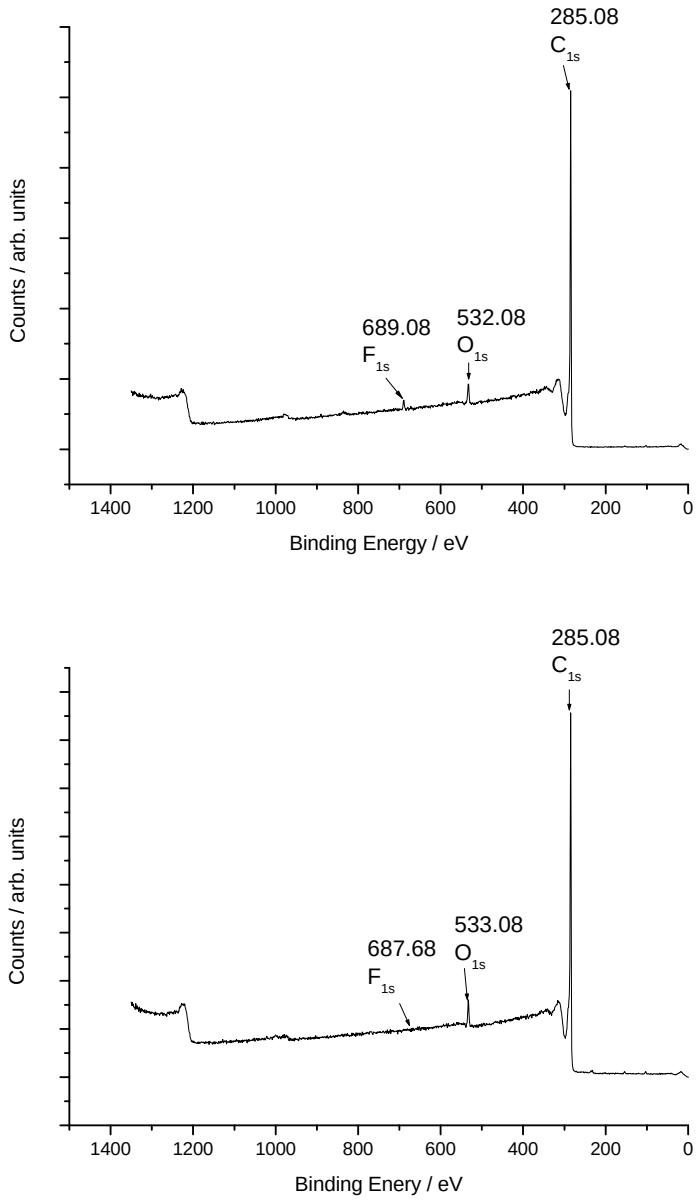

Figure 5.17. XPS survey spectra with signals from F 1s, O 1s and C 1s resulting from graphite (top) and hollow-tube MWCNT (bottom) modified with **28**

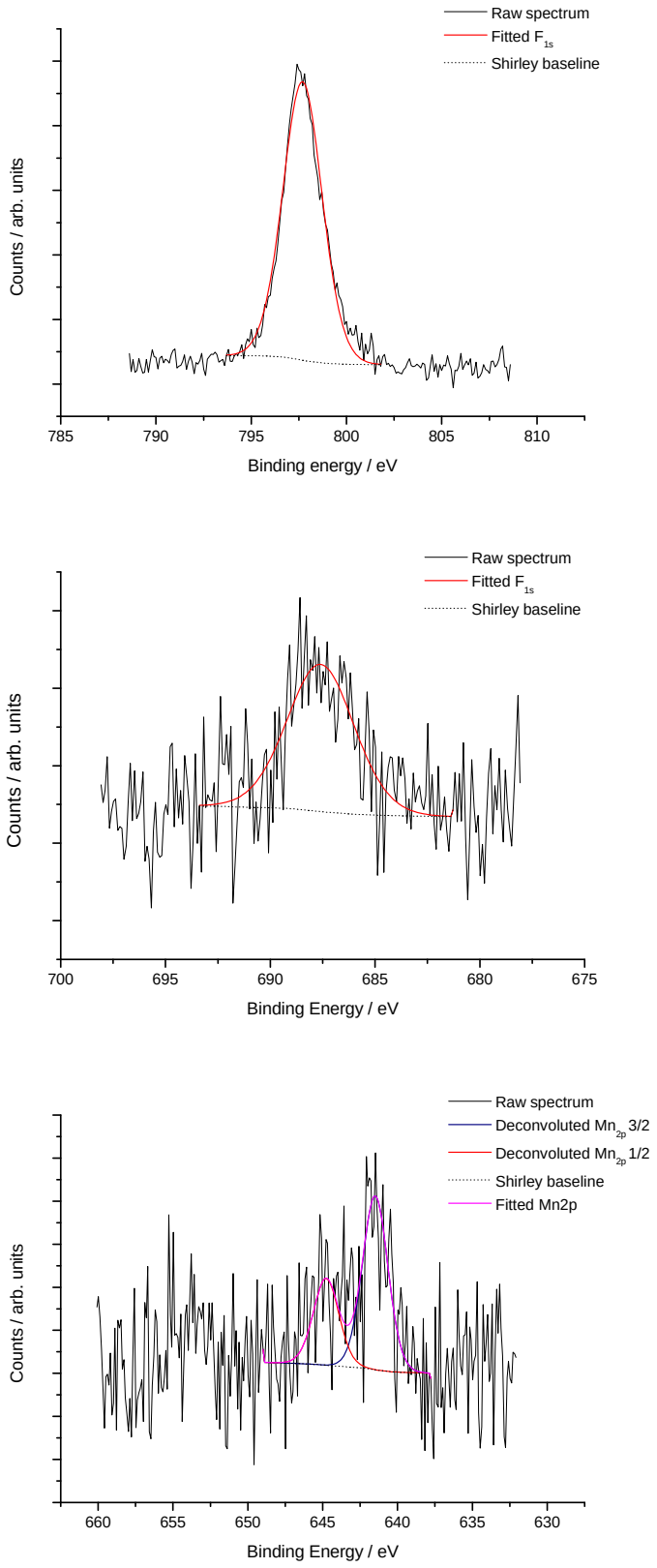

Figure 5.18. Peak fitted spectra showing the F1s signal region for (top left) graphite and (top right) MWCNTs. (Bottom) Deconvoluted Mn $2p_a$ and Mn $2p_b$ for graphite

5.4.3. Surface coverage estimation: carbene insertion method

Using the same method as in chapter4 the surface coverage achieved from irradiation of the diazirine derivatised cymantrene on the GCE can be estimated. At a scan rate (ν) of 100 mV s^{-1}, the peak area for the electrochemical oxidation for the diazirine modified GCE corresponds to a charge of 4.38 $\times 10^{-7}$ C. Using equation 4.1:

$$\Gamma = \frac{4.38 \times 10^{-7}}{96485 \times 0.064}$$
$$\Gamma = 7.09 \times 10^{-11} \text{mol cm}^{-2}$$

we find that the surface concentration is 7.09 $\times 10^{-11}$ mol cm^{-2}. To estimate the area that one surface bound cymantrene molecule would occupy (a_{max}) on the electrode surface, the parameters of the crystal structure were used. This value was determined to be 76 Å^2. The theoretical minimum surface concentration possible (Γ_{min}) can be estimated using Avogradro's number ($N_{\text{A}} = 6.0221 \times 10^{23}$).

$$\Gamma_{\text{min}} = \frac{1}{a_{\text{max}} \times 6.0221 \times 10^{23}}$$
$$\Gamma_{\text{min}} = \frac{1}{7.6 \times 10^{-19} \times 6.0221 \times 10^{23}}$$
$$\Gamma_{\text{min}} = 2 \times 10^{-10} \text{mol cm}^{-2}$$

Using equation 4.2, the fraction of surface coverage can then be calculated:

$$\Theta = \frac{7.09 \times 10^{-11}}{2 \times 10^{-10}}$$
$$\Theta = 0.35$$

Therefore from the data recorded, a 35 % coverage can be estimated.

5.4.4. Modification with cyrhetrene diazirine derivative

As described in section 5.3.2, cyrhetrene can be successfully derivatised with the diazirine moiety. Therefore compound **30** was prepared under the same conditions for that of **28**, except on a smaller scale. The product was characterised by multinuclear NMR, IR, UV vis and solution phase electrochemistry. A GCE was modified in the same manner as with the cymantrene diazirine (section 5.4.1); a solution of **30** was drop cast onto the electrode surface, left to evaporate and cured under UV light for 90 minutes. The electrode was then washed with acetone, and sonicated in acetone and CH_2Cl_2 for 3 minutes each. Cyclic voltammetry was then recorded in a solution of $[^nBu_4N][B(C_6F_5)_4]$ with no solution phase analyte present. As the oxidation of **30** in solution phase is close to the solvent limit of the $CH_2Cl_2/[^nBu_4N][B(C_6F_5)_4]$ system, a background scan before electrode modification was recorded, to allow the rhenium oxidation to be more easily observed. The result is a small irreversible wave apparent at a potential just less positive that the solvent window (figure 5.19). The resulting cyclic voltammogram is consistant with that of an EC' mechanism, where the cyrhetrene core is abstracting a chloride from the CH_2Cl_2 solvent.

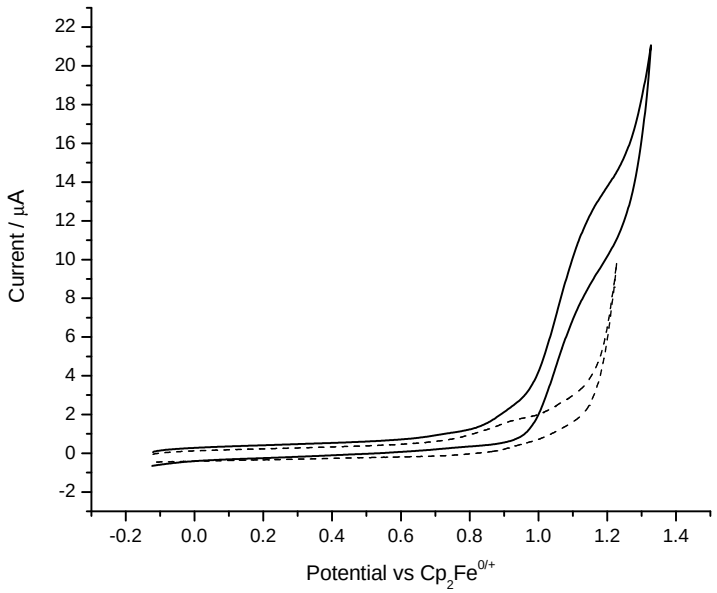

Figure 5.19. Cyclic voltammogram of a GCE in an analyte free solution of $[^nBu_4N][B(C_6F_5)_4]$, after irradiation with compound **30** drop cast onto the electrode surface, (dashed line): blank electrode, (solid line): modified electrode.

As Geiger has reported that the oxidised form of cyrhetrene will activate the C-H bond in cyclic alkenes, the voltammetry of the electrode treated with diazirine derivatised cyrhetrene was repeated with increasing concentrations of cyclopentene present in the cell. Interestingly, the oxidative current of the surface bound wave increases with the concentration of cyclopentene. This indicates that despite the surface bound rhenium abstracting a chloride from the solvent, the C-H activation can still occur. Excitingly, this demonstrates that the HOMER concept (heterogeneous organometallic electrocatalytic reactions) can be realised with the appropriate linker and organometallic species.

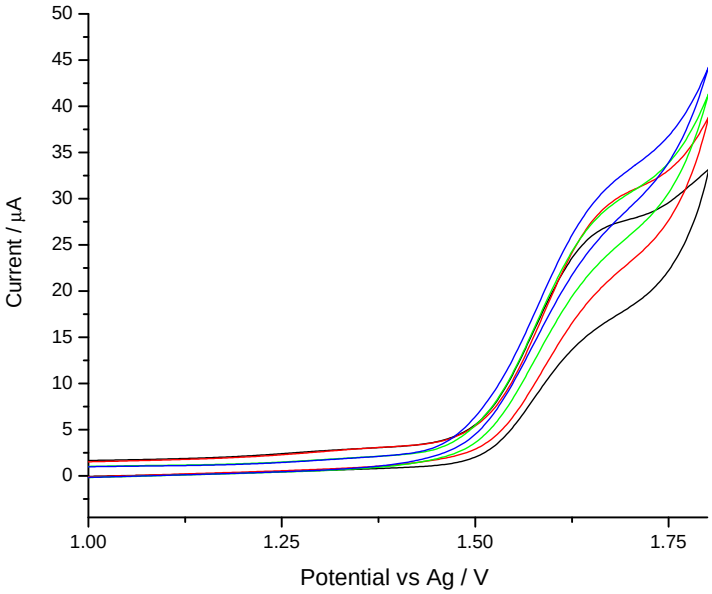

Figure 5.20. Responce of cyrhetrene diazirine treated electrode upon the presence of cyclopentene. Black: 0 mM, Red 0.5 mM, Green, 1.0 mM, Blue 2.0 mM C_5H_8

5.5. Characterisation with X-ray Photoelectron Spectroscopy

Graphite powder and hollow-tube MWCNTs modified with **30** were analysed by XPS, in order to reinforce the observed cyclic voltammetry. Fluorine and rhenium were used as the spectroscopic labels here, as they are unique to the modifying species. In the survey spectra on both graphite and MWCNTs, the F_{1s} signal is clearly visibile, indicating a surface bound trifluoromethyl group. Detalied scans showed the presence of signals corresponding to the Re_{4f} binding energy. Combined with the F_{1s} signal, this is strong evidence for a successful surface modification.

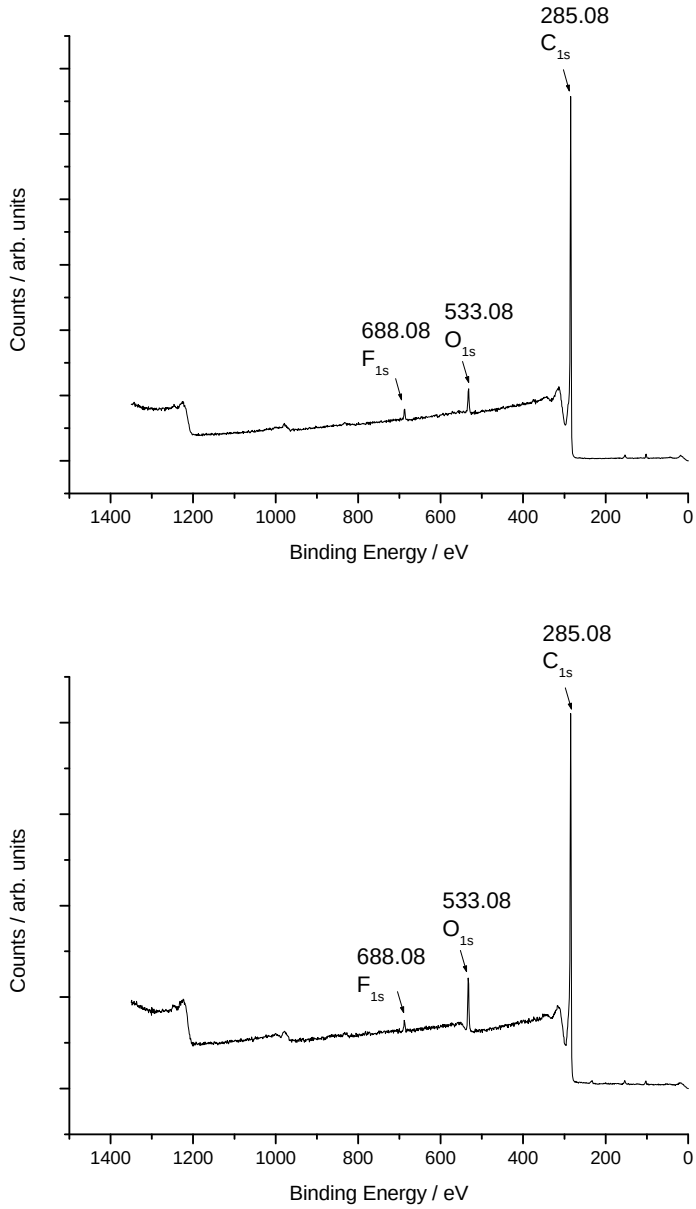

Figure 5.21. XPS survey spectra with signals from F 1s, O 1s and C 1s resulting from graphite (top) and hollow-tube MWCNT (bottom) modified with **30**

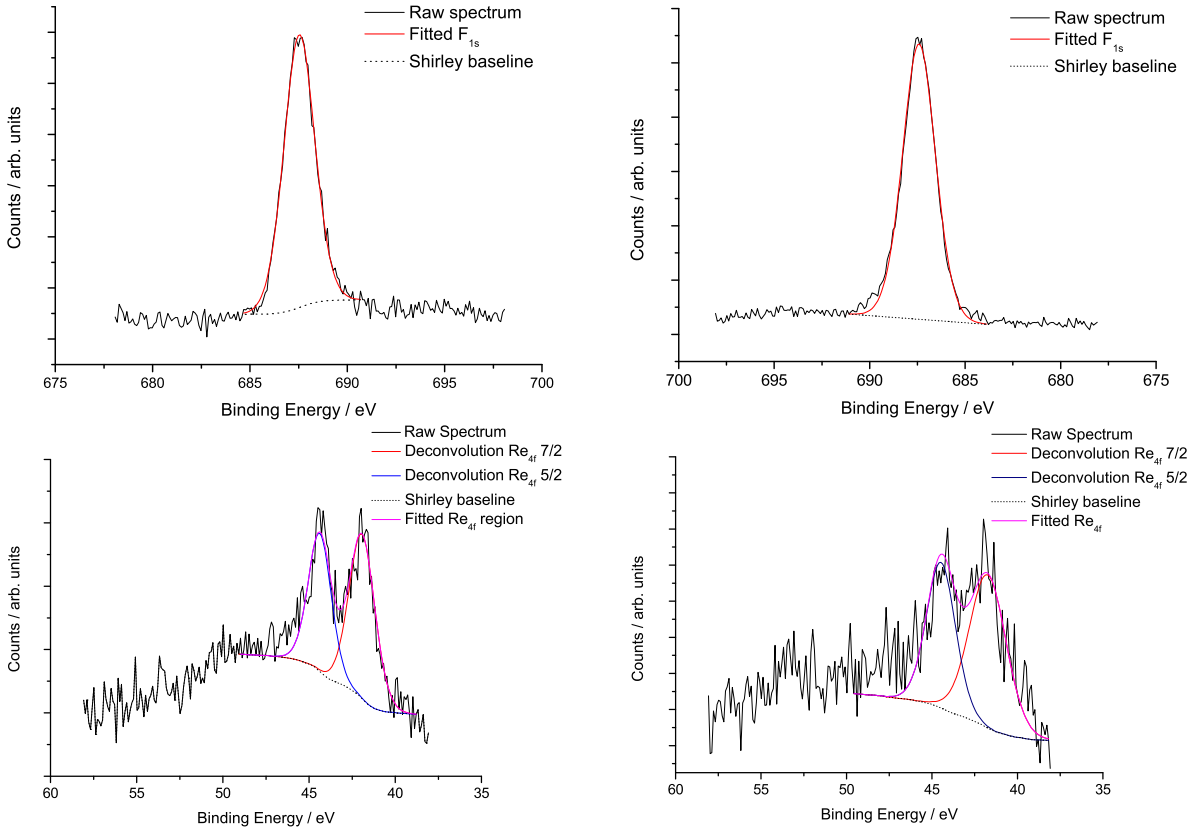

Figure 5.22. Peak fitted spectra showing the F1s signal region for (top) graphite and (middle) MWCNTs. (Bottom) Deconvoluted Re $4f_a$ and Re $4f_b$ for graphite

5.6. Conclusion

Diazirine derivatised cymantrene and cyrhetrene have been successfully prepared in good yields, and fully characterised. Cyclic voltammetry of the diazirine derivatised cymantrene shows a fully reversible oxidation at 1.17 V vs $Cp_2Fe^{0/+}$, similar to the parent cymantrene but influenced by the electron effect of the ester group. Upon treatment of a polished GCE with diazirine derivatised cymantrene **28** and irradiation, a partially reversible oxidation at ca. 1.1 V is observed in the voltammetry recorded in a solution containing only electrolyte, indicating a surface bound cymantrenyl species. This is supported by the presence of F_{1s} and Mn_{2p} peaks in the XPS survey spectra of graphite and CNTs. Cyrhetrene has been shown to activate C-H bonds in unactivated alkene substrates. Therefore the diazirine derivatised cyrhetrene **30** has been attached to a GCE surface using the same methodology. Successful surface attachment is shown by a clear EC' mechanism visible in the cyclic voltammetry, which is interpreted as the reaction of the cyrhetrene radical cation abstracting a chloride from the CH_2Cl_2 solvent.

Surface attachment is supported by XPS analysis, where F_{1s} and Re_{4f} peaks are observed. Interestingly, the oxidative current increases with addition of cyclopentene, showing that the cyrhetrene core can activate C-H bonds while surface bound. This is the realisation of the HOMER concept

References

(1) M. T. H. Liu, *Chem. Soc. Rev.*, 1982, **11**, 127–140.

(2) A. Blencowe, K. Cosstick and W. Hayes, *New J. Chem.*, 2006, **30**, 53.

(3) R. F. R. Church and M. J. Weiss, *J. Org. Chem.*, 1970, **35**, 2465–2471.

(4) E. Schmitz, D. Habisch and A. Stark, 1963, **2**, 548–548.

(5) W. H. Graham, *J. Am. Chem. Soc.*, 1962, **84**, 1063–1064.

(6) W. H. Graham, *J. Am. Chem. Soc.*, 1965, **87**, 4396–4397.

(7) H. M. Frey and A. W. Scaplehorn, *J. Chem. Soc. A*, 1966, 968–970.

(8) M. G. Rosenberg and U. H. Brinker, *J. Org. Chem.*, 2003, **68**, 4819–4832.

(9) J. Brunner, H. Senn and F. M. Richards, *J. Biol. Chem.*, 1980, **255**, 3313–3318.

(10) A. Blencowe and W. Hayes, *Soft Matter*, 2005, **1**, 178–205.

(11) J. Randles, *Trans. Faraday. Soc.*, 1948, **44**, 327.

(12) D. R. Laws, D. Chong, K. Nash, A. L. Rheingold and W. E. Geiger, *J. Am. Chem. Soc.*, 2008, **130**, 9859–9870.

(13) M. Schlosser, *Pure Appl. Chem.*, 1988, **60**, 1627–1634.

(14) S. K. Richardson and R. J. Ife, *J. Chem. Soc., Perkin Trans. 1*, 1989, 1172–1174.

(15) L. J. Farrugia, C. Evans, D. Lentz and M. Roemer, *J. Am. Chem. Soc.*, 2009, **131**, 1251–1268.

(16) D. H. R. Barton, J. C. Jaszberenyi, E. A. Theodorakis and J. H. Reibenspies, *J. Am. Chem. Soc.*, 1993, **115**, 8050–8059.

(17) E. J. Lawrence, G. G. Wildgoose, L. Aldous, Y. A. Wu, J. H. Warner, R. G. Compton and P. D. McNaughter, *Chem. Mater.*, 2011, **23**, 3740–3751.

(18) D. Chong, D. R. Laws, A. Nafady, P. J. Costa, A. L. Rheingold, M. J. Calhorda and W. E. Geiger, *J. Am. Chem. Soc.*, 2008, **130**, 2692–2703.

(19) *National Institute of Standards and Technology (NIST), http://srdata.nist.gov/xps/.*

6. Conclusion

In conclusion, the work in this thesis has shown the power of organometallic electrochemistry to address a variety of problems beyond simply measuring redox potentials versus ferrocene. We have taken advantage of electrochemisty to determine the reaction pathway that occurs upon the reduction of a series of gold(III) pincer complexes. This indicated the formation of a gold(II) homobimetallic dimer, confirmed by cyclic voltammetric analysis of an authentic sample of the gold(II) dimer. We present the first example of experimental determination of the gold(II)-gold(II) bond energy of the dimer, by construction of a Hess cycle using the standard electrochemical redox potentials for the gold(III) hydride, hydroxide, dimer and water. This analysis agrees with results from DFT calculations, indicating the power of mechanistic electrochemistry.

We have shown that organometallic electrochemistry can be applied even where the central metal is redox-inactive. The redox non-innocence of a series of Zn(II) complexes containing (bis)formazanate ligands was investigated by cyclic voltammetry, determining that the ligand can exist in three oxidation states. This result coupled with full characterisation of the chemically reduced compounds has shown the potential for formazante ligands to be employed as electron reserviours in catalytic reactions.

In this work we have developed a number of redox active organometallic systems that can be surface bound to a carbon electrode via an organic linker. Formation of an phenylaniline substituted triazole moeity on the cyclopentadienyl ring of group VII 'piano stool' complexes allows surface attachment via reduction of the diazonium salt. Detalied mechanistic information derived from cyclic voltammetric studies of triazole substituted piano stool complexes has shown that the redox active nature of the triazole makes application to electrocatalytic reactions difficult. By instead utilising a photoactivated carbene insertion

method by preparation of diazirine derivatised sandwhich complexes, we have achieved a surface bound rhenium based system that shows promise as a heterogeneous electrocatalyst.

7. Methods and Materials

7.1. General Considerations

All synthetic reactions and manipulations were performed under a dry N_2 atmosphere (BOC Gases) using either an MBraun glovebox or standard Schlenk-line techniques on a dual manifold vacuum/inert gas line. All glassware was dried under vacuum at 170 °C before use. Diethyl ether and light petroleum either were dried via reflux over Na/benzophenone diketyl, dichloromethane was dried via distillation over CaH_2, and collected by distillation. All solvents were sparged with nitrogen gas to remove any trace of dissolved oxygen and stored in ampoules over activated 3 Å molecular sieves. Bromopentafluorobenzene was purchased from Fluorochem and used without further purification. Mg turnings were purchased from Alfa Aesar and used as supplied. All other reagents were purchased from SigmaAldrich and were of the highest grade available and used without further purification. Deuterated NMR solvents ($CDCl_3$, 99.8%; CD_2Cl_2, 99.9%, C_6D_6, 99.9%) were purchased from Cambridge Isotope Laboratories Inc. and were dried over P_4O_{10}, degassed using a triple freeze–pump–thaw cycle and stored over activated 3 Å molecular sieves. NMR spectra were recorded using a Bruker Advance DPX-300 MHz spectrometer. Chemical shifts are reported in ppm and are referenced relative to residual solvent peaks.

7.2. X-ray Crystallography

Single crystals of **13** and **15** were grown by slow evaporation of a 1:1 CH_2Cl_2/petroleum ether solution of the compound. Single crystals of **28** were grown by slow evaporation of a 2:1 petroleum ether/acetone solution of the compound. Single crystals of **15** were grown by slow evaporation of a 7:1 petroleum ether/acetone solution of the compound. Suitable crystals of

13, **15** and **28** were selected, encapsulated in a viscous perfluoropolyether and mounted on an Agilent Technologies Xcaliber-3 single crystal X-ray diffractometer using Mo Kαradiation (λ= 0.71073 Å) where the crystals were cooled to 140 K during data collection and a full sphere of data collected. The data was reduced and an absorption correction performed using Agilent Technologies CrysAlisPro.[1] The crystal data for **20** was collected, absorption corrected and reduced at the EPSRC national crystallographic service.

Using Olex2,[2] the structure of **28** and **20** was solved and space group assigned with SuperFlip/EDMA[3,4] using charge flipping, and then refined with the ShelXL-2013/4[5] refinement program using least squares minimisation.

Using WinGX[6,7] the structure of **13** and **15** was solved and space group assigned with ShelXS-97[5] using direct methods, and then refined with the ShelXL-97[5] refinement progam using least squares minimisation.

7.3. Electrochemistry

All electrochemical measurements were performed under an inert atmosphere using an Autolab PGSTAT 302N computer-controlled potentiostat. Cyclic voltammetry (CV) was performed using a three-electrode configuration comprising of a Pt wire counter electrode (GoodFellow, Cambridge, UK; 99.99 %), a Ag wire pseudoreference electrode (GoodFellow, Cambridge, UK; 99.99 %) and either a glassy carbon (GC) macrodisk working electrode (Bioanalytical Systems, Indiana, USA; 3 mm diameter) or a Pt microdisk working electrode (GoodFellow, Cambridge, UK; 99.99 %; radius 19.0 ± 0.5 µm. The GC working electrode was polished between experiments using successively fine grades of diamond slurry (3-0.25 µm), rinsed in ethanol and subjected to brief ultrasonication to remove any adhered diamond particles. The Pt working electrode was polished between experiments using alumina slurry (0.3 µm), rinsed in distilled water and subjected to brief ultrasonication to remove any adhered alumina microparticles. The electrodes were then dried in an oven at 120 °C to remove any residual traces of water. The working electrode area was calibrated before each experiment using a 5.0 mmolsolution of ferrocene in CH_3CN solvent containing 0.1 M $[^nBu_4N][PF_6]$ as the supporting electrolyte. The GC macrodisk working electrode area was accurately determined by construction of a Randles–Sevcik plot of peak current vs. the square root of the voltage scan

rate obtained from cyclic voltammograms recorded at varying scan rates from 50 to 750 $mV\,s^{-1}$. The Pt microdisk working electrode area was accurately determined using the steady–state current measured using linear sweep voltammetry (scan rate = $mV\,s^{-1}$).[8] The Ag wire pseudo–reference electrode was calibrated to the ferrocene/ferrocenium couple in CH_2Cl_2 at the end of each run to allow for any gradual drift in potential, following IUPAC recommendations.[9] All electrochemical measurements were performed at ambient temperatures under an inert N_2 atmosphere in CH_2Cl_2 containing 0.05 mol$[^nBu_4N][B(C_6F_5)_4]$ as the supporting electrolyte, and iR-compensated using positive-feedback to within 85 $\pm$ 5% of the uncompensated solution resistance. The electrolyte precursor $[Li(OEt_2)_n][B(C_6F_5)_4]$[10] and the weakly coordinating electrolyte $[^nBu_4N][B(C_6F_5)_4]$[11] were prepared by literature methods. Data were recorded with Autolab NOVA software. CV simulations were performed using DigiElch – Professional (v 7.030) software.

7.3.1. 2,2,2-Trifluoro-1-(3-methoxyphenyl)ethanone

3-bromoanisol (5.0 g, 26.9 mmol) was dissolved in dry degassed THF (150 mL) to give a clear colourless solution. The solution was cooled to -78 °C and *n*-BuLi (17 mL, 27.2 mmol) was added drop-wise, causing the solution became turbid white. After 5 minutes N,N-diethyltrifluoroacetamide (5.0 g, 26.9 mmol) was added drop-wise, giving a pale yellow turbid solution. The mixture was left to stir for 2 h at -78°C, after which it become clear orange. Saturated NH_4Cl (50 mL) was added with vigorous stirring for 1 h to give a green solution that effervesced. The mixture was then extracted withEt_2O (3 x 100 mL), with the organic phase dried over magnesium sulfate. Removal of the solvent under reduced pressure gave a yellow oil of low viscosity (5.28 g, 97 %). ^1H NMR (400 MHz, $CDCl_3$ δ 7.67 (m, 1H), 7.57 (s, 1H), 7.46 (t, J = 8.4 Hz, 1H), 7.28 (m, 2H), 3.88 (s, 3H)

7.3.2. 2,2,2-Trifluoro-1-(3-methoxyphenyl)ethanone oxime

2,2,2-Trifluoro-1-(3-methoxyphenyl)ethanone (5.6 g, 27.43 mmol) was dissolved in degassed ethanol to give a yellow solution. Hydroxylamine hydrogen chloride (4.01 g, 57.7 mmol) was added and the mixture set to reflux at 78 °C for 2 hours, after which NaOH solution (4 $mol\,dm^{-3}$, 12.5 mL) was added. This caused the solution to become turbid. After further

reflux for 1.5 hours, the ethanol was removed under reduced pressure and the residue taken up in water (100 mL). This was extracted with Et_2O (3 x 150 mL) with the combined extracts washed with HCl (0.25 mol dm^{-3}, 200 mL) and water. The organic phase was dried over magnesium sulfate and the solvent removed under reduced pressure to yield the desired product as a yellow oil. (5.30 g, 88 %) ^{1}H NMR (300 MHz, $CDCl_3$) δ8.84 (s, 1H), 7.38 (m, 1H), 7.02 (m, 3H), 3.83 (s, 3H). ^{19}F NMR (282 MHz, $CDCl_3$) δ-66.8 (s, 3F)

7.3.3. O-Tosyl-2,2,2-trifluoro-1-(3-methoxyphenyl)ethanone oxime

2,2,2-Trifluoro-1-(3-methoxyphenyl)ethanone oxime (5.3 g), DMAP (23 mg), *p*-toluene sulfonylchloride (4.63 g,) and triethylamine (5.1 mL,) were dissolved in dry degassed CH_2Cl_2 (100 mL). The resulting mixture was left to stir in the dark for 48 hours. The reaction mixture was then washed with water (2 x 150 mL) and HCl (0.25 mol dm^{-3}, 2 x 150 mL). The combined aqueous layers were extracted with CH_2Cl_2 (2 x 100 mL) and the resulting organic solution washed with saturated sodium hydrogen carbonate solution and dried over magnesium sulfate. The solvent was removed under reduced pressure to give the desired product as a pale yellow solid (6.9 g, 76 %) ^{1}H NMR (400 MHz, $CDCl_3$ δ 7.87 (m, 2H), 7.36 (m, 3H), 7.04 (m, 1H), 6.92 (m, 1H), 6.86 (m, 1H), 3.30 (s, 3H), 2.46 (s, 3H). $CDCl_3$) δ-66.91 (s, 3F)

7.3.4. 3-(Trifluoromethyl)-3-(3-methoxyphenyl)diaziridine

Ammonia (50 mL) was condensed in flask immersed in liquid nitrogen. o-Tosyl-2,2,2-trifluoro-1-(3-methoxyphenyl)ethanone oxime (5.3 g, 14.2 mmol) was dissolved in dry degassed CH_2Cl_2 (20 mL) to give a yellow solution, which was cooled to -78 °C and added drop-wise to the liquid ammonia to give a grey suspension, which turned yellow over time. The solution was left to stir for 16 hours in the dark. Water (100 mL) and CH_2Cl_2 (50 mL) were added and the mixture was left to stir for 2 hours. The aqueous phase was extracted CH_2Cl_2 (3 x 100 mL) and the combined organic phases were dried over magnesium sulfate. The solvent was removed under reduced pressure to give the desired product as a yellow oil of low viscosity. (2.96 g, 96 %) ^{1}H NMR (300 MHz, $CDCl_3$) δ7.35 (t, J = 7.9 Hz, 1H), 7.21 (m, 1H), 7.16 (m, 1H), 7.00 (m, 1H), 3.82 (s, 3H), 2.79 (d, 1H), 2.25 (d, 1H). ^{19}F NMR (282 MHz, $CDCl_3$) δ-75.5 (s, 3F)

7.3.5. 3-(Trifluoromethyl)-3-(3-methoxyphenyl)diazirine

Oxalyl chloride (0.42 mL, 5.0 mmol) was dissolved in CH_2Cl_2 (20 mL) and the solution cooled to -78 °C. After 5 minutes stirring, DMSO (0.38 mL, 5.48 mmol) was added and the mixture stirred for a further 5 minutes, after which 3-(Trifluoromethyl)-3-(3-methoxyphenyl)diaziridine (1.0 g, 4.58 mmol) was added as a solution in CH_2Cl_2 (5 mL). The solution became yellow and after 15 minutes stirring, triethylamine (3.19 mL, 22.9 mmol) was added. The mixture was left to stir for 1.5 hours, then quenched with water. The organic phase was separated and the aqueous phase extracted with CH_2Cl_2 (50 mL). The combined organic phases were dried over magnesium sulfate and filtered through celite. Removal of solvent under reduced pressure gave the desired product as a yellow oil (0.940 g, 94 %) ^{1}H NMR (300 MHz, $CDCl_3$) δ7.23 (t, J = 8.0 Hz, 1H), 6.87 (m, 1H) 6.69 (m, 1H) 6.61 (m,1H) 3.72 (s, 3H) ^{19}F NMR (282 MHz, $CDCl_3$) δ-65.17 (s, 3F)

7.3.6. 3-(Trifluoromethyl)-3-(3-hydroxyphenyl)diazirine

3-(Trifluoromethyl)-3-(3-methoxyphenyl)diazirine (0.50 g) was dissolved in degassed and anhydrous DCM (30 mL) to give an pale yellow solution. 1 mol dm^{-3} BBr_3 in CH_2Cl_2 (12 mL, 7.8 mmol) was added over 5 minutes to give a dark orange solution which was stirred in the dark at room temperature for 20 hours. Water (30 mL) was added to the reaction mixture followed by CH_2Cl_2 (30 mL), and the mixture was allowed to stir for 1 hour. The organic phase was extracted and the aqueous phase washed with DCM (3 x 50 mL). The combined organic layers were dried using anhydrous magnesium sulfate, filtered and concentrated in vacuo to give the title compound (0.432 g) as an orange oil in (94 % yield). UV-Vis (MeOH) λ345 nm. νmax (oil)/ cm^{-1} 3400 (broad), 2871, 2552, 1711, 1647, 1588, 1465, 1399, 1345, 1274, 1202, 1154, 835, 782. ^{1}H NMR (400 MHz,$CDCl_3$) δ7.27 (t, J = 8 Hz, 1 H), 6.88 (m, 1H), 6.74 (m, 1H), 6.67 (m, 1H), 5.05 (s, 1H). ^{19}F NMR (282 MHz, $CDCl_3$) δ-65.1 (s, 3F).

7.3.7. Cymantrene azide $CymN_3$ 12

To a solution of cyclopentadienylmanganese tricarbonyl 1 (1.0 g, 4.9 mmol) in 50 mL of THF at -78°C was added 1.6 M solution of *n*-BuLi in hexanes (3.1 mL, 4.9 mmol), and the reaction mixture left to stir at -78°C for 2 h. A solution of *p*-toluenesulfonylazide (1.0 g,

4.9 mmol) dissolved in THF (50 mL) was then added via cannula dropwise to the stirred solution over a period of 10 minutes. The resultant orange solution was allowed to warm to room temperature for 13 h in the dark. Removal of remaining solvents under reduced pressure afforded the thermally unstable cymantrenyl azide **12** as a light brown solid (0.78 g, 65%), which was used without further purification. FT-IR (ATR) ν_{max} (oil)/ cm^{-1} 2120 (ν_{NN}), 2016 (ν_{CO}), 1910 (ν_{CO}). ^{1}H NMR (500 MHz,CD_2Cl_2): δ4.67 (t, 2H, J = 2 Hz), 4.74 (t, 2H, J = 2 Hz). ^{13}C NMR (500 MHz,CD_2Cl_2): δ72.9, 80.4, 116.8.

7.3.8. Cyrhetrene azide, $CyrN_3$ 19

To a solution of cyclopentadienylrhenium tricarbonyl 1 (1.0 g, 3.0 mmol) in 50 mL of THF at -78°C was added 1.6 M solution of *n*-BuLi in hexanes (1.9 mL, 3.0 mmol), and the reaction mixture left to stir at -78°C for 2 h. A solution of *p*-toluenesulfonylazide (0.6 g, 3.0 mmol) dissolved in THF (50 mL) was then added via cannula dropwise to the stirred solution over a period of 10 minutes. The resultant orange solution was allowed to warm to room temperature for 13 h in the dark. Removal of remaining solvents under reduced pressure afforded the thermally unstable cyhretrene azide **19** as a brown solid. Purification by silica gel column chromatography with light petroleum ether/acetone yielded the product as an off white solid. (0.8 g, 71%) FT-IR (ATR) ν_{max} (oil)/ cm^{-1} 3121, 2963, 2125 (ν_{NN}), 2019 (ν_{CO}), 1907 (ν_{CO}), 1468, 1282, 813. ^{1}H NMR (500 MHz,$CDCl_3$): δ5.23 (t, 2H, J = 2 Hz), 5.33 (t, 2H, J = 2 Hz). ^{13}C NMR (500 MHz,$CDCl_3$): δ73.5, 81.7, 119.4, 193.0

7.4. Synthesis of cymantrene derivatives

7.4.1. η^5-methylcarboxylate cyclopentadienyl tricarbonyl manganese(I) 23

A solution of cymantrene (0.5 g, 2.4 mmol) and potassium *tert* butoxide (33.0 mg, 0.16 mmol) was dissolved in THF (150 ml) was cooled to -78 °C, after which *tert*-butyllithium (3.03 ml, x mmol) was added. The resulting deep red solution was left stirring for 1 hour at -78 °C, then transferred by cannula to a solution of methyl chloroformate (0.8 ml, 9.8 mmol) in THF at -78 °C.The mixture was slowly warmed to room temperature to give a dark red solution, which was quenched with a drop of distilled water. The solvent was removed under reduced pressure and the residue taken up in diethyl ether, washed with water and dried over magnesium sulfate.

Removal of the solvent yields the product as a red oil, which affords pure product as yellow crystals upon recrystallisation from petroleum ether. (0.420 g, 65 %) FT-IR (ATR) ν_{max} / cm^{-1} 2959, 2024 (ν_{CO}), 1919 (ν_{CO}), 1719 ($\nu_{C=OOMe}$) ^{1}H NMR (500 MHz,$CDCl_3$) δ5.46 (t, J = 2.3 Hz, 2H) 4.80 (t, J = 2.3 Hz, 2H) 3.81 (s, 3 H) ^{13}C NMR (125 MHz, $CDCl_3$): δ 87.48, 83.34, 52.37

7.4.2. η^5-[carboxyl]cyclopentadienyl tricarbonyl manganese(I) 24 - method I

Cymantrene methyl ester (150 mg, 0.57 mmol) was dissolved in ethanolic potassium hydride solution (5 gin 100 ml, 2.5 mol dm^{-3}) and held at reflux for 1 hour. All volatiles were removed and the residue taken up in water, which was neutralised with HCl (200 ml, 0.25 mol dm^{-3}). The aqueous phase was extracted with diethyl ether (3 x 150 ml) and the organic layers combined and dried over magnesium sulfate. The solvent was removed under reduced pressure to give the desired product as a yellow powder. (136 mg, 96 %) FT-IR (ATR) ν_{max} / cm^{-1} 3626, 3544, 2030 (ν_{CO}, 1946 (ν_{CO}), 1730 ($\nu_{C=OOH}$) ^{1}H NMR (500 MHz,$(CD_3)_2CO$) δ5.59 (m, 2H) 5.23 (m , 2H) ^{13}C NMR (125 MHz), $(CD_3)_2CO$: δ 84.49, 83.43

7.4.3. η^5-[carboxyl]cyclopentadienyl tricarbonyl manganese(I) 24 method II

A solution of cymantrene (0.345 g, 1.68 mmol) and potassium *tert* butoxide (22.0 mg, 0.2 mmol) was dissolved in THF (100ml) was cooled to -78 °C, after which *tert*-butyllithium (1.27 ml, 2.02 mmol) was added. The resulting deep red solution was left stirring for 1 hour at -78 °C. Carbon dioxide was introduced through a cannula and drying column from the sublimation of dry ice. The solution became pale yellow instantly, with CO_2(g) bubble through the solution for a further 5 minutes. The solution was then warmed to room temperature and the solvent removed under reduced pressure to give a pale yellow resiude. This was suspended in water and acidified with 0.1 mol dm^{-3} HCl causing a yellow solid to precipitate. The mixture was then extracted with Et_2O (3 x 50 ml) and dried over magnesium sulfate. (0.297 g, 70.8 %)

7.4.4. η^5-[4-phenyltriazol-1-yl]cyclopentadienyl tricarbonyl manganese(I) 13

To a solution of cymantrenyl azide (0.25 g, 1.0 mmol) in acetonitrile (10 ml) was added phenylacetylene (0.1 g, 1.0 mmol) and $Cu(OAc)_2 \cdot H_2O$ (0.02 g, 0.1 mmol) and stirred

at ambient temperature under a nitrogen atmosphere. Reaction progress was monitored by thin layer chromatography, and upon completion solvents were removed under reduced pressure. The residue was purified directly using silica gel flash column chromatography (petroleum ether 60/40: acetone, 15:2) yielding the title compound as a fine yellow solid. Slow recrystallization from petroleum ether:dichloromethane afforded single colourless plates (0.29 g, 83 %). ATR-FT-IR (ATR) ν_{max} cm^{-1} 3131, 2027 (ν_{NN} triazole), 1962, 1938 (ν_{CO}), 1919 (ν_{CO}), 1533, 1453, 1377, 1232. ^{1}H NMR (500 MHz, CD_2Cl_2): δ7.99 (s, 1H), 7.85 (d, 2H, J = 8 Hz), 7.47 (t, 2H, J = 8 Hz), 7.38 (t, 1H, J = 8 Hz), 5.48 (t, 2H, J = 2 Hz), 4.86 (t, 2H, J = 2Hz). ^{13}C NMR (125 MHz), CD_2Cl_2): δ 148.8, 130.3, 129.5 (2C), 129.2, 126.3 (2C), 118.9, 108.1, 80.8 (2C), 75.4 (2C). Anal. calcd for $C_{16}H_{10}MnN_3O_3$: C, 55.35; H, 2.90; N, 12.10; Found: C, 55.27; H, 3.05; N, 11.95. HRMS (ASAP):$[C_{16}H_{10}MnN_3O_3 + H]^+$ requires 348.0175; Found 348.0174 [M+H]+.

7.4.5. η^5-[4-(amino)-4-phenyltriazol-1-yl]cyclopentadienyl tricarbonyl manganese(I) 14

To a solution of cymantrenyl azide (0.76 g, 3.0 mmol) in acetonitrile (30 ml) was added 4-ethynylaniline (0.36 g, 3.0 mmol) and $Cu(OAc)_2 \cdot H_2O$ (0.06 g, 0.3 mmol) and stirred at ambient temperature under a nitrogen atmosphere. Reaction progress was monitored by thin layer chromatography, and upon completion solvents were removed under reduced pressure. The residue was purified directly using silica gel flash column chromatography (petroleum ether 60/40: acetone, 4:1) yielding 5 as a fine yellow powder (0.81 g, 75 %). FT-IR (ATR) ν_{max} / cm^{-1} 3364 (ν_{NH}), 3116, 2021 (ν_{NN} triazole), 1923 (ν_{CO}), 1619, 1498, 1171. 1H NMR (500 MHz, $CDCl_3$): δ7.77 (s, 1H), 7.65 (s, 2H), 6.75 (s, 2H), 5.41 (s, 2H), 4.80 (s, 2H), 3.82 (bs, 2H). 13C NMR (125 MHz,$CDCl_3$): δ 149.0, 147.2, 127.3 (2C), 120.0, 116.8, 115.4 (2C), 107.9, 80.0 (2C), 74.5 (2C). Anal. calcd for $C_{16}H_{11}MnN_4O_3$: C, 53.05; H, 3.06; N, 15.47; Found: C, 53.19; H, 2.97; N, 15.34. HRMS (ASAP):$[C_{16}H_{11}MnN_4O_3 + H]^+$ requires 363.0284; Found 363.0282 [M+H]+.

7.4.6. η^5-[3-(amino)-4-phenyltriazol-1-yl]cyclopentadienyl tricarbonyl manganese(I) 15

To a solution of cymantrenyl azide (0.20 g, 0.8 mmol) in acetonitrile (10 ml) was added 3-ethynylaniline (0.10 g, 0.8 ml) and $Cu(OAc)_2 \cdot H_2O$ (0.02 g, 0.08 mmol) and stirred at ambient temperature under a nitrogen atmosphere. Reaction progress was monitored by thin layer chromatography, and upon completion solvents were removed under reduced pressure. The residue was purified directly using silica gel flash column chromatography (petroleum ether 60/40: acetone, 7:1) yielding 6 as a dark yellow oil (0.12 g, 41 %). FT-IR (ATR) ν_{max} / cm^{-1} 3356 (μ_{NH}), 3112, 2022 (μ_{NN} triazole), 1926 (μ_{CO}), 1616, 1592, 1481, 1032. ^{1}H NMR (500 MHz, CD_2Cl_2): δ 7.93 (s, 1H), 7.16-7.23 (m, 3H), 6.69 (m, 1H), 5.46 (s, 2H), 4.85 (s, 2H), 3.84 (bs, 2H). ^{13}C NMR (125 MHz, $CDCl_3$): δ149.0, 148.0, 131.1, 130.4, 118.9, 116.3, 115.7, 112.5, 108.2, 80.8 (2C), 75.3 (2C). Anal. calcd for $C_{16}H_{11}MnN_4O_3$: C, 53.05; H, 3.06; N, 15.47; Found: C, 52.88; H, 2.90; N, 15.35. HRMS (ASAP): $[C_{16}H_{11}MnN_4O_3 + H]^+$ requires 363.0284; Found 363.0281 [M+H]+.

7.4.7. 3-[3-(Trifluoromethyl)diazirin-3-yl]phenyl cymantrene monocarboxylate 28

3-(Trifluoromethyl)-3-(3-hydroxyphenyl)diazirine (86.4 mg, 0.43 mmol), cymantrene carboxylic acid (106.0 mg, 0.43 mmol), N,N'-dicyclohexylcarbodiimide (88.2 mg, 0.43 mmol) and 4-dimethylaminopyridine (17.5 mg, 0.22 mmol) were dissolved in dry degassed CH_2Cl_2 and stirred in the dark for 24h. The solvent was then removed to give a white crystalline solid in a brown viscous oil. This was purified by column chromatography in 1:2 CH_2Cl_2 hexane eluent to give the desired product as a pale yellow oil. The oil was recrystallised from petroleum ether and CH_2Cl_2 to yield pale yellow crystals. (62.9 mg, 32 % yield) FT-IR (CH_2Cl_2) ν_{max} / cm^{-1} 2036 (ν_{CO}), 1958 (ν_{CO}), 1745 ($\nu_{C=OOMe}$) ^{1}H NMR (500 MHz, $CDCl_3$): δ 7.45 (t, 1H, J = 8.1 Hz), 7.23 (m, 1H), 7.09 (m, 1H), 6.99 (m, 1H), 5.61 (m, 1H), 5.61 (t, J = 2.2 Hz, 2H), 4.92 (t, J = 2.2 Hz, 2H). ^{13}C NMR (125 MHz, $CDCl_3$): δ130.29, 123.31, 124.35, 120.03, 86.07, 84.04. ^{19}F NMR (470 Hz, $CDCl_3$ δ65.14 (s, 3F) Anal. calcd for $C_{17}H_8F_3MnN_2O_5$: C, 47.24; H, 1.87; N, 6.48; Found: C, 47.17; H, 1.81; N, 6.39 HRMS (ASAP) $[C_{17}H_8F_3MnN_2O_5 + H]^+$ Requires: 432.1891, Found: 432.9837

7.5. Synthesis of cyrhetrene derivatives

7.5.1. η^5-[carboxyl]cyclopentadienyl tricarbonyl rhenium(I)

A solution of cyrhetrene (0.072 g, 0.2 mmol) and potassium *tert* butoxide (2.8mg, 0.03 mmol) was dissolved in THF (50ml) was cooled to -78 °C, after which *tert*-butyllithium (0.13 ml, 0.2 mmol) was added. The resulting deep red solution was left stirring for 1 hour at -78 °C. Carbon dioxide was introduced through a cannula and drying column from the sublimation of dry ice. The solution became pale yellow instantly, with CO_2(g) bubbled through the solution for a further 5 minutes. The solution was then warmed to room temperature and the solvent removed under reduced pressure to give a pale yellow residue. This was suspended in water and acidified with 0.1 mol dm^{-3} HCl causing a red solid to precipitate. The mixture was then extracted with Et_2O (3 x 50 ml) and dried over magnesium sulfate to yield the product as a white solid. (0.055 g, 68 %) FT-IR (ATR) ν_{max} / cm^{-1} 2028 (ν_{CO}), 1912 (ν_{CO}), 1676 ($\nu_{C=OOMe}$) ^{1}H NMR (500 MHz,$(CD_3)_2CO$) δ6.21 (t, J = 2.4 Hz, 2H), 5.71 (t, J = 2.4 Hz, 2H)

7.5.2. 3-[3-(Trifluoromethyl)diazirin-3-yl]phenyl cyrhetrene monocarboxylate 30

3-(Trifluoromethyl)-3-(3-hydroxyphenyl)diazirine (31.1 mg, 0.15 mmol), cyrhetrene carboxylic acid (57.7 mg, 0.15 mmol), N,N'-dicyclohexylcarbodiimide (31.7 mg, 0.15 mmol) and 4-dimethylaminopyridine (9.4 mg, 0.08 mmol) were dissolved in dry degassed CH_2Cl_2 and stirred in the dark for 24h. The solvent was then removed to give a grey microcrystalline solid. This was purified by column chromatography in 1:2 CH_2Cl_2 hexane eluent to give the desired product as a pale yellow oil. The oil was recrystallised from petroleum ether and CH_2Cl_2 to yield pale yellow crystals. (35.9 mg, 41 % yield) FT-IR (CH_2Cl_2) ν_{max} / cm^{-1} 2033 (ν_{CO}), 1941 (ν_{CO}), 1745 ($\nu_{C=OOMe}$) ^{1}H NMR (500 MHz, $CDCl_3$): δ 7.45 (t, 1H, J = 8.1 Hz), 7.22 (m, 1H), 7.10 (m, 1H), 6.97 (m, 1H), 6.16 (m, 1H), 5.47 (t, J = 2.2 Hz, 2H) ^{19}F NMR (470 Hz, $CDCl_3$ δ65.16 (s, 3F) Anal. calcd for $C_{17}H_8F_3MnN_2O_5$: C, 36.24; H, 1.43; N, 4.97; Found: C, 36.36; H, 1,535; N, 5.11 HRMS (ASAP) $[C_{17}H_8F_3N_2O_5Re + H]^+$ Requires: 563.4580, Found: 565.0021

7.5.3. η^5-[4-phenyltriazol-1-yl]cyclopentadienyl tricarbonyl rhenium(I) 20

To a solution of cyclopentadienylrhenium tricarbonyl azide **19** (0.1 g, 0.27 mmol) in acetonitrile (10 mL) was added phenylacetylene (0.03 g, 0.27 mmol) and $Cu(OAc)_2 \cdot H_2O$ (0.005 g, 0.027 mmol) and stirred at ambient temperature under a nitrogen atmosphere. Reaction progress was monitored by thin layer chromatography, and upon completion solvents were removed under reduced pressure. The residue was purified directly using silica gel flash column chromatography (petroleum ether 60/40: acetone, 15:2) yielding **20** as a white crystals after slow evaporation (0.072 g, 56%) FT-IR (ATR) ν_{max} / cm^{-1} 3125, 2961, 2012 (ν_{CO}), 1907 (ν_{CO}) 1530 ($\nu_{C=C}$), 1452, 1260, 1088, 1022, 875, 797 . ^{1}H NMR (500 MHz, $(CD_3)_2CO$): δ8.86 (s, 1H), 7.92 (s, 2H, d, J = 7 Hz), 7.47 (t, 2H, J = 7 Hz), 7.38 (t, 1H, J = 7Hz), 6.46 (s, 2H, J = 2 Hz), 5.78 (t, 2H, J = 2 Hz) 13C NMR (125 MHz,$CDCl_3$): δ 149.0, 147.2, 127.3 (2C), 120.0, 116.8, 115.4 (2C), 107.9, 80.0 (2C), 74.5 (2C). Anal. calcd for $C_{16}H_{11}MnN_4O_3$: C, 40.16; H, 2.11; N, 8.78; Found: C, 40.27; H, 2.01; N, 8.67. HRMS (ASAP):$[C_{16}H_{11}MnN_4O_3 + H]^+$ Requires 480.0353; Found 480.0346 [M+H]+.

7.5.4. η^5-[4-(amino)-4-phenyltriazol-1-yl]cyclopentadienyl tricarbonyl rhenium(I) 21

To a solution of cyrhetrenyl azide (0.12 g, 0.32 mmol) in acetonitrile (20 ml) was added 4-ethynylaniline (37.4 mg, 0.32 mmol) and $Cu(OAc)_2 \cdot H_2O$ (6.4 mg, 0.03 mmol) and stirred at ambient temperature under a nitrogen atmosphere. Reaction progress was monitored by thin layer chromatography, and upon completion solvents were removed under reduced pressure. The residue was purified directly using silica gel flash column chromatography (petroleum ether 60/40: acetone, 4:1) yielding [RECPHN] as a brown powder (0.041 g, 75 %). FT-IR (ATR) ν_{max} / cm^{-1} 3503 (ν_{NH}), 3407 (ν_{NN} triazole), 2025 (ν_{CO}), 1939 (ν_{CO}), 1908 (ν_{CO}). ^{1}H NMR (500 MHz, $CDCl_3$): δ7.77 (s, 1H), 7.65 (s, 2H), 6.75 (s, 2H), 5.41 (s, 2H), 4.80 (s, 2H), 3.82 (bs, 2H). 13C NMR (125 MHz,$CDCl_3$): δ 149.9, 130.4, 127.6, 119.4, 118.4, 115.2, 113.0, 84.1, 77.2. Anal. calcd for $C_{16}H_{11}MnN_4O_3$: C, 38.94; H, 2.25; N, 11.35; Found: C, 39.02; H, 2.14; N, 11.19. HRMS (ASAP):$[C_{16}H_{11}MnN_4O_3 + H]^+$ Requires 495.0462; Found 495.0457 [M+H]+.

References

(1) *CrysAlisPro, Agilent Technologies, Yamton, U.K.*

(2) O. V. Dolomanov, L. J. Bourhis, R. J. Gildea, J. A. K. Howard and H. Puschmann, *J. Appl. Crystallogr.*, 2009, **42**, 339–341.

(3) L. Palatinus and G. Chapuis, *J. Appl. Crystallogr.*, 2007, **40**, 786–790.

(4) L. Palatinus, S. J. Prathapa and S. van Smaalen, *J. Appl. Crystallogr.*, 2012, **45**, 575–580.

(5) G. M. Sheldrick, *Acta Crystallographica Section A Foundations of Crystallography*, 2007, **64**, 112–122.

(6) L. J. Farrugia, *J. Appl. Cryst.*, 1999, **32**, 837–838.

(7) J. L. Farrugia, *J. Appl. Cryst.*, 2012, **45**, 849–854.

(8) R. G. Compton and I. M. Banks, *Understanding Voltammetry*, Imperial College Press, 2nd, 2011.

(9) G. Gritzner and J. Kuta, *Electrochim. Acta*, 1984, **29**, 869–873.

(10) E. Martin, D. L. Hughes and S. J. Lancaster, *Inorg. Chim. Acta*, 2010, **363**, 275–278.

(11) R. J. LeSuer, C. Buttolph and W. E. Geiger, *Anal. Chem.*, 2004, **76**, 6395–6401.

A. Crystallography Data

Table A.1. Crystal structure analysis of compound **13**

Crystal data and structure refinement for **13**	
Elemental formula	$C_{16}H_{10}MnN_3O_3$
Formula weight	347.21
Crystal system, space group	Orthorhombic, $P2_1cn$
Unit Cell Dimensions	a = 33.3395(13) Å α= 90° b = 5.9474(12) Å β= 90° c = 14.4477(5) Å γ= 90°
Volume	2864.74(18) Å
Z, calculated density	8, 1.610 Mg/m^3
F(000)	1408
Absorption coefficient	0.940 mm^{-1}
Crystal size	0.35 x 0.28 x 0.02 mm
Crystal mounting	on a glass fibre, in oil, fixed in cold N_2 stream
On the diffractometer	
Theta range for data collection	3.36 to 30.00 °
Limiting indices	-46≤h≤46, -8≤k≤8, -20≤1≤20
Reflections collected (not including absences)	51567
No. of unique reflections	8347 [R(int) for equivalents = 0.084]
Data / restraints / parameters	8347 / 1 / 423
Goodness-of-fit on F^2	1.160
Final R indices ('observed' data)	R_1 = 0.071, WR_2 = 0.0158
Final R indices (all data)	R_1 = 0.077, WR_2 = 0.0161
Largest diff. peak and hole	0.71 and -0.93 $eÅ^{-3}$

Table A.2. Crystal structure analysis of compound **15**

Crystal data and structure refinement for **15**	
Elemental formula	$C_{16}H_{11}MnN_4O_3$
Formula weight	362.23
Crystal system, space group	Triclinic, P-1$_1$cn
Unit Cell Dimensions	a = 5.8394(3) Å α= 106.742(5) ° b = 9.7556(5) Å β= 94.508(4) ° c = 13.9033(8) Å γ= 102.614(4)
Volume	731.61(7) Å
Z, calculated density	2, 1.644 Mg/m^3
F(000)	368
Absorption coefficient	0.926 mm^{-1}
Crystal size	0.42 x 0.11 x 0.045 mm
Crystal mounting	on a glass fibre, in oil, fixed in cold N_2 stream
On the diffractometer	
Theta range for data collection	3.10 to 27.50 °
Limiting indices	-7≤h≤7, -12≤k≤12, -18≤1≤18
Reflections collected (not including absences)	11972
No. of unique reflections	3366 [R(int) for equivalents = 0.040]
Data / restraints / parameters	3366 / 0 / 225
Goodness-of-fit on F^2	1.173
Final R indices ('observed' data)	R_1 = 0.048, WR_2 = 0.117
Final R indices (all data)	R_1 = 0.058, WR_2 = 0.121
Largest diff. peak and hole	0.59 and -0.29s eÅ^{-3}

Table A.3. Crystal structure analysis of compound **20**

Crystal data and structure refinement for **20**	
Elemental formula	$C_{16}H_{10}N_3O_3Re$
Formula weight	478.47
Crystal system, space group	orthorhombic, *Pbn*2$_1$
Unit Cell Dimensions	a = 5.8939(17) Å α= 90 ° b = 14.717(5) Å β= 90 ° c = 33.422(10) Å γ= 90 °
Volume	2899.1(15) Å
Z, calculated density	8, 2.192 Mg/m^3
F(000)	1808
Absorption coefficient	0.714 mm^{-1}
Crystal size	0.09 x 0.01 x 0.01 mm
Crystal mounting	on a glass fibre, in oil, fixed in cold N_2 stream
On the diffractometer	
Theta range for data collection	2.8 to 27.6 °
Limiting indices	-7≤h≤7, -18≤k≤18, -41≤1≤41
Reflections collected (not including absences)	31312
No. of unique reflections	5496 [R(int) for equivalents = 0.1664]
Data / restraints / parameters	5495 / 1 / 417
Goodness-of-fit on F^2	1.041
Final R indices ('observed' data)	R_1 = 0.0616, WR_2 = 0.1519
Final R indices (all data)	R_1 = 0.0644, WR_2 = 0.1553
Largest diff. peak and hole	3.421 and -2.712 s eÅ^{-3}

Table A.4. Crystal structure analysis of compound **28**

Crystal data and structure refinement for **28**	
Elemental formula	$C_{17}H_8F_3MnN_2O_5$
Formula weight	432.19
Crystal system, space group	triclinic, P-1
Unit Cell Dimensions	a = 7.7058(5) Å α= 87.115(4) ° b = 9.8674(4) Å β= 86.088(4) ° c = 11.4575(5) Å γ= 87.641(4) °
Volume	867.43(8) Å
Z, calculated density	2, 1.655 Mg/m^3
F(000)	432
Absorption coefficient	0.825 mm^{-1}
Crystal size	0.2 x 0.05 x 0.05 mm
Crystal mounting	on a glass fibre, in oil, fixed in cold N_2 stream
On the diffractometer	
Theta range for data collection	3.096 to 32.569 °
Limiting indices	-11≤h≤11, -14≤k≤14, -16≤1≤17
Reflections collected (not including absences)	18534
No. of unique reflections	5756 [R(int) for equivalents = 0.0551]
Data / restraints / parameters	5756 / 0 / 285
Goodness-of-fit on F^2	1.043
Final R indices ('observed' data)	R_1 = 0.0482, WR_2 = 0.1026
Final R indices (all data)	R_1 = 0.0719, WR_2 = 0.1134
Largest diff. peak and hole	0.510 and -0.396 $eÅ^{-3}$